ADVANCED STEEL CONSTRUCTION

An International Journal

Volume 21 Number 2

April 2025

CONTENTS

Technical Papers

Website: *http://www.hkisc.org*
ISSN 1816-112X
Science Citation Index Expanded, Materials Science Citation Index and ISI Alerting
Cover: 'Weaving Love' 3D Printed Metal Pavilion. Photo@ Siwei Liu
e-copy of IJASC is free to download at "www.ascjournal.com" in internet and mobile apps.

ADVANCED STEEL CONSTRUCTION

VOL.21, NO.2 (2025)

ADVANCED STEEL CONSTRUCTION

an International Journal

ISSN 1816-112X

Volume 21 Number 2 *April 2025*

ISSN 1816-112X

Science Citation Index Expanded, Materials Science Citation Index and ISI Alerting

Advanced Steel Construction
an international journal

Cover: 'Weaving Love' 3D Printed Metal Pavilion. Photo@ Siwei Liu
e-copy of IJASC is free to download at "www.ascjournal.com" in internet and mobile apps.

General Information
Advanced Steel Construction, an international journal

Aims and scope

The International Journal of Advanced Steel Construction provides a platform for the publication and rapid dissemination of original and up-to-date research and technological developments in steel construction, design and analysis. Scope of research papers published in this journal includes but is not limited to theoretical and experimental research on elements, assemblages, systems, material, design philosophy and codification, standards, fabrication, projects of innovative nature and computer techniques. The journal is specifically tailored to channel the exchange of technological know-how between researchers and practitioners. Contributions from all aspects related to the recent developments of advanced steel construction are welcome.

Subscription inquiries and change of address. Address all subscription inquiries and correspondence to Member Records, IJASC. Notify an address change as soon as possible. All communications should include both old and new addresses with zip codes and be accompanied by a mailing label from a recent issue. Allow six weeks for all changes to become effective.

The Hong Kong Institute of Steel Construction
HKISC
c/o Prof. SL Chan,
Unit 209B, Photonics Centre, No. 2 Science Park East Avenue,
Hong Kong Science Park, Shatin, N.T., Hong Kong, China.
Tel: 852- 3595 6150 Fax: 852- 3619 7238
Email: ceslchan@connect.polyu.hk Website: *http://www.hkisc.org/*
ISSN 1816-112X
Science Citation Index Expanded, Materials Science Citation Index and ISI Alerting

ISSN 1816-112X

Science Citation Index Expanded, Materials Science Citation Index and ISI Alerting

Advanced Steel Construction
an international journal

VOLUME 21 NUMBER 2 April 2025

Technical Papers

Advanced Steel Construction – Vol. 21 No. 2 (2025) 95–109
DOI:10.18057/IJASC.2025.21.2.1

AXIAL COMPRESSION BEHAVIOR OF DOUBLE-SKIN COMPOSITE SHEAR WALL WITH T-STIFFENER AND HEADED STUD CONNECTORS

Mohammed Amer [1, *], Zhi-Hua Chen [1, 2, 3], Yan-Sheng Du [1, 2, 3, *], W. A. H Mashrah [4] and Saleh Ahmad Laqsum [1]

[1] *School of Civil Engineering, Tianjin University, Tianjin, 300072, China*
[2] *Key Laboratory of Coast Civil Structure Safety of Ministry of Education, Tianjin University, Tianjin, China*
[3] *State Key Laboratory of Hydraulic Engineering Intelligent Construction and Operation, Tianjin University, Tianjin, China*
[4] *Dali Construction Group Co., Ltd, Hangzhou, 310000, China*
** (Corresponding author: E-mail: amer@tju.edu.cn; duys@tju.edu.cn)*

ABSTRACT

Double-skin composite shear walls (DSCSWs) offer high strength and improve construction processes in tall structures, offshore constructions, and nuclear power plants. This paper investigates the compressive performance of DSCSWs, which consist of concrete sandwiched between two external steel faceplates and bonded with connectors at regular intervals. Three-dimensional finite element (FE) modeling is established and verified against five axial compression test specimens to predict the ultimate compressive capacity and failure modes of DSCSWs with bolts, head studs, and T-stiffener connectors. Parametric studies evaluate the impact of five factors on the compressive performance of DSCSWs. The results show that different connectors provide confinement to the concrete core, enhancing the compressive capacity of DSCSWs, with T-stiffeners being the most effective. Furthermore, variations in the thickness of the steel plates, concrete core, and height of the walls significantly affect the strength and ductility of DSCSWs, while changes in bolt spacing have insignificant effect. Finally, the ultimate compressive capacity of DSCSWs is calculated using code equations and an analytical method. The prediction results show a good correlation with the numerical results. These findings provide valuable insights for implementing DSCSWs in engineering applications, particularly in design for practical use.

ARTICLE HISTORY

Received: 12 August 2024
Revised: 18 December 2024
Accepted: 20 December 2024

KEYWORDS

Double-skin-composite shear wall (DSCSW);
Compressive performance;
T-stiffener connector;
Local buckling;
Finite element modeling (FEM)

1. Introduction

Over the past few decades, reinforced concrete (RC) shear walls have been the primary structural element to resist lateral forces in tall structures, supporting vertical and horizontal loads. Despite their widespread use, RC shear walls have several drawbacks, including limited ductility, susceptibility to cracking, considerable thickness, and complex construction requirements [1-4]. To enhance the performance of shear walls, researchers have proposed various composite shear walls including steel plate shear walls [5-8], concrete-encased profile steel composite shear walls [9], steel plate-reinforced concrete shear walls [10] and double steel plate composite shear walls (DSCSWs) [11-14]. Among these, the double steel plate DSCSWs is particularly advantageous due to its superior performance, reduced wall thickness, and potential for prefabrication. This type of DSCSWs consists of two steel plates on the surface, with concrete sandwiched in between, and the steel plates are connected to the concrete using different shear connectors. To improve the bond between steel plates and concrete, researchers have explored various types of shear connectors, including welded stiffeners [15], welded short studs [16], welded or mechanical pulling bars [17, 18], welded trusses [19], and specially designed connectors [20]. These types of connectors aim to increase the bold interactions between steel plates and concrete core, preventing the local buckling and improve the compressive capacity of walls [21-23]. The DSCSWs has many applications such as nuclear power plant walls, offshore walls, offshore constructions, urban roads, bridges, shield tunnels, military shelters [22-27].

This study focuses on DSCSWs constructed with thin-walled steel plates. The shear studs, which are commonly employed as connectors in conventional DSCSWs, are recognized for their straightforward manufacturing process and robust connection performance. Research by Choi et al. [28] and Fan et al. [29] explored the behavior of DSCSWs subjected to axial compression with shear stud connectors. Their findings revealed that the primary failure mechanism in these structures under axial loads is the local buckling of the steel plates. Yan et al. [30] examined the performance of DSCSWs connected with shear studs of varying lengths under axial compression. They discovered that while increasing shear stud length improved the axial load capacity, it had minimal impact on the localized buckling characteristics of the steel plates. On the other hand, Nie et al. [15] evaluated DSCSWs incorporating stiffeners and batten plate connectors, finding that the combination of shear studs with other types of connections could effectively reduce local buckling. This indicates that pairing shear studs with alternative connection designs can enhance the resistance to local buckling in thin-walled steel plate DSCSWs.

Several researchers have proposed novel designs incorporating profiled steel components to improve both the assembly process and mechanical performance of DSCSWs. Chen et al. [31, 32] introduced a DSCSW utilizing C-shaped steel units, while Guo et al. [32] and He et al. [33, 34] recommended the use of H-shaped and L-shaped steel units, respectively. These innovations help reduce the width-to-thickness ratio of the steel face plates, enhancing steel-concrete interaction and increasing stiffness due to the structural stability of the cross-sectional shapes. Moreover, these profiled steel units can act as formwork for concrete pouring, offering cost savings in construction. The standardization of these units also paves the way for increased industrial production. However, there are challenges with C- and H-profiled steel units, as shear connectors cannot be welded into their narrow web flanges, and L-profiled units require significant welding during assembly. To overcome these challenges, a new DSCSW design featuring Z-profiled steel units with shear studs welded into the flange has been proposed [11-13, 35, 36]. Studies examining the cyclic and axial compression performance of these DSCSWs, using iron tiling recycled aggregate concrete revealed that the cyclic tests exhibited strong bearing capacity, stiffness, and energy dissipation, suggesting that iron tiling recycled aggregate concrete could serve as a viable alternative to traditional concrete. The axial compression tests indicated that incorporating shear studs improved both the axial bearing capacity and initial stiffness. However, increasing the spacing of the inner diaphragm led to a decrease in axial bearing capacity, initial stiffness, and ductility. On the other hand, increasing the height-to-thickness ratio significantly enhanced both initial stiffness and ductility, with minimal impact on bearing capacity.

Since the time and cost of conducting testing program, the finite element technique becomes more used and offers alternative methods to analyze structural performance [14, 37-40]. FE modeling provides acceptable results and a practical approach to simulating different parts of the DSCSWs, with complicated interactions among concrete slab, steel plates and connections, different load and boundary conditions, and different grade materials. Former researchers concentrated on the push-out shear tests of headed connectors [41-45]. On the other hand, a series of numerical investigations on structural performance on DSCSWs with ultra-lightweight concrete, cementitious materials, including several parameters and types of connectors, were developed and compared with experimental results [20, 27, 43, 46], resulting to a great understanding on the impact of key factors that might impact the structural performance which can lead to the implementation to researcher and designers. FE modeling analysis was also used to simulate the load-deflection curves, ultimate compressive capacity, and deformation patterns of the walls, and experimental and numerical results proved that all the proposed equations could be used for the design of DSCSWs with all types of connectors [46]. Yan et al. [47] proposed a three-dimensional damage plasticity-based FE model to simulate the ultimate compressive capacity of DSCSWs subjected to axial load. The concrete damage plasticity model (CDPM) was used to simulate the ultimate capacity of the concrete, and the continuum damaged model (CDM)

was also used to simulate the evolution of steel materials. The results showed that the FE model provided reliable estimations of ultimate strength, load-deflection behavior, and failure modes in Steel-concrete-steel sandwich plates, offering a useful tool for analyzing steel-composite structures with mechanical shear connectors.

This study focuses on the compressive behavior of DSCSWs using bolts, headed studs, and T-stiffener connectors. The ultimate axial load-bearing behavior of walls incorporating normal-weight concrete is investigated. FE models were developed using ABAQUS CAE software to study the compressive behavior and failure modes. The FE modeling findings were verified against five tested specimens to enhance the reliability of the findings. This study also examines the impact of various factors on the ultimate compressive capacity, initial stiffness, ductility index, and ultimate vertical displacement of DSCSWs. Additionally, calculation methods from AISC 360, Eurocode 4, and analytical approaches are included to predict the ultimate axial bearing capacity, with a comparison to the FE modeling results.

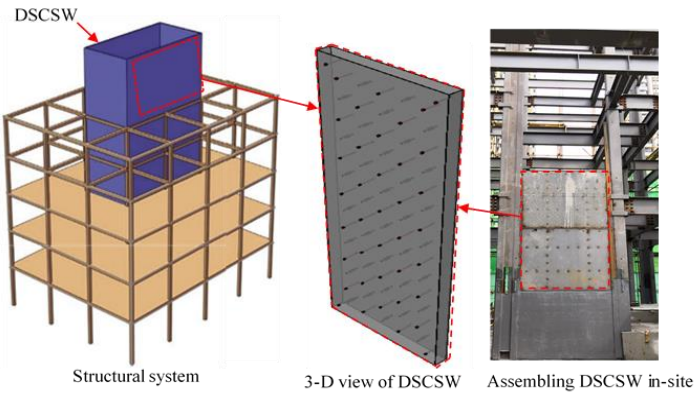

(a) High-rise buildings

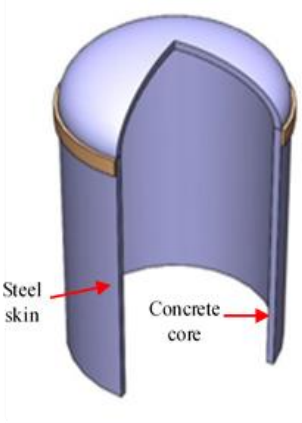

(b) Nuclear power plant

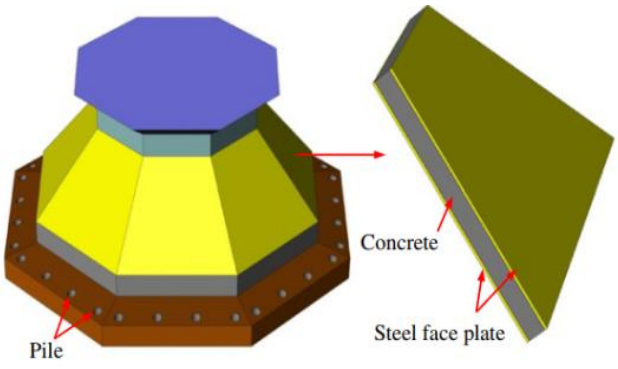

(c) DSCSW in protective Arctic offshore constructions

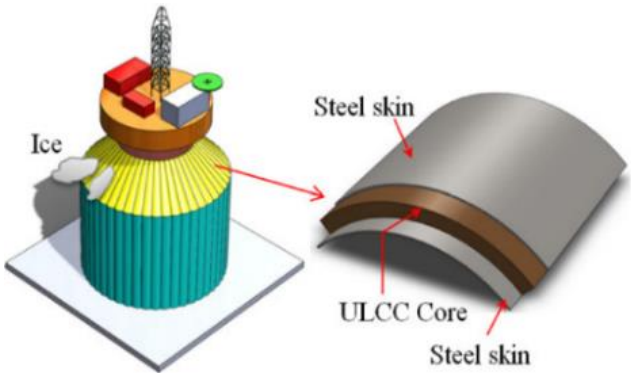

(d) Conical Arctic structure

Fig. 1 Applications of DSCSW in different structures

2. Experimental program

2.1. Specimen design

A total of five specimens were created and tested to examine the axial compression performance of DSCSWs. Each specimen consisted of four primary components: a concrete core, steel faceplates, side steel plates, and connectors, as illustrated in Fig. 2(a-e). Specimen W1 had a height of 600 mm, while specimens W2, W3, W4, and W5 were designed with heights of 1500 mm and 3000 mm to investigate the effect of height on DSCSW performance. The steel faceplate and concrete core thicknesses were kept constants for all specimens at 6 mm and 118 mm for all specimens, respectively. Three types of connectors were used in this study: bolts, headed studs, and T-stiffeners, as depicted in Fig. 2(c-e). The detailed specifications of the specimens are provided in Table 2, which presents the geometric dimensions, including length, height, width, steel plate thickness, concrete core thickness, connector spacing, and connector types.

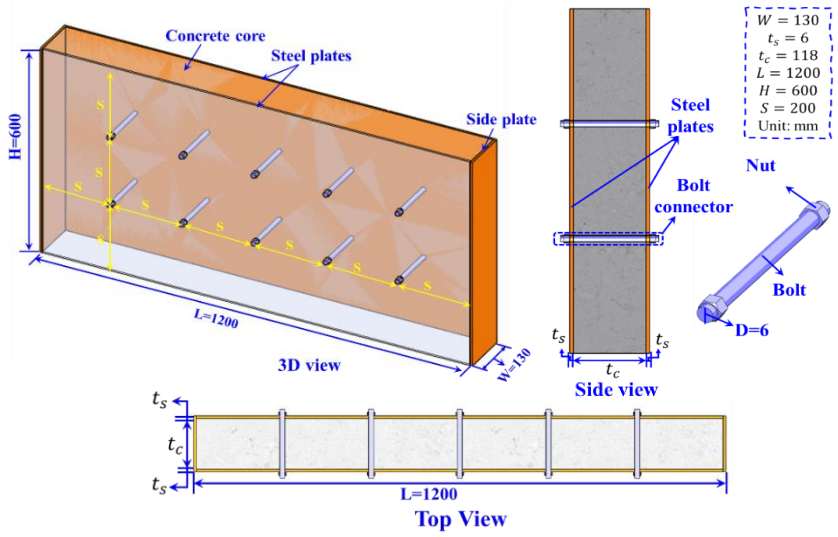

(a) W-1

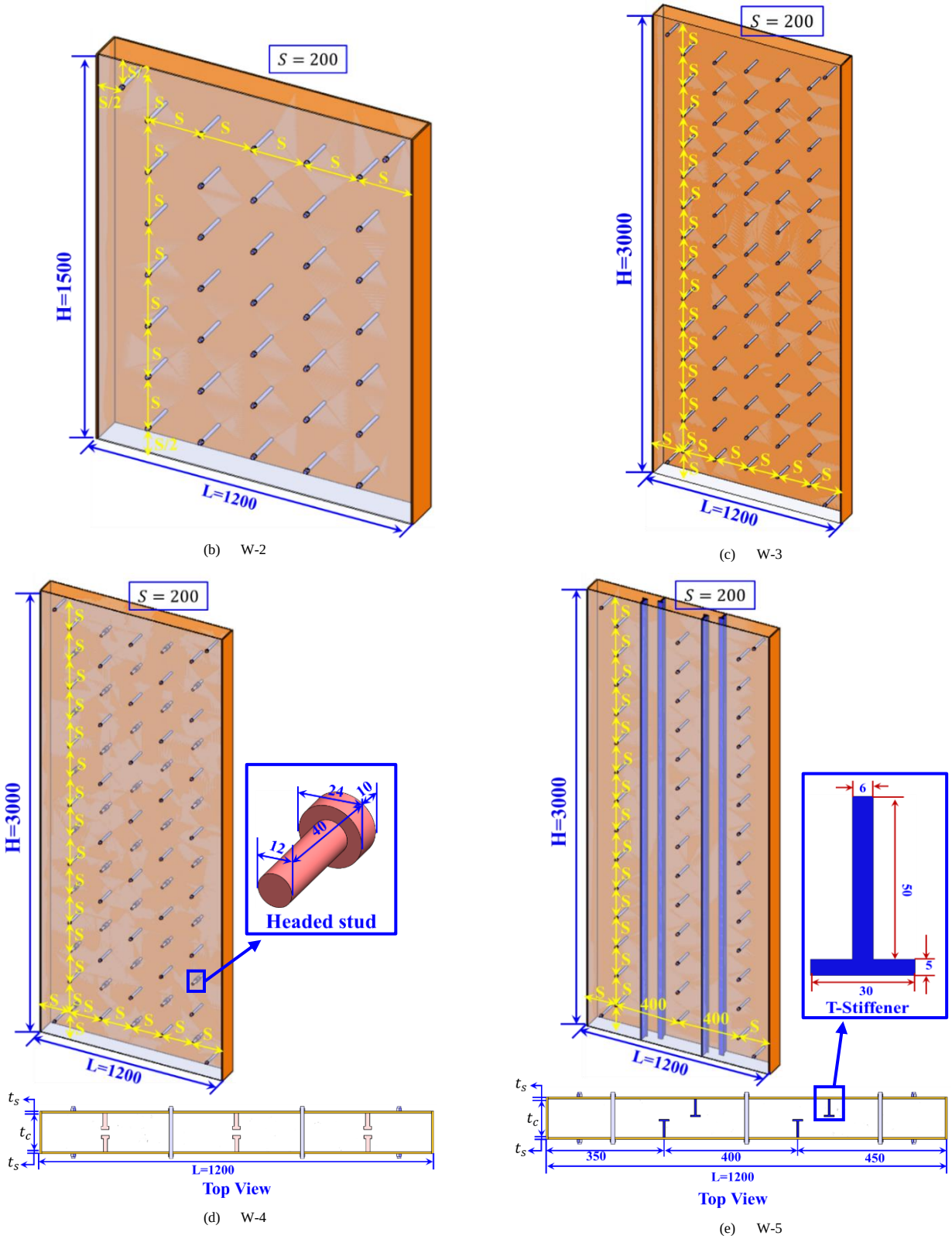

Fig. 2 Details of DSCSW with different types of connectors

Table 1
General details of the specimens

Specimens ID	L (mm)	H (mm)	w (mm)	H/w	t_s (mm)	t_c (mm)	S (mm)	S/t_s	Type of connectors
W-1	1200	600	130	4.62	6	118	200	33.33	Bolts
W-2	1200	1500	130	11.08	6	118	200	33.33	Bolts
W-3	1200	3000	130	23.08	6	118	200	33.33	Bolts
W-4	1200	3000	130	23.08	6	118	200	33.33	Bolts & headed stud
W-5	1200	3000	130	23.08	6	118	150/200/250	33.33	Bolts &T-Stiffeners

where $L, H, and\ w$ indicate to the length, height and width of the wall respectively, $t_s\ and\ t_c$indicate the thickness of steel plates and thickness of concrete core respectively, S indicates the spacing between connectors

2.2. Materials properties

The concrete cubic blocks, with dimensions of 100 × 100 × 100 mm, were tested in accordance with the GB/T50081-2010 standard [48]. The average compressive strength of the concrete was 28.57 MPa, with a Young's modulus of 31.6 GPa. Q355 steel was adopted for the manufacture of steel plates and T-stiffeners. Table 2 lists the results of three coupons of the same thickness that were prepared and tested, including the yield strength and ultimate strength.

Table 2
Test results in steel material properties

Thickness (mm)	Yield strength (MPa)	Ultimate strength (MPa)	Modulus of Elasticity (GPa)
6 (Steel plate)	345.32	522.50	186
5 (stiffener)	366.49	470.53	193

2.3. Test setup

Fig. 3 shows the testing setup for DSCSWs under in-plane compression load. It demonstrates that all specimens were positioned directly on a rigid support to simulate the fixed support at the bottom loading plate, using a 1500-ton MTS testing machine. The loading procedure was divided into two phases: pre-loading and formal loading. During the pre-loading phase, 10% of the ultimate load was applied, held for 5 minutes, and then unloaded to zero. This ensured proper contact between the specimens and the loading apparatus and confirmed the measuring instruments' functionality. In the formal loading phase, the load gradually increased at the same rate as in the pre-loading phase until the ultimate bearing capacity of the wall was reached. After achieving the compressive capacity, significant visible deformation was observed. The concrete cracking and buckling of the steel plates were recorded during each loading stage.

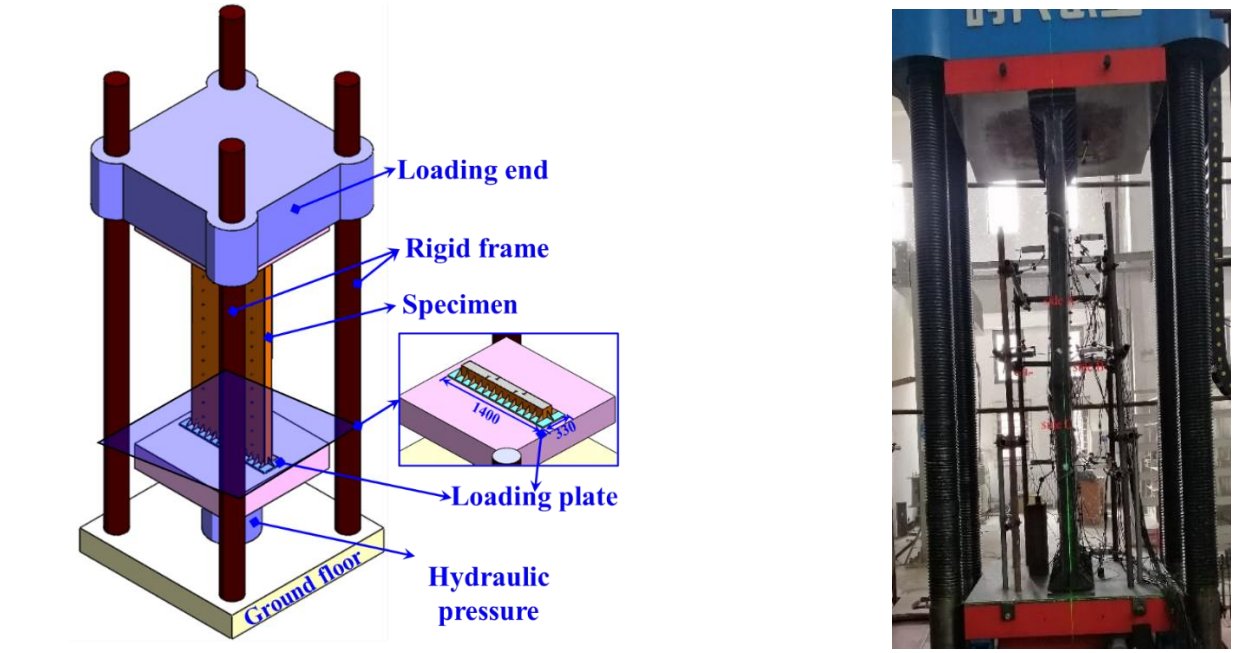

(a) 3-D diagram of testing setup

(b) Loading process in laboratory

Fig. 3 Testing machine and test setup

3. Finite element model on DSCSWs

Based on experimental investigations cited in reference [49], FE models were established in ABAQUS/standard [50] to investigate the compressive behavior and structural stability of DSCSWs under axial compression load. Geometrical, material nonlinearities, meshing convergence, the complexity of contact, loading, and boundary conditions were considered. Parametric studies were elaborated to comprehend the effect of key parameters on the compressive behavior of DSCSWs, including types of connectors, height of the wall, steel plates' thickness, bolt connectors' spacing, and thickness of the concrete core. The details of FE models are listed in Table 3.

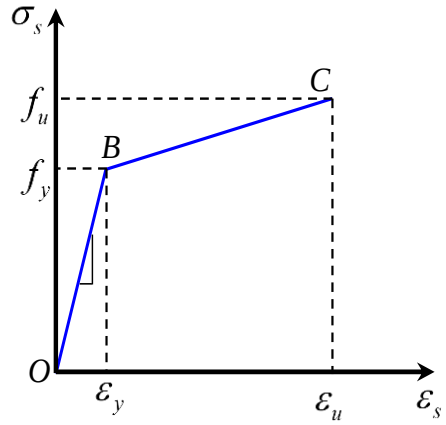

Fig. 4 Stress-Strain steel material model

3.1. Material model

3.1.1. Steel model

A nonlinear isotropic/kinematic hardening model was used to simulate all steel elements. The von Mises yield criterion was applied to represent the isotropic yielding of all components in the FE model. The model exhibited bi-linear behavior with strain hardening, as illustrated in Fig. 4. The values for the modulus of elasticity, yield strength, and ultimate strength are provided in Table 2.

3.1.2. Concrete constitutive

The Concrete Damage Plasticity Model (CDPM), a continuum and plasticity-based damage model in ABAQUS, is used to simulate the core concrete of the DSCSW. Two deformations methods are considered: compressive crushing and tensile cracking of the concrete. The compressive stress-strain curve for C30 concrete was gotten according to GB50010-2010 [51], which was adopted to standardize the input data for compressive stress versus inelastic strain ($\tilde{\varepsilon}_c^{in}$), as shown in Fig. 5(a). For compressive behavior, the stress-strain response of plain concrete in uniaxial compression outside the elastic range can be stated using plasticity and damage parameters. Unloading data is provided in CDPM based on compressive damage curves [50], as described by the following equation.

$$\tilde{\varepsilon}_c^{pl} = \tilde{\varepsilon}_c^{in} - \frac{d_c}{(1-d_c)}\frac{\sigma_c}{E_0} \quad (1)$$

where $\varepsilon_c^{el} = \frac{\sigma_c}{(1-d_c)E_0}$ which is defined as the difference between total strain ε_c and plastic strain $\tilde{\varepsilon}_c^{pl}$; $\tilde{\varepsilon}_c^{el}$ is the elastic strain corresponding to the undamaged materials with $\tilde{\varepsilon}_c^{el} = \frac{\sigma_c}{E_0}$, which is equal to $\varepsilon_{0c}^{el} = \varepsilon_c - \tilde{\varepsilon}_c^{in}$; $\tilde{\varepsilon}_c^{in}$ is the inelastic strain instead of plastic strain $\tilde{\varepsilon}_c^{pl}$, by which ABAQUS automatically converts the inelastic strain values $\tilde{\varepsilon}_c^{in}$ to plastic strain values $\tilde{\varepsilon}_c^{pl}$. Besides, σ_c denotes the uniaxial compressive stress, and E_0 denotes young's modulus. For tensile behavior, ABAQUS automatically converts the inelastic strain to plastic strain. As shown in Fig. 5.(b), unloading data can be given in CDPM based on the tensile damage curve expressed by the following equation.

$$\tilde{\varepsilon}_t^{pl} = \tilde{\varepsilon}_t^{ck} - \frac{d_t}{(1-d_t)}\frac{\sigma_t}{E_0} \quad (2)$$

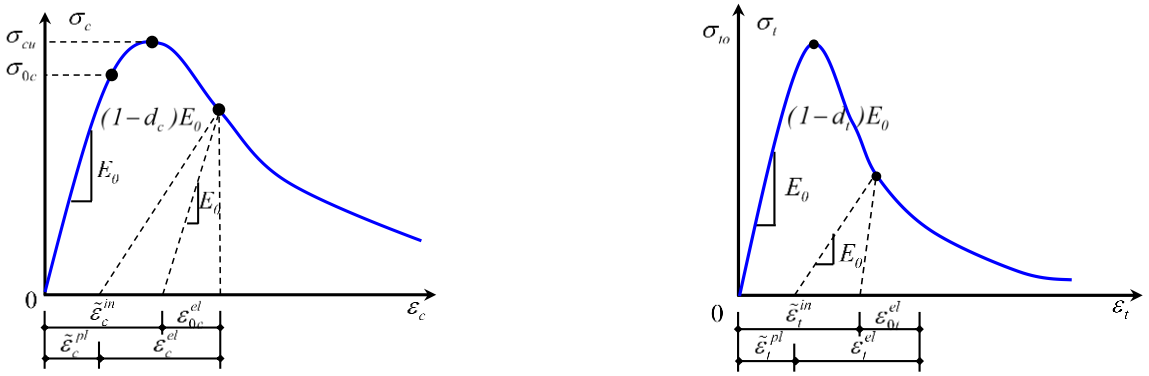

(a) Compressive damage curves (b) Tensile damage curves

Fig. 5 Damage curves of concrete

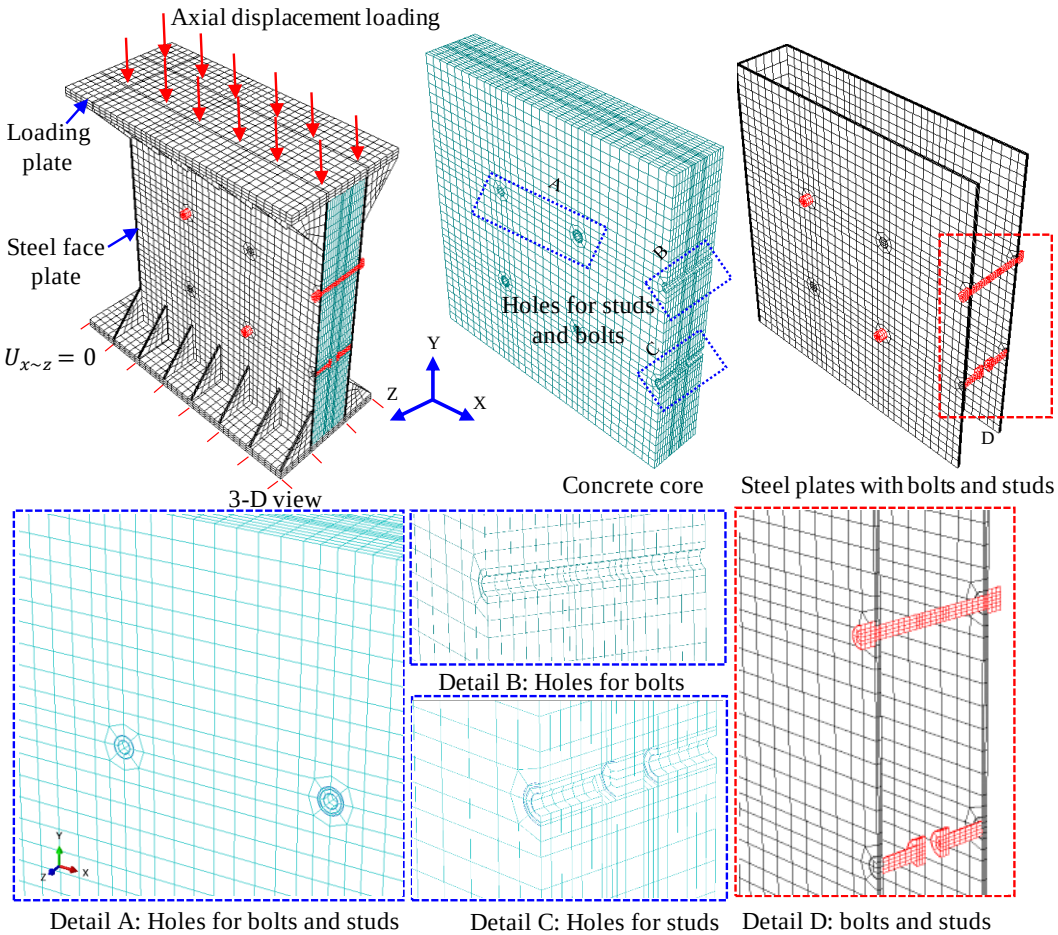

Fig. 6 Typical finite element model for DSCSW

3.2. Element mesh and interactions

ABAQUS/CAE offers a wide range of element types, including link, beam, connection, solid, thin-film, and infinite elements. An eight-node solid element with reduced integration (C3D8R) was selected to model all components, including the loading plates, steel plates, concrete core, bolts, headed studs, and T-stiffener connectors [47, 52-54]. A series of mesh sensitivity considers were performed to balance the accurateness of the FE model with computational efficiency. As a result, the general mesh size for all elements was set to 20mm, except for the bolts and headed studs, which were meshed with sizes of 10mm and 4mm, respectively. The geometry of the DSCSW node is generally symmetrical, and for a more detailed simulation, the connectors were explicitly modeled. Holes were incorporated in the steel plates and concrete core to accommodate the connectors, as shown in Fig. 6.

The contact relationship of the DSCSW wall's node model is defined as frictional contact. A surface-to-surface contact algorithm was used to model the interactions among various elements of the DSCSW, including the bolts, headed studs, T-stiffeners, the concrete core and the steel plates. The contact surfaces

were defined based on the material hardness, with the bolts, headed studs, T-stiffeners, and steel plates elected as the master surface, and the concrete core selected as the slave surface. The contact algorithm allows penetration of the master surface into the slave surface, but not the reverse. The interaction properties account for the transfer of forces in both the tangential and normal directions at the steel-concrete interface. In the tangential direction, "penalty friction" was used to simulate the frictional force between the concrete and steel, with a friction coefficient of $\mu = 0.4$ [37, 55]. Additionally, a tie constraint was applied to simulate the welding behavior of the steel plates.

3.3. Loading process and boundary conditions

The axial load was applied as a point displacement load on the top loading plate, with a coupling constraint created between the loading point and the surface of the loading plate. The load was applied in two steps. The first step represented the pre-loading phase in the experiments, while the second step represented the main loading phase. The point load was considered as the master surface, and the loading plate surface was treated as the slave surface. The point load was constrained to prevent movement in any direction, while the bottom plate surface was also constrained from moving in any direction [54, 56, 57]. Symmetrical restraints were applied to the corresponding surface in the FEM, as shown in Fig. 6.

3.4. Validations of FE models

Fig. 7(a-e) presents a comparison of the load-displacement behavior between the experimental and FE modeling results. Table 4 summarizes the comparison of the ultimate compressive capacity, initial stiffness, and ductility index between the experimental and FE results. The FE models tend to slightly overestimate both the ultimate compressive capacity and initial stiffness of DSCSWs by about 7%, with standard deviations of 0.06 for the ultimate compressive capacity and 0.04 for initial stiffness. The ductility predicted by the FE models is highly accurate, although it shows a minor overestimation of 2%. The small discrepancies observed for specimens W-2 and W-3, where the FE modeling calculates higher ultimate compressive capacity and stiffness than the experimental data, could be attributed to factors such as manufacturing imperfections, variations in the concrete's modulus of elasticity, or differences in the loading process. Overall, the FE models demonstrate good accuracy for all parameters, indicating their reliability for further parametric studies on the compressive behavior of DSCSWs.

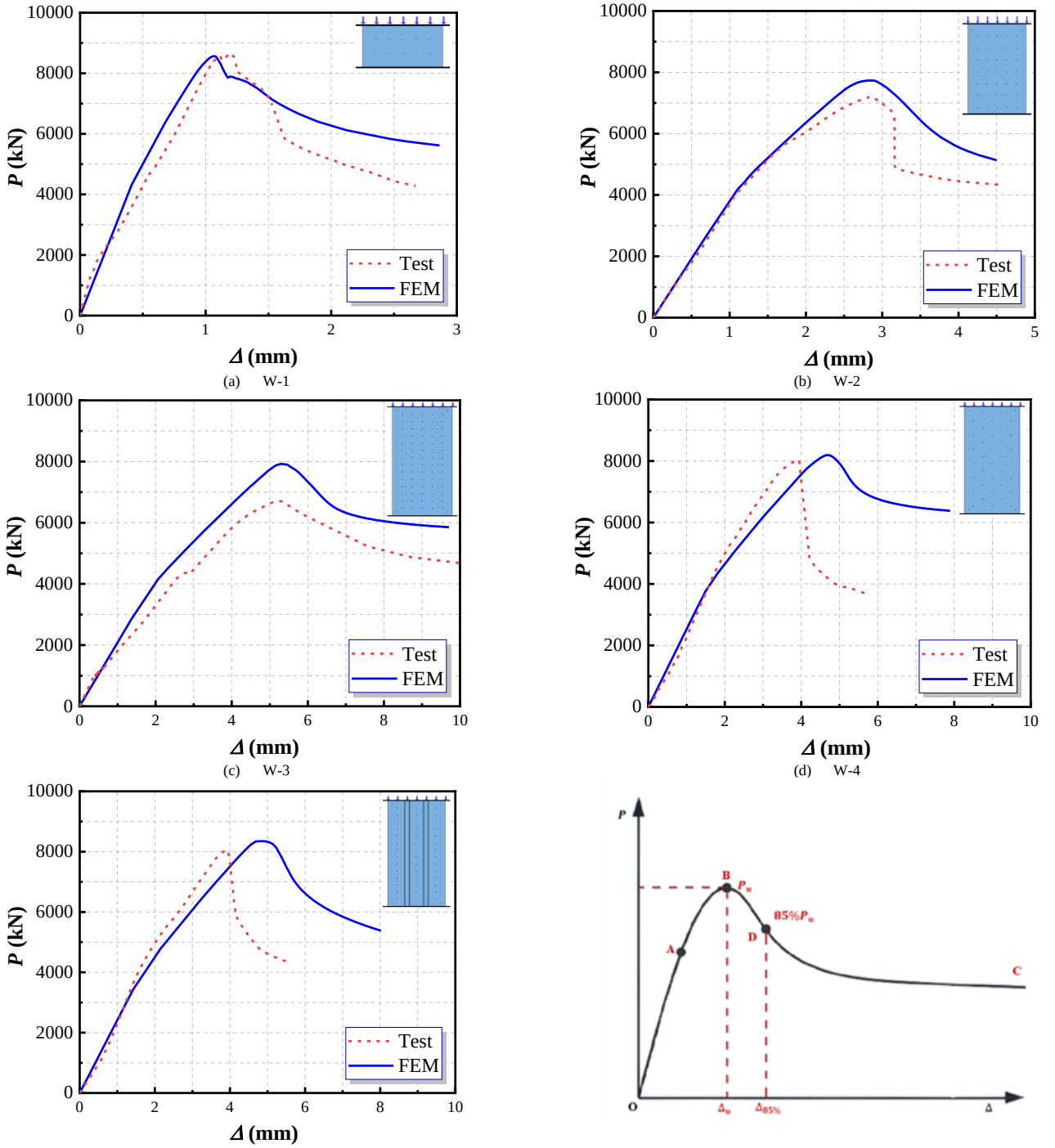

Fig. 7 Experimental and FE modeling of load-displacement curves (P − Δ) of DSCSW

Table 3
Accuracy of FE modeling results

`	$P_{u,FEM}$ (kN)	$P_{u,FE}$ (kN)	$\frac{P_{u,Test}}{P_{u,FE}}$	$K_{e,Test}$ (kN/mm)	$K_{e,FE}$ (kN/mm)	$\frac{K_{e,Test}}{K_{e,EFM}}$	DI_{Test}	DI_{FEM}	$\frac{DI_{Test}}{DI_{FEM}}$
W-1	8659	8870	0.98	9845	10424	0.94	1.20	1.35	0.94
W-2	7200	8226	0.88	3595	4054	0.89	1.12	1.21	0.93
W-3	6735	7853	0.86	1797	2088	0.87	1.31	1.18	1.11
W-4	8060	8191	0.98	2308	2406	0.96	1.17	1.19	0.98
W-5	8063	8350	0.97	2342	2413	0.93	1.13	1.15	0.98
average			0.93			0.93			0.98
Std.v			0.06			0.04			0.07

where H/w denotes the ratio of height to width of the specimens; $P_{u,Test}$ and $P_{u,FEM}$ denote the compressive capacity from experimental and FE modeling , respectively; $K_{e,Test}$, $K_{e,FEM}$ denote the initial stiffness from experimental and FE modeling , respectively. DI_{Test} and DI_{FEM} are the ductility index that obtained from test and FE modeling.

Fig. 8(a-e) compares the deformation patterns between the FE models and the experimental results. steel plates' local buckling was observed and compared for specimens W-1 and W-2. However, the FE models were not able to precisely capture the local buckling, likely due to uncertainties in the initial imperfections of the steel plates and the tensile fracture at the welds connecting the steel faceplates to the side plates. Generally, The FE modeling provide an acceptable results in term of the failure modes and deformation patterns.

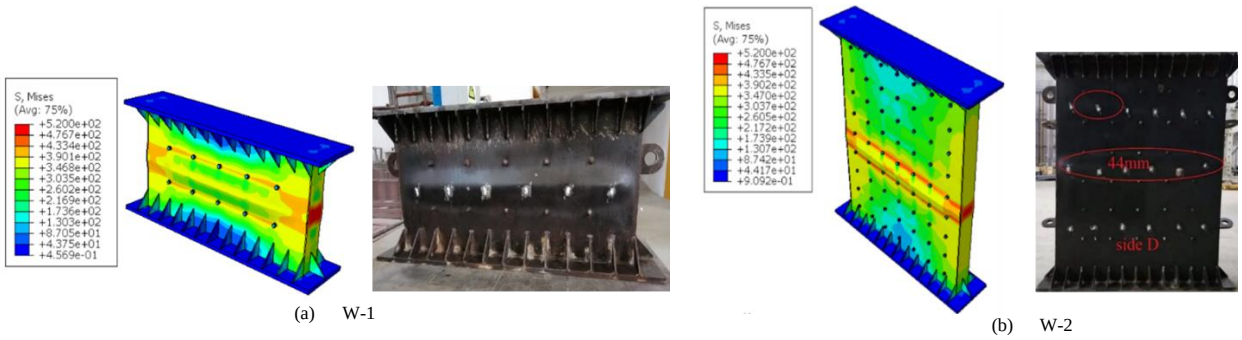

(a) W-1 (b) W-2

Fig. 8 Comparison of failure modes between test results and FE modeling

4. Results and discussions

4.1. General behavior

Fig. 7(a–f) shows the axial compression load versus vertical displacement (P-Δ) curves for the five DSCSW models. Based on experimental investigations, the load-displacement curves can be divided into three stages: the elastic stage, the non-linear elastic stage, and the degradation stage. In the first stage (curve OA), the curve is nearly linear, indicating that the displacement increases proportionally with the load, and the specimens achieve 50%-85% of their ultimate capacity, as shown in Fig. 7(f). In the second stage (curve AB), the DSCSWs exhibit non-linear behavior due to the material non-linearities of concrete, steel plates, and connectors. At the end of this stage (point B), the models reach their ultimate capacity. Finally, the degradation stage (curve BC) begins, where the load capacity declines. The rate of decline depends on the type of connectors and the height of the DSCSWs. For instance, the ultimate resistance of DSCSWs decreases with height but increases when bolts are replaced with headed studs and T-stiffeners (see Fig. 7).

4.2. Ductility index (DI)

In structural stability, the ductility index reflects the capability to experience significant plastic failure without essential capacity breakdown. The following equation can determine the ductility index.

$$DI = \frac{\Delta_{0.85}}{\Delta_u} \tag{3}$$

where $\Delta_{0.85}$ indicates the shorting reaction force of DSCSW declined to its 85% ultimate value during the recession stage; Δ_u indicates the shorting corresponding to ultimate capacity.

4.3. Initial stiffness

The initial stiffness K_e of the compression behavior of DSCSW can be determined based on [58] method from the load-displacement curve, using the ratio of 30% from ultimate axial compassion resistance $P_{0.3}$ and its corresponding displacement as the following equation.

$$K_e = \frac{P_{0.3}}{\Delta_{0.3}} \tag{4}$$

where K_e denotes the initial stiffness of DSCSW based on numerical analysis.

In addition, the initial stiffness of DSCSW subjected to an axial load can be calculated based on the equation as follows.

$$K_{ca} = \frac{E_c A_e}{H} \tag{5}$$

$$A_e = A_c + A_s(E_s/E_c) \tag{6}$$

where K_{ca} denotes initial theoretical stiffness of DSCSW, E_s and E_c denote the elastic modules and of concrete and steel plates, respectively, H is the height of the wall, A_e is the equivalent area of cross-section of the DSCSW, A_c and A_s denote the total area of concrete core and steel plates, respectively.

Fig. 9 shows the scattering distributions of initial theoretical stiffness K_{ca}. It can be noticed that theoretical predictions of initial stiffness are overestimated by 13% with stander deviations due to only considering the capacity and height of the material without different types of connectors.

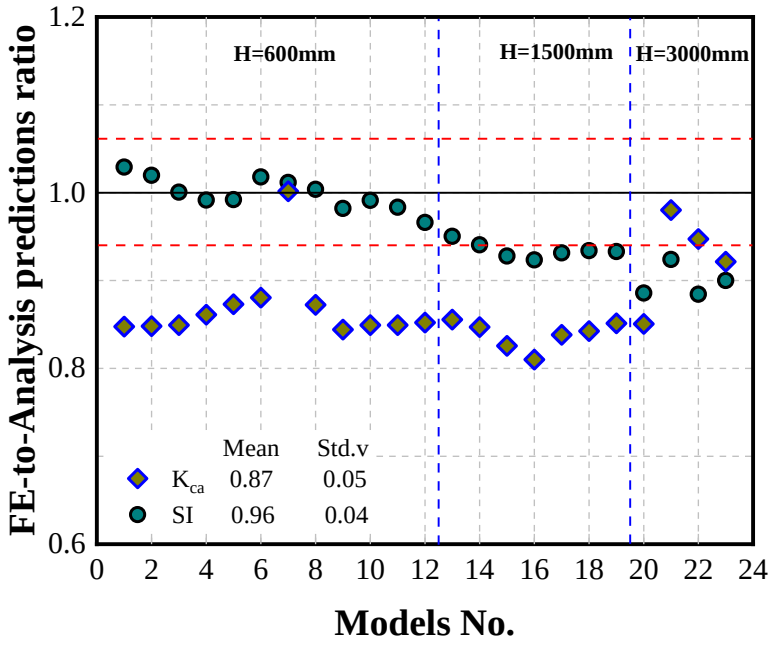

Fig. 9 Scatter of FE-to-predictions of (K_{ca}) and (SI)

4.4. Strength Index (SI)

In order to eliminate the variation of models' sectioned configurations and height, the strength index is proposed, which is able to be determined as the following.

$$SI = \frac{P_{u,FEM}}{0.85 f_c A_c + f_y A_s} \tag{7}$$

where SI is the strength index of the DSCSW subjected to compression load; $P_{u,FEM}$ is the ultimate compressive capacity based on FE analysis; f_c and A_c indicate the yield strength and cross-sectional area of the concrete core; f_y and A_s indicate the yield strength and cross-sectional area of steel plates.

The scatter distribution of the strength index ratio is illustrated in Fig. 9. It is noticeable that the ratio was close to the linear fitting, which means the wall's ultimate compressive capacity takes the full section capacity. However, the ultimate compressive capacity tends to decrease with the height of the wall being raised. This exhibits that the shear wall cannot achieve its section capacity due to premature failure, which causes local bucking, concrete crushing, and global buckling. Additionally, the mean ratio value of the strength index is 96% with standard deviations (Std.v) 0.04.

4.5. Ultimate compressive capacity and failure modes

4.5.1. Ultimate compressive capacity

The ultimate compressive capacity of FE models can be calculated from load-displacement curves as presented in Table.4. Test results revealed that increasing the wall height led to a decrease in ultimate compressive capacity, initial stiffness, and ductility, while vertical displacement increased. Specifically, at a wall height of 600mm, the ultimate bearing capacity was 8659kN, but it decreased to 7200kN and 6735kN for heights of 1500mm and 3000mm, respectively. The initial stiffness was 9845 kN/mm, then declined by roughly 37% and 18% when the height increased from 600mm to 1500mm and 3000mm, respectively. The ductility index was 1.20%, 1.12%, and 1.31%, with heights changing from 600mm to 1500mm and 3000mm. Therefore, height is a significant factor influencing the overall performance of the DSCSWs.

Using different types of connectors showed that both compressive capacity and initial stiffness increased with the use of headed studs and T-stiffeners, while the ductility index and vertical displacement exhibited the opposite behavior. Specifically, the axial bearing capacity increased from 6735kN to 8060kN and 8063kN when bolt connectors, headed studs, and T-stiffeners were used. Initial stiffness was 1759kN/mm with bolt connectors, and it increased by 76% with both headed studs and T-stiffeners, as shown in the table. 4. The ductility index showed minimal variation, the ductility index was 1.31% with bolt connectors, then declined to 1.17% and 1.13% with the use of headed studs and T-stiffeners, respectively. Overall, the axial bearing capacity, stiffness, and ductility index of the DSCSWs are primarily influenced by the steel faceplate and material resistance of the wall. Headed stud and T-stiffener connectors outperformed bolt connectors and are recommended for enhancing the overall performance of the DSCSWs.

4.5.2. Failure modes

Three main styles of deformation patterns were observed in the FE simulation of compression tests of DSCSWs. The first failure mode, concrete crushing deformation, is described by the high yielding of the concrete core between two vertical connectors, where the concrete tends to crush, as depicted in Fig. 10(a). This type of deformation occurs due to the straight growth of the concrete core under axial compression. The excessive axial load causes the concrete to reach its compressive limit, leading to localized crushing. This failure mode emphasizes the need for sufficient confinement within the wall system to prevent premature crushing and improve the axial load capacity. The second failure mode is steel faceplate buckling, as presented in Fig. 10(b-c). In this case, the steel faceplates tend to buckle outward in the middle due to insufficient connections between the concrete core and the steel plates. This poor connection allows the steel plates to deform, resulting in a deformation strip zone along the shear connectors. The confinement effect afforded by the steel faceplates is crucial for enhancing the compressive capacity of the concrete core. By improving the steel-concrete interface and using effective connectors, the ultimate capacity of DSCSWs can be significantly increased, as evidenced by the absence of this failure mode in well-designed models. The third failure mode, global buckling, occurs when the height-to-width H / w ratio of the wall is greater than 22 with the arranging both bolts and T-stiffeners connectors, as depicted in Fig. 10(c). In this case, out-of-plane deformation happens, especially when the wall height reaches 3000mm, leading to several buckling strips along the length of the wall. This global buckling is more likely when the wall is taller relative to its width, and it results in a noticeable deflection under axial load. However, the steel faceplates and connectors continue to provide confinement to the concrete core, mitigating the severity of this failure mode and protecting the wall from large-scale deflections.

The findings from the FE simulations highlight critical failure modes in DSCSWs and provide valuable insights for improving the design and structure of these systems. To prevent concrete crushing failure, it is essential to ensure adequate confinement of the concrete core using high-performance shear connectors, which can increase the axial load-bearing capacity. Enhancing the connection between the steel plates and concrete core is vital in terms of steel faceplate buckling. This can be achieved by using more robust connectors, such as T-stiffeners or headed studs, which improve the steel-concrete bond and prevent excessive deformation of the faceplates. Lastly, global buckling can be mitigated by optimizing the height-to-width ratio of the shear wall to maintain a balance between the wall's stiffness and its ability to resist axial loads.

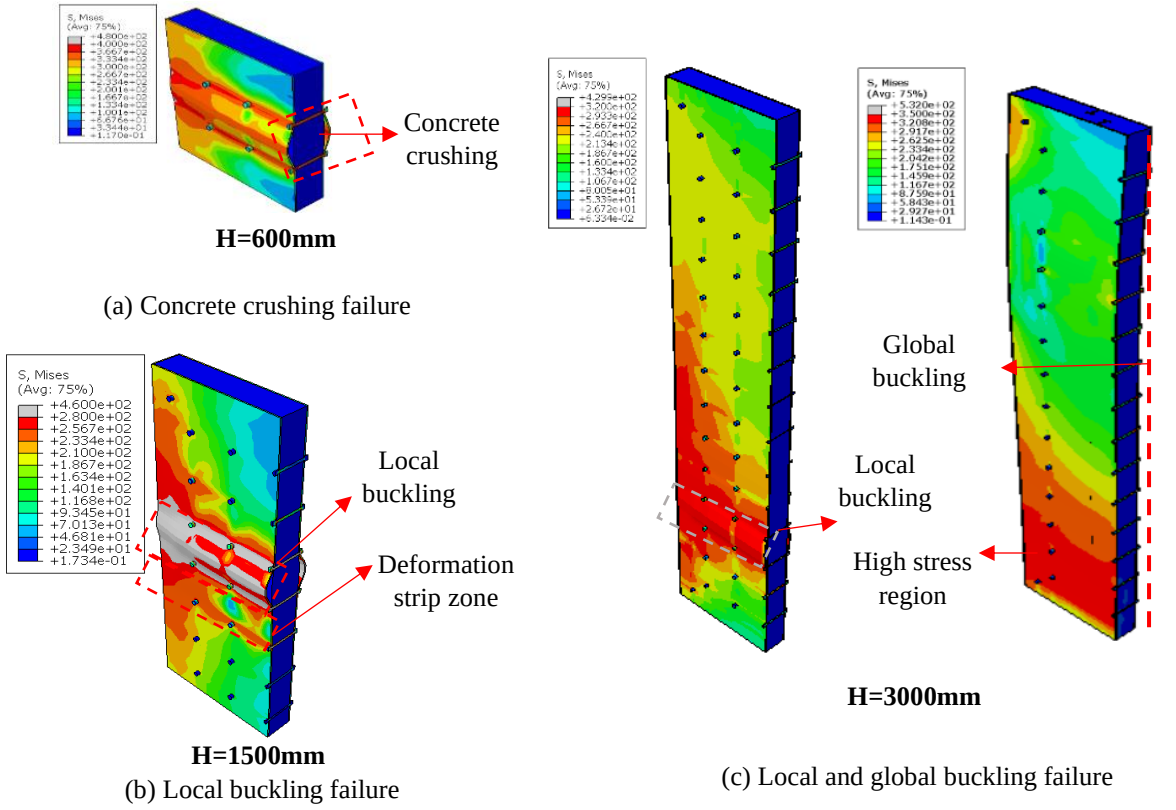

Fig. 10 FE Failure modes of DSCSWs

5. Discussions of parametric analyses

Based on the verified models, FE parametric analyses were operated to examine the impact of five factors on the compressive behavior of DSCSWs. These factors include the type of connectors, wall height, steel plate thickness, bolt connector spacing, and concrete core thickness. This section will examine the influence of these parameters on ultimate compressive capacity, initial stiffness, ultimate vertical displacement, and ductility index.

5.1. Effect of different types of connectors

Three types of connectors were used in this research: bolts, headed studs, and T-stiffeners. These connectors were installed in the FE models across four scenarios: bolts, headed studs, bolts with headed studs, and bolts with T-stiffeners, as presented in Fig. 11(a). The ultimate compressive capacity and ductility index increased with the use of bolts, headed studs, bolts with headed studs, and bolts with T-stiffeners. Among these, bolts, headed studs, and T-stiffeners provided higher ultimate capacity, stiffness, and ductility index compared to bolt connectors. Specifically, the ultimate compressive capacity slightly increased when bolts and headed studs were used separately. However, using bolts with headed studs and bolts with T-stiffeners increased the compressive capacity by 1.9% and 7.1%, respectively. In terms of initial stiffness, the value was 10424 kN/mm when bolts were used. This gradually increased by 2.65% with headed studs and by 3.54% with bolts with headed studs. A significant increase of 18.29% was observed when bolts with T-stiffeners were used. Additionally, the ductility index showed a substantial increase, following the order: 1.22, 1.49, 1.82, and 2.43. These results suggest that the initial stiffness, ductility index, and ultimate compressive capacity of DSCSWs are primarily influenced by the steel plates and the material's resistance. It can be concluded that installing bolts with T-stiffener connectors provides comparable composite action and structural performance to other types of connectors. Therefore, bolts with T-stiffeners are highly recommended for use in composite structures. Furthermore, as shown in Fig. 11(b), T-stiffener connectors resulted in less vertical displacement compared to other connectors, with reductions of approximately 6.67%, 14%, and 16.41% compared to bolts, headed studs, and bolts with headed studs, respectively. Consequently, it can be concluded that bolts with T-stiffener connectors offer comparable compressive behavior to other connectors in terms of vertical displacement, ultimate bearing axial load, initial stiffness, and ductility index. This was further validated by another comparison in this study involving different wall heights, as shown in Figs. 12(a-b) and 13(a-b).

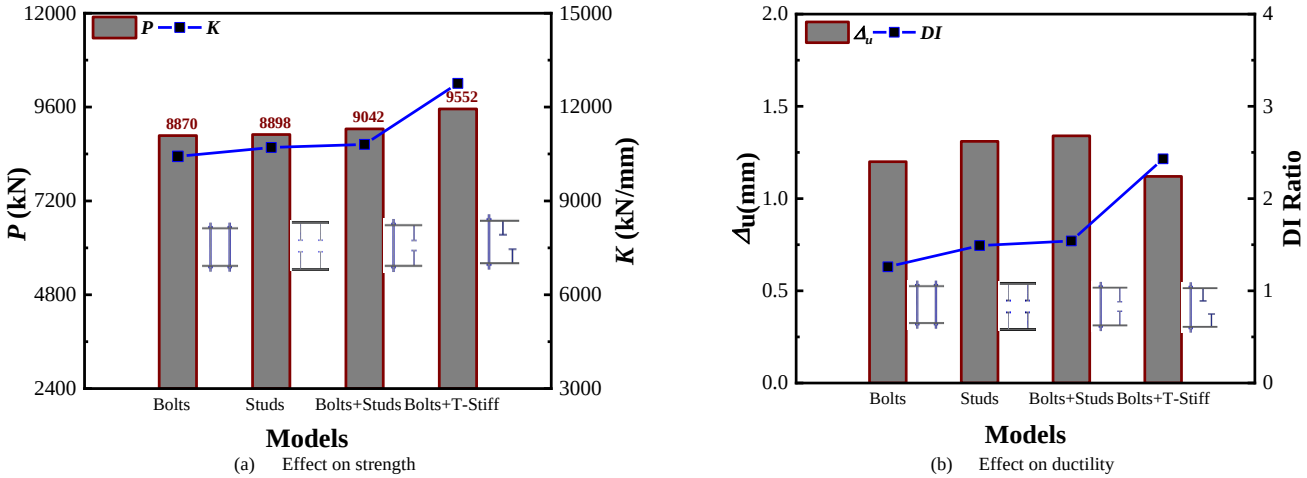

Fig. 11 Effect of different types of connectors on compressive performance with 600mm heights

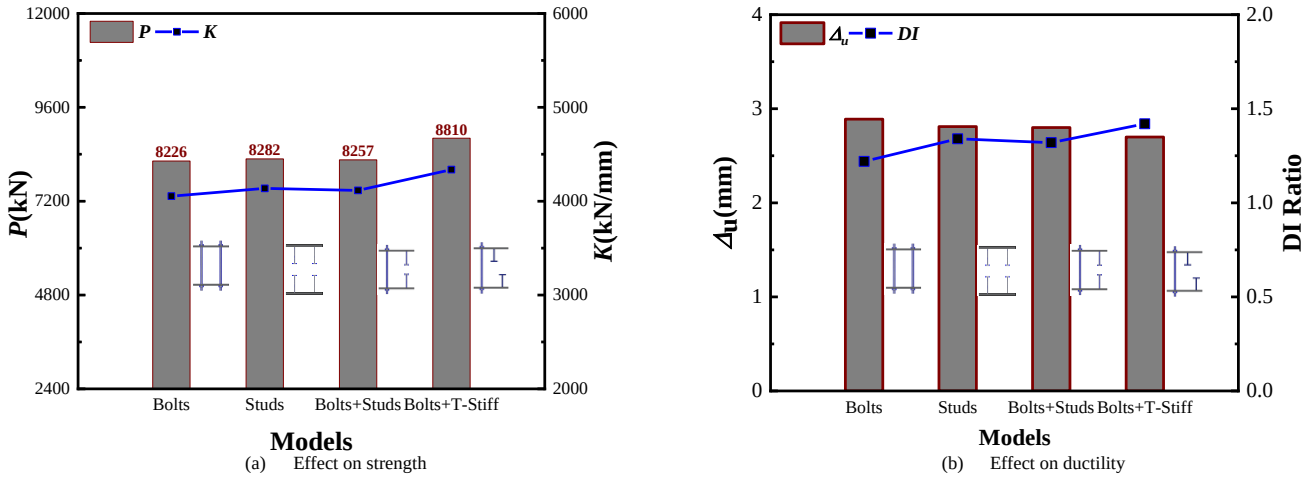

(a) Effect on strength (b) Effect on ductility

Fig. 12 Effect of different types of connectors on compressive performance with 1500mm heights

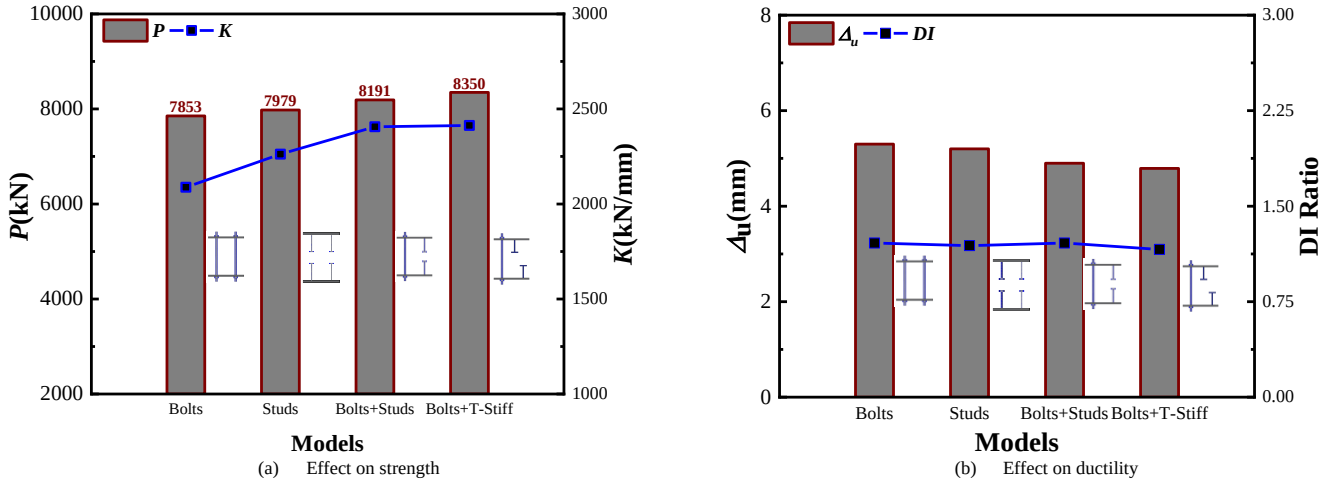

(a) Effect on strength (b) Effect on ductility

Fig. 13 Effect of different types of connectors on compressive performance with 3000mm heights

5.2. Effect height of DSCSW walls

The height of the DSCSWs was modified to study its effect on strength and ductility, as shown in Fig. 14. The results revealed that the ultimate compressive capacity of the walls decreased with increasing height. Similarly, the initial stiffness and ductility exhibited the same trend as the ultimate compressive capacity. In contrast, the vertical displacement increased with the height. Specifically, the ultimate axial compression load was 8870 kN when the height was 600 mm. This value decreased by 7.3% and 11.5% for heights of 1500 mm and 3,000 mm, respectively. The initial stiffness was 10424 kN/mm for the 600 mm height, but it significantly decreased by 61.1% and 79.9% for the 1500 mm and 3000 mm heights, respectively. Meanwhile, the vertical displacement gradually increased from 1.22 mm at 600 mm height to 2.83 mm and 5.30 mm at 1,500 mm and 3,000 mm, respectively, as shown in Fig. 14. Thus, height has a major impact on the ultimate compressive capacity, initial stiffness, ductility, and displacement of the walls, as the models are more likely to fail due to global and local buckling with increasing height, as shown in Fig. 14. These results have been not only numerically validated but also experimentally verified (see Fig. 7(a-e) and Table 4).

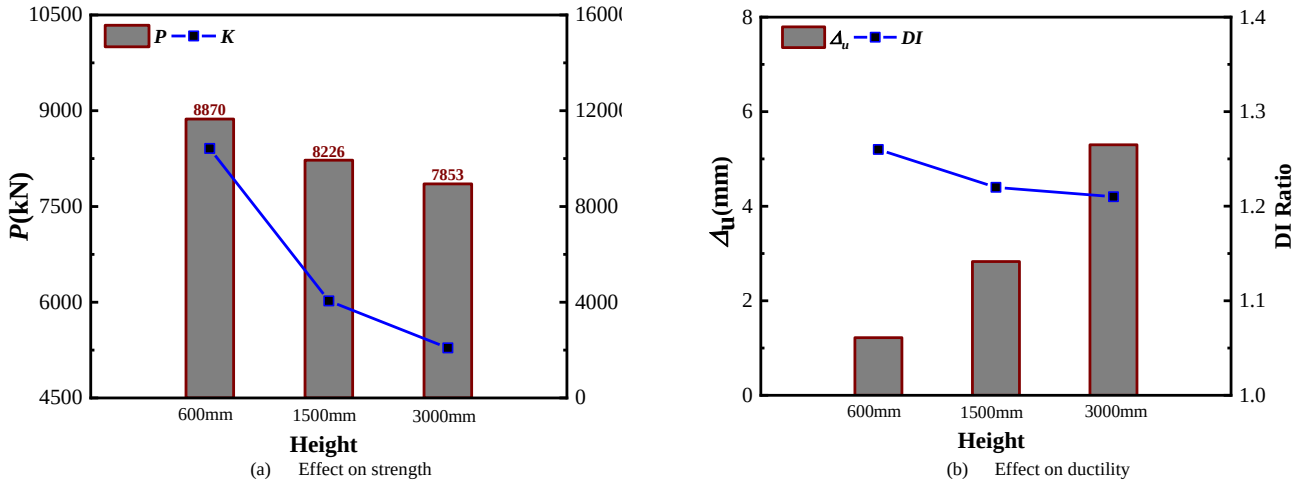

(a) Effect on strength (b) Effect on ductility

Fig. 14 Effect of heights of the wall on the compressive performance of DSCSW

5.3. Effect of thickness of steel plates

Fig. 15 illustrates the influence of the steel plate thickness on the strength and ductility of DSCSWs. The graph shows that the ultimate compressive capacity increased from 7239 kN to 8105 kN, 8870 kN, 9702 kN, and 10621 kN as the thickness of the steel plates increased from 4 mm to 5 mm, 6 mm, 7 mm, and 8 mm, respectively, as shown in Fig. 15(a). Furthermore, reducing the thickness of the steel plates would lower the confinement of the concrete core due to increased local buckling resistance, directly affecting the wall's stiffness. A thinner steel plate would also negatively affect the tensile strength of the bolt connectors, as reduced plate thickness leads to higher buckling. The initial stiffness of the walls slightly increased with the rising thickness of the steel plates. Specifically, when the steel plate thickness was 4 mm, the initial stiffness was 9010 kN/mm. This increased by 7.8%, 15.7%, 25.2%, and 35.0% for thicknesses of 5 mm, 6 mm, 7 mm, and 8 mm, respectively, as displayed in Fig. 15(a). Additionally, the thickness of the steel faceplate significantly impacted vertical displacement. As the steel plate thickness increased, vertical displacement decreased. For example, with a 4 mm thickness, the vertical displacement was 1.65 mm. However, increasing the thickness to 5 mm, 6 mm, 7 mm, and 8 mm reduced the ultimate vertical displacement to 1.42 mm, 1.26 mm, 1.22 mm, and 1.02 mm, respectively, as shown in Fig. 15(b). On the other hand, the ductility index exhibited an opposite trend to vertical displacement, increasing as the steel plate thickness rose. Specifically, when the steel plate thickness was 4 mm, the ductility index was 0.93%. This value steadily increased to 1.18%, 1.32%, 1.38%, and 1.42% for thicknesses of 5 mm, 6 mm, 7 mm, and 8 mm, respectively, as shown in Fig. 15(b). In conclusion, the thickness of the steel plates has a significant impact on the overall mechanical properties of DSCSWs. Increasing the steel plate thickness enhances the DSCSW's compressive performance by increasing the steel content in the section, improving the system's overall mechanical properties.

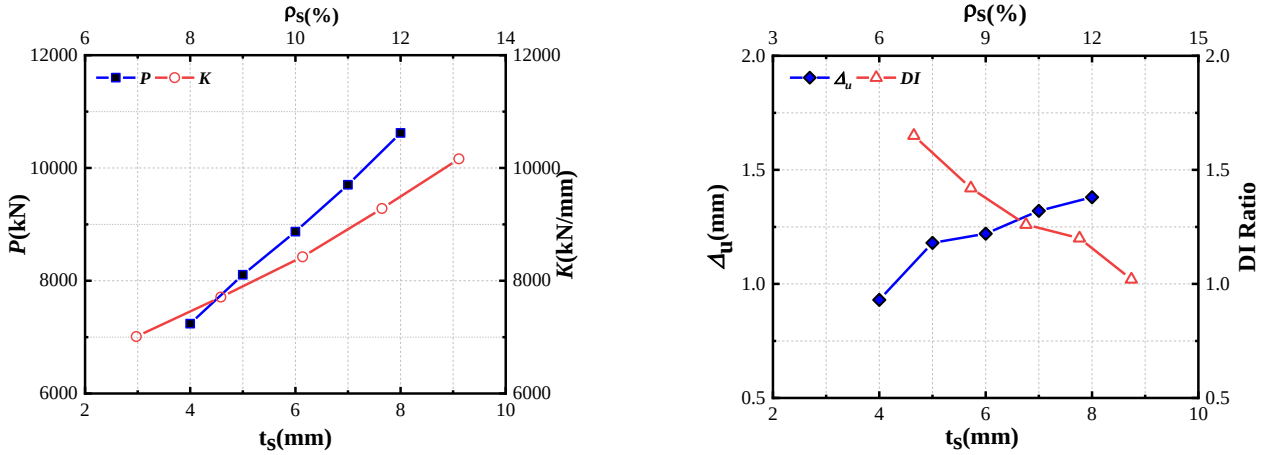

(a) Effect on strength (b) Effect on ductility

Fig. 15 Effect of thickness of steel plates on axial compression behavior of DSCSW

5.4. Effect of spacing of bolt connectors

Different bolt spacing values were used to study the impact of spacing on the overall mechanical properties of DSCSWs under axial compression. Fig. 16 presents the impact of bolt connector spacing on strength and ductility. It can be observed that there is no significant difference in compressive capacity or initial stiffness with varying spacing. Specifically, when the spacing between bolts was 120 mm, the ultimate axial bearing load of the wall was 8425 kN. This value decreased as the spacing increased. When the spacing was adjusted to 160 mm, 200 mm, and 240 mm, the compressive capacity decreased by 1%, 2.4%, and 3.1%, respectively. This reduction is attributed to the increasing slenderness ratio, which rose from 20% to 26.67%, 33.33%, and 40%. Furthermore, increasing the spacing had a minor effect on the initial stiffness of DSCSWs. As the spacing increased from 120 mm to 160 mm, 200 mm, and 240 mm, the initial stiffness values declined from 4200 kN/mm to 4,59 kN/mm, 4054 kN/mm, and 3977 kN/mm, respectively, as illustrated in Fig. 16(a). In addition, Fig. 16(b) illustrates the effect of spacing on the ductility index and ultimate displacement. The graph clearly shows that the ductility index slightly decreased as the bolt spacing increased. Specifically, when the spacing was 120 mm, the ductility index was 1.93%. This value progressively reduced by 31.6%, 36%, and 45.6% for spacings of 160 mm, 200 mm, and 240 mm, respectively. Similarly, the ultimate vertical displacement increased as the ductility index decreased due to the increasing spacing. When the spacing was 120 mm, the ultimate displacement was 2.69 mm. This value increased to 2.89 mm, 2.92 mm, and 3.15 mm for spacings of 160 mm, 200 mm, and 240 mm, respectively. In conclusion, the spacing between bolt connectors has a minor impact on compressive capacity and initial stiffness but significantly affects ultimate vertical displacement and the ductility index.

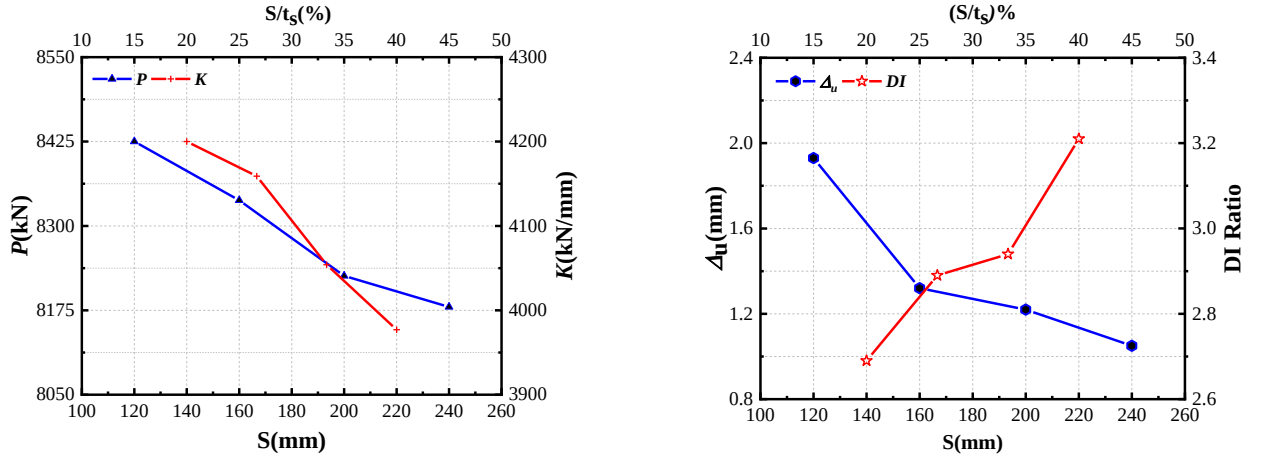

(a) Effect on strength (b) Effect on ductility

Fig. 16 Effect of spacing between bolts connectors on compressive performance DSCSW

5.5. Effect of thickness of the concrete core

Fig. 17 illustrates the effect of thickness of concrete core on the overall compressive stability of DSCSWs. It can be observed that raising the concrete core thickness significantly enhanced both the ultimate compressive capacity and initial stiffness. Specifically, strengthening the core thickness from 98 mm to 108 mm, 118 mm, 128 mm, and 138 mm resulted in a 4.8%, 9.2%, 10.9%, and 12.5% increase in the ultimate compressive capacity of the walls,

respectively. Additionally, the initial stiffness increased with the thickness of the concrete core. More specifically, the initial stiffness rose from 9244 kN/mm to 9861 kN/mm, 10424 kN/mm, 10985 kN/mm, and 11,587 kN/mm, respectively, as shown in Fig. 17(a). This reveals that the concrete core significantly impacts the ultimate compressive capacity and initial stiffness of the wall. It is also evident that the concrete core thickness minimally influences the ultimate vertical displacement and ductility index. The ultimate vertical displacement ranged from 1.12 mm to 1.30 mm, and the ductility index varied from 1.16% to 1.36%, as shown in Fig. 17(b), which can be considered negligible. In conclusion, the core thickness significantly impacts the ultimate compressive capacity and initial stiffness of DSCSWs but has a minor effect on the ductility index and ultimate vertical displacement.

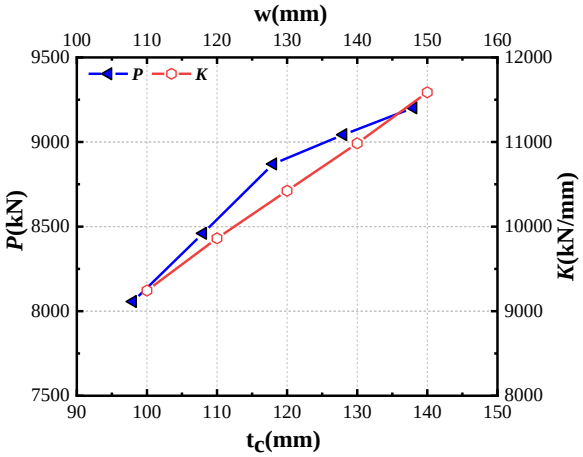

(a) Effect on strength

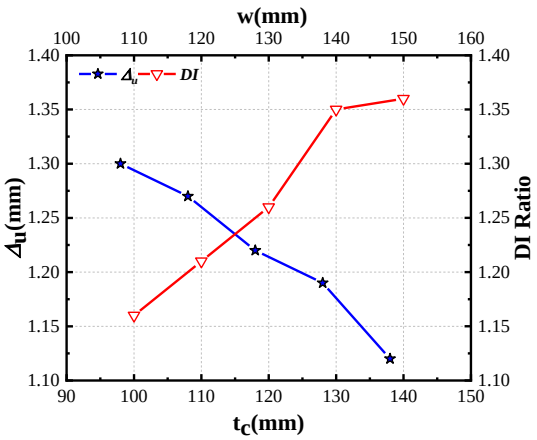

(b) Effect on ductility

Fig. 17 Effect of concrete core' thickness on axial compression behavior of DSCSW

6. Analysis of compressive resistance of DSCSW

6.1. Code methods

In AISC 360 [59], the ultimate compressive capacity of composite structures subjected to axial compression load can be calculated as follows.

$$P_u = \begin{Bmatrix} P_{no}(0.658)^{\frac{P_{no}}{P_e}} \\ 0.877P_e \end{Bmatrix} \quad \text{when} \quad \begin{Bmatrix} P_{no}/P_e \le 2.25 \\ P_{no}/P_e > 2.25 \end{Bmatrix} \tag{8}$$

$$P_{no} = f_y A_s + 0.85 f_c A_c \tag{9}$$

$$P_{cr} = \frac{\pi^2 (EI_{eff})}{(KL)^2} \tag{10}$$

where P_{no} denotes section capacity of DSCSW subjected to axial load and, A_s and A_c are the cross-sectional area of concrete and steel plates, f_y denotes yield strength of steel plates f_c denotes compressive strength of concrete P_{cr} elastic critical buckling load that can be calculated by effective flexural rigidity $(EI_{eff}) = E_s I_s + C_3 E_c I_c$; $C_3 = 0.6 + 2(A_s/A_s + A_c) \le 0.9$, K denotes effective length factor, L is laterally unbraced length of the member.

The ultimate compressive capacity of DSCSW could be determined based on Eurocode 4 [60], as the following

$$P_o = f_y A_s + 0.85 f_c A_c \tag{11}$$

For composite structures, the buckling strength can be predicted by multiplying the section capacity by bucking reduction factor χ

$$P_u = \chi P_o \tag{12}$$

$$\chi = \frac{1}{\varphi + \sqrt{\varphi^2 - \bar{\lambda}^2}} \tag{13}$$

$$\bar{\lambda} = \sqrt{\frac{P_o}{P_{cr}}} \tag{14}$$

$$\varphi = 0.5[1 + \alpha_g(\bar{\lambda} - 0.2) + \bar{\lambda}^2] \tag{15}$$

where P_o is ultimate strength of composite shear wall under compression force, χ reduction factor which is function of the relative slenderness $\bar{\lambda}$ and imperfection, α_g is an imperfection factor corresponding to appropriate buckling curve, and it can be gotten from Table 6.5 in Eurocode 4. P_{cr} elastic critical buckling force that determined by effective flexural rigidity as follow $(EI_{eff}) = E_s I_s + 0.6 E_c I_c$.

6.2. Analytical method

To simplify the ultimate compressive resistance calculations, the following assumptions may be applied.

(1) As DSCSW is composed of steel plates and concrete core, so the ultimate compressive resistance (P_u) provided by the compressive strength of steel (P_s) plates and concrete core (P_c) .

$$P_u = P_c + P_s \tag{16}$$

(2) In the loading stage, the concrete core and steel plates work compositely, and the previous research on composites shears walls showed that the compressive of concrete core P_c can be determined as follows;

$$P_c = \phi A_c \sigma_c \tag{17}$$

where ϕ denotes to reduction factor equals 0.85 according to AISC-360 and Eurocode 4; A_c and σ_c denotes the concrete core's cross-sectional and ultimate compressive capacity, respectively. Yan has suggested a method to calculate (σ_c) in Ref [20].

(3) According to Akiyama [61] study, the yield stress of steel plates can be determined as follows:

$$\sigma_{cr} = \frac{\pi^2 E_s}{12K^2(S/t_s)^2} \tag{18}$$

where E_s Modules of elasticity of steel; S denotes spacing among connectors; t_s denotes the thickness of steel plates; K is the coefficient of effective length, and its value is considered as 0.7 for the safety factor.

In order to investigate the influence of the slenderness ratio of steel plates on the buckling behavior of DSCSWs, Wei et al. [62] conducted buckling analysis and ultimate stress state, and the following equation was suggested to consider the steel plates' buckling stress.

$$\sigma_{cr}=\begin{cases} f_y & ,S/t_s \le \pi\sqrt{E_s/(12K^2 f_y)} \\ \dfrac{\pi E_s}{12K^2(S/t_s)^2} & ,S/t_s > \pi\sqrt{E_s/(12K^2 f_y)} \end{cases} \quad (19)$$

(4) Based on numerical and experimental results on DSCSWs, the type of connectors with steel plates provide confinement to the concrete core and raise the ultimate capacity of composite walls. In contrast, it is noticeable that neither AISC-360 nor Eurocode 4 included the effect of connectors. However, Yan et al. [20] suggested that the steel on the concrete deformation plane could be considered to offer confinement. The confinement stress (σ_h) was defined as an average equal stress allocated across the relevant area, which can be represented by

$$\sigma_h=\frac{T_H}{S^2} \quad (20)$$

where T_H denotes the tensile strength of connectors; S denotes the spacing between two connectors. The tensile resistance of connectors in the DSCSW can be determined according to the degree of confining stress acting on the concrete core. Hence, T_H can be calculated by the equations recommended by Yan at [20, 63-65].

(5) According to test and FE results, the failures of slender DSCSW are inelastic local and global buckling correlating with yielding of steel plates and crushing of concrete core. Therefore, general slenderness and stability of the wall should be taken into considerations, and it can be considered by multiplying the section capacity by stability coefficient (φ) as follows

$$P_u=\varphi P_0 \quad (21)$$

$$\varphi=\begin{cases} 1-0.65\lambda_0^2 \; for \lambda_0 \le 0.215 \\ \dfrac{1}{2\lambda_0^2}[(0.965+0.3\lambda_0+\lambda_0^2)-\sqrt{(0.965+0.3\lambda_0+\lambda_0^2)^2-4\lambda_0^2}] \; for \lambda_0 > 0.215 \end{cases} \quad (22)$$

$$\lambda_0=\frac{l_0}{\pi\sqrt{\dfrac{I_s+I_c E_c/E_s}{A_s+A_c\sigma_c/\sigma_{cr}}}}\sqrt{\frac{\sigma_{cr}}{E_s}} \quad (23)$$

where P_u is ultimate compressive capacity; φ is stability coefficient [66]; λ_0 is generalized slenderness ratio; l_0 is the effective unbraced length of the member; elastic modulus of concrete and steel; I_c and I_s inertia moment of concrete and steel.

6.3. Validations

The ultimate compressive capacity projections are validated with the FE modeling outcomes in Table 5. Fig. 18 shows a scatter plot illustrating the numerical-to-prediction ratio for the results obtained using AISC-360, Eurocode 4, and the analytical method. The mean ratios for AISC-360 and Eurocode 4 are 1.04 and 1.02, respectively, both with the same standard deviation (Std. v) of 0.05. This similarity arises since the criteria in these code methods were initially developed for concrete-filled steel tube columns and do not account for variations in connector types or premature local buckling of steel plates. Additionally, both Table 5 and Fig. 18 reveal that the prediction ratios from these code methods were lower for walls with a height of 600mm, as they were treated as short shear walls. In contrast, the analytical method yields the average percentage of 1.00 with a standard deviation (Std. v) of 0.03. These high mean ratios and low standard deviations emphasize the enhanced accuracy of the analytical method, which incorporates the confinement effect of steel plates and various connector types. Furthermore, Fig. 18 demonstrates that more than 90% of the analytical models fall within the ±5% prediction error range. In conclusion, the analytical method provides reliable estimates of the ultimate compressive capacity for DSCSWs with different connector types.

Table 4
Comparison of ultimate compressive capacity between the numerically and analytically

items	$P_{u,FEM}$	$P_{u,AISC}$	$P_{u,EC4}$	$P_{u,Analytical}$	$P_{u,FE}/P_{u,AISC}$	$P_{u,FE}/P_{u,EC4}$	$P_{u,FE}/P_{u,Analytical}$
DSCSW-1	7239	6970	7035	6993	1.04	1.03	1.04
DSCSW-2	8105	7879	7948	7906	1.03	1.02	1.03
DSCSW-3	8870	8791	8864	8818	1.01	1.00	1.01
DSCSW-4	9702	9705	9783	9732	1.00	0.99	1.00
DSCSW-5	10621	10623	10705	10650	1.00	0.99	1.00
DSCSW-6	9024	8791	8864	8800	1.03	1.02	1.03
DSCSW-7	9552	9359	9442	9387	1.02	1.01	1.02
DSCSW-8	8898	8791	8864	8800	1.01	1.00	1.01
DSCSW-9	8057	8110	8204	8137	0.99	0.98	0.99
DSCSW-10	8460	8452	8534	8478	1.00	0.99	1.00
DSCSW-11	9043	9128	9195	9156	0.99	0.98	0.99
DSCSW-12	9202	9465	9525	9493	0.97	0.97	0.97
DSCSW-13	8425	8416	8482	8613	1.00	0.99	0.98
DSCSW-14	8338	8416	8482	8530	0.99	0.98	0.98
DSCSW-15	8226	8416	8482	8491	0.98	0.97	0.97
DSCSW-16	8186	8416	8482	8469	0.97	0.97	0.97
DSCSW-17	8257	8416	8482	8474	0.98	0.97	0.97
DSCSW-18	8280	8416	8482	8474	0.98	0.98	0.98
DSCSW-19	8810	8937	9004	9020	0.99	0.98	0.98
DSCSW-20	7853	7201	7207	7672	1.09	1.09	1.02
DSCSW-21	8191	7201	7207	7659	1.14	1.14	1.07
DSCSW-22	8350	7580	7548	8111	1.10	1.11	1.03
DSCSW-23	7979	7201	7207	7659	1.11	1.11	1.04
average					1.04	1.02	1.00
Std.v					0.05	0.05	0.03

where $P_{u,FE}$ denotes numerical results of compressive capacity, $P_{u,AISC}$, $P_{u,EC4}$ and $P_{u,Analytical}$ indicate predictions of compressive resistance by AISC-360, Eurocode 4 code and analytical method, respectively.

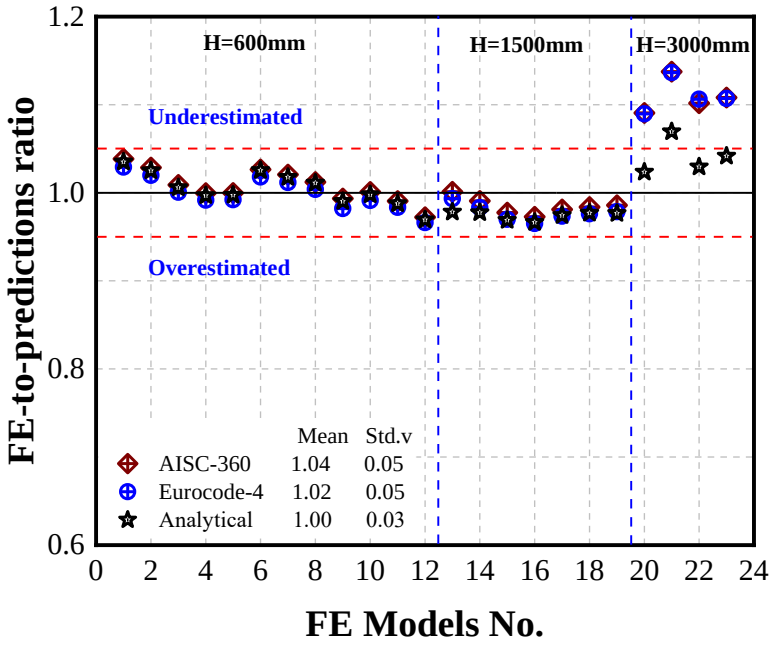

Fig. 18 Comparison between FE analysis results and prediction equations

7. Conclusion

This paper examines the axial compression behavior of DSCSWs. Steel faceplates are prone to buckling between two rows of connectors due to the weak bond between the steel faceplates and the concrete core. To prevent local buckling, separation of steel plates, and to enhance the overall compressive performance of DSCSWs, various methods such as bolts, headed studs, and T-stiffeners have been proposed. In this study, FE modeling was developed and validated with five tested specimens to ensure the accuracy of the results. A parametric analysis was then performed to investigate several key factors based on the verified results. Lastly, the ultimate compressive capacity of DSCSWs was predicted using AISC-360, Eurocode 4, and the analytical method, and the results were compared with those obtained from FE parametric studies. The conclusions drawn from the study are as follows.

(1) The comparison between test and FE modeling results shows that the FE models slightly overestimate both the ultimate compressive capacity and initial stiffness of DSCSWs by 7%. The standard deviations for compressive capacity and stiffness test-to-FE predictions are 0.06 and 0.04, respectively. Discrepancies in the FE models are primarily due to variations in the concrete modulus of elasticity and the loading process. Although the FE models can capture the failure modes including local buckling, concrete crushing and global buckling.

(2) As the wall height increased, the ultimate bearing capacity, initial stiffness, and ductility index showed a decreasing trend, suggesting that height significantly influences the overall performance of DSCSWs. Different types of connectors were also tested, with the results showing that headed studs and T-stiffeners enhanced both compressive capacity and initial stiffness while they reduced the ductility index and vertical displacement. Specifically, using headed studs and T-stiffeners improved axial bearing capacity and stiffness compared to bolt connectors, although ductility slightly decreased with these connectors. Overall, steel faceplate material and connector type play key roles in the performance of DSCSWs, with headed studs and T-stiffeners proving to be more effective than bolt connectors.

(3) The study also identified three primary failure modes in the FE simulations: concrete crushing, steel faceplate buckling, and global buckling. These failure modes emphasize the importance of adequate confinement for the concrete core and the need for robust connections between the steel plates and concrete core to prevent deformation and improve axial load capacity. Furthermore, optimizing the height-to-width ratio of the shear wall is crucial in mitigating global buckling and maintaining overall stability.

(4) T-stiffeners and headed studs significantly improve the compressive capacity, initial stiffness, and ductility of DSCSWs compared to bolts. Combining bolts and T-stiffeners provides the best performance, including reduced vertical displacement. Wall height greatly impacts compressive capacity, stiffness, and displacement, with taller walls showing reduced strength and increased displacement, highlighting a higher risk of buckling. These findings emphasize the importance of selecting appropriate connectors and optimizing height-to-width ratios in DSCSW design to ensure stability and enhanced performance.

(5) The compressive capacity of DSCSWs is substantially impacted by the thickness of the steel plates, the spacing of bolt connectors, and the thickness of the concrete core. Increasing the thickness of the steel plate improves compressive capacity, with values rising as the thickness increases from 4 mm to 8 mm. The concrete core thickness also plays a key role, with greater thicknesses leading to higher compressive capacity. On the other hand, the spacing between bolt connectors has a minor effect on compressive capacity, with only a slight decrease observed as the spacing increases. In conclusion, increasing steel plate thickness and concrete core thickness enhances the compressive capacity of DSCSWs, while bolt connector spacing has a relatively minor impact.

(6) The predictions of ultimate compressive capacity based on the AISC-360-10 code and Eurocode 4 method showed reasonable agreement with the FE results. The average values for these two methods are 1.04 and 1.02, respectively, with the same standard deviation of 0.05. On the other hand, the analytical method was proposed to predict the ultimate compressive capacity of DSCSWs by considering the confinement effect of steel faceplates and different types of connectors. The mean value of this method is 1.00, with a standard deviation of 0.03. Therefore, this method provides acceptable results and can be used for design purposes.

Acknowledgment

The Key Laboratory of New Technology supported this research for the Construction of Cities in Mountain Area (Grant No. LNTCCMA-20240116). The authors also appreciate the fundings from The National Natural Science Foundation of China (Grant No. 52378176) and the S&T Program of Hebei (Grant No. 22375409D).

References

[1] J. Shin and S. Park, "Optimum retrofit strategy of FRP column jacketing system for non-ductile RC building frames using artificial neural network and genetic algorithm hybrid approach," *Journal of Building Engineering*, vol. 57, p. 104919, 2022.

[2] T. Kim and J. M. LaFave, "Proposed new equivalent lateral force design method for low-rise reinforced concrete wall-frame mixed building systems," *Engineering Structures*, vol. 152, pp. 87-101, 2017.

[3] L.-H. Han, W. Li, and R. Bjorhovde, "Developments and advanced applications of concrete-filled steel tubular (CFST) structures: Members," *Journal of constructional steel research*, vol. 100, pp. 211-228, 2014.

[4] Z.-H. Chen, R. Ma, Y.-S. Du, and M. Lian, "Experimental and Theoretical Research on Rcft Beam-Columns Fabricated with Q420b High-Strength Steel Subjected To Eccentric Load," *ADVANCED STEEL CONSTRUCTION*, vol. 16, no. 4, pp. 287-296, 2020.

[5] M. Amer, Z. Chen, Y. Du, W. Mashrah, and W. Zhang, "Experimental and numerical investigations on cyclic performance of L-shaped-CFT column frame-buckling restrained and unrestrained steel plate shear walls with partial double-side/four corner connections," *Journal of Building Engineering*, p. 107568, 2023.

[6] A. Mohammed, Y. Du, Z. Chen, and J. Huang, "Research on Seismic Behavior of CFT-Frame-Buckling Restrained Steel Plate Shear Wall Structures Using Recycled Aggregate Concrete," in *Proceedings of The 17th East Asian-Pacific Conference on Structural Engineering and Construction, 2022: EASEC-17, Singapore*, 2023: Springer, pp. 140-151.

[7] Z. Chen, M. Amer, Y. Du, W. Mashrah, B. Zhao, and J. Huang, "Experimental and numerical study on seismic performance of square and l-shaped Concrete-filled steel tubes column Frame-Buckling steel plate shear walls," *Engineering Structures*, vol. 274, p. 115155, 2023.
[8] Y. Du, M. Amer, Z. Chen, M. Al-Haaj, and J. Huang, "Seismic behaviors of CFT-column frame-four-corner bolted connected buckling-restrained steel plate shear walls using ALC/RAC panels," *Thin-Walled Structures*, vol. 195, p. 111365, 2024.
[9] J. Zhou, P. Li, and N. Guo, "Seismic performance assessment of a precast concrete-encased CFST composite wall with twin steel tube connections," *Engineering Structures*, vol. 207, p. 110240, 2020.
[10] B. Wang, H. Jiang, and X. Lu, "Seismic performance of steel plate reinforced concrete shear wall and its application in China Mainland," *Journal of Constructional Steel Research*, vol. 131, pp. 132-143, 2017.
[11] Y. Zhang, Y. Du, Z. Chen, J. Wang, Y. Xu, and G. Liu, "Research on seismic performance of ITRAC-filled double steel plate composite shear wall," *Journal of Building Engineering*, p. 107073, 2023.
[12] Y. Zhang, Y. Du, Z. Chen, Y. Liu, and W. Zhang, "Material properties of ITRAC and cyclic behavior of double steel plate composite shear wall filled with ITRAC," *Construction and Building Materials*, vol. 394, p. 131635, 2023.
[13] Y. Du, C. Shi, Z. Zhao, Y. Zhang, and T. Li, "Compressive behavior of an innovative double-steel-plate composite shear wall with iron tailings and recycled aggregate concrete," *Journal of Building Engineering*, vol. 91, p. 109523, 2024.
[14] J.-B. Yan, E.-C. Kang, and J. Xie, "BEHAVIOURS OF STEEL-CONCRETE COMPOSITE BEAMS AT LOW TEMPERATURES: MATERIALS AND STRUCTURES," 2023.
[15] J.-G. Nie, H.-S. Hu, J.-S. Fan, M.-X. Tao, S.-Y. Li, and F.-J. Liu, "Experimental study on seismic behavior of high-strength concrete filled double-steel-plate composite walls," *Journal of Constructional Steel Research*, vol. 88, pp. 206-219, 2013.
[16] M. Takeuchi, M. Narikawa, I. Matsuo, K. Hara, and S. Usami, "Study on a concrete filled structure for nuclear power plants," *Nuclear engineering and design*, vol. 179, no. 2, pp. 209-223, 1998.
[17] S. K. Clubley, S. S. Moy, and R. Y. Xiao, "Shear strength of steel–concrete–steel composite panels. Part I—testing and numerical modelling," *Journal of Constructional Steel Research*, vol. 59, no. 6, pp. 781-794, 2003.
[18] Q. Zhao, Y. Li, and Y. Tian, "Cyclic behavior of double-skin composite walls with flat and corrugated faceplates," *Engineering Structures*, vol. 220, p. 111013, 2020.
[19] Y. Qin, G.-P. Shu, G.-G. Zhou, J.-H. Han, and X.-L. Zhou, "Truss spacing on innovative composite walls under compression," *Journal of Constructional Steel Research*, vol. 160, pp. 1-15, 2019.
[20] J.-B. Yan, Z. Wang, Y.-B. Luo, and T. Wang, "Compressive behaviours of novel SCS sandwich composite walls with normal weight concrete," *Thin-Walled Structures*, vol. 141, pp. 119-132, 2019.
[21] K. Kang, "Blast resistance of steel-concrete composite structures," Ph. D. thesis, Department of Civil & Environmental Engineering, National …, 2012.
[22] K. Sohel and J. R. Liew, "Behavior of steel–concrete–steel sandwich slabs subject to impact load," *Journal of Constructional Steel Research*, vol. 100, pp. 163-175, 2014.
[23] M. Xie and J. Chapman, "Developments in sandwich construction," *Journal of Constructional Steel Research*, vol. 62, no. 11, pp. 1123-1133, 2006.
[24] Z.-Y. Huang, J.-Y. Wang, J. R. Liew, and P. W. Marshall, "Lightweight steel–concrete–steel sandwich composite shell subject to punching shear," *Ocean Engineering*, vol. 102, pp. 146-161, 2015.
[25] J. R. Liew and T. Wang, "Novel steel-concrete-steel sandwich composite plates subject to impact and blast load," *Advances in Structural Engineering*, vol. 14, no. 4, pp. 673-687, 2011.
[26] Xiong *et al.*, "Structural behaviour of double skin composite system using ultra-lightweight cement composite," *Construction and Building Materials*, 2015.
[27] Z. Wang, J.-B. Yan, and X.-M. Liu, "NUMERICAL AND THEORETICAL STUDIES ON DOUBLE STEEL PLATE COMPO-SITE WALLS UNDER COMPRESSION AT LOW TEMPERATURES," *Advanced Steel Construction*, vol. 17, no. 4, pp. 376-384, 2021.
[28] B.-J. Choi, C.-K. Kang, and H.-Y. Park, "Strength and behavior of steel plate–concrete wall structures using ordinary and eco-oriented cement concrete under axial compression," *Thin-Walled Structures*, vol. 84, pp. 313-324, 2014.
[29] Y. Yang, J. Liu, and J. Fan, "Buckling behavior of double-skin composite walls: An experimental and modeling study," *Journal of Constructional Steel Research*, vol. 121, no. Jun., pp. 126-135, 2016.
[30] J.-B. Yan, X.-T. Wang, and T. Wang, "Compressive behaviour of normal weight concrete confined by the steel face plates in SCS sandwich wall," *Construction and Building Materials*, vol. 171, pp. 437-454, 2018.
[31] Z. Chen, Y. Jiang, X. Zhang, Q. Yang, and W. Li, "Research on resilience model of steel tube bundle composite shear wall," *Earthq. Eng. Dyn*, vol. 37, pp. 115-122, 2017.
[32] X. Zhang, Y. Qin, and Z. Chen, "Experimental seismic behavior of innovative composite shear walls," *Journal of Constructional Steel Research*, vol. 116, pp. 218-232, 2016.
[33] W. He *et al.*, "Experimental study on seismic behaviors of the welded L-shaped double steel plate-concrete composite shear wall," *Journal of Constructional Steel Research*, vol. 187, p. 106944, 2021.
[34] W. He, Y. Wan, Y. Li, and L. Chen, "Development Research of the Double "L" Shaped Steel Plate-Concrete Composite Shear Wall," in *IOP Conference Series: Earth and Environmental Science*, 2021, vol. 719, no. 2: IOP Publishing, p. 022039.
[35] Y. Du, Y. Zhang, H. Liu, L. Wang, and M. Fu, "Behaviors of restrained rectangular high-strength CFT column under elevated temperature," *Construction and Building Materials*, vol. 432, p. 136616, 2024.
[36] J.-B. Yan, Z. Wang, and X. Wang, "Behaviour of steel-concrete-steel sandwich plates under different ice-contact pressure," *Advanced Steel Construction*, vol. 15, no. 1, pp. 116-122, 2019.
[37] M. Amer, Z.-H. Chen, Y.-S. Du, W. Mashrah, Y.-T. Zhang, and M.-W. Wei, "Research on seismic behavior of L-shaped concrete-filled steel tubes column frame-buckling restrained steel plate shear walls," *ADVANCED STEEL CONSTRUCTION*, vol. 19, no. 3, pp. 273-292 2023.
[38] M. Amer, Y. Du, Z. Chen, S. A. Laqsum, and Y. Zhang, "Seismic behavior of concrete-filled steel tubes column frame-buckling restrained steel plate shear walls connected with bolt/weld," *Thin-Walled Structures*, vol. 189, p. 110911, 2023.
[39] J.-K. Tan *et al.*, "Finite element modelling and design of steel plate shear wall buckling-restrained by hat-section cold-formed steel members," *Journal of Constructional Steel Research*, vol. 174, p. 106274, 2020.
[40] C.-H. Li, J.-B. Yan, H.-N. Guan, and H.-L. Wang, "Numerical study on shear behaviour of enhanced C-channels in steel-UHPC-steel sandwich structures," *ADVANCED STEEL CONSTRUCTION*, vol. 17, no. 3, pp. 253-263, 2021.
[41] S. Guezouli and A. Lachal, "Numerical analysis of frictional contact effects in push-out tests," *Engineering Structures*, vol. 40, pp. 39-50, 2012.
[42] O. Mirza and B. Uy, "Effects of the combination of axial and shear loading on the behaviour of headed stud steel anchors," *Engineering Structures*, vol. 32, no. 1, pp. 93-105, 2010.
[43] M. Pavlović, Z. Marković, M. Veljković, and D. Buđevac, "Bolted shear connectors vs. headed studs behaviour in push-out tests," *Journal of Constructional Steel Research*, vol. 88, pp. 134-149, 2013.
[44] J. Qureshi, D. Lam, and J. Ye, "Effect of shear connector spacing and layout on the shear connector capacity in composite beams," *Journal of constructional steel research*, vol. 67, no. 4, pp. 706-719, 2011.
[45] J.-B. Yan, J. Fan, R. Ding, and X. Nie, "Steel-concrete-steel sandwich composite structures: A review," *Engineering Structures*, vol. 302, p. 117449, 2024.
[46] Z. Huang and J. R. Liew, "Compressive resistance of steel-concrete-steel sandwich composite walls with J-hook connectors," *Journal of Constructional Steel Research*, vol. 124, pp. 142-162, 2016.
[47] J.-B. Yan and W. Zhang, "Numerical analysis on steel-concrete-steel sandwich plates by damage plasticity model: From materials to structures," *Construction and Building Materials*, vol. 149, pp. 801-815, 2017.
[48] *GB/T 50081, Ordinary Concrete Mechanices Performance Test Method Standard, 2019*. (In Chinese).
[49] Wuyapeng, "Experimental Axial Compression Stability of Thin Double Steel-Concrete Composite Shear Wall," Master Academic, 2018-019, Tianjin University, Tianjin, 2019.
[50] H. David, "ABAQUS standard user's manual (Version 6.12. 1)," ed: USA, 2012.
[51] C. S. D. Specifications, "GB50010-2010," *China Building Industry Press: Beijing, China*, 2011.
[52] Y. Du, C. Shi, S.-B. Kang, M. Amer, B. Zhao, and Y. Zhang, "Eccentric compression behaviors of iron tailings and recycled aggregate concrete-filled steel tube columns," *Journal of Constructional Steel Research*, vol. 223, p. 109070, 2024.
[53] Liew, J., Y., Richard, Huang, and Zhenyu, "Numerical studies of steel-concrete-steel sandwich walls with J-hook connectors subjected to axial loads," *Steel & Composite Structures An International Journal*, 2016.
[54] J.-B. Yan, H.-N. Guan, Y.-Y. Yan, and T. Wang, "Numerical and parametric studies on SCS sandwich walls subjected to in-plane shear," *Journal of Constructional Steel Research*, vol. 169, p. 106011, 2020.
[55] X. Liu, Z. Chen, Y. Du, M. Amer, Q. Zhang, Y. Li, J. Chen, "Experimental and theoretical studies on lateral behavior of prefabricated composite concrete-filled steel tubes truss column," *Structures*, vol. 66, p. 106920 2024.
[56] C.-H. Li, J.-B. Yan, and H.-N. Guan, "Finite element analysis on enhanced C-channel connectors in SCS sandwich composite structures," in *Structures*, 2021, vol. 30: Elsevier, pp. 818-837.
[57] J.-B. Yan, A. Chen, and T. Wang, "Compressive behaviours of steel-UHPC-steel sandwich composite walls using novel EC connectors," *Journal of Constructional Steel Research*, vol. 173, p. 106244, 2020.
[58] A. Committee, "Seismic provisions for structural steel buildings (AISC 341-10)," *American Institute of Steel Construction, Chicago-Illinois*, 2010.
[59] A. ANSI, "AISC 341-10," *Seismic provisions for structural steel buildings. Chicago (IL): American Institute of Steel Construction*, 2010.
[60] C. R. Hendy and R. P. Johnson, *Designers' Guide to Eurocode 4: Design of Composite Structures EN 1994-2*. Thomas Telford, 2006.
[61] H. Akiyama, H. Sekimoto, M. Fukihara, K. Nakanishi, and K. Hara, "A compression and shear loading tests of concrete filled steel bearing wall," 1991.
[62] W. Fang-fang, Z. Ze-jun, Y. Jun, and W. Yong-quan, "Computational method for axial compression capacity of double steel-concrete composite shear walls with consideration of buckling," *Engineering Mechanics*, vol. 36, no. 2, pp. 154-164, 2019.
[63] J. Yan, J. Liew, and M. Zhang, "Tensile resistance of J-hook connectors in SCS sandwich composite structure," *J Constr Steel Res*, vol. 100, pp. 146-162, 2014.
[64] J.-B. Yan, J.-Y. Wang, J. R. Liew, X. Qian, and L. Zong, "Ultimate strength behaviour of steel–concrete–steel sandwich plate under concentrated loads," *Ocean Engineering*, vol. 118, pp. 41-57, 2016.
[65] J.-B. Yan, J. R. Liew, X. Qian, and J.-Y. Wang, "Ultimate strength behavior of curved steel–concrete–steel sandwich composite beams," *Journal of Constructional Steel Research*, vol. 115, pp. 316-328, 2015.
[66] CECS-159:2004, "Technical specifications for steel tube concrete structures," no. 8, pp. 35-41, 2004 (In Chinese).

Advanced Steel Construction – Vol. 21 No. 2 (2025) 110–118
DOI:10.18057/IJASC.2025.21.2.2

A REVIEW ON: MECHANICAL, AND MICROSTRUCTURAL BEHAVIORS OF DUPLEX AND AUSTENITIC STAINLESS-STEEL REINFORCING REBAR AFTER EXPOSURE TO ELEVATED TEMPERATURES

Haitham Abdallah Khamis AL Adawani [1], Tuan Zaharinie Tuan Zahari [1, 2, *], and Muhammad Khairi Faiz bin Ahmad Hairuddin [1, 2]

[1] *Department of Mechanical Engineering, Universiti Malaya, 50603 Kuala Lumpur, Malaysia*
[2] *Centre of Advanced Manufacturing and Material Processing, Universiti Malaya,50603 Kuala Lumpur, Malaysia*
** (Corresponding author: E-mail: tzaharinie@um.edu.my)*

ABSTRACT

The utilization of structural stainless steel has risen due to its attractive aesthetic and architectural features as well as its durability. This paper examines previous research on the use of duplex and austenitic stainless steel reinforcement bars in reinforced concrete structures, focusing on their material properties affected by prolonged exposure to high temperatures and different cooling methods. It is important to know that for duplex stainless steel reinforcing rebar, the manufacturing process plays a critical role in preventing the formation of excessively brittle phases, such as sigma phases, within the microstructure. Duplex stainless steel rebars exhibit a less stable microstructure, making them more susceptible to changes under similar conditions compared to austenitic rebars. This paper provides a comprehensive review of the literature on reinforcing bars comprised of duplex and austenitic stainless steel for use in reinforced concrete constructions.

ARTICLE HISTORY

Received: 20 March 2024
Revised: 20 December 2024
Accepted: 20 December 2024

KEYWORDS

Structural stainless steel;
Duplex and austenitic stainless-steel reinforcing rebar;
Mechanical properties;
High temperatures;
Manufacturing process

1. Introduction

In recent times, there has been a rise in the utilization of structural stainless steel, largely due to its attractive aesthetic and architectural features as well as its durability. Santonen et al. [1] classified stainless steels as iron alloys with a minimum of 10.5% chromium by weight and a maximum of 1.2% carbon. Mustapha Karkarna et al. [2] clarified that chromium content is crucial for the formation of a self-repairing oxide layer, referred to as a passive layer, which ensures the alloy's corrosion resistance. The metallurgical composition of stainless steel is significantly affected by various alloying elements, leading to the classification of stainless steels into four distinct categories, each possessing unique mechanical, chemical, and physical properties. The categories include martensitic, ferritic, duplex, and austenitic stainless steels as illustrated in Fig.1[3]. Therefore, the presence of additional alloying elements, such as titanium, molybdenum, nitrogen, and niobium can influence these stainless-steel groups. Two grades in the same category might show comparable mechanical strength, for instance, the presence of molybdenum improves the corrosion resistance of one stainless steel type compared to another that does not contain molybdenum [4].

Austenitic and duplex grades are the most used for structural purposes. Austenitic steels typically consist of a minimum of 18% chromium and 8% nickel. These varieties offer distinct benefits for reinforcing concrete due to their specific metallurgical composition and unique physical characteristics as illustrated by Muwila [5].

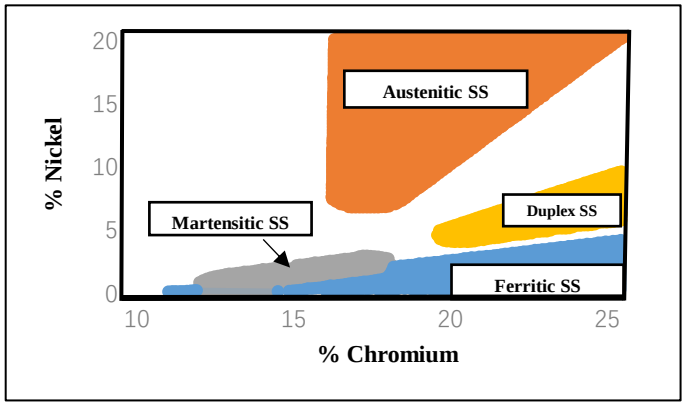

Fig. 1 Stainless steel types and their typical chemical compositions

The main two types of austenitic materials are 304 (designated by ASTM A240), sometimes referred to as UNS S30400 or 1.4301, and X5CrNi18-10 in Europe. The second classification is 316, designated by ASTM A240, known as UNS S31600 or 1.4401, and represented as X5CrNiMo17-12-2 [6].

Markeset [7] demonstrated that these varieties have specific benefits for reinforcing concrete because of their metallurgical composition and physical characteristics. Duplex stainless steels typically include 22-23% chromium and 4-5% nickel, resulting in a two-phase microstructure that comprises both austenitic and ferritic phases [8]. The three main types of duplex stainless steel are UNS S32101–1.4162/X2CrMnNiN21-5-1, UNS S32304–1.4362/X2CrNiN23-4 and UNS S32205–1.4462/X2CrNi-MoN22-5-3. Austenitic steels exhibit lower mechanical strength compared to duplex steels whereas, the higher chromium content and lower nickel and molybdenum levels in duplex steels enhance their attractiveness, providing a favorable balance of corrosion resistance, cost-effectiveness, and stable pricing [9].

Dainezi et al. [10] determined that in DSS, limitations related to operational temperature could lead in the formation of hard, chromium-rich intermetallic phases, affecting both mechanical and corrosion properties. The adjustment of the alloy elements such as (Cr, Mo, Ni, Mn, N, C) along with the alloy processing enables the development of a two-phase microstructure characteristic of DSS. This homogeneous microstructure comprises primary ferrite and austenite phases, which can be altered to redissolve undesirable substances through heat treatments, including dissolution and aging [10]. For instance, Cronemberger et al. [11], and Mohammed et al. [12] noted that elevating the temperature and extending the solubilization process resulted in a microstructure characterized by larger grains. However, the cooling rate, especially slow cooling in a furnace, affects the formation of intermetallic phases (sigma, chi, and alpha line), which subsequently influences mechanical properties, including reduced strength, increased hardness, decreased toughness, and increased susceptibility to corrosion. Therefore, analyzing the effect of secondary phase precipitation and various cooling methods on stainless steel reinforcing rebar after high-temperature exposure is important to understand its behavior in fire scenarios.

This paper provides a comprehensive analysis of prior research on the use of duplex and austenitic stainless steel reinforcement bars in reinforced concrete structures. It further explores the investigation of material properties that are influenced by extended exposure to elevated temperatures and various cooling methods. The objective is to improve understanding of how these conditions affect the mechanical and microstructural behavior of duplex and austenitic stainless steel reinforcement bars. The following is the structure of this paper: section 2 reviews a general background of stainless-steel reinforcement with its material property. Section 3 expresses the behavior of stainless-steel

reinforcement under elevated temperatures, it gives a detailed scenario of post fire, secondary phase precipitation and thermal aging impact on duplex and austenitic stainless steel reinforcing bar. Finally, Section 4 expresses the current challenges, conclusion and future expectations.

2. Stainless steel reinforcing bars

Stainless steel is available in a variety of forms, including structural components, plates, bars, and sheets. M. Rabi et al. [13] have made significant research progress in recent years, as stainless steel rebars are becoming increasingly common in load-bearing constructions due to their properties. Structural elements subjected to corrosive conditions can benefit from stainless steel reinforcing bars, which minimize the frequency and expense of required maintenance [13] and compared to carbon steel, its chloride ion corrosion resistance reduces their need for concrete alkalinity and increases their design life beyond 100 years and they also reduce concrete cover, deck, and substructure weight [13].

3. Material property

3.1. Duplex and Austenitic stainless steel reinforcing rebar families

Stainless steels are classified into four types: ferritic, martensitic, austenitic, and duplex. This classification is defined by the steel's microstructure and allows for an easy examination of the physical and mechanical properties within each group, as explained by Rosso et al. [14]. The characteristics of one group may significantly differ from those of another. Austenitic stainless steels are non-magnetic, whereas ferritic and duplex stainless steels exhibit magnetic properties [14]. The following grades of austenitic and duplex reinforcing bars are commonly used, as clarified by Outokumpu [15]: where EN1.4301, 1.4307, and 1.4311 for austenitic, and 1.4362, 1.4462, and 1.4162 for duplex:

1- According to M. M. Rabi [16], grade EN 1.4162 is a type of duplex stainless steel with reinforcing properties. With a reduced nickel concentration, this material is less expensive while still providing great corrosion resistance and being nearly twice as strong as austenitic stainless steels.
2- Gardner [17] stated that EN 1.4362 is a duplex stainless steel, sometimes referred to as lean duplex, which has superior corrosion resistance compared to austenitic grades. The comparatively high nickel concentration and optimal metal composition make it particularly effective against localized corrosion and stress corrosion cracking.
3- Grade EN 1.4462 has better mechanical strength and comparable corrosion resistance to grade EN 1.4362 [13].
4- The most used stainless steel in structural applications is grade EN 1.4301, which contains 18% chromium and 8% nickel. This grade is widely used in a variety of applications due to its exceptional corrosion resistance, as well as its excellent strength, formability, and weldability [13].
5- The 1.4311 austenitic stainless steel has high tensile strength and increased toughness at low temperatures due to its high nickel, nitrogen content, and low carbon content [13].
6- Grade EN 1.4307 can be substituted for grade 1.4301 due to its reduced carbon content, which leads to enhanced weldability and increased resistance to intergranular corrosion [13].

3.2. Chemical composition

Stainless steel often contains iron as the primary metal, as well as chromium, nickel, and other alloying components. Covert et al. [18] concluded that the chemical composition of stainless steel may vary depending on the exact grade or type. The elemental composition of the stainless-steel alloy primarily affects the mechanical properties and corrosion resistance of each grade for example:

- Nickel promotes the production of austenite in stainless steel, preventing corrosion. Its presence enhances the alloy's ductile characteristics and adds to its strength [13].
- Chromium is known for its high corrosion resistance because of its self-repairing passive properties. This makes it an important component in various stainless-steel compositions. According to F.-U. Rehman [19], adding chromium increases the alloy's ductility and strength while also increasing the formation of a ferritic phase.
- Manganese is a key ingredient in stainless steel manufacture, acting as a deoxidizing agent and improving crack resistance. It enhances the production of a ferrite phase at higher temperatures and an austenite phase at lower temperatures [19].
- At temperatures as high as 500°C, molybdenum has fire-resistant properties and is a useful element for corrosion resistance. Similar to chromium, molybdenum greatly increases ferrite's strength [19].
- The addition of nitrogen (N) significantly enhances the mechanical properties of stainless steel, including its strength and ductility, as demonstrated by [20] and Markeset et al. [21].
- Stainless steel alloys frequently include additional elements such as phosphorus (P), copper (Cu), carbon (C), silicon (Si), and sulfur (S). Table 1 outlines the chemical composition of commonly utilized grades of stainless-steel reinforcement.

Table 1
Outlines the chemical composition of commonly utilized grades of stainless-steel reinforcement [22]

Stainless steel grade	Chemical composition (%)- Upper acceptable % limits for every component									
	C	**Si**	**Mn**	**S**	**Cr**	**Ni**	**Mo**	**Cu**	**P**	**N**
1.4162	0.04	1.0	4.0-6.0	0.015	21.0-22.0	1.35-1.70	0.10-0.80	0.10-0.80	0.040	0.20-0.25
1.4462	0.03	1.0	2.0	0.015	21.0-23.0	4.5-6.5	2.5-3.5	-	0.035	0.10-0.22
1.4311	0.03	1.0	2.0	0.030	17.5-19.5	8.5-11.5	-	-	0.045	0.12-0.22
1.4404	0.03	1.0	2.0	0.030	16.5-18.5	10.0-13.0	2.0-2.5	-	0.045	≤0.11
1.4362	0.03	1.0	2.0	0.015	22-24.5	3.5-5.5	0.10-0.60	0.10-0.60	0.035	0.05-0.20
1.4436	0.05	1.0	2.0	0.030	16.5-18.5	10.5-13.0	2.5-3.0	-	0.045	≤0.11

3.3. Mechanical property

The mechanical properties of stainless-steel reinforcement bars relate to the physical characteristics that affect their strength, durability, and resistance to external forces. The properties include tensile strength, yield strength, elongation, toughness, and impact resistance. Stainless steel reinforcement bars offer significant tensile strength, allowing them to support loads and withstand deformation [23].

3.3.1. Stress and strain characteristics of stainless-steel alloys

Stainless steel reinforcement has excellent mechanical properties, including high strength and stiffness, as well as exceptional ductility, toughness, and fatigue resistance. However, those properties may differ depending on the grade and production method. Duplex and austenitic stainless steels are frequently utilized in concrete construction projects due to their exceptional corrosion resistance, and widespread availability as demonstrated by Pardeshi et al. [24] and M. Rabi et al.[25].

Stainless steel grades of this nature generally provide enhanced strength, superior strain hardening, and greater ductility compared to carbon steel reinforcement. Furthermore, they demonstrate a unique constitutive response in comparison to carbon steel [13]. Unlike carbon steel, stainless steel does not display a distinct yield point at a typical room temperature. The stress-strain relationship is non-linear, exhibiting increased strength and reduced stiffness as demonstrated in Fig.2[25]. The yield strength is often assessed by measuring the 0.2% proof stress ($f_{0.2p}$). In contrast, carbon steel exhibits a behavior that is either elastic-plastic or elastic-linear hardening, defined by a distinct yield point and a moderate level of strain hardening [13]. Table 2 presents the mechanical properties of several widely used stainless steel reinforcements, providing the 0.2% proof strength ($\sigma_{0.2}$), ultimate strength (σ_u), Young's modulus (E), and ultimate strain (ε_u) as outlined by Medina et al. [26]. The ability of stainless steel to deform without fracture significantly improves its structural integrity, allowing it to withstand substantial damage and distortion under loading conditions, such as seismic environments. Investigations conducted by Pardeshi et al. [24], Di Sarno et al. [27], and Xu et al. [28] have demonstrated that this

characteristic aids in the redistribution of loads and stresses across the structure.

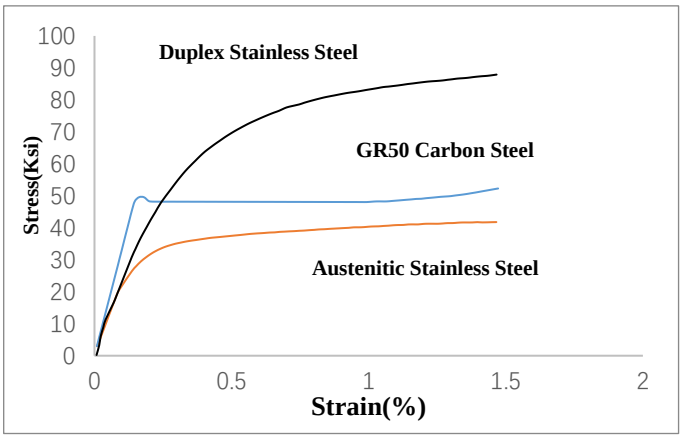

Fig. 2 An illustrative representation of stress-strain diagrams for Austenitic and Duplex stainless steel, alongside carbon steel. [25]

Table 2
Mechanical properties of Stainless steel and carbon steel reinforcement [26]

References	Grade	Dia mm	$\sigma_{0.2}$ (N/mm^2)	σ_u (N/mm^2)	E (kN/mm^2)	E_u (%)
Gardner et al. **[29]**	1.4162	12	682	874	199.1	32.4
	1.4162	16	646	844	195.2	32.9
	1.4311	12	480	764	202.6	48.3
	1.4311	16	528	717	199.9	47.9
	1.4307	12	562	796	210.2	39.9
	1.4307	16	537	751	211.1	42.4
	1.4362	16	608	834	171.4	35.1
M. Rabi et al. **[30]**	Carbon steel	10	525	627	196	20.1
	1.4301	8	720	888	156	44.6
	1.4301	10	668	799	148.6	38.3
	1.4301	12	670	795	186.8	26.7
	1.4436	8	614	823	178.5	36.5
	1.4436	10	661	793	179.3	25.6
	1.4436	12	645	803	198.6	25.3
Q. Li et al. **[31]**	Carbon steel	12	380	530	230	31
	1.4462	6.5	595	800	141	32.5
	1.4462	12	660	830	141	37.8
	1.4462	16	640	795	151	33.9
Q. Li et al. **[32]**	Carbon steel	16	477	654	202	26.8
	1.4362	12	637	872	156	33
	1.4362	16	532	768	156	36.4
	1.4362	25	543	761	202	31.1
	1.4362	32	527	748	139	36.9
	Carbon steel	10	589	661	201.4	12.49
M. Rabi et al. **[25]**	Carbon steel	12	554	635	211.8	9.21
	1.4301	10	515	790	200.9	32.4
	1.4301[grip-rib]	12	715	868	184.0	21.1

3.3.2. Modulus of Elasticity in Stainless Steel Alloys

Rehman et al. [33] recommended to select a Young's modulus in the range of 190-200 kN/mm^2 for various grades of stainless steel. Eurocode 2 specifies that the Young's modulus of carbon steel is around 200 kN/mm^2 [34]. The complex constitutive behavior of stainless-steel reinforcement requires further investigation, particularly related to evaluation of reliability in future uses. Recent academic literature indicated that a reduced value for the Young's modulus of stainless-steel reinforcement could be more suitable in design considerations as concluded by Medina et al. [26], M. Rabi et al. [30], and Rabi et al. [13]. The stress-strain characteristics of carbon steel are precisely represented using a simple bilinear model. The material behavior of stainless steel is characterized by the modified Ramberg-Osgood model, which defines a continuous and nonlinear relationship. The initial version of this model was introduced in 1943 by Giardina Jr et al. [35] to represent the elastic phase, and to include the inelastic phase which was subsequently revised by Jr et al. [36] and Mirambell et al. [37]. The modified Ramberg-Osgood material model is extensively utilized to characterize the behavior of stainless steel in design and simulation scenarios, with its parameters obtained from Equations 1 and 2.

$$\varepsilon = \frac{\sigma}{E} + 0.002\left(\frac{\sigma}{\sigma_{0.2}}\right)^{n} \qquad for \quad \sigma \le \sigma_{0.2} \qquad (1)$$

$$\varepsilon = \varepsilon_{0.2} + \frac{\sigma-\sigma_{0.2}}{E_2} + (\varepsilon_u - \varepsilon_{0.2} - \frac{\sigma_u-\sigma_{0.2}}{E_2})(\frac{\sigma-\sigma_{0.2}}{\sigma_u-\sigma_{0.2}})^{m} \qquad for\ \sigma_{0.2} < \sigma \le \sigma_u \qquad (2)$$

The equations contain variables for engineering strain (ε) and stress (σ), including a tangent modulus (E_2) at 0.2% proof stress, ultimate stress (σ_u), its associated strain (ε_u), and the strain at a 0.2% increase in stress ($\varepsilon_{0.2}$). The constants n and m relate to material hardening in response to strain. These parameters are generally obtained from tensile tests, as outlined in Eurocode 3 Part 1-4, which provides recommended values for structural stainless steel and their applicability may differ when used for stainless steel reinforcement.

4. Behavior of stainless-steel reinforcements subjected to elevated temperatures

4.1. Post-fire examination of stainless-steel reinforcement bars

The post-fire scenario regarding stainless steel reinforcing bars involves the properties and condition of these bars after exposure to fire conditions. Gardner et al. [29] determined that the fire intensity, heat exposure, and duration can affect the mechanical properties of stainless-steel reinforcing bars. F. U. Rehman et al. [33] identified that elements such as strength, malleability, and corrosion resistance are crucial and assessing the condition of stainless-steel reinforcing bars post-fire exposure is vital for verifying their structural integrity and functional performance for future uses [33]. Stainless steel reinforcement bars, commonly referred to as rebar, are utilized in construction to enhance the durability of concrete structures.

Stainless steel reinforcement bars exhibit exceptional resistance to corrosion, heat, and oxidation. This characteristic significantly reduces the effect of fire on its mechanical properties. A crucial element in creating fire-resistant structures is the material's ability to preserve its stiffness and strength even under elevated temperatures. Badoo [39] clarified that stainless steel maintains considerable strength and stiffness under elevated temperatures. Extensive research has been conducted on the behavior of structural stainless steel in fire conditions, as demonstrated in Table 3. For example, Tao et al. [40] found that EN 1.4462, 1.4362, 1.4307, 1.4404, and 1.4003 stainless steels, heated from 300 to 1200 °C for 20 minutes, exhibited negligible influence of thermal conditions on the stress-strain (σ-ε) characteristics at temperatures of 500 °C or below. However, the strength significantly decreases at temperatures above 600 °C. Austenitic alloys typically perform well, with mild steel and duplex alloys having similar efficacy. Ferritic alloys, on the other hand, have superior strength when compared to high-strength steels, but they are susceptible to embrittlement at temperatures above 800 °C.

Gao et al. [41] investigated both EN 1.4401 and 1.4301, which were heated from 200 to 1100 °C for durations of 30 and 180 minutes. The study concluded that initial findings indicate a modest decline in the post-fire mechanical characteristics of stainless steels S30408 and S31608 when exposed to temperatures below 1000 °C. Furthermore, the modulus of elasticity increases following fire exposure, peaking at a temperature of 800°C, with an approximate rise in the coefficient of 50%. On the other hand, exposure to fire results in a notable reduction in nominal yield strength, with decreases of around 30% for S30408 and 20% for S31608 at temperatures of 1100°C.

A further investigation conducted by Fan et al. [42] on EN 1.4301 involved heating the material at temperatures ranging from 100 to 900 °C for durations of 5 and 15 minutes. The analysis revealed significant discrepancies in the

stress-strain curves of stainless steel at elevated temperatures, specifically between 600 and 800 °C, when contrasting steady-state and transient testing methodologies. The observed variances were notably reduced within the temperature range of 100–500 °C.

Table 3
Notable Results from Prior Research

Material Type	heating rate	Target Temperature (°C) & aging time	Cooling mode	Findings	Reference
EN 1.4462 1.4362 1.4307 1.4404 & 1.4003	20°C/min	Heated from 300 to 1200°C for 20 min	Slow cooling in air	Up to 500 °C, stainless steel exhibits stable stress-strain characteristics; however, above 600 °C, it begins to deteriorate. At high temperatures, different steel types behave differently in terms of strength and brittleness.	Z.Tao et al. **[40]**
EN 1.4401 & 1.4301	20° C/ min	Heated from 200 to 1100°C for 30 and 180 min	Rapid quenching in water and gradual ambient air cooling	The research indicated a reduction in the strength of stainless steels S30408 and S31608 at temperatures below 1000°C. Furthermore, exposure to fire led to notable decreases in yield strength, approximately 30% for S30408 and 20% for S31608, at temperatures reaching 1100°C..	Gao et al. **[41]**
EN 1.4301	10 &20° C/ min	Heated between 100 and 900°C for 5 and 15 min	n/a	Significant differences in the stress-strain curves of stainless steel were observed at elevated temperatures ranging from 600 to 800 °C when comparing steady-state and transient testing methods. The variances were lower within the temperature range of 100–500 °C.	Fan et al. **[42]**
EN 1.4301, 1.4436, B500B & 1.4401	10° C/ min	Heated from 100 & 900°C for 1 hour	Rapid quenching in water, gradual cooling in ambient air, and within a furnace environment	Stainless steel reinforcement bars preserved their mechanical properties after exposure to elevated temperatures, with the cooling rate exerting minimal influence. Notable alterations in behavior were observed at moderate temperature levels.	F.U. Rehman et al. **[33]**
EN 1.4301	10° C/ min	Heated from 300, 400 to 1000 °C for 20 min	Gradual air cooling	The material properties of austenitic stainless steel remain stable at elevated temperatures, with notable alterations occurring beyond 600 °C to 800 °C.	(A. He et al. **[43]**
EN 1.4162 & 1.4462	20° C/ min	Heated from 1 & 10 hours heated from 600 to 800 °C	Slow cooling in the furnace and fast cooling in water	The materials retain their strength and flexibility post-exposure to fire, demonstrating their capacity to withstand high pressures without affecting safety.	Maslak et al. **[44]**
EN 1.4462	n/a	For 30 min, heated at 1050°C	Rapid quenching within water, gradual cooling in ambient air, and internal furnace cooling.	The addition of particular components decreased the material's strength; however, high-temperature treatment followed by quenching improved its toughness without causing further phase formation.	Chaudhari et al. **[45]**
EN 1.4162	20° C/ min	For 0,60, 180 mins,heated from 200 till 1000°C	The material is heated in the furnace until 150°C and then cooled to room temperature.	The mechanical properties of lean duplex stainless steel specimens remained stable at elevated temperatures and across different exposure durations.	Y.et al.**[46]**
EN 1.4406	n/a	Within the temperature range of 250 to 850°C, utilizing increments of 50°C.	Rapid quenching in aqueous solution	The research investigated the influence of temperature and strain rate on the tensile characteristics of nitrogen-alloyed low carbon grade 316L(N) austenitic stainless steel. Increased temperatures led to enhanced ductility and reduced flow stress and work hardening rate due to dynamic recovery phenomena.	Choudhary **[47]**
EN 1.4372 & 1.4404	n/a	For one hour heated at 1050 °C	Rapid quenching in aqueous solution	The reduction in heat input enhanced tensile strength and microhardness. The morphology of ferrite was influenced by the level of heat applied, where low heat yielded both skeletal and lathy ferrites, while high heat resulted exclusively to the formation of skeletal ferrite.	Tandon et al. **[48]**
EN 1.4162, 1.4571& 1.4301	40-60°C/ min	For 5-10 mins heated at 350, 650 & 950°C	Gradual temperature reduction in an atmospheric environment	The research indicated that samples cooled at distinct temperatures exhibited differing impacts on ultimate strengths. Samples cooled at 350 and 650 °C demonstrated increased strength, whereas those cooled at 950 °C showed reduced strength. The failure mechanisms in stainless steel connections following fire exposure were similar to those seen in specimens tested under non-post-fire conditions.	Cai **[49]**
EN 1.4462 & RS	n/a	For 30,60,120,180,300 & 10080 min, heated for 500 °C	Rapid quenching within water	The research indicates that spinodal decomposition enhances the tensile strength while diminishing the ductility of 2205 Duplex Stainless Steel. It also preserves mechanical properties superior to rebar steel at temperatures below 500°C for short durations.	X. Li et al. [**50]**

S235JR & EN 1.4404	10° C/ min	For 15 mins, heated from 100 till 950 °C	n/a	The mechanical integrity of SC bimetallic steel can get weakened at elevated temperatures, and current predictive models for carbon-manganese or stainless steel are considered not sufficient.	Ban et al**. [51]**
EN 1.4410[LN]	n/a	For 1 hour, heated at 1100,1150 &1200 °C	Rapid quenching within water	Additive manufacturing can produce type 25Cr duplex stainless steel with enhanced mechanical properties, including strength and ductility. This makes it applicable to various applications.	J. He et al. **[52]**
EN 1.4959, 2.4663, 1.4841, 1.4404& 1.4990	10, 15 & 20° C/ min	For 30 & 180 min,heated between 400 till 700 °C	n/a	The materials demonstrated improved ductility at higher temperatures, correlated with an increase in nickel content.	Calmunger et al. **[53]**
EN 1.4301	20° C/ min	For 30 min heated at 200 & 300 °C, for 800 °C is heated for 45,90 & 135 min	Gradual temperature reduction within a furnace	The effect of duration of exposure to high temperatures on the mechanical characteristics of stainless steel after combustion seems limited. Nonetheless, a significant decrease in yield strength is noted for both flat and curved specimens when subjected to temperatures above 500 °C. When compared to carbon steel, stainless steel exhibits better durability and maintains superior strength after exposure to fire events.	Wang et al. **[54]**

4.2. Precipitation of secondary phases and thermal aging conditions in stainless steel reinforcement bars

Sathirachinda [55] clarified that the emergence of secondary phases requires the development of supplementary chemical compounds or structures within a stainless-steel substrate. This may occur as a result of thermal aging or exposure to specific environmental conditions. X. Li et al. [56] concluded that thermal aging may induce secondary phase precipitation in stainless steel reinforcing bars, potentially affecting their mechanical properties and overall performance. J. Li et al. [57] indicated that the existence of secondary phases can induce modifications in the material's microstructure, as illustrated by the formation of chromium carbides. This phenomenon may reduce corrosion resistance and increase brittleness in stainless steel. Moreover, the conditions of thermal aging significantly influence the formation of these secondary phases which are determined by factors such as temperature duration and the metal composition of the alloy as clarified by Byun et al. [58]. Table 4 summarizes the notable results from prior research for the secondary phases precipitations and thermal aging conditions.

Austenitic stainless steels are made up only of the austenitic phase, whereas duplex steels typically include both austenite and ferrite as their main phases, as illustrated in Fig. 3 which was done by Raha [59]. Li [60] noted that the microstructure of duplex steels typically displays a predominance of a ferritic matrix scattered with austenitic islands, which is due to initial precipitation and higher ferrite content. The ratios of ferrite to austenite significantly affect the corrosion resistance and mechanical properties of duplex Stainless Steels. Chromium, molybdenum, and nitrogen are all known for their important functions in reducing pitting corrosion, with higher concentrations linking to enhanced resistance [60]. Variations in properties arise from differences in chemical composition, which depend on the enrichment of ferrite or austenite with stabilizing elements like chromium and molybdenum for ferrite, and nitrogen (N) for austenite [60]. The temperature used in heat treatment can alter the ratio of ferrite to austenite, as well as its composition as shown in Fig. 4 which was done by Tan et al. [61].

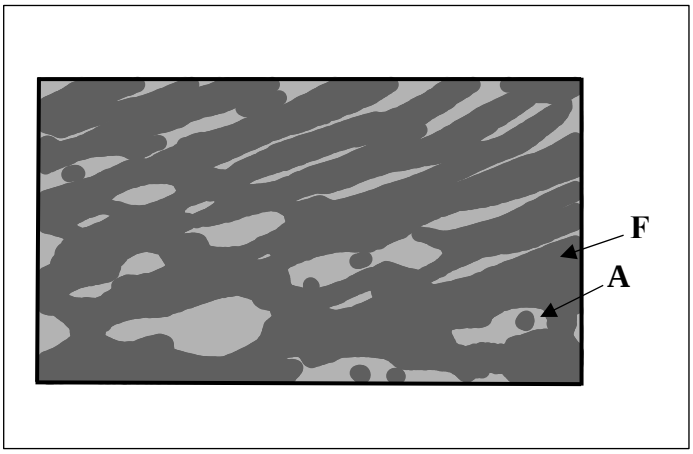

Fig. 3 Microstructure of Duplex stainless steel

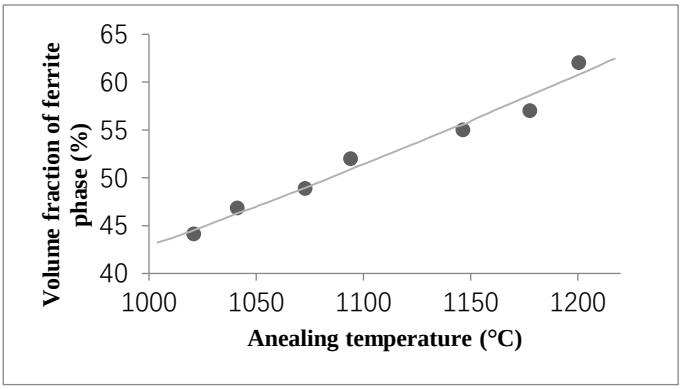

Fig. 4 Fractional volume of the ferrite phase after undergoing thermal treatment across different temperatures for a duration of 2 hours

Thermal aging involves exposing stainless steel rebars to high temperatures for an extended duration. H. Y. Huang et al. [62] concluded that prolonged exposure to elevated temperatures can result in additional microstructural alterations, including grain growth and the formation of new phases. Thus, variations in phase ratios and changes from thermal aging due to different heat treatments may lead to modifications in mechanical properties which are influenced by the amount of ferrite phase and its initial morphology at temperatures above 1000°C [63]. Furthermore, the increased concentration of alloying elements leads to the formation of various intermetallic phases, nitrides, and carbides, including sigma phase, chi phase, and $M_{23}C_6$, during heat treatment processes conducted at temperatures below 1000 °C [60]. For example, DSS undergoes phase changes via spinodal decomposition at temperatures lower than 525°C, with reactions occurring more rapidly around 475°C. This mechanism enables the transformation of the initial phase, x, into a chromium-deficient X phase and a chromium-enriched (x') phase, as explained by Chan et al. [64] and Tavares et al. [65] and the following points explain those phases:

σ (Sigma) phase: Shamanth et al.[66] found out a precipitate enriched with chromium and molybdenum, exhibits hardness and brittleness, typically forming in the temperature range of 650 to 1000°C. This formation is frequently linked to a decrease in both impact toughness and corrosion resistance. Ferrite has higher mobility and concentrations of molybdenum and chromium than austenite, so the **σ**-phase precipitates primarily in the ferritic phase. It can also develop in the heat affected zone during welding processes. This substance has a tetragonal crystal structure, with 32 atoms per unit cell and five distinct crystallographic sites for atom placement. The morphological characteristics of the **σ**-phase change with temperature. At 750°C, it has a structure similar to coral, however, at 950°C, its shape becomes larger and more densely packed.

The decrease in Mo content is significantly larger compared to that of Cr, indicating that Mo primarily influences the precipitation of the **σ**-phase. The σ-phase develops quickly, requiring a very rapid cooling rate to prevent its development during the quenching process from solutionizing temperatures. For EN 1.4462 duplex stainless steel, it is crucial to maintain a cooling rate of 0.23 Kelvin per second to ensure that the formation of **σ**-phase remains below 1% [67]. The addition of significant amounts of alloying elements into DSS results in the formation of various carbides, intermetallic compounds, and secondary phases. These constituents precipitate at varying kinetics within specific temperature ranges, as illustrated in Fig. 5[68].

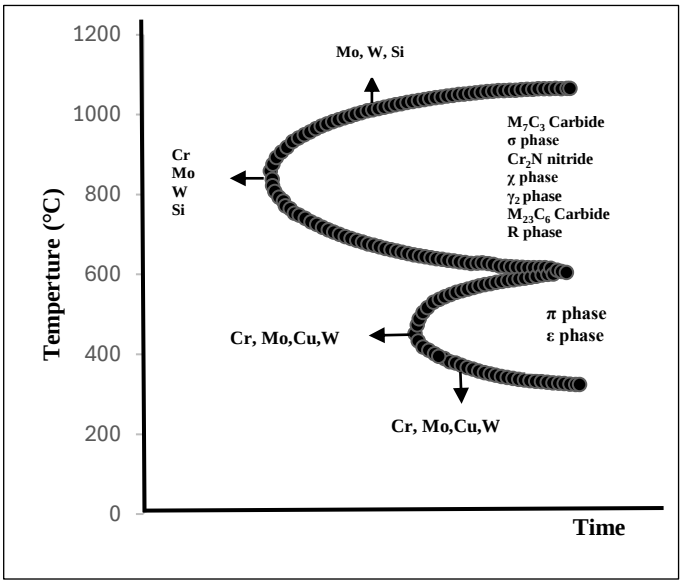

Fig. 5 Isothermal cooling curve for the ternary Fe-Cr-Ni system illustrating the impact of alloying additions on the precipitation of secondary phases during cooling

χ (Chi) phase:

The addition of ferrite with elements that can form intermetallic compounds during extended thermal exposure around 700°C allows the precipitation of the Chi (χ) phase. It generally begins at the δ/γ interface and extends into the δ matrix, and evaluating its influence on corrosion and toughness is difficult due to the common coexistence with the **σ** phase. An increase in aging duration leads to a higher concentration of Mo and a decrease of Fe in the χ-phase. During isothermal aging, the precipitation of the χ-phase consistently precedes that of the **σ**-phase, however, under continuous cooling conditions, the formation of the χ-phase occurs only at decreased cooling rates, as concluded by Redjaïmia [67].

α′ (alpha prime) phase:

The BCC crystal structure in this phase corresponds with the α phase, consisting of approximately 62-83 % of chromium. Within the temperature range of 300 to 550 °C, alpha prime mainly develops as the principal precipitation phase due to spinodal decomposition. This phenomenon is commonly referred to as 475 °C embrittlement, characterized by increased hardness, yield strength, and tensile strength, accompanied by reduced elongation and impact resistance [60]. For more than fifty years, researchers have systematically investigated the phenomenon of spinodal decomposition in stainless steels.

Epsilon phase:

A study by Shamanth et al. [66] found that in duplex alloys containing copper, reduced solubility at lower temperatures leads to the super-saturation of ferrite. This condition leads to the precipitation of very fine Cu-rich epsilon (ε) phase particles within the ferrite grains after 100 hours of exposure at 500°C. This significantly expands the lower temperature strengthening range for duplex stainless steels. ε-phase is often incorrectly identified as γ_2 due to similar formation temperatures.

R phase:

The isothermal treatment of duplex stainless steels at temperatures between 550 and 650°C results in a consistent and finely dispersed distribution of the R-phase within δ grains [67]. The R-phase, characterized by its enrichment in molybdenum, exhibits a trigonal crystal structure and its emergence reduces both the toughness and the critical pitting temperature in duplex stainless steels. Nilsson [69] clarified that R-phase precipitations can occur as either intergranular or intragranular, with the former potentially presenting a higher risk for pitting corrosion due to their capacity to contain up to 40% Mo. The extension of the aging process results in the conversion of R-phase into σ-phase, which is due to the diffusion of Mo from the former phase to the latter. As a result, there is a decrease in the volume fraction of R-phase, as concluded by S. Zhang et al. [70].

G, π and τ phases:

The G-phase forms at α/α′ interfaces within a temperature range of 300 to 400°C following extended exposure, due to the accumulation of Ni and Si at these particular locations [66]. The π-nitride precipitate, which has a cubic crystal structure and is enriched in chromium and molybdenum, appears at intergranular locations within duplex stainless-steel welds after undergoing isothermal treatment at 600°C for a prolonged duration [66]. The η-phase is a precipitate defined by significant faulting and needle-like morphology, formed as a result of heat treatment at temperatures between 550 and 650°C. This phase exhibits an orthorhombic crystal structure [67].

Table 4

Summarizes the notable results from prior research for the secondary phases precipitations and thermal aging conditions

Material type	Target Temperature (°C) ,aging time & cooling mode	Findings	Reference
EN1.4462	Within the temperature range of 600 to 1000 °C for a duration of 2600 minutes, followed by rapid quenching in water.	The effects of aging temperature on the corrosion resistance of duplex stainless steel were not significant; however, aging at temperatures ranging from 700 to 900°C results in a reduction in pitting corrosion resistance. W-substituted steel showed better pitting corrosion resistance compared to its Mo-only counterpart	Ahn et al. [71]
EN 1.4501	Within the temperature range of 900 to 1100 °C for a duration of 120 minutes, followed by rapid quenching in water	Sigma phase particles develop at the interfaces of ferrite and austenite grains, with the soaking temperature determining their dissolution and the ferrite-to-austenite ratio. Higher heat treatment temperatures increase ferrite content, preventing sigma phase formation above 1060°C for a balanced distribution of approximately 50% each - affecting material hardness inversely with heating temperature.	Martins et al. [72]
EN 1.4662	Subjected to heating at a temperature of 475°C for durations of 100, 300, 600, 1100, and 2000 hours followed by quenching in water.	After 1100 hours, chromium stabilizes at 5%, decreasing corrosion resistance and significantly influencing mechanical properties. Low Duplex Stainless Steel 2404 has lower corrosion resistance than Duplex Stainless Steel 2205 due to the division of α and α′ phases during spinodal decomposition.	Silva et al. [73]
EN 1.4462	The samples were subjected to heating at temperatures of 450°C, 475°C, 800°C, and up to 850°C for durations of 1 hour, 3 hours, and 12 hours followed by quenching in water	Exposure to high temperatures leads to phase precipitation in the ferrite matrix, reducing steel hardness and corrosion resistance. Prolonged aging reduced corrosion resistance and increased sensitization due to phase precipitates at higher temperatures.	Dainezi et al. [10]
EN 1.4162	Subjected to heating at 700 °C for durations of 3, 10, 30, 120, and 240 minutes followed by rapid quenching in water	After aging lean Duplex Stainless Steel 2101 at 700°C, intermetallic precipitates with higher chromium concentration formed between the α/γ and α/α boundaries. A secondary phase of austenite with lower chromium content was found near these precipitate regions.	L. Zhang et al. [74]

EN 1.4501	Subjected to a temperature of 300 °C for durations of 3,000, 6,000, and 12,000 hours.	Variations in Chromium concentration during aging affect the hardness of the ferrite phase and result in a reduction of impact toughness. Aging causes a change in fracture behavior from ductile to cleavage, with crack propagation mainly occurring through the ferrite phase along deformation twin interfaces, while delamination between austenite and ferrite phases becomes visible.	Pettersson et al.[75]
EN 1.4462	Heated from 700 to 1050 °C for intervals of 5, 30, 60, and 120 minutes	The alpha phase becomes more noticeable in 2205 Duplex Stainless Steel when the levels of nitrogen and carbon are low. It forms inside or on the edges of ferrite grains. After being aged at 850°C, it's most common. At first, the π-phase is seen, but between 700°C and 750°C, the χ-phase mostly forms because of stronger thermodynamic forces. This was proven with Thermo-Calc software, which also showed that sigma expands more quickly. But c-phase concentrations have a bigger effect on steel's impact toughness than χ-phase concentrations because π-phase does not occur as frequently.	Y. L. He et al. [76]
EN 1.4462	Subjected to heating at a temperature of 850 °C for durations of 6, 40, and 600 minutes followed by rapid quenching in water	The different phases of microstructure development in stainless steel, such as the formation of chromium nitrides and carbides and the evolution of the sigma phase, were examined using a variety of etching techniques. Sigma phase development and embrittlement from the precipitation of chromium carbides and nitrides were caused by aging heat treatments that were performed at temperatures higher than 850°C for longer than six minutes. Sigma phase emergence was not detected by the Charpy impact test.	Zucato et al. [77]
EN 1.4162	Heated to a temperature of 750°C for a duration of 3 and subsequently 480 hours, followed by quenching in water.	The study on EN 1.4162 lean duplex stainless steel shows that exposure to 750°C for a duration of up to 480 hours leads to the formation of precipitates at the phase boundaries and intersections of ferrite grains. Nitride formation was initially observed, whereas extended durations resulted in σ phase precipitation. The aging process affected mechanical properties, resulting in a decrease in ductility while improving yield strength and ultimate tensile strength.	Dandekar et al. [78]
EN 1.4462	Within a temperature spectrum of 450 to 1000 °C, for a duration of 10 minutes followed by rapid quenching in water.	Aging at temperatures ranging from 600 to 950 °C results in the formation of new phases, including Cr2N, σ, and χ. The most significant decrease in pitting corrosion resistance and impact energy occurs at 850 °C. Temperatures reaching 600 °C leads to a change of the pitting initiation site from austenite to an altered ferritic phase because of precipitation incidents.	Deng et al. [79]
EN 1.4462	Subjected to heating at 300 and 400°C for durations of 3,000; 5,000; and 7,000 hours.	When heating to 400 ºC, the ferrite phase in 2205 DSS steel exhibits an increase in hardness due to the formation of new phases. However, this does not occur when heated up to 300 ºC for up to 7000 hours. Furthermore, extended heating at 400 °C results in increased chromium loss in the material, with no noticeable self-repairing occurring despite prolonged exposure.	Rovere et al.[80]
EN 1.4410	Heated at 700-900 °C for varying durations with rapid water quenching.	The aging of the samples led to sigma-phase precipitation in both ferrite and austenite regions, resulting in decreased stability and resistance to pitting corrosion. Exposure to chloride-containing aggressive environments caused localized damage to previously ferritic regions that had transformed due to aging at temperatures above 700 ºC for more than 1 hour.	Angelini et al. [81]

5. Conclusion

Both duplex and austenitic stainless steel reinforcement bars have excellent strength and corrosion resistance which making them an ideal option for reinforced concrete structure. However, the absence of standardized practices and recommendations for employing duplex stainless-steel rebar may raise concerns about its effectiveness and long-term durability in concrete constructions. When evaluating duplex grade rebars, it is essential to understand the manufacturing process to avoid the development of highly brittle phases, such as sigma phases, within the microstructure. Additionally, duplex stainless steel rebars exhibit a less stable microstructure in comparison to austenitic rebars, making them more susceptible to changes under similar conditions. Consequently, this paper provides a comprehensive review of research on reinforcing bars made of duplex and austenitic stainless steel used in reinforced concrete structures. Furthermore, it examines the effects of prolonged high-temperature exposure on material characteristics, as well as various cooling methods. Sufficient information has been provided in the current literature to enable engineers to make well-informed decisions on the structural integrity of duplex and austenitic stainless steel reinforced concrete structures after being exposed to fire. A detailed analysis of various temperature exposure levels was conducted, covering a wide range of potential behaviors to maximize informative value. The examined cooling methods were analyzed to replicate real-world conditions that the rebar could experience.

In conclusion, the engineering research community has recognized the significant benefits that stainless steel reinforced concrete offers to the construction industry, especially when a durable, low-maintenance life cycle is required. In addition, this paper summarized the mechanical behavior of duplex and austenitic reinforcement rebars when subjected to static loads. Potential future investigations could include an assessment of material strength and resistance to fracture, alongside an examination of their behavior during repeated loading cycles.

Acknowledgments

The authors gratefully acknowledge the Universiti Malaya (UM) for providing the necessary facilities and resources for this research. This research was supported by the Faculty of Engineering Programme under a special funding aid, Bantuan Khas Penyelidikan (BKPFK-2024-15), Universiti Malaya.

References

[1] Santonen, T., Stockmann-Juvala, H., & Zitting, A. (n.d.). Review on toxicity of stainless steel.

[2] Mustapha Karkarna, Y., Bahadori-Jahromi, A., Zolghadr Jahromi, H., Halliwell, E., & Mohammad Rabi, M. (2022). Reinforced Concrete Design with Stainless Steel. In Reinforced Concrete Structures - Innovations in Materials, Design and Analysis. IntechOpen. https://doi.org/10.5772/intechopen.106327 [3] Zhu S.Y. and Qiu C.X., "Performance-based plastic design of self-centering steel braced frame", Proceedings of the 2nd International Conference on Performance-based and Life-cycle Structural Engineering (PLSE 2015), Brisbane, QLD, Australia, 1259-1259, 2015.

[3] Stoica, M., Alexe, P., Dinica, R., & Carac, G. (2012). Electrochemical Behaviour of AISI 304 Stainless Steel Immersed in Mixtures Consisting by Biocide and Fungal Suspensions. In Food Industrial Processes - Methods and Equipment. InTech. https://doi.org/10.5772/30839.

[4] Stainless steel reinforcement bar the sustainable cost effective choice for concrete infrastructure knowledge for a brighter future. (n.d.).

[5] Muwila, A. (2006). The Effect of Manganese, Nitrogen and Molybdenum on the Corrosion Resistance of a Low Nickel (<2 wt%) Austenitic Stainless Steel.

[6] Steels, A. (n.d.). Atlas TechNotes. www.atlassteels.com.au

[7] Markeset, G. (2009). SINTEF Building and Infrastructure Gro Markeset Stainless steel reinforcement in con-crete structures-State of the art COIN Project report 4-2008. www.coinweb.no .

[8] Kahar, Dr. S. D. (2017). Duplex Stainless Steels-An overview. International Journal of Engineering Research and Application, 07(04), 27–36. https://doi.org/10.9790/9622-0704042736

[9] The Use of Stainless Steel for the Construction Industry. (2020).

[10] Dainezi, I., Borges, S. H., & Mariano, N. A. (2023). Effect of Precipitation of Alpha Line and Sigma Phases on the Microstructure and Corrosion Resistance of the Duplex Stainless Steel SAF 2205.

[11] Cronemberger, M. E. R., Nakamatsu, S., Rovere, C. A. Della, Kuri, S. E., & Mariano, N. A. (2015). Effect of cooling rate on the corrosion behavior of as-cast SAF 2205 duplex stainless steel after solution annealing treatment. *Materials Research*, *18*, 138–142. https://doi.org/10.1590/1516-1439.352114.

[12] Mohammed, A. M., Shrikrishna, K. A., & Sathiya, P. (2016). Effects of post weld heat treatment on friction welded duplex stainless-steel joints. Journal of Manufacturing Processes, 21, 196–200. https://doi.org/10.1016/J.JMAPRO.2015.10.005

[13] Rabi, M., Shamass, R., & Cashell, K. A. (2022). Structural performance of stainless steel reinforced concrete members: A review. In Construction and Building Materials (Vol. 325). Elsevier Ltd. https://doi.org/10.1016/j.conbuildmat.2022.126673.

[14] Rosso, M., Peter, I., & Suani, D. (2013). About heat treatment and properties of Duplex Stainless Steels. www.journalamme.org

[15] Outokumpu, ©. (n.d.). Handbook of Stainless Steel.

[16] Rabi, M. M. (2019). Analysis and design of stainless steel reinforced concrete structural elements.

[17] Gardner, L. (2005). The use of stainless steel in structures. In Progress in Structural Engineering and Materials (Vol. 7, Issue 2, pp. 45–55). https://doi.org/10.1002/pse.190.

[18] Covert, R. A., & Tuthill, A. H. (n.d.). Pages 506-517 Copyright© International Association for Food Protection, 6200 Aurora Ave (Vol. 20, Issue 7).

[19] Rehman, F.-U. (2022). Mechanical tensile testing and metallurgical investigation of the residual properties of stainless-steel reinforcing bar after exposure to elevated temperatures.

[20] Avesta Welding. (2009). The Avesta welding manual : practice and products for stainless steel welding. Avesta Welding.

[21] Markeset, G., Rostam, S., & Klinghoffer, O. (2006). Guide for the use of stain-less steel reinforcement in concrete structures.

[22] Version, E. (2014). Stainless steels-Part 1: List of stainless steels.

[23] Mcgurn, J. F. (n.d.). Stainless Steel Reinforcing Bars in Concrete.

[24] Pardeshi, R., Thakur, B., & Parghi, A. (2020). Seismic investigation of longitudinally aligned shape memory alloy-stainless steel reinforced concrete column. IOP Conference Series: Materials Science and Engineering, 814(1).

[25] Https://www.aisc.org/publications/steel-standards/stainless-steel- standards/?_gl=1*hkj6z9*_gcl_au*NzY2NDM5MTkxLjE3MzMxMDg3Njc.*_ga*MTczNjcyNzQzMC4xNzI5NjY0OTE2*_ga_97VGG712JL*MTczMzEwODc 2Ny4xLjEuMTczMzEwODk1NS4zNS4wLjA

[26] Medina, E., Medina, J. M., Cobo, A., & Bastidas, D. M. (2015). Evaluation of mechanical and structural behavior of austenitic and duplex stainless-steel reinforcements. Construction and Building Materials, 78, 1–7. https://doi.org/10.1016/j.conbuildmat.2015.01.008.

[27] Di Sarno, L., Elnashai, A. S., & Nethercot, D. A. (2003). Seismic performance assessment of stainless steel frames. Journal of Constructional Steel Research, 59(10), 1289–1319. https://doi.org/10.1016/S0143-974X(03)00067-1

[28] Xu, C., Nehdi, M. L., Youssef, M. A., Wang, T., & Zhang, L. V. (2021). Seismic performance of RC beam-column edge joints reinforced with austenite stainless steel. Engineering Structures, 232. https://doi.org/10.1016/j.engstruct.2020.111824.

[29] Gardner, L., Bu, Y., Francis, P., Baddoo, N. R., Cashell, K. A., & McCann, F. (2016). Elevated temperature material properties of stainless-steel reinforcing bar. Construction and Building Materials, 114, 977–997. https://doi.org/10.1016/j.conbuildmat.2016.04.009 .

[30] Rabi, M., Shamass, R., & Cashell, K. A. (n.d.). Experimental investigation on the flexural behaviour of stainless steel reinforced concrete beams.

[31] Li, Q., Guo, W., Liu, C., Kuang, Y., & Geng, H. (2020). Experimental and Theoretical Studies on Flexural Performance of Stainless Steel Reinforced Concrete Beams. Advances in Civil Engineering, 2020. https://doi.org/10.1155/2020/4048750.

[32] Li, Q., Cui, Y., & Wang, J. (2021). Basic mechanical properties of duplex stainless-steel bars and experimental study of bonding between duplex stainless-steel bars and concrete. Materials, 14(11). https://doi.org/10.3390/ma14112995.

[33] Rehman, F. U., Cashell, K. A., & Anguilano, L. (2022). Experimental Study of the Post-Fire Mechanical and Material Response of Cold-Worked Austenitic Stainless-Steel Reinforcing Bar. Materials, 15(4). https://doi.org/10.3390/ma15041564.

[34] EN 1992-1-1: Eurocode 2: Design of concrete structures - Part 1-1: General rules and rules for buildings. (2004).

[35] Giardina Jr, R., Wei, D., & Joseph Giardina, R. (2020). Ramberg-Osgood material behavior expression and large deflections of Euler beams Ramberg-Osgood material behavior expression and large deflections of Euler beams Journal Title XX(X):1-26. https://doi.org/10.1177/ToBeAssigned.

[36] Jr, K., & Msceng, R. (2001). Full-range Stress-strain Curves for Stainless Steel Alloys. http://www.civil.usyd.edu.au/.

[37] Mirambell, E., & Real, E. (2000). On the calculation of deflections in structural stainless steel beams: an experimental and numerical investigation. In Journal of Constructional Steel Research (Vol. 54). www.elsevier.com/locate/jcsr.

[38] EN 1993-1-4: Eurocode 3: Design of steel structures - Part 1-4: General rules – Supplementary rules for stainless steels. (2006).

[39] Baddoo, N. R. (2008). Stainless steel in construction: A review of research, applications, challenges and opportunities. *Journal of Constructional Steel Research*, *64*(11), 1199–1206. https://doi.org/10.1016/j.jcsr.2008.07.011

[40] Tao, Z., Wang, X. Q., Hassan, M. K., Song, T. Y., & Xie, L. A. (2019). Behaviour of three types of stainless steel after exposure to elevated temperatures. Journal of Constructional Steel Research, 152, 296–311. https://doi.org/10.1016/j.jcsr.2018.02.020.

[41] Gao, X., Zhang, X., Liu, H., Chen, Z., & Li, H. (2018). Residual mechanical properties of stainless steels S30408 and S31608 after fire exposure. Construction and Building Materials, 165, 82–92. https://doi.org/10.1016/j.conbuildmat.2018.01.020.

[42] Fan, S., He, B., Xia, X., Gui, H., & Liu, M. (2016). Fire resistance of stainless-steel beams with rectangular hollow section: Experimental investigation. *Fire Safety Journal*, *81*, 17–31. https://doi.org/10.1016/j.firesaf.2016.01.013.

[43] He, A., Liang, Y., & Zhao, O. (2019). Experimental and numerical studies of austenitic stainless steel CHS stub columns after exposed to elevated temperatures. Journal of Constructional Steel Research, 154, 293–305. https://doi.org/10.1016/j.jcsr.2018.12.005.

[44] Maslak, M., Pancikiewicz, K., Pazdanowski, M., Stankiewicz, M., Wozniczka, P., & Zajdel, P. (2023). Quantification of the Post-Fire Strength Retention Factors for Selected Standard Duplex and Lean Duplex Stainless Steel Grades. https://doi.org/10.20944/preprints202312.0286.v1.

[45] Chaudhari, A., Diwakar, N., & Kalpande, S. (n.d.). Mechanical characteristics, morphology and corrosion behavior of duplex stainless steel 2205. In Eur. Chem. Bull (Vol. 2023).

[46] Huang, Y., & Young, B. (2018). Mechanical properties of lean duplex stainless steel at post-fire condition. *Thin-Walled Structures*, *130*, 564–576. https://doi.org/10.1016/j.tws.2018.06.018.

[47] Choudhary, B. K. (2014). Influence of strain rate and temperature on tensile deformation and fracture behavior of type 316L(N) austenitic stainless steel. Metallurgical and Materials Transactions A: Physical Metallurgy and Materials Science, 45(1), 302–316.

[48] Tandon, V., Thombre, M. A., Patil, A. P., Taiwade, R. V., & Vashishtha, H. (2020). Effect of Heat Input on the Microstructural, Mechanical, and Corrosion Properties of Dissimilar Weldment of Conventional Austenitic Stainless Steel and Low-Nickel Stainless Steel. Metallography, Microstructure, and Analysis, 9(5), 668–677. https://doi.org/10.1007/s13632-020-00681-y

[49] Cai, Y., & Young, B. (2019). Structural behaviour of cold-formed stainless steel bolted connections at post-fire condition. *Journal of Constructional Steel Research*, *152*, 312–321. https://doi.org/10.1016/j.jcsr.2018.03.024

[50] Li, X., Lo, K. H., Kwok, C. T., Sun, Y. F., & Lai, K. K. (2018a). Post-fire mechanical and corrosion properties of duplex stainless steel: Comparison with ordinary reinforcing-bar steel. Construction and Building Materials, 174, 150–158. https://doi.org/10.1016/j.conbuildmat.2018.04.110.

[51] Ban, H., Bai, R., Yang, L., & Bai, Y. (2019). Mechanical properties of stainless-clad bimetallic steel at elevated temperatures. *Journal of Constructional Steel Research*, *162*. https://doi.org/10.1016/j.jcsr.2019.105704

[52] He, J., Lv, J., Song, Z., Wang, C., Feng, H., Wu, X., Zhu, Y., & Zheng, W. (2023). Maintaining Excellent Mechanical Properties via Additive Manufacturing of Low-N 25Cr-Type Duplex Stainless Steel. Materials, 16(22). https://doi.org/10.3390/ma16227125.

[53] Calmunger, M., Chai, G., Eriksson, R., Johansson, S., & Moverare, J. J. (2017). Characterization of Austenitic Stainless Steels Deformed at Elevated Temperature. Metallurgical and Materials Transactions A: Physical Metallurgy and Materials Science, 48(10), 4525–4538. https://doi.org/10.1007/s11661-017-4212-9.

[54] Wang, X. Q., Tao, Z., Song, T. Y., & Han, L. H. (2014). Stress-strain model of austenitic stainless steel after exposure to elevated temperatures. Journal of Constructional Steel Research, 99, 129–139. https://doi.org/10.1016/j.jcsr.2014.04.020

[55] Sathirachinda, N. (2010). Relative nobility of precipitated phases in stainless steels Evaluation with a combination of local probing techniques. KTH Chemical Science and Engineering, Royal University of Technology.

[56] Li, X., Lo, K. H., Kwok, C. T., Sun, Y. F., & Lai, K. K. (2018b). Post-fire mechanical and corrosion properties of duplex stainless steel: Comparison with ordinary reinforcing-bar steel. Construction and Building Materials, 174, 150–158. https://doi.org/10.1016/j.conbuildmat.2018.04.110

[57] Li, J., Du, C. W., Liu, Z. Y., Li, X. G., & Liu, M. (2018). Effect of microstructure on the corrosion resistance of 2205 duplex stainless steel. Part 1: Microstructure evolution during isothermal aging at 850 °C and evaluation of anticorrosion properties by methods of cyclic potentiodynamic polarization and electrochemical impedance tests. Construction and Building Materials, 189, 1286–1293. https://doi.org/10.1016/j.conbuildmat.2018.08.186.

[58] Byun, T. S., Yang, Y., Overman, N. R., & Busby, J. T. (n.d.). Thermal Aging Phenomena in Cast Duplex Stainless Steels.

[59] Raha, B. (2024). Useful Steps Recommended for the Production of Thick-Walled Duplex Stainless Steel Casting. *International Journal of Metalcasting*, *18*(1), 505–511.

[60] Li. (1968). Microstructural development of duplex stainless steels during thermomechanical processing. https://doi.org/10.26190/unsworks/21479.

[61] Tan, H., Jiang, Y., Deng, B., Sun, T., Xu, J., & Li, J. (2009). Effect of annealing temperature on the pitting corrosion resistance of super duplex stainless steel UNS S32750. Materials Characterization, 60(9), 1049–1054. https://doi.org/10.1016/j.matchar.2009.04.009

[62] Huang, H. Y., Wang, Y., & Xie, J. X. (2014). Stress-induced phase transformation characteristics and its effect on the enhanced ductility in continuous columnar-grained polycrystalline Cu-12wt%Al alloy. *Materials Science and Engineering: A*, *596*, 103–111. https://doi.org/10.1016/j.msea.2013.12.041.

[63] Unnikrishnan, K., & Mallik, A. K. (1987). Microstructure—Strength relations in a duplex stainless steel. Materials Science and Engineering, 94(C), 175–181. https://doi.org/10.1016/0025-5416(87)90331-4.

[64] Chan KW, Tjong SC. Effect of Secondary Phase Precipitation on the Corrosion Behavior of Duplex Stainless Steels. Materials (Basel). 2014 Jul 22;7(7):5268-5304. doi: 10.3390/ma7075268. PMID: 28788129; PMCID: PMC5455814.

[65] Tavares, S. S. M., da Silva, M. R., Pardal, J. M., Abreu, H. F. G., & Gomes, A. M. (2006). Microstructural changes produced by plastic deformation in the UNS S31803 duplex stainless steel. Journal of Materials Processing Technology, 180(1–3), 318–322. https://doi.org/10.1016/j.jmatprotec.2006.07.008

[66] Shamanth, V., S. Ravishankar, K., & Hemanth, K. (2019a). Duplex Stainless Steels: Effect of Reversion Heat Treatment. In *Stainless Steels and Alloys*. IntechOpen. https://doi.org/10.5772/intechopen.80007.

[67] Redjaïmia, A. (1992). Decomposition of Delta Ferrite in a Fe-22Cr-5Ni-3Mo-0.03C Duplex Stainless Steel. A Morphological and Structural Study. https://www.researchgate.net/publication/262724866

[68] Vicente, A. D. A., Botelho Junior, A. B., Sartori Moreno, J. R., Abreu Santos, T. F., Romano Espinosa, D. C., & Soares Tenório, J. A. (2019). Micro-Structural Characterization and Semi Quantitative Chemical Analysis of Ferrite and Austenite Phases in Duplex Stainless Steels. Available at SSRN 3309760.

[69] Nilsson, J. O. (1992). Super duplex stainless steels. Materials Science and Technology (United Kingdom), 8(8), 685–700. https://doi.org/10.1179/mst.1992.8.8.685

[70] Zhang, S., Shi, X., Liang, Y., Xu, H., Yan, C., Yan, W., Rong, L., & Yang, K. (2023). χ phase and its effect on the mechanical properties of a Mo-bearing high–Si austenitic stainless steel after aging at 650 °C. Journal of Materials Research and Technology, 23, 4280–4292. https://doi.org/10.1016/j.jmrt.2023.02.069.

[71] Ahn, Y. S., Kim, J. M., & Jeong, B. H. (2002). Effect of aging treatments and microstructural evolution on corrosion resistance of tungsten substituted 2205 duplex stainless steel. Materials Science and Technology, 18(4), 383–388. https://doi.org/10.1179/026708302225001642.

[72] Martins, M., & Casteletti, L. C. (2005). Heat treatment temperature influence on ASTM A890 GR 6A super duplex stainless-steel microstructure. Materials Characterization, 55(3), 225–233. https://doi.org/10.1016/j.matchar.2005.05.008.

[73] Silva, R., Baroni, L. F. S., Kugelmeier, C. L., Silva, M. B. R., Kuri, S. E., & Rovere, C. A. D. (2017). Thermal aging at 475 °C of newly developed lean duplex stainless steel 2404: Mechanical properties and corrosion behavior. Corrosion Science, 116, 66–73. https://doi.org/10.1016/j.corsci.2016.12.014.

[74] Zhang, L., Jiang, Y., Deng, B., Zhang, W., Xu, J., & Li, J. (2009). Effect of aging on the corrosion resistance of 2101 lean duplex stainless steel. *Materials Characterization*, *60*(12), 1522–1528. https://doi.org/10.1016/j.matchar.2009.08.009.

[75] Pettersson, N., Wessman, S., Thuvander, M., Hedström, P., Odqvist, J., Pettersson, R. F. A., & Hertzman, S. (2015). Nanostructure evolution and mechanical property changes during aging of a super duplex stainless steel at 300°C. *Materials Science and Engineering: A*, *647*, 241–248. https://doi.org/10.1016/j.msea.2015.09.009.

[76] He, Y. L., Zhu, N. Q., Lu, X. G., & Li, L. (2010). Experimental and computational study on microstructural evolution in 2205 duplex stainless steel during high temperature aging. Materials Science and Engineering: A, 528(2), 721–729. https://doi.org/10.1016/j.msea.2010.09.067.

[77] Zucato, I., Moreira, M. C., Machado, I. F., & Giampietri Lebrão, S. M. (2002). 385 Microstructural Characterization and the Effect of Phase Transformations on Toughness of the UNS S31803 Duplex Stainless Steel Aged Treated at 850 °C Microstructural Characterization and the Effect of Phase Transformations on Toughness of the UNS S31803 Duplex Stainless Steel Aged Treated at 850 °C. In *Materials Research* (Vol. 5, Issue 3).

[78] Dandekar, T. R., Kumar, A., Khatirkar, R. K., Singh, J., & Kumar, D. (2021). Effect of isothermal aging at 750 °C on microstructure and mechanical properties of UNS S32101 lean duplex stainless steel. Materials Today Communications, 29. https://doi.org/10.1016/j.mtcomm.2021.102753.

[79] Deng, B., Wang, Z., Jiang, Y., Sun, T., Xu, J., & Li, J. (2009). Effect of thermal cycles on the corrosion and mechanical properties of UNS S31803 duplex stainless steel. Corrosion Science, 51(12), 2969–2975. https://doi.org/10.1016/j.corsci.2009.08.015.

[80] Rovere, C. A. D., Santos, F. S., Silva, R., Souza, C. A. C., & Kuri, S. E. (2013). Influence of long-term low-temperature aging on the microhardness and corrosion properties of duplex stainless steel. Corrosion Science, 68, 84–90. https://doi.org/10.1016/j.corsci.2012.10.038.

[81] Angelini, E., De Benedetti, B., & Rosalbino, F. (2004). Microstructural evolution and localized corrosion resistance of an aged superduplex stainless steel. Corrosion Science, 46(6), 1351–1367. https://doi.org/10.1016/j.corsci.2003.09.024.

Advanced Steel Construction – Vol. 21 No. 2 (2025) 119–124
DOI:10.18057/IJASC.2025.21.2.3

PROPOSAL FOR ENHANCING THE STRUCTURAL DESIGN OF DOUBLE-SKIN TRUSS-REINFORCED COMPOSITE SHEAR WALL

Jian-Hong Han [1, *], Gan-Ping Shu [2] and Ying Qin [2]

[1] *BIM and Intelligent Construction Industry-Education Integration Research Center, School of Civil Engineering, Xinjiang Institute of Engineering, Urumqi, China*
[2] *School of Civil Engineering, Southeast University, Nanjing, China*
** (Corresponding author: E-mail: jianhong312@126.com)*

ABSTRACT

The double-skin truss-reinforced composite shear wall is a type of composite wall with steel plates connected by truss connectors. Established studies have demonstrated the improvement of compressive and shear performance of double steel plate composite shear walls by truss connectors. The structural design of truss connectors is discussed in detail in this article. The upper limit of the connector spacing-to-thickness ratio is investigated based on the elastic stability theory and the superposition principle, and a limit value of 65 k is recommended. Based on the plastic hinge theory, the existing test results and the relevant standards, the design recommendations of truss steel bar diameter and bending angle are provided. Other strengthening construction measures are also given to minimize wall damage.

ARTICLE HISTORY

Received: 5 April 2024
Revised: 26 December 2024
Accepted: 1 January 2025

KEYWORDS

Double-skin composite wall;
Truss-reinforced;
Structural design suggestion;
Spacing-to-thickness ratio;
Connectors design

1. Introduction

The double-skin composite wall is a type of composite structure composed of two steel plates, core concrete and connectors, which is first used in submarine submerged tube tunnels, nuclear containment structures, and oil or gas storage vessel structures (Wright *et al*., 1991). With its high load-bearing capacity, ease of fabrication and transportation, and the absence of the need for additional concrete forms during construction, the application of double steel plate composite walls is gradually expanding to buildings.

The strength of a double-skin composite wall depends not only on the cross-section performance of the steel plate and inner concrete, but also benefits from the combined action between the two, which is usually achieved through the bonding action between the two and the connection construction. Early axial compression test results show that for double-skin composite walls without connectors, the steel plate quickly detaches from the concrete wall at the boundary. Thus, only the compressive capacity of the concrete wall can be reflected. This results in the wall's compressive bearing capacity being significantly lower than the calculated strength of the composite members (Wright *et al*., 1995). On the contrary, the strong boundary constraint generated by the installation of the connectors allows the steel plate to work cooperatively with the concrete even after separation (Hossain *et al*., 2004). This indicates that the combined action cannot solely be achieved through bonding action but requires connectors. Consequently, double-skin composite walls with various connecters are proposed. Such as shear studs (Liang *et al*., 2004; Choi *et al*., 2014), friction welded bars (Pryer *et al*., 1998; Xie *et al*., 2007), tie bolt (Othuman *et al*., 2011; Rafiei *et al*., 2011; Zhu *et al*., 2019), enhanced C-channel connectors (Yan *et al*., 2020; Wang *et al*., 2020), J-hook connector (Liew *et al*., 2009), batten plate (Nie *et al*., 2013), L-shaped and C-shaped connectors (Chen *et al*., 2019), U-steel (Zhang *et al*., 2016), and H-steel (Guo *et al*., 2018).

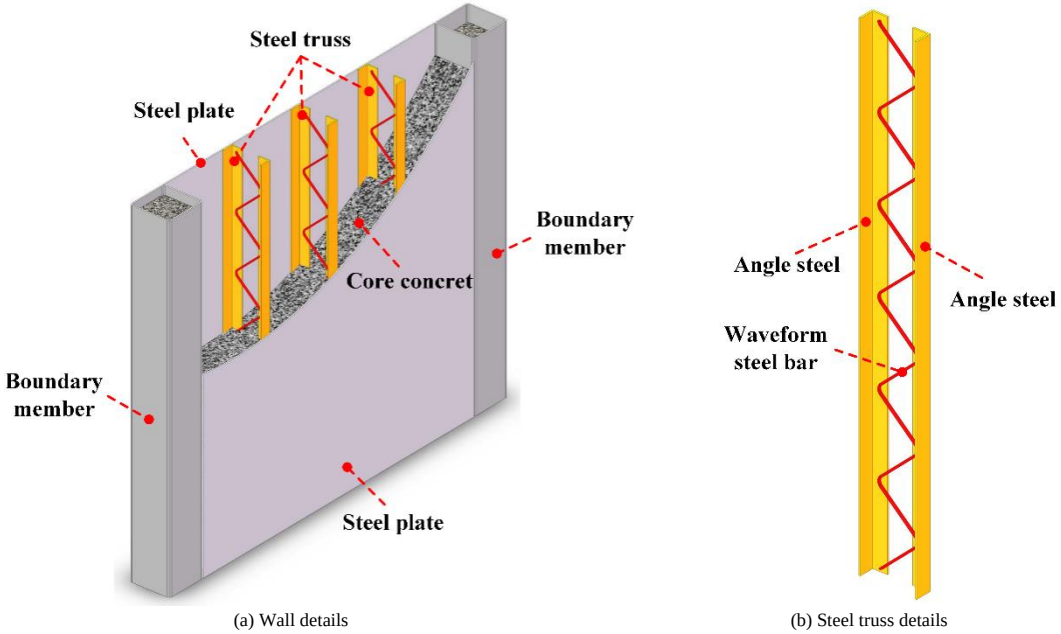

(a) Wall details (b) Steel truss details

Fig. 1 Double-skin truss-reinforced composite shear wall details

To ensure convenient construction and maintain the lateral stiffness of the wall, a double-skin composite shear wall reinforced with truss connector which is composed of angle steel and waveform steel bar was designed, as shown in Fig. 1. The truss connectors are easy to position and weld, and do not obstruct concrete flow during construction, avoiding the reduction in wall shear stiffness caused by the separation of the core concrete walls by the connectors.

Experimental research and theoretical analysis have been conducted on the compression performance (Qin *et al*., 2019; Qin *et al*., 2019; Qin *et al*., 2019) and seismic performance (Han *et al*., 2021; Han *et al*., 2021) of the double-skin truss-reinforced composite shear wall. Compared to the traditional double-skin composite wall, the truss connector also provides a strong constraint effect on both sides of the steel plate. The effects of different truss spacing on the shear bearing capacity, ductility coefficient, and buckling geometric parameters of composite walls were preliminarily studied by experiments, based on which, the design requirements for the spacing-to-thickness ratio and the truss connectors of the double-skin truss-reinforced composite shear wall were discussed in this paper.

2. Design requirements of the spacing-to-thickness ratio

As illustrated in Fig. 2, under the combined action of pressure, shear and bending moment, the buckling deformation of the strips separated by truss connectors, where a and b represent the length (or wall height H) and width (or truss connector spacing s) of the strips, respectively. At the boundaries $y = 0$ and $y = a$, the embedded effect of the core concrete wall not only restrains the relative movement of the truss connectors as steel plate stiffening ribs, but also provides them with strong torsional stiffness, and can thus be regarded as the fixed boundary of the steel plate. The boundaries $x = 0$ and $x = b$ are the loading edges for vertical pressure and horizontal shear, which can be regarded as simply supported boundaries. Therefore, the strips separated by truss connectors can be considered as narrow rectangular plates with two sides simply supported and the other two sides fixed.

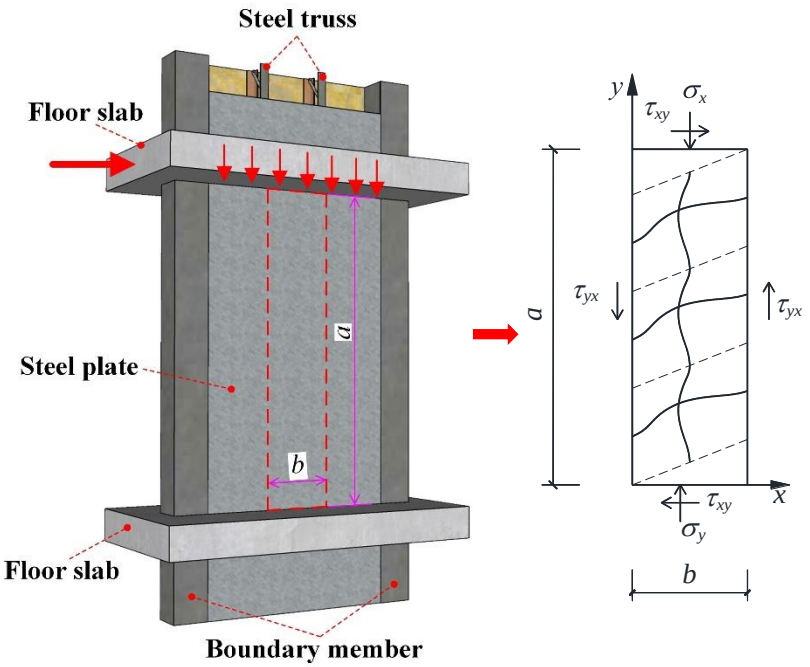

Fig. 2 Sketch of strip buckling deformation calculation

According to the energy method and superposition principle, the critical buckling normal stress σ_{cr} and shear stress τ_{cr} of a narrow rectangular plate should satisfy Eq. (1) under vertical compression and shear (Zhou, 1981):

$$\frac{\sigma_{cr}}{\sigma_{cr0}}+\left(\frac{\tau_{cr}}{\tau_{cr0}}\right)^2=1 \tag{1}$$

where, σ_{cr} and τ_{cr} are the buckling critical normal stress and shear stress under compound stress, respectively, σ_{cr0} and τ_{cr0} are the critical normal stress and shear stress of buckling under the separate action of vertical pressure and shear, which can be calculated by Eq. (2) and Eq. (3), respectively. Equation 1 shows that under the compound stress, the buckling critical normal stress and shear stress are less than the buckling critical stress under pure compression or pure shear, respectively, and the direction of the shear stress does not affect the value of the critical stress.

$$\sigma_{cr0}=k_\sigma\frac{\pi^2 D}{b^2 t_s} \tag{2}$$

$$\tau_{cr0}=k_\tau\frac{\pi^2 D}{b^2 t_s} \tag{3}$$

$$D=\frac{E_s t_s^3}{12\left(1-v^2\right)} \tag{4}$$

where, k_σ and k_τ are the buckling coefficients of vertical compression acting alone or shear acting alone, respectively; t_s are the steel plate thickness; D represents the buckling stiffness of a plate per unit width; E_s are the elastic modulus of the steel with a value of 2.06×10^5 N/mm^2; v is the Poisson's ratiowith a value of 0.3.

Introducing the critical normal stress buckling coefficients K_σ and critical shear stress buckling coefficients K_τ under composite stress, the following equations can be obtained:

$$\sigma_{cr}=K_\sigma\frac{\pi^2 D}{b^2 t_s} \tag{5}$$

$$\tau_{cr}=K_\tau\frac{\pi^2 D}{b^2 t_s} \tag{6}$$

Substituting σ_{cr}, τ_{cr}, σ_{cr0} and τ_{cr0} into Eq. (1), the relationship between buckling coefficients K_σ and K_τ can be derived as follows:

$$\frac{K_\sigma}{k_\sigma}+\left(\frac{K_\tau}{k_\tau}\right)^2=1 \tag{7}$$

Typically, the ratio of wall height to truss connector spacing, i.e. a/b, is taken to be much higher than 3.0 (this is because, for a floor height of 2700 mm, a/b less than 3.0 means that the truss connector spacing will exceed 900mm, which rarely occurs in the practical application of double-skin truss-reinforced composite shear wall). According to the values of the flexure coefficients of the two-sided simply supported two-sided fixed rectangular plate in pure compression provided in the literature (Chen, 2014) and the values of the flexure coefficients of the two-sided simply supported two-sided fixed rectangular plate in pure shear provided in the literature (Timoshenko *et al*., 1985), when a/b>3.0,

k_σ and k_τ are 6.97 and 8.99, respectively. By substituting k_σ and k_τ into Eq. 7, the relationship curve of the buckling coefficients K_σ and K_τ can be plotted as shown in Fig. 3. A portion of the buckling coefficients K_σ and K_τ are presented in Table 1.

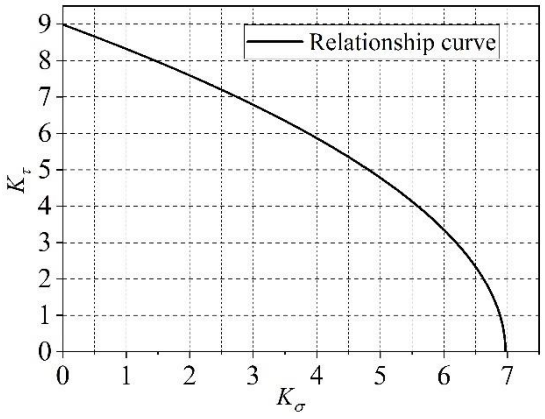

Fig. 3 Relationship curve of buckling coefficients K_σ and K_τ

Table 1
K_σ and K_τ values for the combined effect of unidirectional compression and shear

K_σ	0	1	2	3	4	5	6	6.97
K_τ	8.99	8.32	7.59	6.78	5.87	4.78	3.35	0

Limit values of b/t_s (that is, distance thickness ratio s/t_s) are discussed below. Based on the theory of shape-changing energy density, under the combined action of vertical compression and shear, the condition that the local buckling of slats does not occur before the strength yield is as follows:

$$\sqrt{\sigma_{cr}^2+3\tau_{cr}^2}\geq f_y \tag{8}$$

By Substituting σ_{cr} and τ_{cr} into Eq. (8), the following equation can be derived:

$$K_\sigma^2\left(\frac{\pi^2 D}{b^2 t_s}\right)^2+3K_\tau^2\left(\frac{\pi^2 D}{b^2 t_s}\right)^2\geq f_y^2 \tag{9}$$

According to Eq. (7),

$$K_\tau^2=k_\tau^2\left(1-\frac{K_\sigma}{k_\sigma}\right) \tag{10}$$

By Substituting K_τ^2 into Eq. (9), and defining $\beta=b/t_s$, the following equation can be derived:

$$\beta^4\leq\frac{1}{f_y^2}\left[\frac{\pi^2 E}{12\left(1-\nu^2\right)}\right]^2\left[K_\sigma^2+3k_\tau^2\left(1-\frac{K_\sigma}{k_\sigma}\right)\right] \tag{11}$$

Obviously, when the rightmost term of Eq. (11) attains its minimum value, β can obtain the minimum upper limit value. Thus, let:

$$y=K_\sigma^2+3k_\tau^2\left(1-\frac{K_\sigma}{k_\sigma}\right) \tag{12}$$

According to the extreme value theorem, y can reach a minimum value when the first-order derivative of y is equal to zero, and the second-order derivative is greater than zero, i.e.

$$\begin{cases} y'=2K_\sigma-\dfrac{3k_\tau^2}{k_\sigma}=0 \\ y''=2>0 \end{cases} \tag{13}$$

Substituting $k_\sigma=6.97$, $k_\tau=8.99$ into Eq. (13), we get $K_\sigma=17.39$. Since $K_\sigma>k_\sigma$, it indicates that under vertical pressure alone, that is, when $K_\sigma=k_\sigma$ $K_\tau=0$, β can reach the minimum limit value, thus:

$$\beta\leq\sqrt{\frac{1}{f_y}\left(\frac{\pi^2 E}{12\left(1-\nu^2\right)}\right)K_\sigma}=74.3\sqrt{\frac{235}{f_y}}=74.3\varepsilon_k \tag{14}$$

where, ε_k is the steel grade correction factor, denoted as $\sqrt{235/f_y}$.

From Eq. (14), the theoretical upper limit of spacing-to-thickness ratio (s/t_s) of truss-stiffened double steel plate combination shear wall is $74.3\varepsilon_k$. According to the test results presented in the literature (Han *et al*., 2021), specimens with a spacing-to-thickness ratio of 100 exhibit significantly lower shear bearing capacity and ductility coefficient compared to those with spacing-to-thickness ratios of 50 and 75. This indicates that the spacing-to-thickness ratio should not exceed 75, which aligns with the results from the theoretical upper limit of the spacing-to-thickness ratio calculated in Eq. (14) (where f_y=235, i.e., ε_k=1.0).

According to the "Technical Specification for Steel Plate Shear Wall" (JGJ/T 380, 2015) in China, when T-stiffeners are used for double-skin composite walls, as shown in Fig. 4, the ratio of stiffener spacing to the steel plate thickness should not exceed $60\varepsilon_k$. While for the tie bar, the ratio should not exceed $52.5\varepsilon_k$ according to the ANSI/AISC 341 (2016). It is not difficult to deduce that the truss connectors have a stronger constraint on the steel plate than the T-stiffeners or the tie bar. Therefore, the limit value for the spacing-to-thickness ratio of the double-skin truss-reinforced composite shear wall can be increased appropriately. Considering the theoretical limit and specification requirements, it is suggested that the spacing-to-thickness ratio should not exceed $65\varepsilon_k$ for double-skin truss-reinforced composite shear walls.

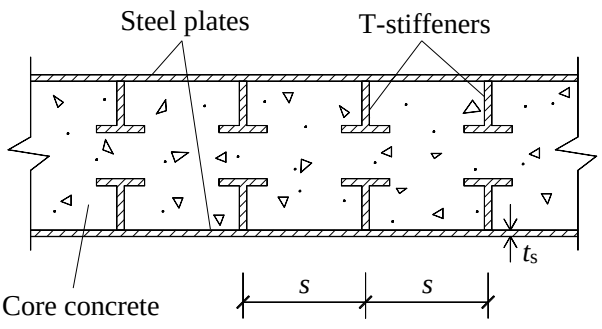

Fig. 4 Double-skin composite wall with T-stiffeners

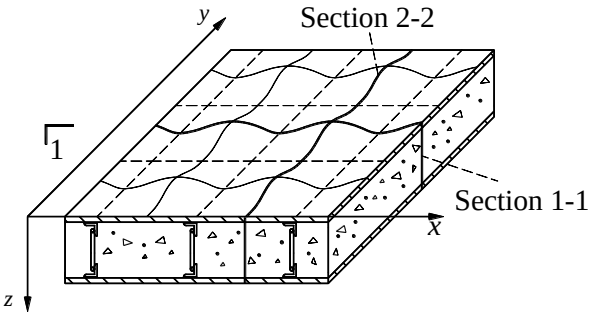

(a) Buckling deformation of steel plate-truss element

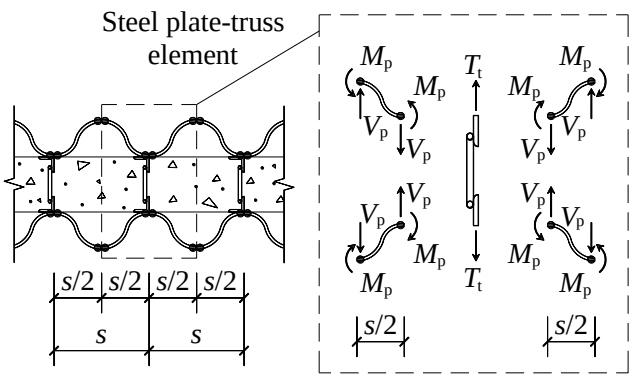

(b) Section 1-1

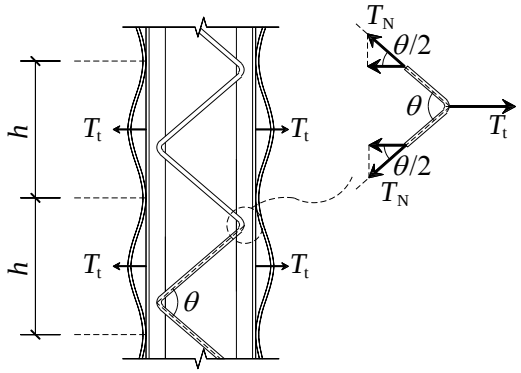

(c) Section 2-2

Fig. 5 Steel plate-truss element

3. Design requirements of the truss connector

3.1. the diameter of the waveform steel bar

Consider the steel plate-truss element shown in Fig. 5. Assume that the plastic hinge is formed at the reverse bending point when the steel plate buckles. The bending moment M_p and shear V_p at the plastic hinge section can be expressed by Eq. (15) and Eq. (16), respectively:

$$M_p = f_y \times \frac{t_s}{2} \times h \times \frac{t_s}{2} = f_y \frac{ht_s^2}{4} \tag{15}$$

$$V_p = \frac{2M_p}{(s/2)} = \frac{4M_p}{s} \tag{16}$$

Based on the force balance condition, the tension T_t of the whole truss connector can be expressed by Eq. (17):

$$T_t = 2V_p = 2f_y \frac{ht_s^2}{s} \tag{17}$$

According to the geometric relation shown in Fig. 5 (c), the tensile force T_N on the waveform steel bar can be expressed as follows:

$$T_N = \frac{T_t}{2\cos(\theta/2)} \tag{18}$$

Thus, the stress of the waveform steel bar satisfies Eq. (19) :

$$\sigma_b = \frac{T_N}{A_b} = \frac{T_t}{2\cos(\theta/2)} \times \frac{4}{\pi d_b^2} = T_t \times \frac{2}{\pi d_b^2 \cos(\theta/2)} \le f_{yb} \tag{19}$$

By Substituting Eq. (17) into Eq. (19), Eq. (20) can be derived as follows:

$$\left(2f_y \frac{ht_s^2}{s}\right) \times \frac{2}{\pi d_b^2 \cos\theta} \le f_{yb} \tag{20}$$

Therefore, the diameter d_b of the waveform steel satisfies Eq. (21).

$$d_b \ge 1.1 t_s \sqrt{\frac{h}{s} \times \frac{f_y}{f_{yb}} \times \frac{1}{\cos(\theta/2)}} \tag{21}$$

where, t_s represents the steel plate thickness, h is the height of steel plate buckling wave, s is the spacing of truss connectors, f_y represents the yield strength of steel plate, f_{yb} represents the yield strength of waveform steel bar, and θ is the bending angle of the waveform steel bar.

3.2. Buckling wave geometry characteristics

According to the literature (Han *et al*., 2021) and (Han *et al*., 2021), the statistical results of shear buckling wave geometric characteristics of each specimen are presented in Fig. 6 and Table 2. The results indicate that the ratio of buckling wave height h to the truss spacing s varies from 0.63 to 1.25, with an average value of 0.90.

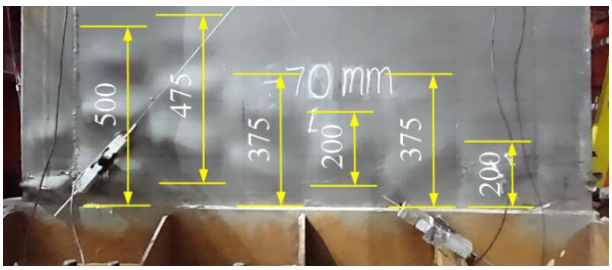

（a）SCW-1

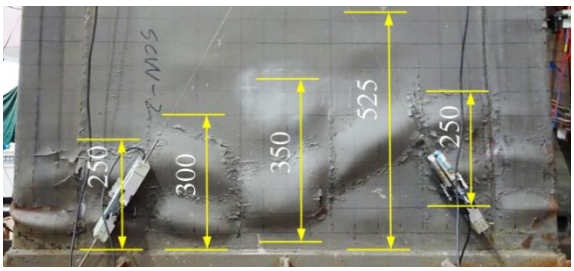

（b）SCW-2

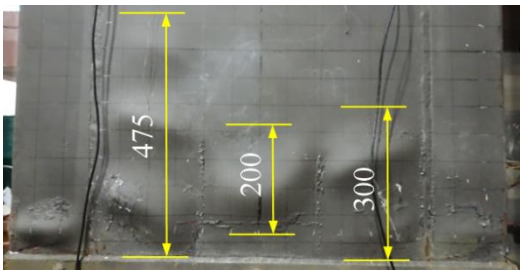

（c）SCW-3

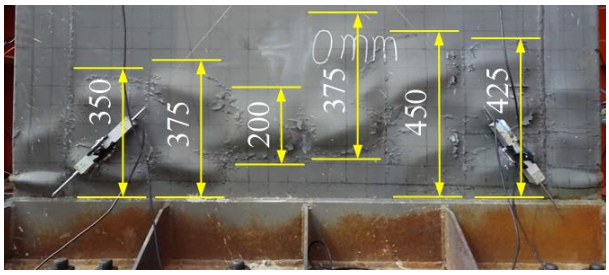

（d）SCW-4

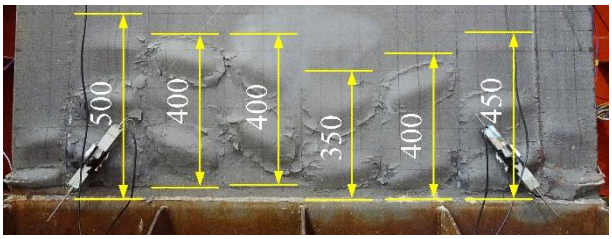

（e）SCW-5

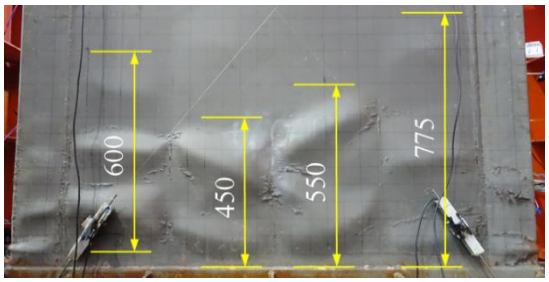

（f）SCW-6

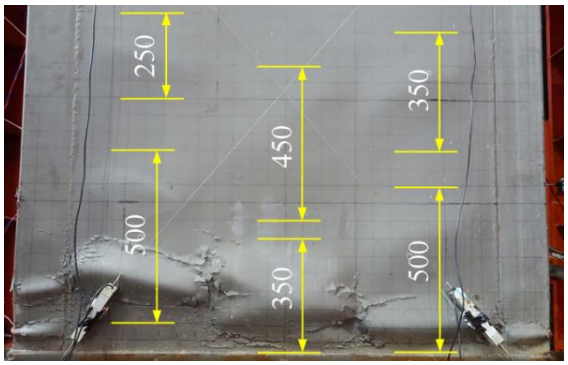

（g）SCW-7

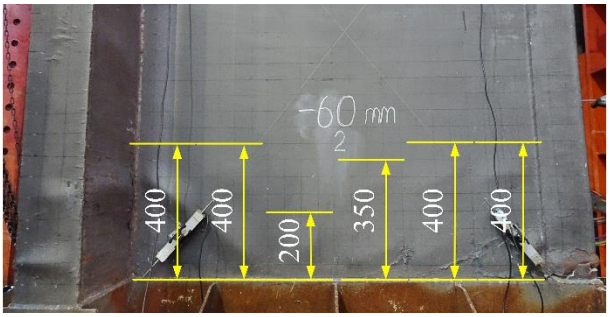

（h）SCWT-1

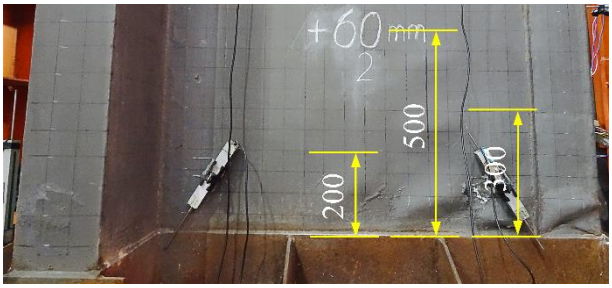

（i）SCWT-2

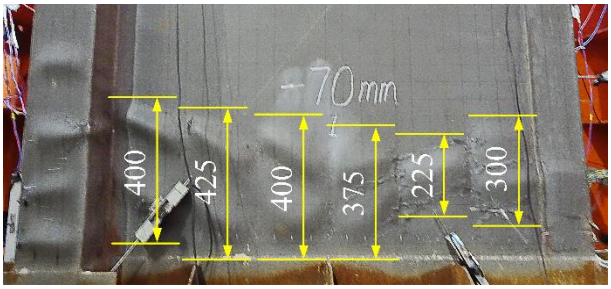

（j）SCWT-3

Fig. 6 Buckling wave height of each specimen（mm）

Table 2
Buckling wave geometry characteristics of each specimen（mm）

Specimen	Buckling wave height *h*			Spacing of truss connectors *s*	*h*/*s*		
	Maximum value	Minimum value	Average value		Maximum value	Minimum value	Average value
SCW-1	200.0	158.3	183.3	200.0	1.00	0.79	0.92
SCW-2	175.0	150.0	166.7	200.0	0.88	0.75	0.83
	125.0	125.0	125.0	150.0	0.83	0.83	0.83
SCW-3	200.0	150.0	169.4	200.0	1.00	0.75	0.85
SCW-4	225.0	141.7	186.1	200.0	1.13	0.71	0.93
SCW-5	200.0	150.0	181.9	200.0	1.00	0.88	0.91
SCW-6	275.0	200.0	239.6	300.0	0.92	0.67	0.80
SCW-7	400.0	250.0	311.1	400.0	1.00	0.63	0.78
SCWT-1	200.0	175.0	195.8	200.0	1.00	0.88	0.98
SCWT-2	250.0	166.7	205.6	200.0	1.25	0.83	1.03
	150.0	150.0	150.0	150.0	1.00	1.00	1.00
SCWT-3	225.0	150.0	195.8	200.0	1.13	0.75	0.98
Average value							0.90

3.3. Design requirements of the truss connector

To facilitate calculation, the values of parameters in Eq. (21) are specified as follows:

(1) According to the statistical results of shear buckling wave size of specimen steel plate, the average ratio of the height of buckling wave h to the spacing s of truss connectors is 0.9, i.e. h/s=0.9. Thus, Eq. (21) can be simplified to Eq. (22):

$$d_b \geq 1.0 t_s \sqrt{\frac{f_y}{f_{yb}} \times \frac{1}{\cos(\theta/2)}} \tag{22}$$

(2) According to the design specifications of steel truss size outlined in the Chinese standard "Steel-bars truss deck" (JG/T 368-2012) and "Technical specification for concrete composite slabs with lattice girders" (T/CECS 715-2020), the height of steel truss internode should be 200mm, and the width of the internode should not be less than 70mm. This requirement ensures that the bending angle of the steel bar θ does not exceed 110 degrees. In addition, to minimize steel usage, the bending angle of the waveform steel bar should be at least 90 degrees.

According to the provisions outlined above, the minimum steel bar diameter that meets the structural requirements can be calculated using Eq. (22) once the steel plate thickness, its strength grade, the waveform steel bar's strength grade, and bending angle are determined.

4. Other structural suggestions

(1) To guarantee the efficient performance of truss connectors in connecting and stabilizing the steel plate, it is recommended to use continuous fillet welds when truss connectors are connected to the steel plate.

(2) The experimental failure phenomenon demonstrates that the bottom of the boundary member, serving as the edge member in the double-skin truss-reinforced composite shear wall, is prone to buckling and tearing seriously under the influence of horizontal forces. Thus, to mitigate this issue, it is advisable to reinforce the bottom of the boundary member.

(3) In order to ensure the welding quality between steel plate and boundary member, it is suggested to appropriately increase the section width of boundary member compared to its wall thickness. The width of the rectangular steel tube should be designed to extend beyond the wall by at least 10mm on each side.

5. Conclusions

The connectors are important components that provide combined action for double steel plate combination shear walls. The truss connectors are convenient to position and weld without diminishing the shear stiffness of the wall, thereby providing adequate restraint and connection action to achieve a desirable compressive and seismic performance of the double steel plate combination shear wall. The research conducted in this paper has led to the following conclusions:

(1) Based on the theory of elastic stability and superposition principle, this study discusses the design requirements for the spacing-to-thickness ratio of double-skin truss-reinforced composite shear walls. Considering the theoretical limitations and current regulations, it is recommended that the spacing-to-thickness ratio of the double-skin truss-reinforced composite shear wall should not exceed $65\varepsilon_k$.

(2) Based on the plastic hinge theory, the diameter of the waveform steel bar in the truss connector assembly can be calculated in Eq. (21). The test results on the shear buckling wave geometric characteristics of the wall, in combination with relevant standards, have determined that a value of h/s=0.9 is taken in Eq. (21). The bending angle of waveform steel bar must have a minimum bending angle of 90 degrees.

(3) To ensure the proper connection and restraint provided by the truss connectors, continuous fillet welding should be employed between the truss connectors and the steel plates.

(4) To minimize the damage to the boundary member, it is recommended to increase the boundary member thickness or set the cladding plate to provide local reinforcement steel tube. And the boundary member should extend at least 10mm from either side of the wall.

Acknowledgments

This work is sponsored by Xinjiang Tianchi Talent Project (Grant No. 2023XGYTCYC05), the Xinjiang Uygur Autonomous Region universities basic scientific research business funds research projects (Grant No.XJEDU2022P124), and the National Natural Science Foundation of China (Grant No.52178117). The authors would like to thank the steel research group of Southeast University for their assistance with the laboratory work.

References

[1] ANSI/AISC 341-16 (2016) Specification Provisions for Structural Steel Buildings, Chicago: American Institute of Steel Construction.
[2] Chen Ji. (2014) Stability of Steel Structures Theory and Design. China Science Publishing & Media Ltd., Beijing.
[3] Chen L. H., Wang S. Y., Lou Y. (2019) Seismic behavior of double-skin composite wall with L-shaped and C-shaped connectors. *Journal of Constructional Steel Research* 160: 255-270, DOI: 10.1016/j.jcsr.2019.05.033
[4] Choi B. J., Kang C. K., Park H. Y. (2014) Strength and behavior of steel plate–concrete wall structures using ordinary and eco-oriented cement concrete under axial compression. *Thin-Walled Structures* 84: 313-324, DOI: 10.1016/j.tws.2014.07.008
[5] Guo L. H., Wang Y. H., Zhang S. (2018) Experimental study of rectangular multi-partition steel-concrete composite shear walls. *Thin-Walled Structures* 130: 577-592, DOI: 10.1016/j.tws.2018.06.011
[6] Han J. H., Shu G. P., Qin Y. (2021) Experimental seismic behavior of double skin composite wall with steel truss. *Journal of Constructional Steel Research* 180: 106569, DOI: 10.1016/j.jcsr.2021.106569
[7] Han J. H., Shu G. P., Qin Y. (2021). Experimental seismic behavior of T-shaped double skin composite wall with steel truss. *Journal of Constructional Steel Research* 184: 106776, DOI: 10.1016/j.jcsr.2021.106776
[8] Hossain K. M. A., Wright H. D. (2004) Experimental and theoretical behaviour of composite walling under in-plane shear. *Journal of Constructional Steel Research* 60(1): 59-83, DOI: 10.1016/j.jcsr.2003.08.004
[9] JGJ/T 380–2015 (2015) Technical specification for steel plate shear walls, China Architecture & building press, Beijing.
[10] JG/T 368-2012 (2012), Steel-bars truss deck, Standards Press of China, Beijing.
[11] Liang Q. Q., Uy B., Wright H. D. (2004) Local buckling of steel plates in double skin composite panels under biaxial compression and shear. *Journal of Structural Engineering* 130(3): 443-451, DOI: 10.1061/(ASCE)0733-9445(2004)130:3(443)
[12] Liew J. Y. R., Sohel K. M. A. (2009) Lightweight steel–concrete–steel sandwich system with J-hook connectors. *Engineering Structures* 31(5): 1166-1178, DOI: 10.1016/j.engstruct.2009.01.013
[13] Nie J. G., Hu H. S., Fan J. S. (2013) Experimental study on seismic behavior of high-strength concrete filled double-steel-plate composite walls. *Journal of Constructional Steel Research* 88: 206-219, DOI:10.1016/j.jcsr.2013.05.001
[14] Othuman M. M. A., Wang Y. C. (2011) Structural performance of lightweight steel-foamed concrete–steel composite walling system under compression. *Thin-Walled Structures* 49(1): 66-76, DOI: 10.1016/j.tws.2010.08.007.
[15] Pryer J. W., Bowerman H. G. (1998) The development and use of british steel Bi-steel. *Journal of Constructional Steel Research* 46(1): 173-178.
[16] Qin Y., Shu G. P., Zhou G. G. (2019) Compressive behavior of double skin composite wall with different plate thicknesses. *Journal of Constructional Steel Research* 157: 297-313, DOI: 10.1016/j.jcsr.2019.02.023
[17] Qin Y., Shu G. P., Zhou G. G. (2019) Truss spacing on innovative composite walls under compression. *Journal of Constructional Steel Research* 160: 1-15, DOI: 10.1016/j.jcsr.2019.05.027
[18] Qin Y., Shu G. P., Zhou X. L. (2019) Height-thickness ratio on axial behavior of composite wall with truss connector. *Steel and Composite Structures* Feb 25;30(4):315–325, DOI: 10.12989/scs.2019.30.4.315
[19] Rafiei S. (2011) Behaviour of double skin profiled composite shear wall system under in-plane monotonic, cyclic and impact loadings. Ph. D. thesis, Ryerson University, Toronto, Canada.
[20] Stephen P. Timoshenko, James M. Gere. (1985) Theory of Elastic Stability. Koon Wan Printing Pte. Ltd.
[21] T/CECS 715-2020 (2020), Technical specification for concrete composite slabs with lattice girders, China Architecture & building press, Beijing.
[22] Wright H. D., Gallocher S. C. (1995) The behaviour of composite walling under construction and service loading. *Journal of Constructional Steel Research* 35(3): 257-273.
[23] Wright H. D., Oduyemi T. O. S., Evans H. R. (1991) The design of double skin composite elements. *Journal of Constructional Steel Research* 19(2): 111-132.
[24] Wang T., Yan J. B. (2020) Developments of steel-concrete-steel sandwich composite structures with novel EC connectors: Members. *Journal of Constructional Steel Research* 175: 106335, DOI: 10.1016/j.jcsr.2020.106335
[25] Xie M., Foundoukos N., Chapman J. C. (2007) Static tests on steel–concrete–steel sandwich beams. *Journal of Constructional Steel Research* 63(6): 735-750, DOI: 10.1016/j.jcsr.2006.08.001
[26] Yan J. B., Chen., Wang T. (2020) Compressive behaviours of steel-UHPC-steel sandwich composite walls using novel EC connectors. *Journal of Constructional Steel Research* 173: 106244. DOI: 10.1016/j.jcsr.2020.106244
[27] Zhang X. M., Qin Y., Chen Z. H. (2016) Experimental seismic behavior of innovative composite shear walls. *Journal of Constructional Steel Research* 116: 218-232, DOI: 10.1016/j.jcsr.2015.09.015
[28] Zhou Ch. T. (1981) Elastic stability theory. Sichuan People's Publishing House, Sichuan.
[29] Zhu J. S., Guo Y. L., Wang M. Z. (2019) Strength design of concrete-infilled double steel corrugated-plate walls under uniform compressions. *Thin-Walled Structures* 141: 153-174, DOI: 10.1016/j.tws.2019.02.021

Advanced Steel Construction – Vol. 21 No. 2 (2025) 125–135
DOI:10.18057/IJASC.2025.21.2.4

RETROFIT EFFECT AND FLEXURAL CAPACITY OF H-SECTION BEAM-THROUGH BEAM-COLUMN CONNECTIONS FOR STEEL MODULAR FRAMES

Hong-Kai Du [1], Fu-Xiong Yang [1], Yuan-Dong Wang [2,*], Peng-Fei Zhao [3] and Jin-Yu Wang [1]

[1] *Beijing Advanced Innovation Center for Future Urban Design, Beijing University of Civil Engineering and Architecture, Beijing, China*
[2] *Exyte, Salt Lake City, Utah, USA*
[3] *China Poly Real Estate Corporation Ltd., Beijing, China*
** (Corresponding author: E-mail: matt.wang@utah.edu)*

ABSTRACT

Beam-through steel beam-column configurations are distinct from traditional column-through steel structures because they discontinue columns at each floor by bolting upper and lower columns to floor beam flanges. It facilitates modular manufacturing and floor/modular erection, which provides more opportunities for low to mid-level steel structures. Compared to its constructability superiority, beam-through configurations typically create a weaker beam-column joint than traditional beam-column connections adopted in the current building codes. In a numerical approach, this study investigates the seismic performance and flexural behavior of beam-through moment-resisting connections with H-section (wide-flange) beams and columns to improve their flexural capacity. Three beam-through moment connections are first simulated numerically and validated by quasi-static experimental tests. Then, five groups of beam-through beam-column connections are designed, calculated, and analyzed. The input parameters include stiffener thickness, doubler plate thickness, doubler plate strength, reduced beam section (RBS) depth, and multiple parameter combinations, while the main output includes yield and ultimate strength, failure mechanisms, hysteretic behavior, backbone curves, energy dissipation capacity, stiffness, ductility, and rotation, which investigates the impact of input parameters on joint flexural capacity. It discovers that increasing the stiffener plates' thickness can better enhance a beam-through joint's bending capacity. Thus, RBS reduces the load-bearing capacity of a through-beam connection and decreases the beam's capacity. However, RBS can successfully transfer the plastic hinge from the joint panel zone to the beam ends with combined with stiffener plates. Finally, an analytical method that can be used to calculate the flexural capacity of beam-through joints is also proposed.

ARTICLE HISTORY

Received: 28 May 2024
Revised: 27 December 2024
Accepted: 1 January 2025

KEYWORDS

Beam-through joint;
Steel modular moment frame;
Web doubler plates;
Reduced beam section;
Finite element analysis;
Analytical method

1. Introduction

Modular steel structures are a highly prefabricated construction system. Their advantages include standardized production, reduced erection time, short construction cycles, flexible spatial layouts, and other significant economic benefits. Prefabricated steel modular buildings have attracted more research focus and have been used in actual engineering applications in recent years [1,2]. Additionally, the prefabrication benefits make them an important structural system gradually adopted by developed countries or regions such as Europe, the United States, and Japan [3,4] due to their higher field labor cost. Beam-column joints in steel structures determine the overall structural performance, and ensure the connection reliability between modules. These joints can be categorized into column-through, diaphragm-through, and beam-through. Among them, column-through joints are the most common and widely applied, with their mechanical properties and seismic performance thoroughly investigated in the past few decades [5-7]. Meanwhile, research and engineering applications on diaphragm-through joints also increase [8-10]. However, research on beam-through joints and the optimization of the panel zone remains insufficient compared to the former two methods.

Beam-through beam-column connections are common in volumetric modular steel structures that can be utilized in low-rise to mid-rise residential and commercial buildings due to their efficiency in shop prefabrication, shop welding, and field bolted connections floor by floor [11-13]. The beam-through configuration also provides more flexibility on column locations and building plan layouts. As building industrialization progresses in eastern Asia, beam-through frame structures (BTFS) become more prevalent in China [14] and Japan [15].

Several beam-through joints have been proposed and studied previously. Chen et al. [16-18] proposed and studied tension-only concentrically braced steel beam-through frames (TCBBFs) with shake table experiments. The test results show that TCBBFs can achieve uniform story drift response with self-centering ability upon loading, which can be easily replaced after major earthquakes. Wang et al. [12] further analyzed the TCBBFs as mentioned above experimentally and numerically and found that the TCBBFs structure was stable at an inter-story drift of 1/10. Then, Yao et al. [13] improved the TCBBFs with eccentrical layout and showed that eccentrically braced beam-through steel frames with replaceable shear links also improved the frames' energy dissipation capacity, stiffness, ultimate capacity, and ductility.

Similarly, Hu et al. [19,20] examined the seismic performance of a beam-through tension-only concentrically braced frame with energy-absorbing rocking core (ERC), which indicated that ERC could control the maximum residual drift within 0.5%. Furthermore, Zhang et al. [21] introduced a combined system of friction spring-based self-centering (SC) devices and self-centering rocking cores (SRC) to improve the resilience of beam-through frames. The proposed system reached target seismic performance under near-field and far-field ground motions by effectively controlling seismic displacement and deformation.

Li et al. [22,23] introduced a beam-through steel frame with T-type curved knee braces (TCKBs) to provide stable strength and full energy dissipating capacity. In addition, Li et al. [24] proposed a beam-through configuration for the connections between steel frames and energy-dissipative rocking columns (EDRCs) to minimize the necessary workload when using EDRCs. The numerical analyses proved that beam-through EDRCs provide satisfying lateral resistance and energy dissipation capacities. Similarly, Jeddi et al. [25] proposed a novel moment-resisting connection named a through rib stiffener beam connection, which is directly passed through a pre-slotted circular column with concrete fill. Thus, Jamali et al. [26] provided a revised H-section beam and boxed column joint with two through stiffener plates, indicating the effects of the through stiffener plates on improving seismic performance.

Since beam-through joints at H-section beams and columns tend to have insufficient capacity in the joint core area, it is common to reinforce the joint area to improve seismic performance. For instance, Chen et al. [27] compared the seismic behaviors of beam-through H-section beam-column joints and traditional column-through joints. It showed that small bolt group slippage can provide better hysteretic behavior, and the beam flange and web thickness significantly affect the joint's ultimate capacity. Tagawa and Gurel [28] utilized stiffener plates to reduce the tensile deformation at column flanges, and added web doubler plates to prevent shear failure of beam-through core joint. Likewise, Zhong et al. [29] found that the changes in stiffener thickness in the panel zone have significant effects on the joint's ultimate rotation capacity and ductility. Čermelj et al. [30] analyzed the low-cycle fatigue behaviors of rib-stiffened (RS) and cover plate (CP) connections, which proved the superiority of CP over RS connections. Ma et al. [31] demonstrated the efficiency of double stiffener plates at H-shaped beam-through beam and column connections in improving joint strength and ductility.

Besides adding double plates in the beam-column joint, it is also common and seismically efficient to introduce reduced beam section (RBS), significantly improving joint deformation and ductility [32]. Chen et al. [33] proposed beam-to-column moment connections with reduced beam sections. The experimental tests proved that with RBS, the ultimate joint capacity remained the same, joint stiffness slightly degraded, and plastic rotation capacity increased dramatically. Furthermore, Sophianopoulos and Deri [34] investigated the influence of RBS

configuration, dimensions, locations, and lateral bracing on beam-column joint seismic performance. Carter and Iwankiw [35] demonstrated that trapezoidal RBS at concave corners might trigger stress concentration, while curve RBS can generate satisfactory plastic performance and provide more ductility. Thus, Jones et al. [36] verified the seismic performance of the RBS beam-column joint by performing experimental tests. Seven groups of specimens reached a rotational angle of 0.04 rad before stiffness degradation occurred.

In addition, Lee et al. [37] found that plastic hinges are prone to be developed in the RBS with regular beam-column joint web stiffnesses when the joint rotation reached 0.01 rad, while Wang et al. [38] found that the ultimate joint rotation with RBS welded beam-column joint could reach a rotational angle of 0.077 rad. In follow-up studies, Chen et al. [39] provided optimal design parameters for RBS connections, and Roudsari et al. [40] showed the contribution of web stiffeners to the seismic performance of beam-column joints with RBS. However, in numerical approaches, no previous study has considered combining beam-through beam-column moment connections with RBS, stiffeners, and doubler plates.

This study proposes cruciform beam-column moment connections with steel H-sections (wide-flanges), as shown in Fig. 1. On contratry to traditional beam-column connections, moment frame beams remain continuous while columns are connected to the top and bottom flanges of through-beams. It starts with validating the numerical model of beam-through beam-column moment connections with previous experimental test data under a quasi-static loading protocol. The second phase is to numerically optimize the design input parameters for beam-through beam-column connections, including stiffener plate thickness, doubler plate thickness, doubler plate strength, RBS, and multiple parameter combinations. One key objective is to understand and optimize the design methods on the flexural capacity of beam-through joints. Finally, a novel analytical method and equations are proposed to calculate beam-through beam-column connections' flexural behavior and capacity.

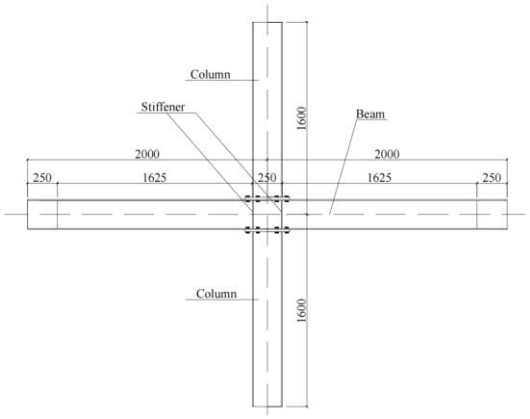

(a) Configuration

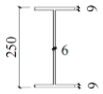

(b) Beam and column section

Fig. 1 Specimen dimensional sections (unit: mm)

2. FEM modeling and experimental validation

The finite element model (FEM) analyses are in ABAQUS to numerically evaluate the seismic performance of beam-through beam-column connections. The FEM tests are first validated by previous cyclic experimental tests under quasi-static loading protocols [32].

2.1. Specimen and test design

Three steel cross beam-through joint assemblages are designed with identical sizes and dimensions. The beam length is 4000 mm (13.12 ft), and the column height is 3200 mm (10.5 ft). The same W-section (wide flange) following the China specifications GB/T 11263-2017 [41] HN250×125×6×9 (Fig. 1) that is equivalent to AISC W10x22 [42] is utilized in the beams and columns for all specimens. Each joint has bolted stiffened end plate at the column flange. Three specimens are named SFT-6, DPT-6, and RBS-30, as shown in Table 1. Fig. 2 presents the critical design parameters for SFT-6, whose panel zone area has two welded 6 mm (1/4 in) thick stiffeners on each side (four in total). DPT-6 incorporates a panel zone doubler plate (6 mm [1/4 in]) welded at the nine 16 mm (0.63 in) welding holes and perimeters, as in Fig. 3. Thus, RBS configuration is included in the same design as SFT-6, namely RBS-30. The RBS is located 80 mm (3.15 in.) to the column flange, and the reduced section cut curve length, depth, and radius is 180 mm (7.067 in), 30 mm (1.181 in), and 150 mm (5.906 in), respectively (Fig. 4).

All steel material is Chinese Q235, which has a yield strength of 235 MPa (34 ksi) [44]. Table 2 summarizes the average properties for the steel samples that were cut from the beams, columns, continuity plate stiffeners, and end plates, which are higher than the code-required yield strength. All experimental tests for this study were performed at the structural lab, Beijing University of Civil Engineering and Architecture. All tested columns were fixed to the structural test frame at both ends by through-bolted connections. The axial force was applied at the column end to maintain a compressive axial ratio of 0.3 by three electro-hydraulic actuators, and quasi-static loading was applied simultaneously at the beam ends in opposite directions. The test setup is shown in Fig. 5, and the experimental loading protocol is shown in Fig. 6.

2.2. Finite element model

The finite element (FE) model overview is shown in Fig. 7, which has the same dimensions as those experimental specimens specified in section 2.1. Eight-node linear hexahedral elements with reduced integration and hourglass control (C3D8R) in ABAQUS are used to mesh all the members. Finer meshes are applied to the beam-through web, beam flanges, and stiffener plates. The mesh size along the beam and column length direction is 60 mm ×49 mm (2.36 in ×1.93 in), the mesh size in the panel zone area is 7 mm ×16 mm (0.28 in ×0.63 in), and the thickness mesh is 2 mm (0.079 in). Since no significant damage is observed at the connection bolts, bolts and nuts are modeled by ignoring the threads' impact. The FE assembly of all components is shown in Fig. 8. Surface-to-surface contact method of ABAQUS is adopted at the column end plates, bolts, and beams. Beam stiffener plates, beam, column, column end plates, and doubler plates are welded together and simulated by the tie method in ABAQUS.

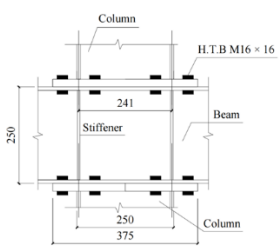

(a) Front elevation view

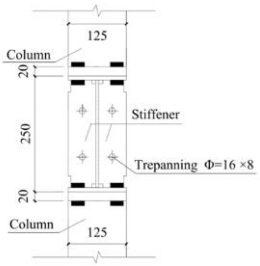

(b) Right section view

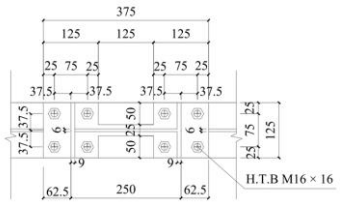

(c) Plan view

Fig. 2 SFT-6 panel zone details (unit: mm)

Table 1
Experimental specimen characteristics

No.	Name	Characteristics
1	SFT-6	Standard H-section beam-through joint with 6 mm (0.236 in) stiffener plates
2	DPT-6	SFT-6 with a 6 mm (0.236 in) web doubler plates in the panel zone
3	RBS-30	SFT-6 with 30 mm (1.18 in) deep RBS at beam ends

Note: These are the three experimental specimens, which are also used in numerical modeling. See Table 4 for the naming definition.

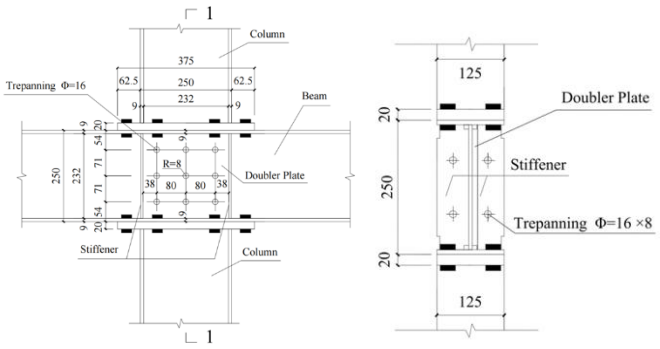

(a) Configuration (b) Beam and column section

Fig. 3 Specimen dimensional sections (unit: mm)

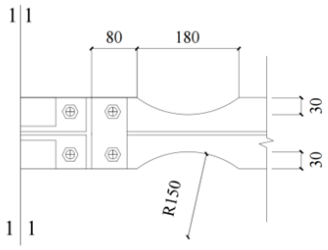

Fig. 4 RBS-30 beam flange dimensional detail (unit: mm)

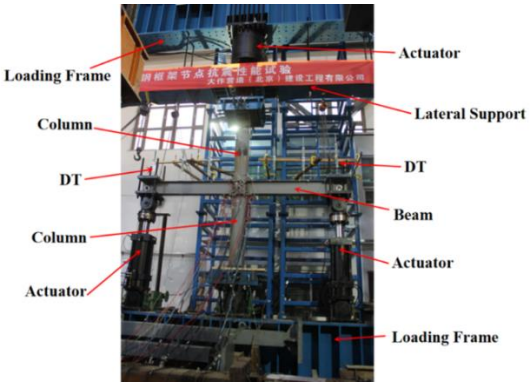

(a) Test picture

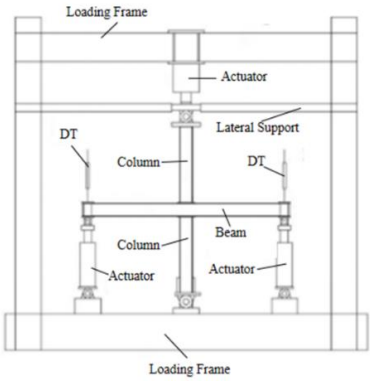

(b) Test sketch

Fig. 5 Experimental setup

Other FEM setup includes a bilinear kinematic hardening material model to model steel elastoplastic deformations from component experimental tests. The bolt pretension force is modeled by the bolt loading modulus, i.e., 107 kN (24 kips) for M16 bolts utilized in this study. Coupling points are set at both the column and beam ends that define the member section properties. The column's bottom-end boundary condition is defined as pin while the column's top end is described as a roller that allows all the rotation and vertical movement. Same boundary conditions are established at the beam ends as the column's miming the experimental testing setup. Finally, the ABAQUS/Standard solver is applied in analyzing the numerical models.

The bolt pre-loading process is divided into three stages under different load magnitudes to improve the FE analysis convergence. Firstly, only 10 N (2.25 LBS) is applied to the bolts to trigger acceptable contact between the bolts and other elements. Then, full loading is imposed, and the bolt loading is modified from force-based to a fixed length, which simulates the pretension effects. Column axial forces and beam cyclic loads are also applied simultaneously during the numerical analysis till the end of the numerical loading process.

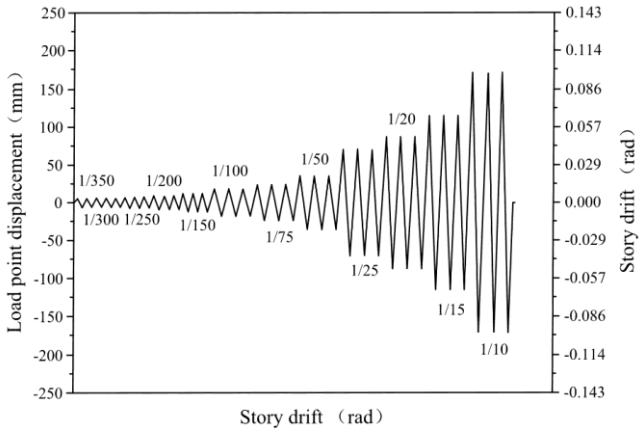

Fig. 6 Beam ends loading protocol

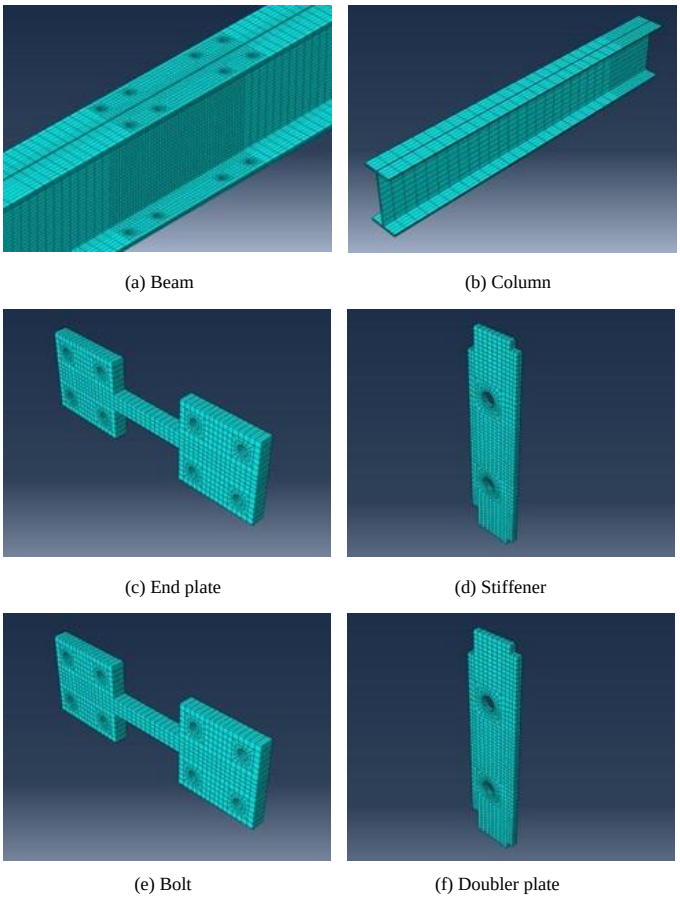

(a) Beam (b) Column

(c) End plate (d) Stiffener

(e) Bolt (f) Doubler plate

Fig. 7 FEM component meshing in beam, column, stiffeners, and doubler plates

2.3. Model validation

The comparison of numerical and experimental failure modes is shown in Fig. 9. Main damage features observed in the experimental tests can be well simulated by the FE model for all three specimens (STF-6, DPT-6, and RBS-30). Take specimen STF-6 as an example. The beam-column panel zone is yielded by exceeding a strength of 368 MPa (53.4 ksi) when reaching a joint

rotation of 0.013 rad (1/75) in the FE analysis, which matches the same progress in the experimental test. As in the experimental test, the 45° buckling deformation in the panel zone further develops, stiffener plates start to bend, and plasticity occurs at the column flange and end plates when rotation angle increases to 0.1 rad (1/10) (Figs. 9a and 9b).

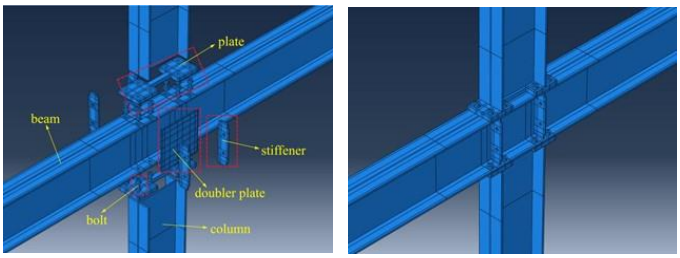

(a) Element decomposition (b) Assembly

Fig. 8 FEM component meshing

In specimen DPT-6, diagonal bulges appear in the panel zone with the rotation angle raised to 0.067 rad (1/15), which also meets the experimental behavior. Compelling yielding deformation can be seen at the beam flanges and column end plates under the same loading magnitude. Once the stiffener plates yields, column flanges also start yielding near the end plate, as in Figs. 9c and 9d. Similarly, the RBS-30 numerical simulation also predicts the experimental specimen test well (Figs 9e and 9f).

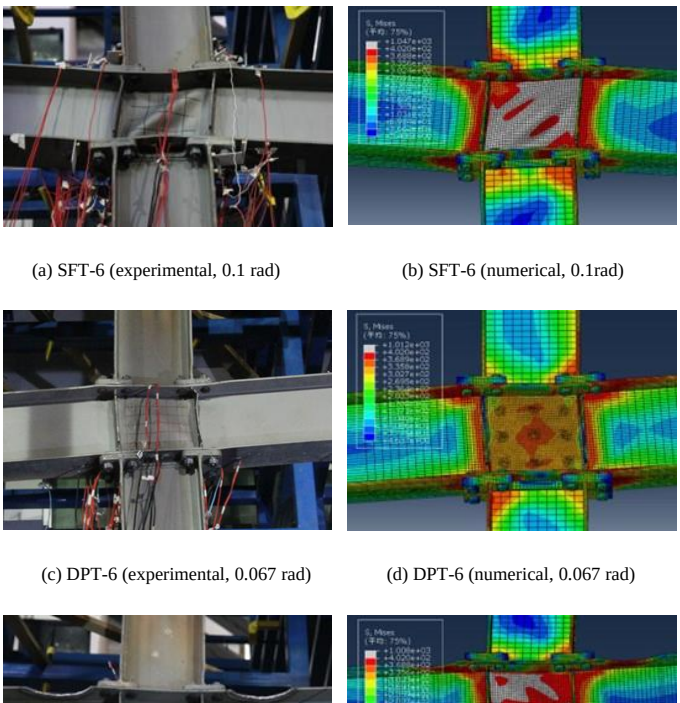

(a) SFT-6 (experimental, 0.1 rad) (b) SFT-6 (numerical, 0.1rad)

(c) DPT-6 (experimental, 0.067 rad) (d) DPT-6 (numerical, 0.067 rad)

(e) RBS-30 (experimental, 0.067 rad) (f) RBS-30 (numerical, 0.067 rad)

Fig. 9 Comparison of numerical and experimental results

The comparison of load-displacement curves is presented in Fig. 10. Both experimental and numerical results show the exact buckling directions and magnitudes in the panel zone area once the beam-through web yields. Similarly, the experimental and numerical moment-rotation angle curves demonstrate close mechanical behavior and performance.

Backbone curve analyses and curve-fitting are applied to both experimental and numerical results to get the elastic stiffness, yield point, yield strength, yield displacement, and ultimate strength, as summarized in Table 3. As observed, the difference between the two is less than 15%, with an average error or difference of 10%. These errors may originate from the boundary conditions of the test model setup. During the experimental tests, it is challenging to constrain the out-of-plane deformation. Therefore, this out-of-plane deformation reduces the test load while amplifying the test displacement, resulting in a test load lower than the simulated load and a test displacement greater than the displacement from numerical analyses. Even though there may be some imperfections or errors in the numerical simulation, it still maintains a high degree of accuracy, which indicates the accuracy and satisfaction of the numerical model for subsequent analyses. As shown in Table 3, the ultimate inter-story drifts of all three specimens exceed 0.04 rad, which is higher than the drift ratios required by the current building codes (e.g., AISC 341 [43]). As noted, all three beam-column joints fail in the joint panel zone, which is not preferable per the current codes.

Table 2
Material property parameters of experimental specimens

Part	Density ρ (kg /m^3)	Elastic Modulus E (MPa)	Yield Strength f_y (N /mm^2)	Ultim. Strength f_u (N/mm^2)	Elongation ε_u
M16 bolt	7850	207510	906	1100	0.089
Beam	7850	207460	369	618	0.249
Column	7850	203880	338	606	0.263
Doubler plate	7850	214220	271	471	0.238
Stiffener	7850	204473	299	528	0.235

Table 3
Numerical and experimental results comparison

Name	Yield displacement (mm)			Yield strength (kN)			Elastic stiffness (kN/m)		
	Exper.	Numer.	Diff.	Exper.	Numeri.	Diff.	Exper.	Numer.	Diff.
SFT-6	23.77	20.8	-12.5%	27.1	27.27	0.5%	1616.4	1698.5	5.1%
DPT-6	29.39	27.0	-8.2%	37.4	42.65	14.5%	1715.5	1898.1	10.6%
RBS-30	23.86	21.7	-9.2%	26.9	27.36	2.5%	1629.4	1626.9	0.2%

Note: $diff. = \frac{Numer. - Exper.}{Exper.}$

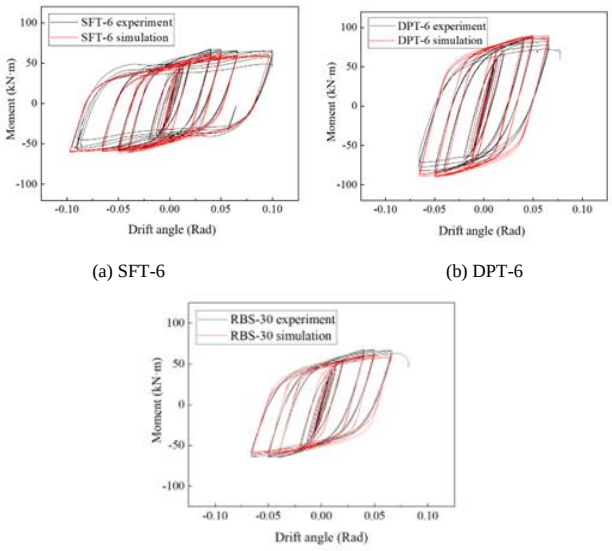

(a) SFT-6 (b) DPT-6

(c) RBS-30

Fig. 10 Comparison of experimental and numerical hysteresis curves

3. Numerical parametric study

In this section, five design or strengthening methods are numerically considered to address the inadequacy of flexural capacity at the panel zone of beam-through beam-column connections. It might even cause global collapse [44,45], starting with local buckling in unbraced flexural members. Therefore, stiffener plates (SFT), doubler plate thickness (DPT), doubler plate strength (DPS), and reduced beam section (RBS) are the main input parameters to improve the flexural capacity in the panel zone. Thus, combinations of the three

methods are also included in this study as combinatorial (COM) components further to investigate the seismic performance of beam-through beam-column connections. Herein, COM-a includes doubler plates, COM-b incorporates RBS configurations, and COM-c encompasses both doubler plates and RBS. In total, five groups of specimens are designed accordingly (Table 4) [46]. All numerical input parameters are directly adopted from previous component experimental tests. Also, the loading methods and loading protocol follow the same experimental setup.

3.1. SFT analysis

Five beam-through joints (SFT-2, SFT-4, SFT-6, SFT-8, and SFT-10) are proposed with different stiffener plate thicknesses, which are 2 mm (0.079 in), 4 mm (0.157 in), 6 mm (0.236 in), 8 mm (0.315 in), and 10 mm (0.394 in), as shown in Table 4. Correspondingly, SFT-2 denotes the joint specimen with 2 mm stiffener plates. As observed, the joint panel zone yields when the rotation angle reaches 0.04 rad, and plate buckling occurs in all five specimens under the 0.067 rad rotation (Fig. 11). The stiffener plates yield in specimens SFT-2 and SFT-4, while no stiffener plates yielding is observed in the other three specimens. It indicates that the strengthening effects increase with the stiffener plate thickness.

Table 5 presents the ultimate moment capacity and total dissipated energy for all five specimens by interpreting the output hysteretic and backbone curves. Fig. 12 presents the backbone curves for all five SFT specimens, whose elastic stiffness and yield points are close. Once SFT specimens yield, all five post-yield curves almost match except SFT-2, whose post-yield curve is a little lower. Compared to SFT-6, whose stiffener and column flange thicknesses are the same, all the other specimens have similar moment and dissipated energy capacity with a difference of less than 2% and 6%, respectively. This phenomenon proves that even though thicker stiffener plate prevents undesirable buckling behavior, thicker stiffener plates have negligible effects on the joint flexural capacity. The panel joint shear capacity provides the flexural behavior of the beam-through joint, while the stiffener plates and the top of the bottom beam flanges form a rectangle that adds limited flexural capacity. However, the stiffener plates between beam-through flanges transfer the vertical forces through beam-column joints, significantly improving the connection integrity. In this study, 6 mm (0.236 in) is the thickest stiffener plate that yields, while the column web thickness is 6 mm (0.236 in). Therefore, the beam-through panel joint stiffener plate thickness should not be smaller than the larger column web thickness.

Table 4
Specimen design detail

Group	No.	Beam/Column Section (mm)	Stiffener thickness (mm)	Doubler plate thickness (mm)	Doubler plate strength (MPa)	RBS depth (mm)	Note
Stiffener thickness	SFT-2	250×125×9×6	2	0	0	0	-
	SFT-4		4				-
	SFT-6		6				Tested
	SFT-8		8				-
	SFT-10		10				-
Doubler plate thickness	DPT-2	250×125×9×6	6	2	300	0	-
	DPT-4			4			-
	DPT-6			6			Tested
	DPT-8			8			-
	DPT-10			10			-
Doubler plate strength	DPS-300	250×125×9×6	6	6	300	0	Same as DPT-6
	DPS-360				360		-
	DPS-420				420		-
Reduced beam section	RBS-30	250×125×9×6	6	6	300	30	Tested
	RBS-40					40	-
	RBS-50					50	-
	RBS-55					55	-
Combinatorial	COM-a	250×125×9×6	6	8	300	0	Same as DPT-8
	COM-b			0		40	-
	COM-c			8		40	-

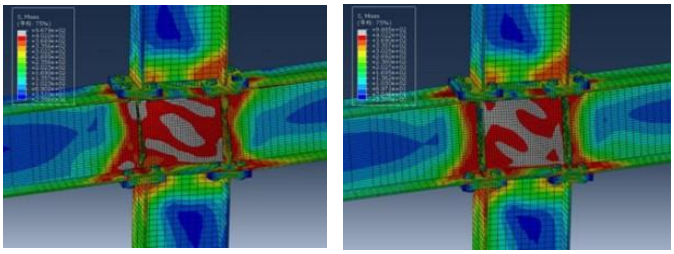

(a) SFT-2 (b) SFT-6

Fig. 11 Group SFT Stress distribution at 0.067 rad

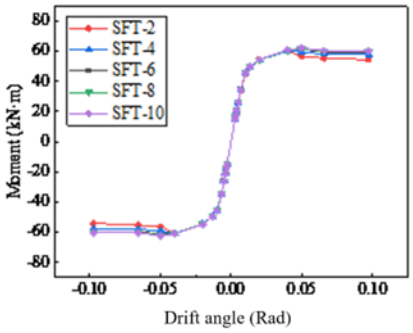

Fig. 12 Group SFT backbone curves

3.2. DPT analysis

This section examines the influence of doubler plates on the seismic performance of beam-through joints. Besides the 6 mm (0.236 in) stiffener plates (i.e., DPT-6), doubler plates with five thicknesses (i.e., 2 mm [0.079 in], 4 mm [0.157 in], 6 mm [0.236 in], 8 mm [0.315 in], and 10 mm [0.394 in]) are also included in the numerical model. See Table 4 for more details. The number in the specimen's name represents the doubler plate thickness. For instance, DPT-2 has 2 mm (0.079 in) thick doubler plates.

Table 5
Numerical results - group SFT

Name	Values					Increment ratio (to SFT-6)			
	SFT-2	SFT-4	SFT-6	SFT-8	SFT-10	SFT-2	SFT-4	SFT-8	SFT-10
Ultimate Moment (kN · m)	60.47	60.5	61.56	62	62.29	-1.77%	-1.72%	0.71%	1.19%
Total dissipated energy (KJ)	111.3	115.45	118.64	120.28	120.9	-6.19%	-2.69%	1.38%	1.90%

As shown in Fig. 13, doubler plate thickness substantially affects the panel zone deterioration and failure under quasi-static and cyclic loading protocols. Under a joint rotation angle of 0.013 rad, the panel zone web stress dramatically decreases with the increase of doubler plate thickness. The stress is highest in DPT-2 and lowest in DPT-10. When the joint rotational angle increases to 0.067 rad, buckling occurs in DPT-2 and DPT-6, while no apparent buckling is observed in DPT-10. The backbone curves of all five DPT specimens are shown in Fig. 14. Once the beam-column joints yield, the joint's secondary stiffness increases as the doubler plate thickness.

Table 6 compiles the yield displacement, yield moment, ultimate moment, and total dissipated energy for all five specimens. Again, the results prove that the doubler plate increases the panel zone capacities. The yield rotational angle of DPT-8 and DPT-10 increases 9.09% and 14.29% from DPT-6, the yield moment of DPT-8 and DPT-10 increases 7.57% and 12.93% from DPT-6, and the ultimate moment of DPT-8 and DPT-10 increases 10.77% and 17.38 % from DPT-6. Considering the material property, the overall panel zone thickness with doubler plate for DPT-8 and DPT-10 increases by 16.7% and 33.3% from DPT-6. Thus, doubler plates increase the shear strength of the panel zone and the out-of-plane moment of inertia for the beam-through web.

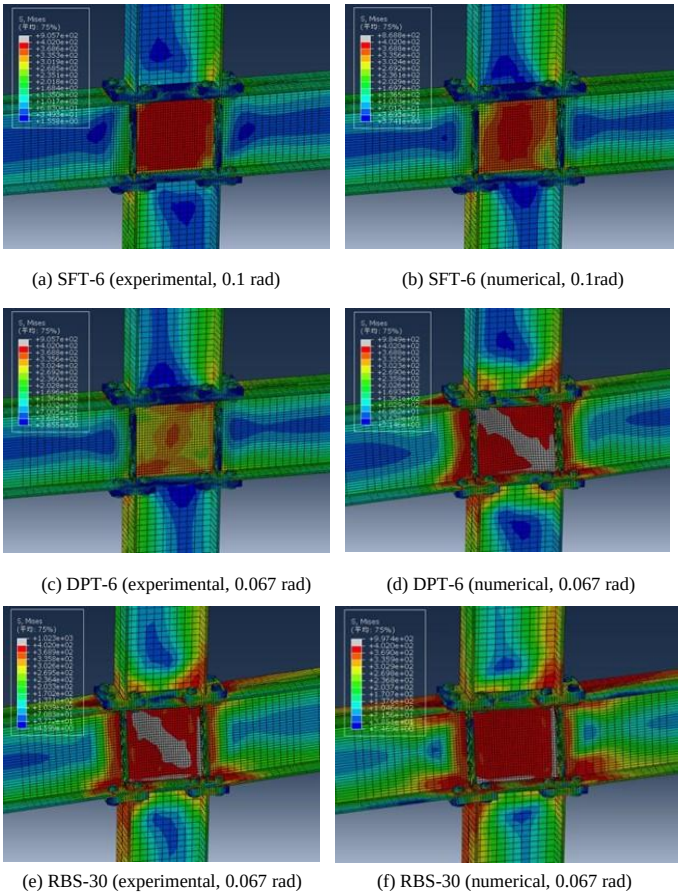

(a) SFT-6 (experimental, 0.1 rad) (b) SFT-6 (numerical, 0.1rad)

(c) DPT-6 (experimental, 0.067 rad) (d) DPT-6 (numerical, 0.067 rad)

(e) RBS-30 (experimental, 0.067 rad) (f) RBS-30 (numerical, 0.067 rad)

Fig. 13 Group DPT stress distribution

A linear correlation can be found between the doubler plate thickness and corresponding beam-column joint capacities, such as yield moment and ultimate moment. In this study, r_{My} denotes the nominal yield moment of a specimen (e.g., DPT-8) over DPT-6, r_{Mu} represents the nominal ultimate moment of a specimen (e.g., DPT-8) over DPT-6, and r_{DPT} is the nominal doubler plate thickness of a specimen (e.g., DPT-8) over DPT-6. The relationship among r_{My}, r_{Mu}, and r_{DPT} can be summarized as Eqs. 1 and 2 by analyzing the numerical results.

$$r_{My} = 0.27 r_{DPT} + 0.70 \quad (1)$$

$$r_{Mu} = 0.30 r_{DPT} + 0.69 \quad (2)$$

The total dissipated energy for all five specimens shown in Table 6 shows that the energy dissipated by DPT-2 and DPT-4 is reduced by 18.57% and 9.90%, compared to DPT-6, while the energy dissipated by DPT-8 and DPT-10 increases by 3.80% and 3.2%. The limited improvement of energy dissipation for DPT-8 and DPT-10 is due to the limited yielding development in the panel zone area for 8 mm and 10 mm thick doubler plates (i.e., DPT-8 and DPT-10). Therefore, increasing doubler plate thickness can productively increase the beam-through joint capacity but has negligible effects on the energy dissipation capacity due to the limited yielding developed.

Table 6
Numerical results - group DPT

Name	Values					Increment ratio (to DPT-6)			
	DPT-2	DPT-4	DPT-6	DPT-8	DPT-10	DPT-2	DPT-4	DPT-8	DPT-10
Yield rotation angle (rad)	0.0128	0.014	0.0154	0.0168	0.0176	-16.88%	-9.09%	9.09%	14.29%
Yield moment (kN · m)	57.5	66.84	74.64	80.29	84.29	-22.96%	-10.45%	7.57%	12.93%
Ultimate moment (kN · m)	70.5	80.15	90.1	99.8	105.76	-21.75%	-11.04%	10.77%	17.38%
Total dissipated energy (KJ)	80.86	89.47	99.3	103.07	102.48	-18.57%	-9.90%	3.80%	3.20%

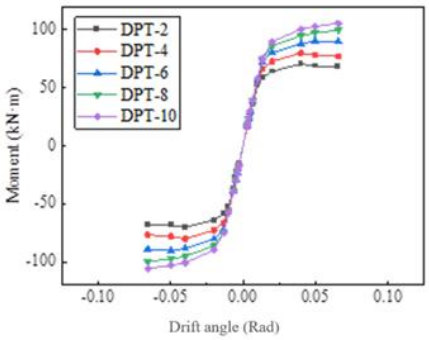

Fig. 14 Group DPT backbone curves

3.3. DPS analysis

Three doubler plate yield strengths (DPS-300, DPS-360, and DPT-420) are studied in this section, which are 300 MPa (43.5 ksi), 360 MPa (52.2 ksi), and 420 MPa (60.9 ksi), as shown in Table 4. DPS-300 denotes the specimen with doubler plates with 300 MPa (43.5 ksi) yield strength. Fig. 15 shows the stress distribution of doubler plates under a joint rotation angle of 0.067 rad. As noted, different plate strength does not impact the plate bulking or stress distribution in the panel zone area stiffened by doubler plates. Fig. 16 shows the backbone curves of all three specimens, where the maximum inter-story drift exceeds 0.05.

Table 7 presents the yield displacement, yield moment, and ultimate moment shown in the three specimens. The yield moment of DPS-360 and DPS-420 is improved by 4.90% and 9.45% from DPS-300, respectively. The yield moment of DPS-360 and DPS-420 increases by 5.18% and 10.0%, with the same doubler plate strength increase of 20% and 50%. Therefore, improving doubler plate strength can slightly improve the seismic performance of beam-through beam-column connections. Finally, the yield moment and ultimate moment ratio for these three specimens with different doubler plate strengths can be summarized below, where r_{DPS} is the strength ratio of a doubler plate over DPS-300.

The same minor improvement of seismic performance by raising the doubler plate strength (by 20% and 50%) can also be observed for the total dissipated energy (only increased by 1.44% and 1.98%) in Table 7. This improvement is due to the limited yielding development in the three specimens designed in this section. In summary, increasing stiffener thickness can restrict the buckling behavior of the panel zone and fully utilize steel's strength and ductility. However, merely improving steel strength is less efficient in leveraging its ultimate strength once buckling occurs in the panel zone. However, increasing doubler plate thickness is more efficient than increasing doubler plate strength since r_{My} and r_{Mu} are 0.27 and 0.30 for doubler plate thickness and 0.24 and 0.25 for doubler plate strength.

$$r_{My} = 0.24r_{DPS} + 0.76 \quad (3)$$

$$r_{Mu} = 0.25r_{DPS} + 0.75 \quad (4)$$

Table 7
Numerical results - group DPS

Name	Values			Increment ratio (to SFT-6)	
	DPS-300	DPS-360	DPS-420	DPS-360	DPS-420
Yield rotation angle (rad)	0.0154	0.0162	0.017	5.19%	10.39%
Yield moment (kN · m)	74.64	78.3	81.69	4.90%	9.45%
Ultimate moment (kN · m)	90.09	94.76	99.1	5.18%	10.00%
Total dissipated energy (KJ)	99.3	100.73	101.26	1.44%	1.97%

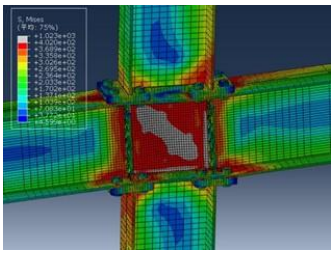

(a) DPS-300 (0.067 rad)

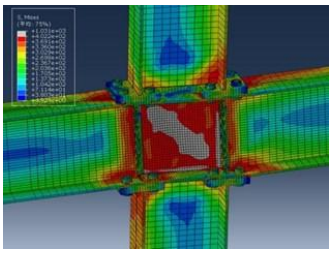

(b) DPS-360 (0.067 rad)

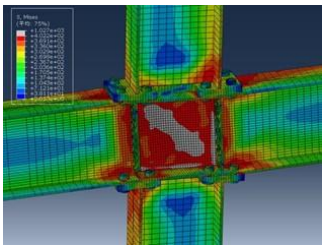

(c) DPS-420 (0.067 rad)

Fig. 15 Group DPS stress distribution

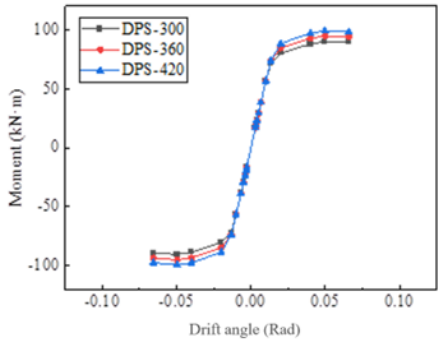

Fig. 16 Group DPT backbone curves

3.4 RBS analysis

The RBS joints are designed following the AISC prequalified connection [47]. The cut curve length and radius are 180 mm (7.067 in) and 150 mm (5.906 in), and the cut curve depths are 30 mm, 40 mm, 50 mm, and 55 mm, which are named RBS-30, RBS-40, RBS-50, and RBS-55. Correspondingly, the beam-through flange is reduced by 48%, 64%, 80%, and 88%, respectively.

The mises stress contour for all four specimens are shown in Fig. 17. All specimens' panel zone reaches yield strain under a joint rotation angle of 0.04 rad. However, the stress distribution near the RBS web is different. With the cut curve length and radius increase, the web stress also greatly increases. When the rotational angle is at 0.067 rad, the RBS web starts buckling, and the panel zone stress slightly decreases. However, no apparent buckling is observed at the other RBS joints' web or flanges.

Fig. 18 shows the backbone curves for all four RBS specimens, which are close before reaching a rotational angle of 0.04 rad. RBS-55 starts to yield and fail after reaching a rotational angle of 0.04 rad, and the post-yielding capacity is only 68.2% of the peak capacity. As noted, plastic hinges may occur at the reduced sections, and panel zone of beam-through joints. When the cut depth is too small, it is tough to develop plastic hinges at the reduced sections, and the joint seismic performance is like that of a panel zone without RBS. In this study, plastic hinges occur only when the beam cut depth is reduced by 88%. In summary, an RBS design can relocate the occurrence of plastic hinges and undermine the beam's flexural capacity, which is only recommended if reinforcing the panel zone web with doubler plates.

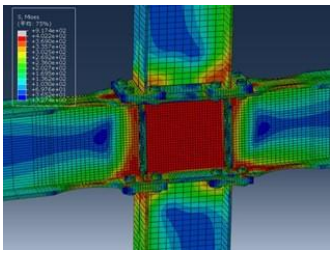

(a) RBS-30 (0.04 rad)

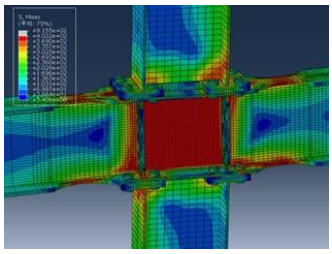

(b) RBS-40 (0.04 rad)

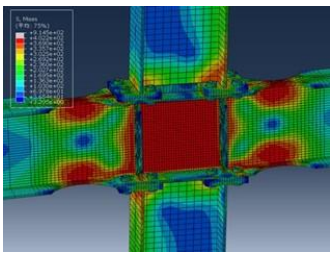

(c) RBS-50 (0.04 rad)

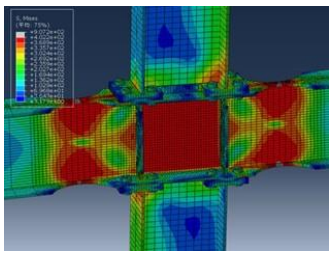

(d) RBS-55 (0.04 rad)

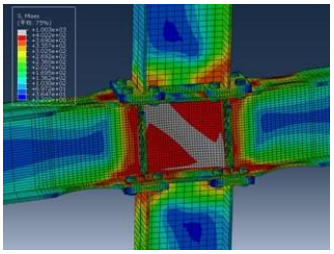

(e) RBS-30 (0.067 rad)

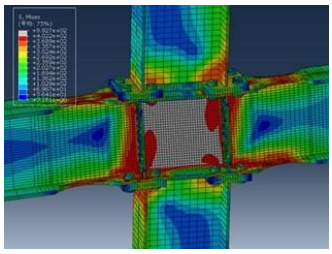

(f) RBS-40 (0.067 rad)

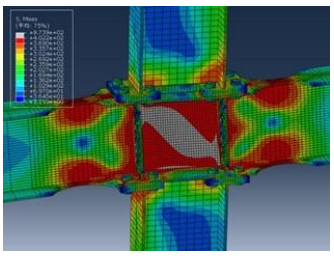

(g) RBS-50 (0.067 rad)

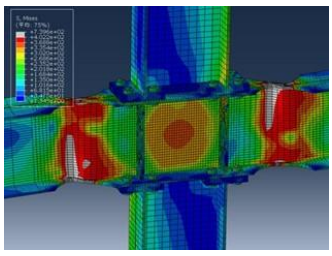

(h) RBS-55 (0.067 rad)

Fig. 17 Group RBS stress distribution

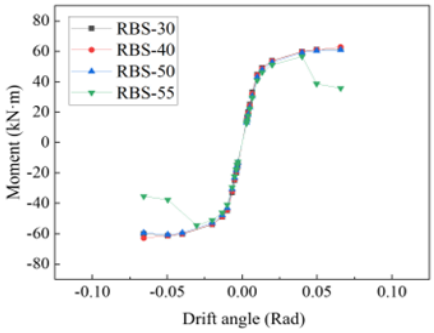

Fig. 18 Group RBS backbone curves

3.5. COM analysis

Three COM (combinational) specimens are designed to find the optimal flexural performance for beam-through beam-column connections. The design parameters are shown in Table 4. All three specimens have 6 mm (0.236 in) stiffener plates to better transfer the gravity load through the beam-through connections from level to level. COM-a includes an 8 mm (0.315 in) doubler plate, COM-b incorporates a 40 mm (1.57 in) deep RBS section cut, and COM-c combines COM-a and COM-b.

The stress distribution of all specimens is shown in Fig. 19. The beam-through panel zone for COM-a and COM-c does not reach flexural strength with a rotational angle is 0.013 rad incorporating the strengthening effects of doubler plates, while the beam-through web for COM-b yields. The peak stress in the COM-c's panel zone is reduced by including RBS compared to that of COM-a, which demonstrates that both RBS and doubler plates can effectively reduce the panel zone stress. As observed in Figs. 19d, 19e, and 19f, only specimen COM-C (doubler plate + RBS) effectively shifts the plastic hinge from the panel zone to the beam ends, while COM-a (doubler plate only) and COM-b (RBS only) still maintain significant plastic deformation in the joint panel zone.

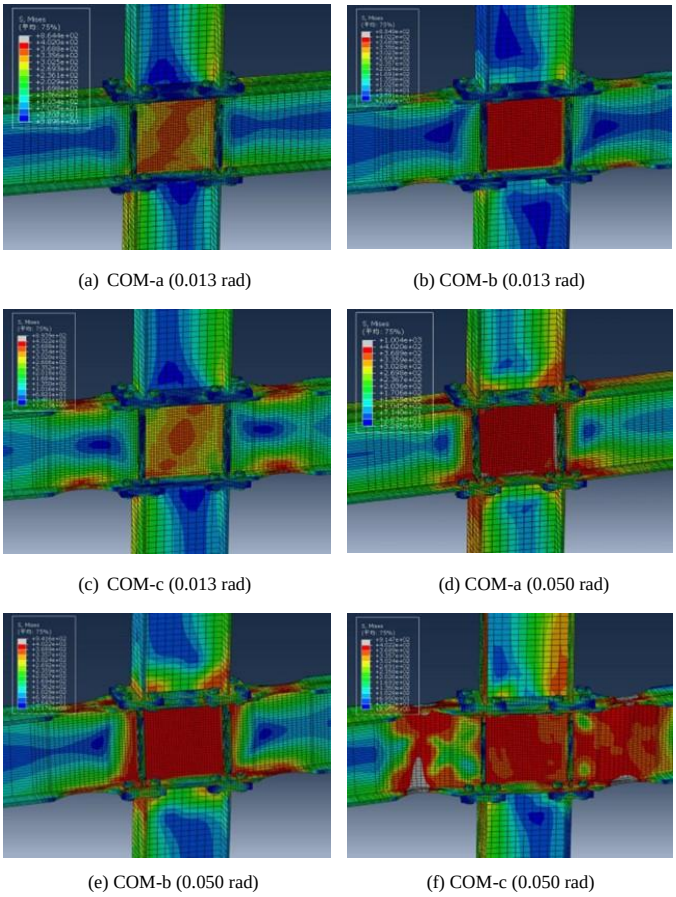

(a) COM-a (0.013 rad) (b) COM-b (0.013 rad)

(c) COM-c (0.013 rad) (d) COM-a (0.050 rad)

(e) COM-b (0.050 rad) (f) COM-c (0.050 rad)

Fig. 19 Group RBS stress distribution

Fig. 20 summarizes the backbone curves for all three COM specimens. Doubler plates can significantly increase the flexural capacity of beam-through beam-column connections. The design capacity of COM-c is reduced once the inter-story drift reaches 0.04 rad, while COM-a does not because plastic hinges occurred at RBS. The occurrence of plastic hinges delays the panel zone buckling and avoids global structural collapse. The Chinese code [38] requires a maximum inter-story drift angle of 0.02 rad, which both COM-a and COM-c meet. It proves the efficiency of RBS in beam-through beam-column moment connections, even though it fails earlier than those specimens without RBS.

The seismic parameter and failure modes are listed in Table 8. The panel zone design of specimens COM-c and COM-a is identical, while COM-c adopts RBS configurations. The ductility and flexural capacity of COM-c decreases by 10.1% and 19.1% from COM-a, respectively. As discussed earlier, the RBS configuration in COM-C has successfully shifted the plastic hinge and weak point to the beam ends. It indicates that the ductility and flexural capacity reduction are from the RBS design. However, even though COM-b also has an RBS configuration, RBS is ineffective due to its design parameter, and the primary failure still occurs in the joint panel zone. In actual engineering design, this study recommends engineers calculate and utilize the smaller capacity of joint panel zone and RBS, which aims to fulfill the functionality of RBS configuration.

Table 8
Numerical results - group COM

Name	Doubler plates	RBS	Failure location	F_y (kN)	Δ (mm)	F_u (kN)	Δ_{max} (mm)	μ
COM-a	Yes	No	Panel Zone	45.88	29.38	56.97	115.0	3.91
COM-b	No	Yes	Panel Zone	27.62	22.74	35.92	115.0	5.06
COM-c	Yes	Yes	RBS	41.26	27.72	49.38	87.0	3.14

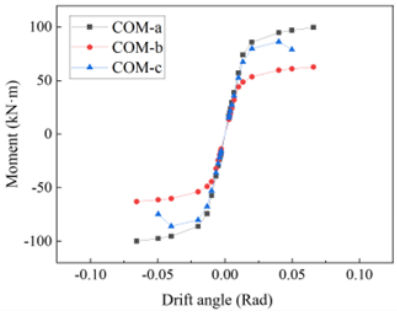

Fig. 20 Group COM backbone curves

4. Panel zone analytical flexural capacity

This section proposes an analytical method to calculate the flexural capacity of beam-through beam-column connections, which is validated by the numerical results received in previous sections. The following assumptions are adopted herein. First, the beam-column panel joints' flexural capacity is mainly provided by the beam-through web and the strengthening doubler plates. Thus, a rigid subframe comprises beam-through flanges, column end plates, and beam-through stiffener plates. Furthermore, a tensile area occurs when the beam-through web buckles, sloped 45° from the horizontal direction in parallel to the beam direction. Last, the impact of axial load on the flexural capacity of beam-column connections is ignored. The analytical beam-through beam-column connection panel joint is sketched in Fig. 21.

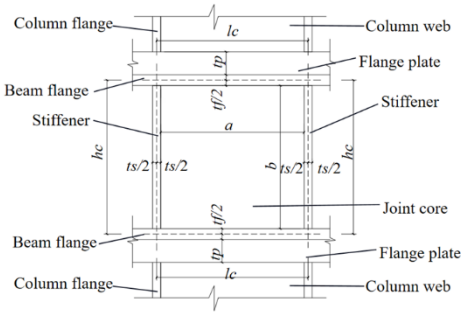

Fig. 21 Joint Panel zone design parameters

Fig. 22 shows the analytical force distribution in a beam-through beam-column panel zone. The beam and column end shear forces compose the moment and shear forces in the panel zone area (Figs. 22a and 22b). The beam-end panel zone moments (M_1) cause a pair of forces V_{m1} in the opposite directions along the beam flanges, and the column-end panel zone moment (M_2) induces another pair of forces in the opposite directions along the beam stiffener plates, as in Fig. 22c. The two pairs of opposite forces denote the perimeter forces around the rigid subframe panel zone area (Fig. 22e). Under the interactions of the shear forces around the panel zone, the beam-through web is in shear actions, which can be seen in Fig. 22f.

The analytical equation to calculate joint panel zone moment capacity can be conducted by analyzing Fig. 21 to 22 as in Eq. 5 to 6.

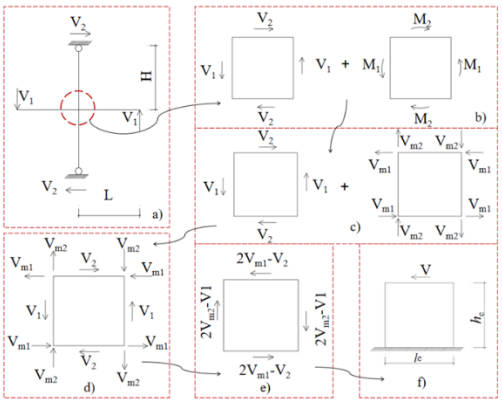

Fig. 22 Joint Panel zone force distribution and diaphragm

$$M_1 = V_1\left(L - \frac{l_c}{2}\right) = V_{m1}h_c \tag{5}$$

$$M_2 = V_2\left(H - \frac{h_c}{2}\right) = V_{m2}l_c \tag{6}$$

By performing moment equilibrium in the panel zone, the following equation is summarized.

$$V_1 L = V_2 H \tag{7}$$

Furthermore, Eq. 8 can be achieved by running force equilibrium.

$$V = 2V_{m1} - V_2 = 2V_{m2} - V_1 \tag{8}$$

By incorporating Eqs. 5, 6, 7 into Eq. 8,

$$V = V_1\frac{2HL - Lh_c - Hl_c}{Hh_c} = V_2\frac{2HL - Lh_c - Hl_c}{Ll_c} \tag{9}$$

The principal stress distribution diagram in the joint panel zone area is shown in Fig. 23a. σ_t, σ_c denotes the principal tensile and compressive stress. The horizontal and vertical stresses in the panel zone steel plate are shown in Figs. 23b and 23c, where σ_{yx} is the shear stress in the horizontal stress component, and θ represents the angle between the tensile stress and the horizontal direction along the through-beam longitudinal direction. The boundary shear and normal stress can be deduced below by performing stresses tensor notation $\sigma'_{mn} = \sigma_{ij}n_{mi}n_{nj}$.

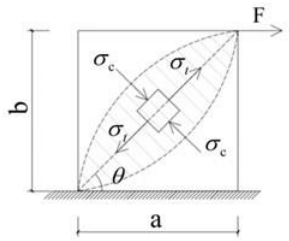

(a) Web principal stress distribution

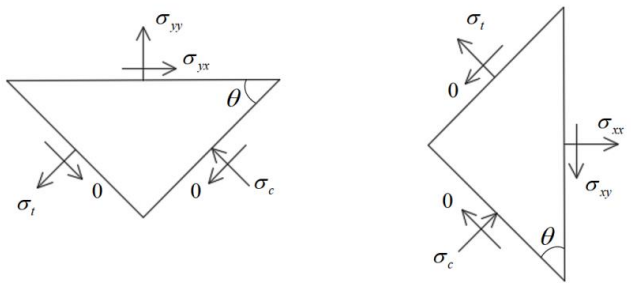

(b) Horizontal stress distribution (c) Vertical stress distribution

Fig. 23 Through-beam web stress distribution

$$\sigma_{xy} = \sigma_{yx} = \frac{1}{2}(\sigma_t + \sigma_c)sin2\theta \tag{10}$$

$$\sigma_{xx} = \sigma_t cos^2\theta - \sigma_c sin^2\theta \tag{11}$$

$$\sigma_{yy} = \sigma_t sin^2\theta - \sigma_c cos^2\theta \tag{12}$$

A tension strip is developed as the beam-through web buckles. Then, the tensile stress becomes uniform, and σ_c equals zero. Referring to the conclusions and recommendations provided by Driver et al. [49] and Elgaaly et al. [50], the inclination angle for the tensile strip in the rigid subframe located in the beam-through beam-column connection is roughly 45°. Thus, Eq. 13 can be summarized by following the von Mises yield criterion [51], where f_y is the steel plate yield strength.

$$(\sigma_{xx} - \sigma_{yy})^2 + {\sigma_{yy}}^2 + {\sigma_{xx}}^2 + 6{\sigma_{xy}}^2 = 2{f_y}^2 \tag{13}$$

The following equations can be compiled by adding Eqs. 10, 11, and 12 into Eq. 13.

$$\sigma_{xy} = \frac{1}{2}f_y \tag{14}$$

Taking the web shear yielding strength $F_u = \sigma_{xy}at_w$ into Eq. 14 leads to the calculation of F_u. A modification factor, μ is adopted into Eq. 15 to reduce the error induced by ignoring the axial load effects. Where a is the panel zone horizontal length in the beam-through direction, t_w represents the panel zone web thickness.

$$F_u = \frac{1}{2}\mu f_y a t_w \tag{15}$$

The panel zone strengthening doubler plates are considered by adopting a doubler strength modification factor because the doubler plates are attached to the panel zone by welding the plate edge and another nine welding points with limited capacities. f'_y is the doubler plate strength, and t'_w denotes the doubler plate thickness.

$$F_u = \frac{1}{2}a(\mu f_y t_w + \beta f'_y t'_w) \tag{16}$$

Assume $F_u = V$,

$$V_1 = \frac{Hh_c a(\mu f_y t_w + \beta f'_y t'_w)}{4HL - 2Lh_c - 2Hl_c} \tag{17}$$

Consider the panel zone moment capacity is $M_u = V_1 L$.

$$M_u = \frac{Hh_c La(\mu f_y t_w + \beta f'_y t'_w)}{4HL - 2Lh_c - 2Hl_c} \tag{18}$$

By further analyzing all the numerical results in section 3 and performing design parameter regression, the modification factor, α equals 1.28, and β can be calculated as follows:

$$\beta = 0.53\gamma^2 - 1.72\gamma + 2.31 \tag{19}$$

$$\gamma = \frac{f'_y t'_w}{f_y t_w} \tag{20}$$

Where γ is the doubler plate strength ratio that denotes the ratio of doubler plate strength over panel zone web strength. Table 9 provides all computational parameters and sample results for all the specimens designed in previous sections. As observed, the analytical method and equations presented in this section can successfully predict the flexural capacity of the panel zone in beam-through beam-column connections. The maximum difference between the analytical and numerical results is 2.47%. Consequently, the proposed analytical equations can be utilized to simulate the flexural capacity for beam-through beam-column moment connections in steel structural design and other earthquake engineering simulations.

With all the equations derived, it is worth noting that they apply not only to the panel zone of beam-through joints but also to the panel zone of traditional column-through beam-column joints. Since the post-yielding tensile band is assumed to maintain a 45° angle from the horizontal direction, the analytical

method can accurately predict the panel zone flexural capacity in any square area. When the panel zone is not a square (i.e., width is not equal to height), the angle between the post-yield tensile band is no longer 45°, when the current analytical method might not be accurate. As the panel zone height-to-width ratio increases, multiple tensile bands may occur, which is totally ignored in this study. However, multiple tensile bands and angles in the panel zone are more complicated topics, requiring further investigation.

5. Conclusions

This study performs numerical and analytical investigations of the flexural behaviors of beam-through H-section (wide-flange) steel beam-column moment-resisting connections. Beam-through beam-column joints can accelerate construction progress by lifting and erecting a portion or even a floor of building structures. Thus, a large portion of sophisticated welding can be performed in factories or on the ground, expediting the completion of complex weld connections with good quality assurance or quality control (QA/QC). In addition, shop welding and modular field erection significantly reduce field labor costs, making this approach highly marketable with promising engineering application possibilities compared to other methods.

Five types of reinforcing methods or combinations are considered. Finally, an analytical method is proposed to calculate the seismic flexural capacity of through-beam beam-column joints. The main findings are summarized below:

1. The thickness of web stiffener plates in through-beam beam-column joints has negligible effects on the joint seismic performance. However, it is still recommended to design the through-beam web stiffener plate not thinner than the column flanges, which aims to transfer the column axial loads through the through beam efficiently.

2. Increasing the doubler plate thickness and strength can both effectively improve the yield and ultimate capacities of beam-through beam-column connections, where the former method is superior.

3. The American Institute of Steel Construction (AISC) prequalified (reduced beam section) RBS can still shift the possible weak points and plastic hinges outside the connection panel zones. Furthermore, this study strongly recommends engineers to calculate the seismic capacity at the beam-column panel zones and RBS, which intends to fully engage the RBS configuration. Also, RBS reduces not only the beam-column joint capacity but also its ductility in the through-beam design.

4. Combining the through-beam beam-column joint doubler plates with RBS can adequately transfer the weak zone and plastic hinges from the joint panel zone to the beam ends, which satisfies the design concept in the current building seismic codes.

5. The proposed simplified analytical method and equations derived from force equilibrium, stress tensor rotation, and von Mises yield criterion can accurately predict the flexural capacity for beam-through beam-column panel joints. This method provides technical and design support for steel seismic-resisting structures with beam-through steel moment frames.

Table 9
Comparison of numerical and analytical results

Name	Beam web strength f_y (MPa)	Beam web thickness t_w (mm)	Doubler plate strength f_y' (MPa)	Doubler plate thickness t_w' (mm)	Doubler plate strength ratio $\gamma = \frac{f_y' t_w'}{f_y t_w}$	Numerical yield moment M_u' (kN.m)	Analytical yield moment M_u (kN.m)	Difference
SFT-6	369	6	0	0	0	47.72	47.53	-0.40%
DPT-2	369	6	300	2	0.27	57.50	56.08	-2.47%
DPT-4	369	6	300	4	0.54	66.84	68.00	1.73%
DPT-6	369	6	300	6	0.81	74.64	75.23	0.79%
DPT-8	369	6	300	8	1.08	80.29	80.13	-0.19%
DPT-10	369	6	300	10	1.36	84.29	85.06	0.91%
DPS-300	369	6	300	6	0.81	74.64	75.23	0.79%
DPS-360	369	6	360	6	0.98	78.30	78.30	0.00%
DPS-420	369	6	420	6	1.14	81.69	81.04	-0.79%

References

[1] Ding Y., Deng E.F., Zong L.,Dai X.M., Lou N., and Chen Y. “Cyclic tests on corrugated steel plate shear walls with openings in modularized-constructions”, Journal of constructional steel research, 138, 675-691, 2017.

[2] Yin X., Liu H., Chen Y., and Al-Hussein M. “Building information modelling for off-site construction: Review and future directions”, Automation in construction, 101, 72-91, 2019.

[3] Liu X.C., Pu S.H., Zhang A.L., and Zhan X.X. “Performance analysis and design of bolted connections in modularized prefabricated steel structures”, Journal of Constructional Steel Research, 133, 360-373, 2017.

[4] Zhang A.L., Shangguan G.H., Zhang Y.X., Wang Q.B., and Cai W.C. “Experimental study of resilient prefabricated steel frame with all-bolted beam-to-column connections”, Advanced Steel Construction, 16(3), 255-271, 2020.

[5] Chu Y.P., Chen X.Q., Zhong Y., and Zhang H.C. “Seismic fragility analysis of steel frames with fully-bolted core tube joints”, Advanced Steel Construction, 20(3), 208-221, 2024.

[6] Zhang X., Zhou B., Gao J.D., Qian H., Song L.Z., and Cai L.M. “Numerical investigation on seismic performance of prefabricated steel beam-to-column connection with replaceable U-shaped plate”, Advanced Steel Construction, 20(4), 7-405, 2024.

[7] Zhang Z.W., Li D., Wang H.J., Qian H.L., Fang W.Q., Jing X.F., and Fan F., “Study of mechanical properties of a novel column-beam-column prefabricated steel frame joint”, Advanced Steel Construction, 20(4), 0-344, 2024.

[8] Qin Y., Chen Z., Wang X., and Zhou T. “Seismic behavior of through-diaphragm connections between CFRT columns and steel beams-experimental study”, Advanced Steel Construction, 10(3), 351-371, 2014.

[9] Rong B., Zhang Y., Sun J., and Zhang R. “Experimental and numerical research on hysteretic behavior of CFST frame with diaphragm-through connections”, Journal of Building Engineering, 45, 103529, 2022.

[10] Wu L., Wang X., Luo S., Wang X., Cui D., and Chen, Z. “Experimental research on seismic performance of the full-bolted diaphragm-through connection to RCFST”, Advances in Structural Engineering, 18(7), 959-973, 2015.

[11] Wang W., Hu S.L., Zou C., and Chen Y.S. “The effects of joint behavior on the seismic performance of floor-by-floor assembled steel beam-through braced frames”, Engineering Mechanics, 36(4), 206-213, 2019 (In Chinese).

[12] Wang W., Zhou Q., Chen Y., Tong L.W., and Chan T.M. “Experimental and numerical investigation on full-scale tension-only concentrically braced steel beam-through frames”, Journal of Construction Steel Research, 80, 369-385, 2013.

[13] Yao Z.C., Wang W., Fang C., and Zhang Z.Y. “An experimental study on eccentrically braced beam-through steel frames with replaceable shear links”, Engineering Structures, 110185, 2020.

[14] Xi Que Wu. 2023. http://www.xiquewu.cn/2020/12/5465/

[15] Sekisui Heim. Factory Production system. 2022. https://www.sekisuichemical.com/about/division/housing/index.html

[16] Chen Y.S., Wang W., and Chen Y.Y. “High-strength steel for resilience of beam-through frames”, Proceedings of the Institutution of Civil Engineering Structures and Building, 170(9), 2017.

[17] Chen Y.S., Wang W., and Chen Y.Y. “Full-scale shake table tests of the tension-only concentrically braced steel beam-through frame”, Journal of Constructional Steel Research, 148, 611-626, 2018.

[18] Dong B.P., Chen Y.S., and Wang W. “Self-centering mechanism and seismic response of steel tension-only concentrically braced beam-through frames”, Structures, 30, 960-972, 2021.

[19] Hu S.L., Wang W., and Qu B. “Enhancing seismic performance of tension-only concentrically braced beam-through frames through implementation of rocking cores”, Engineering Structures, 169, 68-80, 2018.

[20] Hu S., Wang W., Alam M.S., and Qu B. “Improving the Seismic Performance of Beam-through Concentrically Braced Frames Using Energy-absorbing Rocking Core”, Journal of Earthquake Engineering, 26(7), 2022.

[21] Zhang R.B., Wang W., Yang C.Y., Hu S.L., and Shahria A.M. “Hybrid test and numerical study of beam-through frame enhanced by friction spring-based self-centering rocking core”, Engineering Structures, 274, 115157, 2023.

[22] Li J.L., Wang W., and Li P.Y. “Development and experimental study of steel beam-through framed connections with T-type curved knee braces for improving seismic performance”, Engineering Structures, 231, 111722, 2021.

[23] Li J.L., Wang W., and Li P.Y. “Development, testing and performance evaluation of steel beam-through framed connections with curved knee braces for improving seismic performance”, Journal of Constructional Steel Research, 179, 106552, 2021.

[24] Li Y.W., Wang Y.Z., and Wang Y.B. “Experimental and numerical study of beam-through energy-dissipative rocking columns for mitigating seismic responses”, Journal of Constructional Steel Research, 189, 107097, 2022.

[25] Jeddi M.Z., Sulong N.H.R., and Khanouki M.M.A. “Seismic performance of a new through rib stiffener beam connection to concrete-filled steel tubular columns: An experimental study”, Engineering Structures, 131, 477-491, 2017.

[26] Jamali P.F., Ali H.M., and Hamed S. “Seismic behavior of through beam connection to steel box-column”, Journal of Constructional Steel Research, 193, 107261, 2022.

[27] Chen Z.H., Niu X.Y., Liu J.D., Khan, K., and Liu Y.C. “Seismic study on an innovative fully-bolted beam-column joint in prefabricated modular steel buildings”, Eng Struct 2021; 234, 111875.

[28] Tagawa H. and Gurel S. “Application of steel channels as stiffeners in bolted moment connections”, Journal of Constructional Steel Research, 61(12), 2005.
[29] Zhong W.H., Zhao M.J., Zhou L., Tan Z., Sun W., and Zheng Y.H. “Seismic performance of a narrow flange H-beam-to-column full-bolt end-plate weak-axis connection”, Structures, 46, 637-653, 2022.
[30] Čermelj B., Može P., and Sinur F. “On the prediction of low-cycle fatigue in steel welded beam-to-column joints”, Journal of Constructional Steel Research, 117, 49-63, 2016.
[31] Ma H.W., Zheng H., and Zhang W. “Experimental and numerical study of mechanical properties for the double-ribbed reinforced beam-column connection”, Advanced Steel Construction, 16(4), 297-309, 2020.
[32] Du H.K., Zhao P.F., Wang Y.D., and Sun W.T. “Seismic experimental assessment of beam-through beam-column connections for modular prefabricated steel moment frames”, Journal of Constructional Steel Research, 192, 107208, 2022.
[33] Chen S.J., Yeh C.H., and Chu J.M. “Ductile steel beam-to-column connections for seismic resistance”, Journal of Structural Engineering, 122(11), 1292-1299, 1996.
[34] Sophianopoulos D.S. and Deri A.E. “Parameters affecting response and design of steel moment frame reduced beam section connections: an overview”, International Journal of Steel Structures, 11, 133-144, 2011.
[35] Carter C.J. and Iwankiw N.R. “Improved ductility in seismic steel moment frames with dogbone connections”, Journal of Constructructional Steel Research, 1(46), 448, 1998.
[36] Jones S.L., Fry G.T., and Engelhardt M.D. “Experimental evaluation of cyclically loaded reduced beam section moment connections”, Journal of Structural Engineering, 128(4), 441-451, 2002.
[37] Lee C.H., Jeon S.W., Kim J.H., and Uang C.M. “Effects of panel zone strength and beam web connection method on seismic performance of reduced beam section steel moment connections”, Journal of Structural Engineering, 131(12), 1854-1865, 2005.
[38] Wang H.T., Huo J.S., Elchalakani M., Liu Y.Z., and Zhang S.Q. “Dynamic performance of retrofitted steel beam-column connections subjected to impact loadings”, Journal of Constructructural Steel Research, 183, 106732, 2021.
[39] Chen C.W., Qiao H.Y., Wang J.P., and Chen Y. “Progressive collapse behavior of joints in steel moment frames involving reduced beam section”, Engineering Structures, 225, 111297, 2020.
[40] Roudsari M.T., Abdollahi F., Salimi H., Azizi S., and Khosravi A.R. “The effect of stiffener on behavior of reduced beam section connections in steel moment-resisting frames”, International Journal of Steel Structures, 15, 827-834, 2015.
[41] General Administration of Quality Supervision, Inspection and Quarantine of China, Standardization Administration of China. The hot-rolled H and cut T section steel (GB/T 11263-2017). Beijing, China, 2017.
[42] AISC. Steel Construction Manual 15th ed. American Institute of Steel Construction, Chicago, IL, 2017.
[43] AISC 341. Seismic Provisions for Structural Steel Buildings, Chicago, IL, 2016.
[44] Wang Y.D., Ibarra L., and Pantelides C. “Collapse capacity of reinforced concrete skewed bridges retrofitted with buckling-restrained braces”, Engineering Structures, 184, 99-114, 2019.
[45] Wang Y.D., Ibarra L., and Pantelides C. “Seismic retrofit of a three-span RC bridge with buckling-restrained braces”, ASCE Jounral of Bridge Engineering, 21(11), 04016073, 2016.
[46] Ministry of Housing and Urban-Rural Development of China. Standard for design of steel structures. (GB50017-2017). Beijing, China, 2017.
[47] AISC 358. Prequalified connections for special and intermediate moment frames for seismic application. Chicago: American Institute of Steel Construction; 2016.
[48] GB 50011-2016. Code for seismic design of buildings. Ministry of Housing and Urban-Rural Development, Beijing, China, 2016.
[49] Driver R.G., Kulak G.L., Kennedy D.L., and Elwi A.E. “Cyclic test of four-story steel plate shear wall”, Journal of Structructural Engineering, 124(2), 112-120, 1998.
[50] Park H.G., Kwack J.H., Jeon S.W., Kim W.K., and Choi I.R. “Framed steel plate wall behavior under cyclic lateral loading”, Journal of Structructural Engineering, 133(3), 378-388, 2007.
[51] Yang L.T. Introduction to Elastoplastic Mechanics, Tsinghua University, Beijing, China, 2013.

Advanced Steel Construction – Vol. 21 No. 2 (2025) 136–146
DOI:10.18057/IJASC.2025.21.2.5

NONLINEAR ANALYSIS OF REINFORCED BEAM-COLUMN JOINTS WITH HIGH STRENGTH STEEL SINGLE-RIBBED PLATES

Xiu-Yuan Fang [1], Ze-Qing Wan[1, 2, *], Hong-Wei Ma [1, 2] and Yu Zhang [1]

[1] *College of Civil Science and Engineering, Yangzhou University, Yangzhou 225127, China*
[2] *State Key Laboratory of Green Building in Western China, Xi'an University of Architecture & Technology, Xi'an 710055, China*
* *(Corresponding author: E-mail: zqwan@yzu.edu.cn)*

ABSTRACT

In recent years, with the continuous development and wide application of high-strength steel in the field of construction, the research on the performance optimization of beam-column joints in high-strength steel structures has become increasingly important. This study aims to investigate the hysteretic performance of high-strength steel single-ribbed reinforced beam-column joints. Based on high strength steel properties test and tensile test of welded joint plate, two reference groups are established: high-strength steel common beam-column joints and ordinary steel single-ribbed reinforced beam-column joints. Finite element models are developed for the three types of joints to analyze their stress patterns, failure modes, hysteretic curves, skeleton curves, ductility, ultimate bearing capacity, and energy dissipation capacity under low cyclic reciprocating loads. It is found that high-strength steel single-rib reinforced beam-column joints can enhance the deformation capacity and initial stiffness of the joints. They exhibit improved ductility and energy dissipation capacity, as well as increased joint stiffness and a slower rate of stiffness degradation. This study provides valuable data for the design methods of high-strength steel structure beam-column joints.

ARTICLE HISTORY

Received: 6 June 2024
Revised: 23 December 2024
Accepted: 1 January 2025

KEYWORDS

High-strength steel;
Single ribbed plate reinforced type;
Beam-column joints;
Finite element;
Nonlinear analysis

1. Introduction

Driven by the demand of supply-side structural reform, the conditions for the application and development of high-performance steel structures are becoming increasingly mature. High-strength steel structures can reduce component sizes and significantly decrease material volume and weight, offering substantial social and economic benefits [1-2]. However, with the enhancement of strength, plasticity, toughness, and ductility are reduced, making welding high-strength steel challenging and becomes the main factor affecting the fatigue life of components [3], thereby limiting the widespread adoption of high-strength steel. Simultaneously, traditional steel frame beam-column joints are susceptible to brittle fracture, with most damage occurring at the flanges. An effective approach to address this issue is by eliminating the plastic hinge formation at the beam-column flange contact surface [4]. Currently, commonly used improved nodes include weakened nodes and strengthened nodes. Weakened nodes achieve outward plastic hinge formation by reducing the beam's bearing capacity [5], while strengthened nodes force the plastic hinge to occur far from the beam-column butt weld by reinforcing the beam end section [6]. The single-ribbed stiffened joint falls under the category of ribbed stiffened joints and exhibits excellent plastic deformation capacity and energy dissipation capacity.

Currently, many scholars both domestically and internationally have conducted relevant research on high-strength steel single-rib reinforced joints. Zong Liang et al. [7] conducted experiments and numerical simulations on Q690D high-strength steel butt welds, obtaining mechanical properties and fatigue performance and verifying the validity of the numerical simulation method for fatigue assessment. Liu et al. [8] studied the influence of optimized welding parameters on the structural distortion of S690 high strength steel thin-plate. Jordao et al. [9] conducted finite element numerical analysis on beam-column joints composed of S355 ordinary steel and S690 high-strength steel, calibrating it with full-scale model test results. Guo et al. [10] designed a kind of high-strength steel bending beam-column joint connected by angle steel. Through static loading test and finite element analysis, it was verified that this kind of reinforced joint can significantly improve the bearing capacity of the joint.. Hongchao G et al. [11] performed low-cyclic loading tests on six Q690 high-strength steel plate reinforced joints, demonstrating higher bearing capacity of the high-strength steel plate, and a combination of Q690 and ordinary steel yielded higher ductility. Lu et al. [12] made a nonlinear analysis of a beam-end ribs reinforced joint, and the results showed that the joint could make the plastic hinge move outward effectively. Wang et al. [13] analyzed the parameters of reinforced joints with single rib, and gave the design method of reinforced joints with single rib. Yang Tao et al. [14] carried out ANSYS finite element analysis on the mechanical properties of the joint domain with stiffened ribs.

Presently, there exists a plethora of research achievements on the mechanical properties of high-strength steel, yet there is a gap in the investigation of welded joint properties, primarily conducted through experimental methods. The finite element method, used as an auxiliary check calculation, simplifies the setup of its simulated contact.

In this study, the validity of the finite element simulation method is verified by the comparison of uniaxial tensile tests of high strength steel welded joint plates. To provide design data for high-strength steel structure beam-column joints, three sets of beam-column joints were established using ABAQUS software to analyze their hysteretic performance, and further optimization of single-rib joint parameters was conducted.

2. Material test and welded joint plate test

2.1. Q690D high strength steel properties test

In this test, the performance test of Q690D high-strength steel was conducted using the UTM5305 electronic universal testing machine, which has a maximum measuring range of 30 tons. For strain measurement, the YSJ50/10-ZC electronic extensometer with a measuring range of 2mm to 50mm was used. The material property test results serve as the basis for material property parameters used in test data analysis, finite element numerical simulation, and theoretical calculations.

Fig. 1 UTM5305 electronic universal testing machine

Following the guidelines outlined in "Steel and Steel Products - Mechanical Properties Test Sampling Location and Sample Preparation" (GB/T2975-2018) [15], samples were extracted from the same batch of high-strength steel welded joint plate specimens. The samples were then prepared with thicknesses of 6mm, 8mm, 10mm, and 16mm, respectively. The property test for Q690D high-strength steel was conducted in the Structure Laboratory of Yangzhou University, specifically through a unidirectional tensile test. Prior to stretching the specimen, suitable fixtures were chosen based on the plate thickness, and the specimen was positioned vertically at the center. The loading device setup is depicted in Fig.1.

Given that Q690D high-strength steel exhibits no distinct yield platform and directly enters nonlinear strengthening after yield, the nominal stress corresponding to 0.2% strain is considered as the yield strength and denoted as $f_{0.2}$. The results of material properties test for each group are shown in Table 1. The average value in this test is 234.7GPa, providing essential material constitutive parameters for subsequent finite element analysis.

Table 1
Test results of Q690D high strength steel properties

Specimen thickness	The sample number	Sectional area	Modulus of elasticity	Yield strength	Tensile strength	Elongation
		A/mm^2	E/GPa	$f_{0.2}$/MPa	f_u/MPa	ε/%
6mm	6-1	89.82	223.6	712.12	792.53	23.44
	6-2	88.77	242.2	713.53	795.14	19.46
	6-3	89.43	229.4	714.64	796.42	19.62
8mm	8-1	116.74	237.4	710.27	789.63	18.50
	8-2	119.84	236.8	708.74	789.55	18.28
	8-3	117.74	238.0	710.65	787.64	18.37
10mm	10-1	148.63	223.7	713.17	793.44	21.84
	10-2	148.20	229.8	712.43	791.81	20.04
	10-3	149.35	228.7	709.27	789.73	21.16
16mm	16-1	235.04	230.6	707.84	786.92	23.52
	16-2	233.84	254.2	711.77	792.65	21.27
	16-3	230.70	242.2	713.46	795.45	20.27
	Average		234.7	711.49	791.74	20.48
	Deviation from standard value/%		/	-3.02	-2.75	/

2.2. Tensile test of welded joint plate

In order to analyze and study the stress mechanism of beam-column joints in high-strength steel structures, the beam-column joints were simplified with reference to European specification EC3-2015[16]. Two opposite tension plates (representing the flange of beam-column respectively) and an intermediate plate were designed and manufactured, and welded to form a "welded joint plate", as shown in the Fig.2. The uniaxial tensile test was carried out, and the test results were compared with the finite element results to verify the feasibility of the nonlinear modeling method of welded joint plate contact of high strength steel.

The real size was used for modeling in numerical simulation. After setting the constitutive relationship between Q690 high-strength steel and E76 welding rod, three contact pairs were set according to the principle of "surface-to-surface contact", namely, beam and weld, column and weld, weld and intermediate plate. After the constraint was applied at the bottom of the web, concentrated force was applied at the coupling point of its beam flange. The eight-node hexahedral linear reduced integral elements was used for division and simulation. The experimental phenomena and simulation results are shown in the Fig.3.

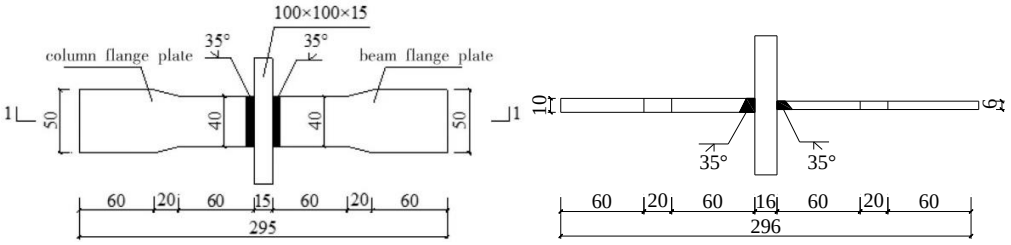

(a) Design drawing of welded joint plate specimen

(b) Welded joint plate specimen

Fig. 2 Welded joint plate

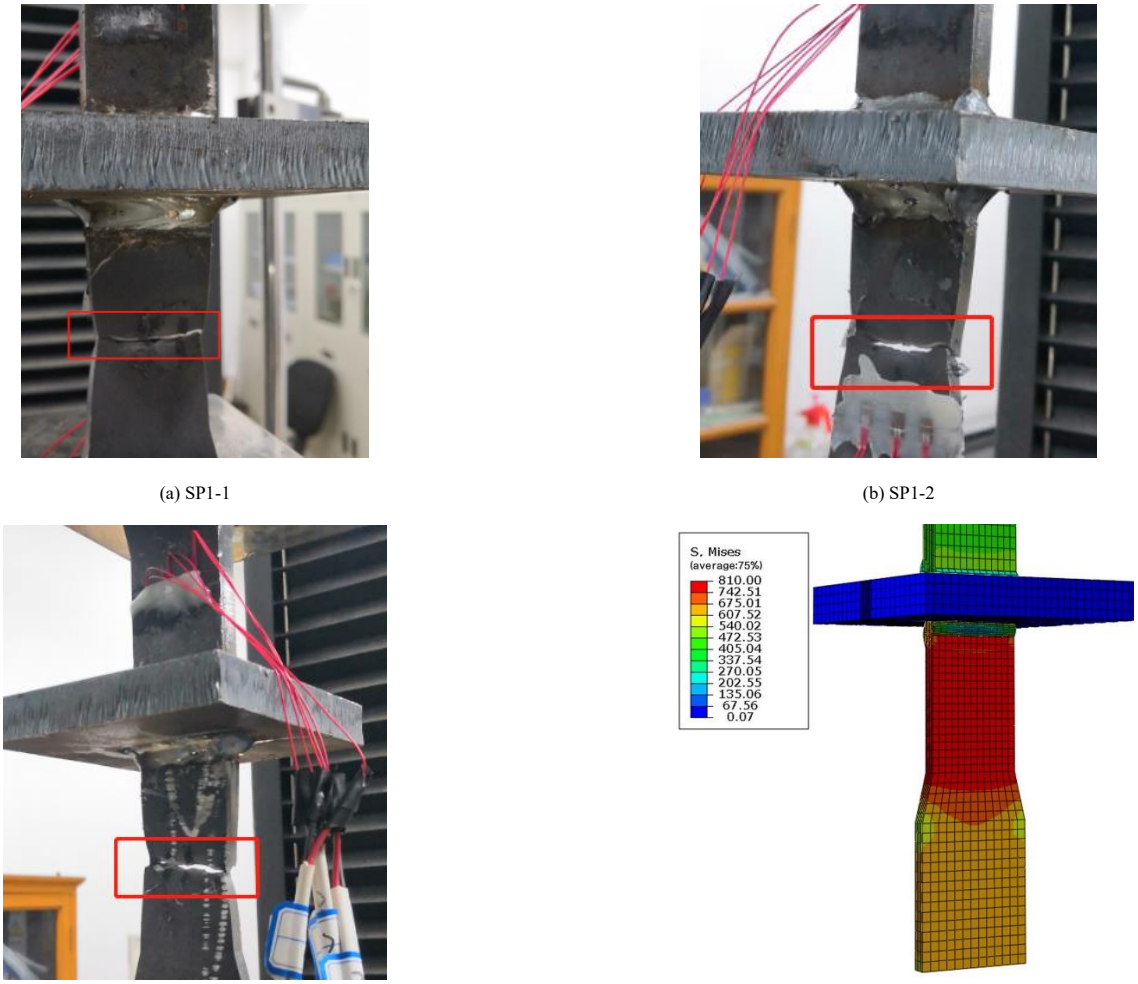

(a) SP1-1 (b) SP1-2

(c) SP1-3 (d) Finite element results

Fig. 3 Comparison of finite element simulation and experimental deformation of specimens under uniaxial tension

When the concentrated force reached 140kN, the three specimens were in the elastic stage and there was no obvious deformation. When the load was 141.63kN, SP1-3 specimen first began to yield, and then SP1-2 specimen and SP1-1 specimen also entered the yield stage. With the increase of load, the cross-sectional area of beam flange tends to decrease, and rust falls off on one side of beam flange, indicating that the steel is about to reach the ultimate bearing capacity at this time. When the load was 168.31kN, SP1-2 specimen broke first, and then SP1-3 specimen and SP1-1 specimen broke at the beam flange about 35mm away from the weld.

As can be seen from Fig.3, the maximum stress in the finite element results also appears at the flange of the beam about 35mm away from the weld, which is roughly the same as the fracture position of the three welded gusset plates in the test, thus indicating the correctness of the finite element simulation results.

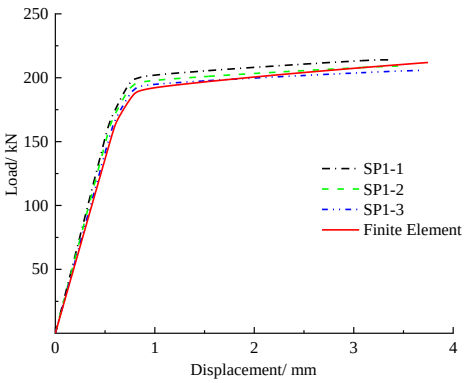

Fig. 4 Load-displacement curve of uniaxial tensile specimen

The trend of load-displacement curve obtained by test and finite element simulation is consistent and basically consistent, as shown in Fig.4. The average values of yield displacement, yield load, ultimate displacement, ultimate load, yield strength, ultimate strength and dissipated energy of the three specimens in the test are all within 5% of the simulated values.

Through the uniaxial tensile test and finite element analysis of welded joint plate specimens of high strength steel, the following conclusions are obtained:

(1) Welded joint plate specimens mostly broke at the flange of beam 35mm away from the weld under the action of uniaxial tensile test, which was similar to the failure mode simulated by finite element method.

(2) The load-displacement curves of test and simulation results under uniaxial tension are basically consistent and the error is small. The feasibility of nonlinear modeling method of welded joint plate contact of high strength steel and the effectiveness of nonlinear finite element analysis are verified, and the above finite element simulation method can continue to be used to study the mechanical properties of reinforced beam-column joints with single rib of high strength steel.

3. Design of beam-column joint specimens

In this study, models were established using Q690D steel and E76 electrode for the high-strength steel ordinary beam-column joint (ORD) and high-strength steel single-rib reinforced beam-column joint (SSR-690). Additionally, the model for the common steel single-rib reinforced beam-column joint (SSR-355) was developed using Q355B steel and J507 welding rod. Subsequently, the common steel single-rib reinforced node (SSR-355) and high-strength steel single-rib reinforced node (SSR-690) are collectively referred to as the single-rib reinforced node (SSR).

Each of the three specimens has a beam length of 1950mm, a beam section size of 300mm×150mm×8mm×13mm, a column height of 2000mm, and a column section size of 300mm×300mm×10mm×15mm. Moreover, the width-to-thickness ratios of the beams and columns comply with the Design Standards for High Strength Steel Structures [17]. The beam-column connections use a

bolt-welding combination, with all bolts being 10.9 M24 high-strength bolts [18].

In summary, the comparison of simulation results from two groups can be observed through finite element analysis: (1) Comparison between the common node and single-rib reinforced node (ORD test piece and SSR test piece); (2)Comparison between ordinary steel single-rib reinforced joints and high-strength steel single-rib reinforced joints (SSR-355 specimens and SSR-690 specimens).

According to the parameter value suggestions of the rib plate given in the US specification FEMA-350 [19] and literature [20], the parameter value of the pseudo-rib plate is $a=210\text{mm}$, $b=120\text{mm}$, $t_s=19.5\text{mm}$, $a'=40\text{mm}$, $b'=25\text{mm}$ as shown in Fig.5.

Fig.6 is a schematic diagram of two T-shaped nodes, sample numbers are shown in Table 2.

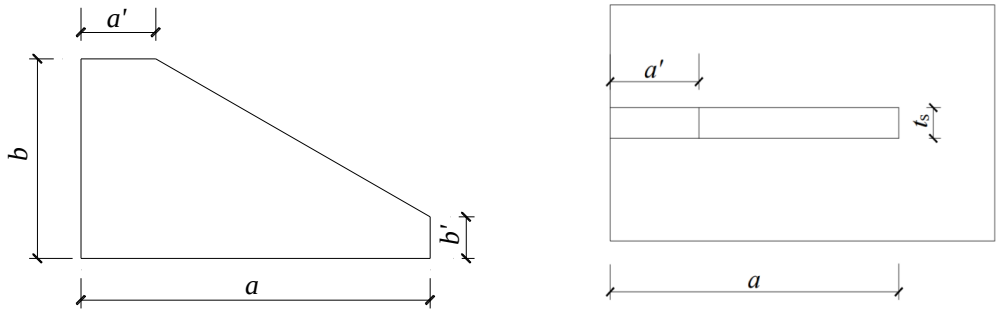

(a) Side view of floor size (b) Top view of floor dimensions

Fig. 5 Dimensional design of the rib

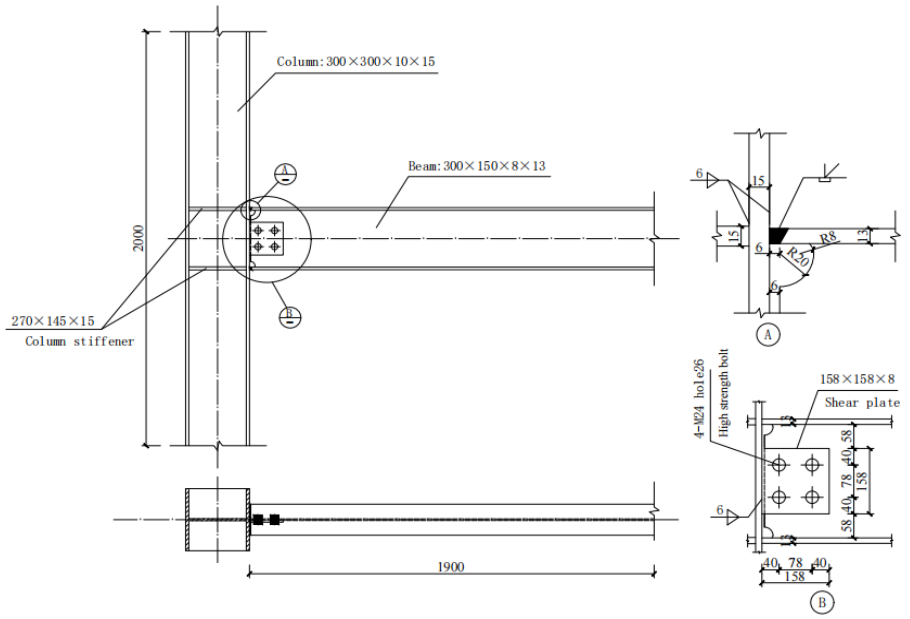

(a) High-strength steel common type joint (ORD specimen)

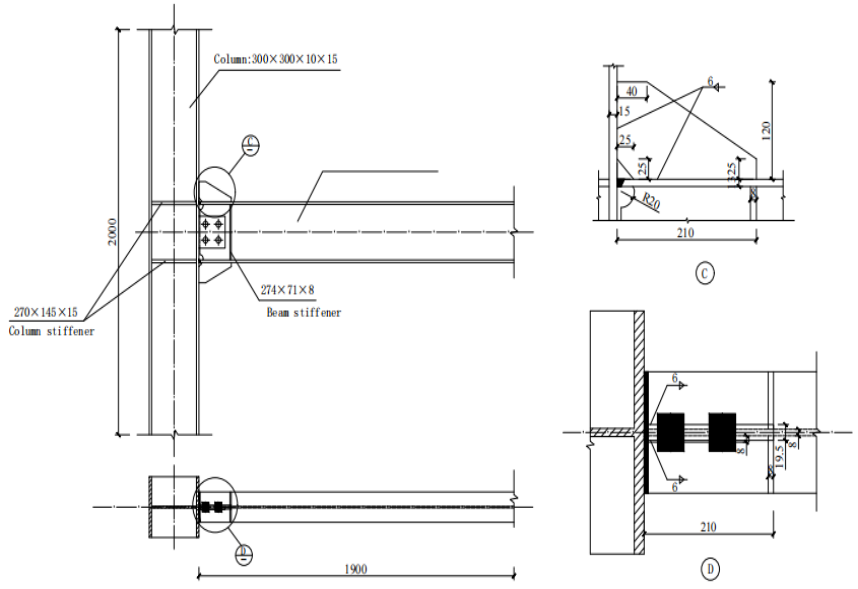

(b) Single rib reinforced joint (SSR specimen)

Fig. 6 Schematic diagram of two T-shaped nodes (unit: mm)

Table 2
Specimen number

Model	Specimen number	Beam section size/mm	Column section size/mm	Rib parameters/mm				
				a	*b*	*a′*	*b′*	t_s
ORD	ORD	300×150×8×13 (Q690D)	300×300×10×15 (Q690D)	/	/	/	/	/
SSR	SSR-355	300×150×8×13 (Q355B)	300×300×10×15 (Q355B)	210	120	40	25	19.5
	SSR-690	300×150×8×13 (Q690D)	300×300×10×15 (Q690D)	210	120	40	25	19.5

4. 3D fine finite element analysis model

4.1. Finite element modeling

All components of the model are discretized into eight-node hexahedral linear reduced integral elements (C3D8R). During the meshing process, an initial global seed layout is implemented with a unit size of approximately 30mm. Following the global distribution, the grid is further refined in key research areas. Specifically, the beam's strengthening end is extended outward by 150mm, the column's strengthening end by 100mm, and the single-rib plate is set to 10mm. The nodal domain area is established as 20mm, the weld as 1mm, and the bolt as 5mm. Additionally, intersections of the column, beam, and single-rib plate are subdivided accordingly.

In non-critical regions, the mesh is diluted, set at intervals of 100mm from 630mm above the column base to 1040mm from the loading end of the beam, as illustrated in Fig.7.

Q690D steel and E76 welding rod were used to establish finite element models for high strength steel ordinary beam-column joint (ORD) and high strength steel single rib reinforced beam-column joint (SSR-690). The material is anisotropic, the density is 7850kg/m^3, the elastic modulus is E_{Q690D}=234.7GPa, and the weld performance is selected according to [1], E_{E76}=206GPa, Poisson's ratio v=0.3. The constitutive relation of Q690D high strength steel and E76 electrode is shown in Fig.8.

Q355B steel and J507 welding rod were used to establish the finite element model of common steel single rib reinforced beam-column joint (SSR-355). Material performance parameters are selected according to [21]. The actual dimensions of all bolts refer to "Large Hexagon Bolts with High Strength for Steel Structures" (GB/T 1228-2006) [22] and are converted into cylindrical shapes and the influence of threads is ignored. 10.9 M24 high strength bolts are selected, and the performance parameters are selected according to [23]. The constitutive relations of Q355B steel and J507 electrode are shown in Fig.9, and the constitutive models of high-strength bolts are shown in Fig.10.

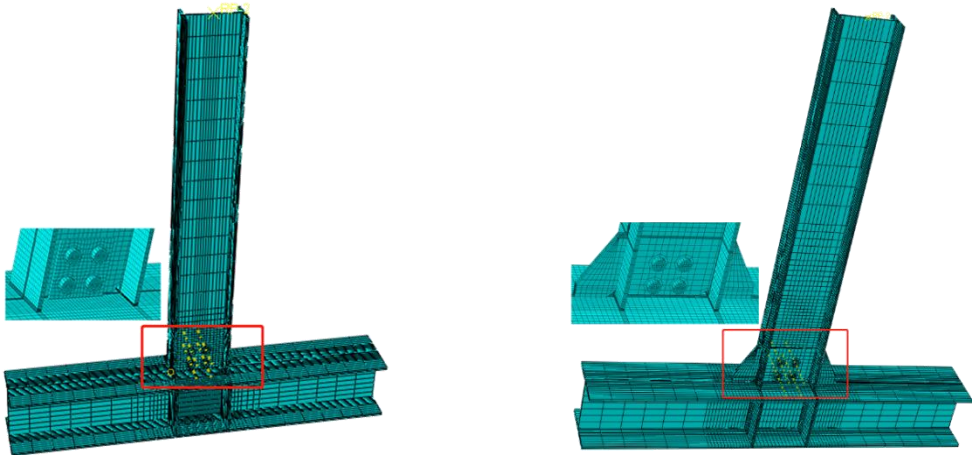

(a) ORD (b) SSR-355, SSR-690

Fig. 7 Schematic diagram of mesh division

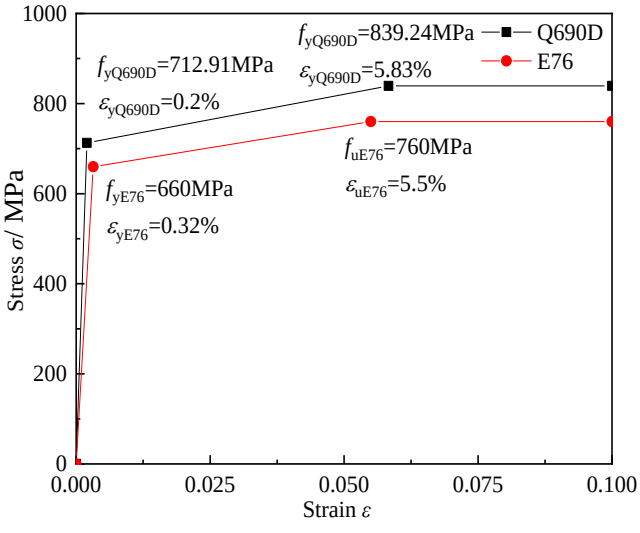

Fig. 8 Constitutive model of Q690D high strength steel and E76 weld

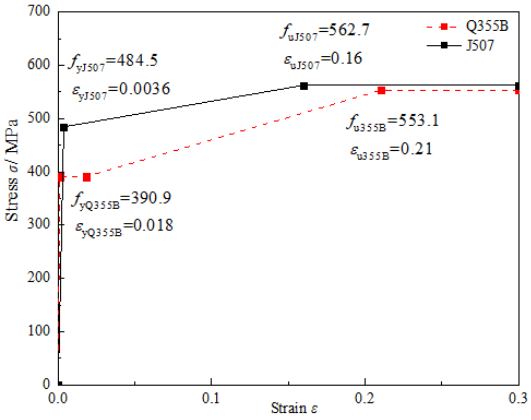

Fig. 9 Constitutive model of Q 355B steel and J507 weld

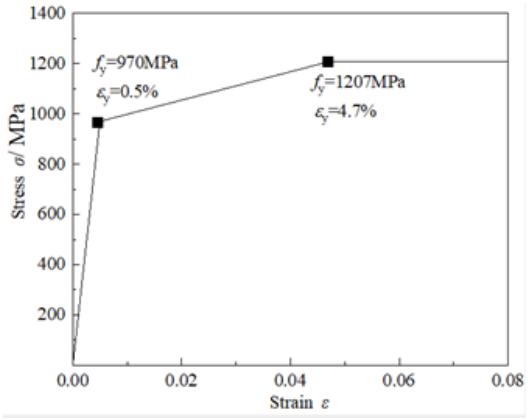

Fig. 10 Bolt constitutive model

4.2. Contact relationship

The components, such as beams, columns, shear plates, bolts, and stiffeners, are assembled into a unified structure, with constraints and contact functions established between the various entities in the interaction module. The reference point RP-2 is coupled to the beam ends through the coupling constraint command.

The binding constraints (ties) in this model include: butt weld connections between plates (between beam flanges and column flanges, horizontal stiffeners in the node domain and column webs, and between column flanges, shear plates, and column flanges), as well as fillet weld connections (between beam flanges and single rib plate, and between column flanges and single rib plate).

Additionally, numerous contact conditions are accounted for in this model, such as plate-to-plate contact (shear plate to beam web contact), plate-to-bolt contact (including contact between shear plate or beam web and bolt head or nut, and contact between the hole wall of the bolt hole and the bolt rod). The friction coefficient in this model is set to 0.5 [17].

The contact interactions in the model are summarized in Table 3, and the component interactions are illustrated in Fig.11.

Table 3
Node Model Contacts

Contact surfaces	Normal	Tangential	Friction coefficient	Quantity	Main side	From side
Shear plate - beam web	hard contact	sliding friction	0.5	1	beam web	Shear plate
Nut-Plate	hard contact	sliding friction	0.5	4	nut	plate
Bolt Head - Plate	hard contact	sliding friction	0.5	4	bolt head	plate
Screw - hole wall	hard contact	/	/	4	screw	hole wall

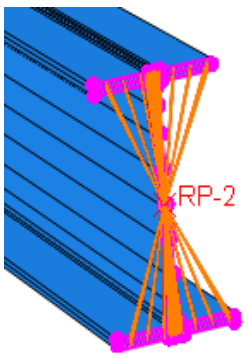

(a) Reference point coupled to beam end section

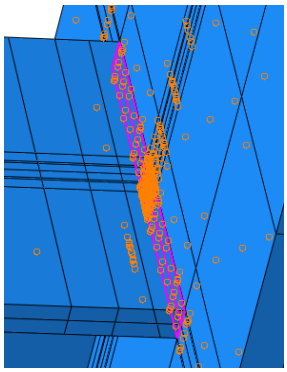

(b) Beam and column binding

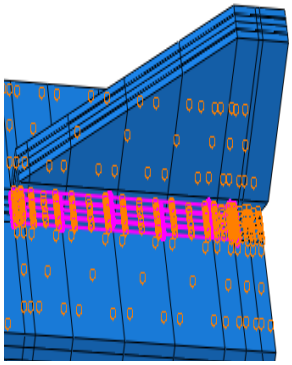

(c) Binding of single rib to beam

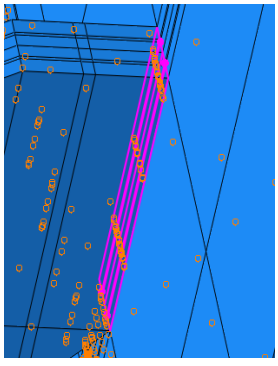

(d) Binding of single rib to column

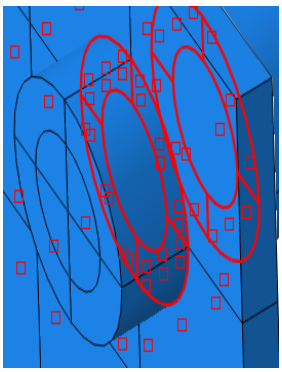

(e) Nut/bolt head in contact with plate surface

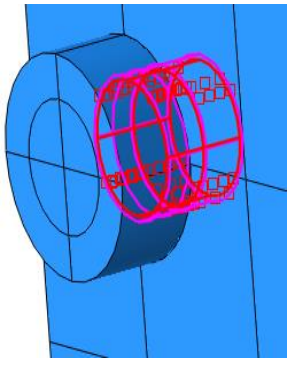

(f) The screw is in contact with the hole wall

Fig. 11 Interaction between components

4.3. Boundary conditions and loading

Based on the specifics of the actual project, the boundary constraints and loads are applied to the specimen, with reference point RP-2 coupled to the beam end through the coupling command.

In the initial analysis step (initial), full fixation is applied to the column top, column bottom, and beam end with U1=U2=U3=UR1=UR2=UR3=0.

For the Step-1 analysis, a pre-tightening force P=225kN is applied to the grade 10.9 M24 high-strength bolt using the "bolt load" command.

Moving to the Step-2 analysis, the method is changed to "fix at current length". Moreover, in this same Step-2 analysis, the "displacement/rotation" command is used to apply displacement along the positive and negative directions of the Z-axis to the reference point of the beam end via the loading system. Consequently, the boundary condition of the beam end is set as U1=UR2=UR3=0.

The model with the applied boundary conditions and loads is depicted in Fig.12.

The loading system refers to the conversion of inter-layer displacement Angle into beam end displacement recommended by ASIC[24], and the model is loaded by beam end displacement. The corresponding parameters are shown in Table 4, and the loading system is shown in Fig.13.

Table 4
Loading grading table

load level	Displacement amplitude/mm	Interlayer displacement angle/rad	Cycles
1	7.313	0.00375	6
2	9.5	0.005	6
3	14.25	0.0075	6
4	19.5	0.01	4
5	29.25	0.015	2
6	39	0.02	2
7	58.5	0.03	2
8	78	0.04	2
9	97.5	0.05	2
10	107.25	0.055	2
11	117	0.06	2

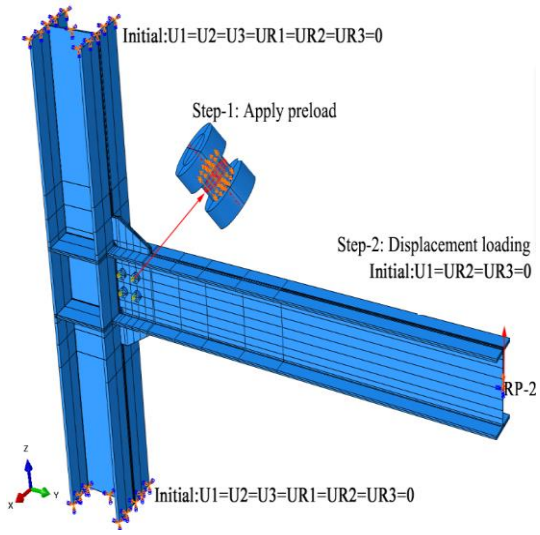

Fig. 12 Schematic diagram of boundary conditions and loading

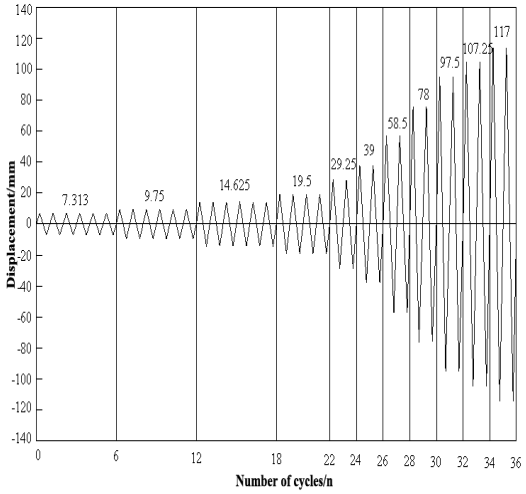

Fig. 13 Loading system

5. Analysis of hysteresis performance results

5.1. Stress cloud and failure pattern

5.1.1. ORD specimen

Fig. 14(a) illustrates that the ORD specimen is in the elastic stage during the fourth loading stage, with notable stress concentrations observed in the joint domain area, bolt, beam flange, and weld seam. Moving to Fig. 14(b), we observe that by the fifth loading stage, the specimen has entered the yield stage. Stress begins to increase in the joint domain, weld, and beam flange, predominantly concentrated in the weld and 45mm away from the column flange in the beam flange. Notably, the stress variations in the beam web, column web, and column horizontal stiffener are less pronounced during both the elastic and plastic stages.

In Fig. 14(c), as loading progresses to the seventh stage, significant stress increases are observed in the joint domain, weld, and beam flange as the specimen reaches its ultimate bearing capacity. Stress on the beam is concentrated primarily in the region 65mm away from the column flange, with stress diffusing from the beam flange to the beam web and column. Concurrently, substantial changes in stress are noted in the beam web, column web, and column horizontal stiffening rib.

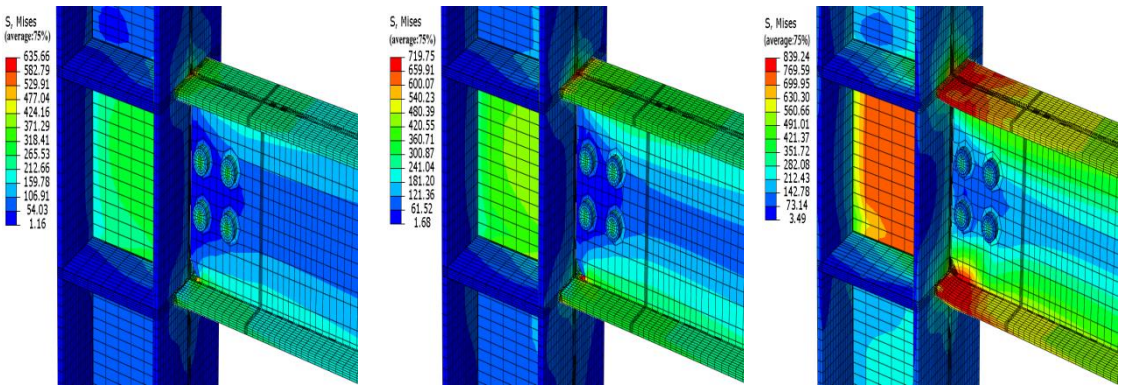

(a) Elastic stage (b) Yield stage (c) Ultimate load

Fig. 14 Stress cloud diagram of ORD specimen

5.1.2. SSR-355 specimen

In Fig. 15(a), it is evident that during the elastic stage of the SSR-355 specimen, significant stress concentrations were observed in the flange, bolt, single rib plate, and node domain, with the largest stress occurring at the bottom of the single rib plate. As the specimen transitioned into the yield stage, stress in the joint domain area, beam flange, and single rib plate began to increase. Stress then evenly diffused from the stiffening end of the rib plate to the column flange. Notable stress variations were observed in the column web and beam web, while the stress changes in the column horizontal stiffening rib were less pronounced, as depicted in Fig. 15(b).

Upon reaching the ninth loading stage, the specimen approached its ultimate bearing capacity. Consequently, stress in the joint domain area increased, and both flanges began to buckle. With continued loading and displacement, the buckling of the flange outside the stiffened end became increasingly apparent, leading to significant stress changes in each component. This highlights the node's effective utilization of the energy dissipation capacity of each component, thereby enhancing the seismic performance of the node, as illustrated in Fig. 15(c).

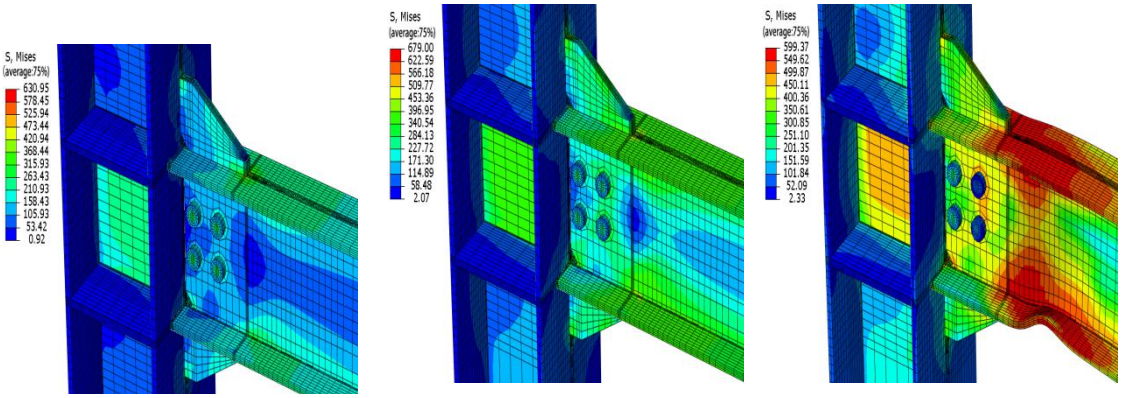

(a) Elastic stage (b) Yield stage (c) Ultimate load

Fig. 15 Stress cloud diagram of SSR-355 specimen

5.1.3. SSR -690 specimen

As depicted in Fig. 16(a), the SSR-690 specimen remained in the elastic stage during the fourth loading stage, with significant stress concentrations observed in the node domain, bolt, beam flange, and single rib plate. The maximum stress was noted at the bottom of the single rib plate end, while the stress at the weld was relatively minimal. Upon loading to the fifth stage, the specimen transitioned into the yield stage, resulting in increasing stress in the joint domain area, beam flange, and single rib plate. Stress uniformly diffused from the strengthening end to the column flange, as illustrated in Fig. 16(b). The stress variations of the web and horizontal stiffener were less pronounced during the elastic and plastic stages.

Upon reaching the ninth loading stage, the specimen approached its ultimate bearing capacity. At this stage, the stress in the joint region notably increased, with the stress on the beam primarily concentrated at the plastic hinge located 150mm away from the strengthening end. Subsequently, the flanges on both sides of the beam began to buckle. As loading continued, the buckling of the flanges became increasingly apparent. At this juncture, the single-ribbed stiffened joints effectively transferred the beam end load to the column flanges. The flanges, in turn, transmitted the force to the web and horizontal stiffeners, fully utilizing the energy dissipation capacity of each component. This enhanced the seismic performance of the joint, as illustrated in Fig. 16(c).

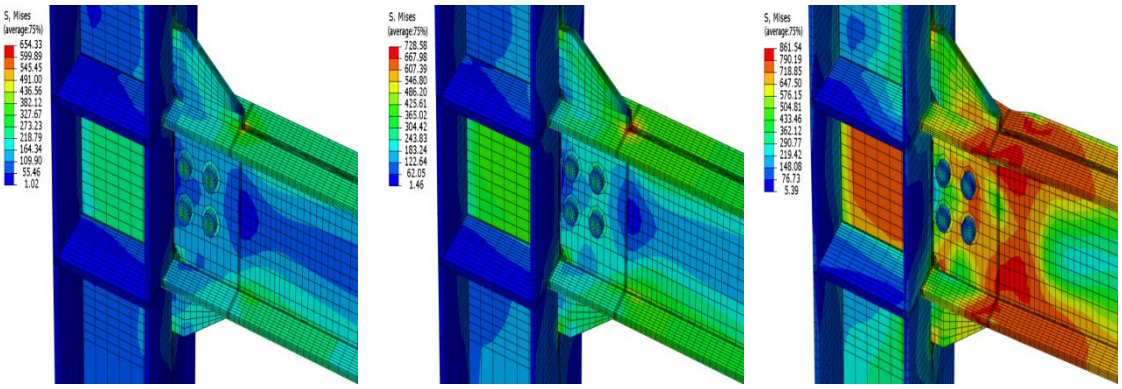

(a) Elastic stage (b) Yield stage (c) Ultimate load

Fig. 16 Stress cloud diagram of SSR-690 specimen

By conducting a comparative analysis of stress distribution maps and failure modes among the three specimens, several conclusions can be drawn. The ORD specimens primarily exhibited significant stress concentrations and damage at the weld and the flange approximately 65mm away from the weld. In contrast to the ordinary joints, the SSR-355 and SSR-690 specimens displayed less noticeable deformation in the weld and heat-affected zone throughout the entire loading process. Damage in these specimens predominantly occurred at the plastic hinge, showcasing a better protection mechanism for the beam-column connection against damage.

From the above numerical results, we can observe that there are significant differences in the failure locations between the ORD specimen and the SSR specimen.

In the ORD specimen, the weld is a critical area. The weld may have inherent defects which can act as stress-raisers and reduce the overall strength of the welded joint. Additionally, the material properties of the weld may not be as favorable as the base material in terms of strength and ductility. The combination of stress concentration and the relatively lower strength of the weld material makes it the most vulnerable location for failure in the ORD specimen.

The SSR specimen, with its single-rib reinforcement, changes the stress distribution pattern. The rib acts as an additional structural element that helps to reduce the stress concentration at the weld area and shifts the stress to other regions. As the load is applied to the SSR specimen, the stress is concentrated in the area where the plastic hinge forms. Eventually, as the plastic deformation accumulates and the material reaches its ultimate deformation capacity, the plastic hinge fails, leading to the overall failure of the SSR specimen.

In summary, the ORD specimen fails at the weld due to the combination of welding-related weaknesses and stress concentration at the weld joint. In contrast, the SSR specimen's single-rib reinforcement changes the stress distribution, leading to the formation and failure of a plastic hinge as the critical failure mode. This difference in failure locations highlights the impact of reinforcement on the structural behavior and failure mechanisms of the specimens.

5.2. Hysteresis curve

Figs. 17(a)-(c) reveal that the hysteresis curves of ORD specimens appear elongated and flat, whereas those of SSR-355 and SSR-690 specimens exhibit a more fusiform and complete shape. The area under the hysteretic curve for SSR-355 and SSR-690 specimens is notably larger compared to that of ORD specimens. This observation suggests that the single rib plate reinforced joints formed plastic hinges outside the strengthened end, thereby enhancing the dissipation of seismic energy and mitigating the risk of brittle failure in the butt weld. Furthermore, as depicted in Fig. 17(d), the ultimate bearing capacity of the SSR-690 specimen surpasses that of the ORD and SSR-355 specimens significantly, indicating the highest bearing capacity among high-strength steel single-rib reinforced joints [25].

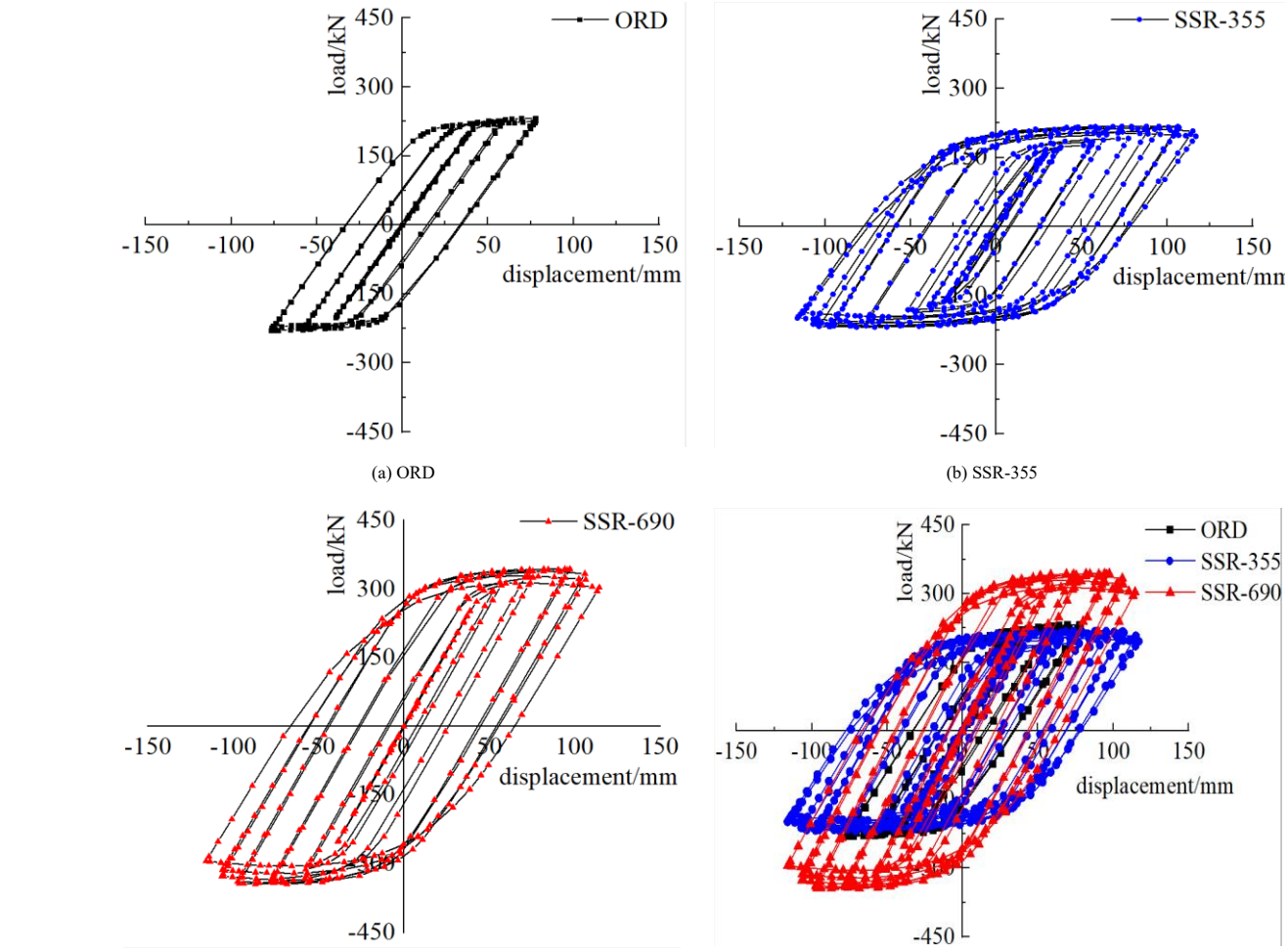

(a) ORD (b) SSR-355

(c) SSR-690 (d) Comparison of hysteresis curves

Fig. 17 Hysteresis curve

5.3. Skeleton Curve

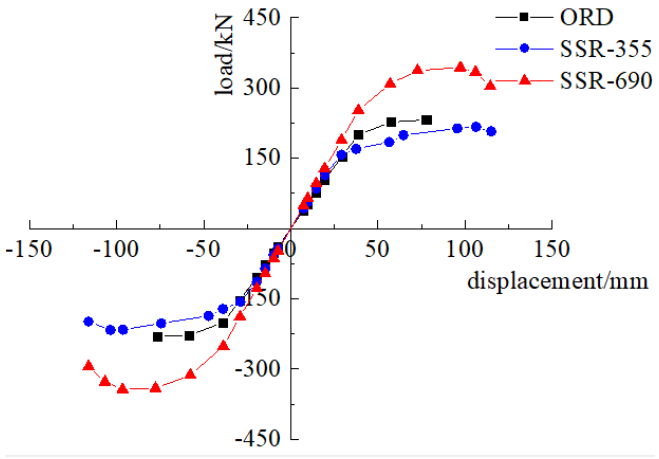

Fig. 18 Skeleton curve

As illustrated in Fig. 18, all three specimens exhibited elastic, yield, and failure stages, indicating the occurrence of plastic deformation in each type of joint. Upon reaching the fourth loading stage, both the ORD specimen and SSR specimen remained in the elastic stage, with the load increasing proportionally to the displacement. Subsequently, when loaded to the fifth stage, all three specimens exhibited a turning point and entered the yield stage. Notably, the ORD specimen reached its ultimate bearing capacity by the seventh loading stage, whereas the SSR specimen achieved its ultimate bearing capacity stage only by the ninth stage, experiencing three additional loading stages compared to the ORD specimen. Throughout each loading stage, the skeleton curve of the SSR-690 specimen consistently enveloped that of the SSR-355 specimen and ORD specimen, underscoring the high bearing capacity of high-strength steel single-rib reinforced joints [26].

5.4. Bearing capacity and ductility properties

Upon reviewing the statistical data presented in Table 5, it becomes apparent that the forward ultimate load of both the ORD and SSR specimens exceeds the negative ultimate load, thus establishing the forward ultimate load as the specimen's ultimate bearing capacity. A comparative analysis reveals that the yield load of the SSR-355 and SSR-690 specimens increased by 2.88% and 23.34%, respectively, in comparison to the ORD specimens. Furthermore, the ultimate displacement exhibited a notable increase of 49.92% and 46.91% for the SSR-355 and SSR-690 specimens, respectively. Particularly, the ultimate load of the SSR-690 specimens showcased a significant surge of 48.16%. Conversely, the ultimate load of the SSR-355 specimen was 6.48% lower than that of the ORD specimen, suggesting that the reinforced single-rib joint enhances the node's deformation capacity, while the node's ultimate bearing capacity can be further enhanced by augmenting the yield strength [27].

In comparison to the SSR-355 specimens, the SSR-690 specimens displayed an increased yield load of 19.89% and an escalated ultimate load of

58.42%. However, there was a marginal decrease of 2.01% in the ultimate displacement. This indicates that high-strength steel single-rib reinforced joints offer an enhancement in the ultimate bearing capacity of joints, albeit with a slight reduction in deformation.

Table 5
Displacement load and ductility coefficient

Specimen	Force direction	Yield displacement (mm)	yield load (kN)	limit displacement (mm)	ultimate load (kN)	Ductility coefficient μ
ORD	just	29.15	152.98	77.97	232.01	2.67
	burden	- 29.13	- 150.64	- 76.83	- 229.82	2.64
SSR-355	just	29.12	157.38	116.90	216.99	4.01
	burden	- 29.01	- 156.42	- 116.11	- 216.81	4.00
SSR-690	just	29.16	188.68	114.54	343.75	3.93
	burden	- 29.21	- 189.39	- 116.05	-343.24	3.97

As indicated in Table 5, the ductility coefficients of ORD specimens, in both positive and negative directions, fall below 3.0. Conversely, the ductility coefficients of SSR-355 and SSR-690 specimens, in both positive and negative directions, exceed 3.0, underscoring the inadequate ductility of ordinary joints and the favorable ductility exhibited by the single-rib reinforced joints. Notably, the ductility coefficients of SSR-355 and SSR-690 specimens surpassed those of ORD specimens by 50.19% and 47.19%, respectively, demonstrating that the reinforced single rib plate facilitates the optimal utilization of joint ductility and ensures its effectiveness. Moreover, the ductility coefficient of SSR-690 specimens exhibited a marginal 2.00% decrease compared to that of SSR-355 specimens, indicating a potential decrease in joint ductility with an increase in yield strength.

5.5. Stiffness degradation

Fig. 19 illustrates the stiffness degradation curves of the three specimens. Upon comparison of these curves, it becomes apparent that, when subjected to the same displacement loading amplitude, the SSR-355 specimen exhibits a notably faster stiffness degradation rate in contrast to the ORD specimen and SSR-690 specimen. This observation suggests that an elevation in the yield strength of steel has the potential to defer the stiffness degradation rate of joints. Moreover, the stiffness degradation rate of the ORD specimen significantly outpaces that of the SSR-690 specimen. This finding underscores that, for high-strength steel beam-column joints, the displacement of the plastic hinge towards the outer regions via a single rib plate can enhance the joint stiffness and delay its degradation, thereby augmenting its seismic resilience.

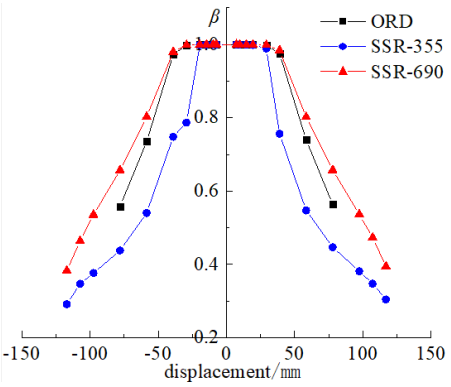

Fig. 19 Comparison of stiffness degradation curves

Based on the above analysis, in comparison with the ORD and SSR-355 joints, the SSR-690 joint exhibits a slower rate of stiffness degradation. Primarily, this is attributable to the fact that the Q690D steel possesses a relatively high yield strength and favorable ductility. Moreover, the geometric configuration of the joint also exerts a non-negligible influence. In contrast to other joints, the single rib plate incorporated in the SSR-690 specimen is capable of augmenting the moment of inertia and section modulus of the joint. This, in turn, facilitates a more efficient distribution of internal forces and mitigates the local stress peaks, thereby contributing to the deceleration of the joint's stiffness degradation. The combination of high-strength materials and the optimized geometric shape endows the SSR-690 joint with enhanced capacity to resist the applied loads.

5.6. Energy consumption capacity

In this study, the equivalent viscous damping coefficient h_e was calculated by energy dissipation coefficient E_h [28]. The energy dissipation calculation diagram is shown in Fig.20. The hysteresis loop in the figure is the last complete hysteresis loop in the load-displacement curve. The calculation formula is as follows:

$$E_h = \frac{S_{ABCD}}{S_{OAE} + S_{OCF}} \tag{1}$$

$$h_e = \frac{1}{2\pi} \cdot E_h \tag{2}$$

where S_{ABCD} is the shaded area in Fig.20, S_{OAE}, S_{OCF} are the areas of triangle OAE and triangle OCF in Fig.20.

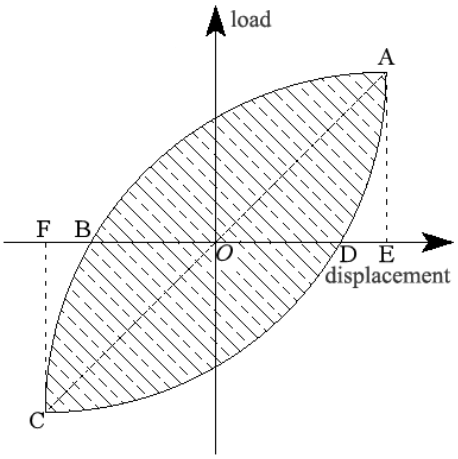

Fig. 20 Calculation diagram of energy dissipation coefficient

Compared with the data in the table, The S_{ABCD} of SSR-355 and SSR-690 specimens increased by 48.52% and 116.41%, respectively, compared with ORD specimens. The sum of the areas of S_{OAE} and S_{OCF} increased by 26.63% and 97.97%, E_h by 17.36% and 9.43%, h_e by 17.30% and 9.48%, respectively. The reason is that all the energy of ORD specimen is absorbed by the weld between the beam and column, while the single rib plate of SSR specimen flexes and absorbs the energy, thus achieving the function of energy dissipation and node protection. It indicates that the reinforced single rib joints have better energy dissipation capacity [29]. Compared with SSR-355, the sum of areas of S_{ABCD}, S_{OAE} and S_{OCF} of SSR-690 specimens increased by 45.71% and 56.34% respectively, while h_e decreased by 6.67%, indicating that energy dissipation capacity decreased slightly with the increase of yield strength.

Table 6
Equivalent Viscous Damping Coefficient h_e

Specimen	S_{ABCD}	$S_{OAE}+S_{OCF}$	E_h	h_e
ORD	46117.27	17383.81	2.65	0.422
SSR-355	68494.32	22013.03	3.11	0.495
SSR-690	99804.17	34415.23	2.90	0.462

6. Conclusions

In this study, ABAQUS finite element analysis was conducted on high-strength steel common joints (ORD specimen), common steel single-rib reinforced joints (SSR-355 specimen), and high-strength steel single-rib reinforced joints (SSR-690 specimen). The study comprehensively investigated the failure modes, hysteretic curves, ductility, load-bearing capacity, stiffness degradation, energy dissipation capacity, and other hysteretic properties of these joints. The following conclusions were drawn from the analysis:

(1) The ORD specimen exhibited severe damage and destruction in the weld and varying degrees of damage in the heat-affected zone. In contrast, SSR-355 and SSR-690 specimens achieved the objective of outward plastic hinge movement through a single rib plate. This resulted in relatively minor deformation at the weld, thereby safeguarding the beam-column butt weld, ultimately leading to buckling failure at the plastic hinge position.

(2) The hysteretic performance indices of SSR specimens demonstrate significant advantages, with the hysteretic area of SSR specimens notably exceeding that of ORD specimens. When compared with ORD specimens, the yield load of SSR-355 and SSR-690 specimens increased by 2.88% and 23.34%, respectively, and the ultimate displacement increased by 49.92% and 46.91%, respectively. Furthermore, the ultimate load of SSR-690 specimens increased by 48.16% compared to ORD specimens.

However, in comparison with ORD specimens, the ultimate load of SSR-355 specimens decreased by 6.48%. Nonetheless, the ductility coefficient increased by 50.19% and 47.19% for SSR-355 and SSR-690 specimens, respectively. Moreover, the initial stiffness increased by 10.42% and 24.62%, and the equivalent viscous damping coefficient he increased by 17.30% and 9.48% for SSR-355 and SSR-690 specimens, respectively. These findings indicate that the single-rib plate stiffened joint can enhance the deformation capacity and initial stiffness of the joint, while also exhibiting improved ductility and energy dissipation capacity.

(3) In comparison with SSR-355 specimens, SSR-690 specimens exhibited an increase of 19.89%, 58.42%, and 12.85% in yield load, ultimate load, and initial stiffness, respectively. The secant stiffness values of SSR-690 specimens surpassed those of SSR-355 specimens. However, there was a decrease of 2.01%, 2.00%, and 6.67% in ultimate displacement, ductility coefficient, and ductility coefficient, respectively. These results indicate that enhancing the steel strength can elevate joint stiffness and decelerate the stiffness degradation rate. However, it also leads to a reduction in energy dissipation capacity and ductility as the yield strength increases.

Acknowledgments

The authors are grateful for the supports of the Opening Fund of State Key Laboratory of Green Building in Western China (No.LSKF202324), and Yangzhou Government-Yangzhou University Cooperative Platform Project for Science and Technology Innovation(No.YZZP202206), and Postgraduate Research & Practice Innovation Program of Jiangsu Province (Yangzhou University) (No.SJCX23_1944).

References

[1] Hu F, Wang Z. Cyclic Behavior of Dual-Steel Beam-to-Column Welded Flange-Bolted Web Connections[J]. Thin-Walled Structures,2024.
[2] Jiang S , Shi G , Zhang N ,et al.Experimental study on seismic behavior of cover-plate connections between steel beams and high strength steel box columns[J].Thin-Walled Structures, 2023, 193.
[3] Jiang J ,Bao W ,Yu Y , et al.Experimental study on crack propagation characteristics of welded high-strength steel Q690CFD joints[J].Journal of Constructional Steel Research,2025,225:109177
[4] ZHENG Hao. Hysteretic performance and parametric analysis of steel frame beam-column joints with replaceable extended-wing T-joints [D]. Jiangsu: Yangzhou University, 2020.
[5] WANG Yan. Seismic Design Theory and application of New Ductile Joints in steel Structure [M]. Beijing: Science Press, 2012.
[6] Ma H.W., Zheng H., Zhang W., et al. Experimental and numerical study of mechanical properties for the double-ribbed reinforced beam-column connection[J]. Advanced Steel Construction, 2020, 4(16): 297-309.
[7] Liang Z ,Shi-Chao G ,Heng L , et al. Experimental and numerical investigation on fatigue behaviors of Q690D butt welds[J].Journal of Constructional Steel Research,2023,211
[8] Shuai L ,Zhiqiang W ,Huan L , et al. Optimization of welding parameters on welding distortion and stress in S690 high-strength steel thin-plate structures[J].Journal of Materials Research and Technology,2023,25382-397.
[9] Jordao S., Da S. L. S., Simoes R. Design formulation analysis for high strength steel welded beam-to-column connections[J]. Engineering Structures, 2014, 70: 63-81.
[10] Guo H ,Zheng D ,Zhang J , et al. Experimental study on the seismic performance of angle connected high-strength steel moment resisting beam-column joint[J].Journal of Constructional Steel Research,2024,222108940-108940.
[11] Hongchao G ,Xizhe Z ,Wei L, et al. Experimental and numerical study on seismic performance of Q690 high-strength steel plate reinforced joints[J].Thin-Walled Structures,2021,161
[12] Lu Linfeng, Yan Ji, Yu Haojie. Finite element analysis on the seismic behavior of the new ribs reinforced connection for minor-axis of I-section column [J]. Steel Construction,2016,31(09):1-6.
[13] Wang Lu, Wang Wuxing, Tang Hongchun. Research on hysteretic behavior of single-rib-reinforced steel moment connections in steel frame [J]. Steel Construction,2019,34(01):7-14.
[14] Yang Tao, Wang Yan. Research on Mechanical Properties of Stiffened Joint Domain of Steel Frame Rib Plate. Steel Structure, 2015, 30(02): 1-6+44.
[15] GB/T 2975-2018. Steel and steel products -- sampling location and sample preparation for mechanical properties test [S]. Beijing: China Architecture and Architecture Press, 2018.
[16] CEN, ENV1993-1-8 Eurocode 3: Design of Steel Structures, Part 1.8: Design of connections[S]. European Committee for Standardization.2015.
[17] JGJ/T 483-2020. High strength Steel structure Design Standard [S]. Beijing: China Architecture and Architecture Press, 2020.
[18] WANG Yan. Seismic Performance Design Theory and application of New Ductile Joints in steel structure [M]. Beijing: Science Press, 2012.
[19] FEMA-350. Recommended Seismic Design Criteria for New Steel Moment-Frame Buildings[S]. Washington D. C.: Federal Emergency Management Agency, 2000
[20] ZHAO Ying. Analysis of hysteretic behavior and fracture behavior of beam-column joints with symmetric double-ribbed reinforced steel frames [D]. Jiangsu: Yangzhou University, 2019.
[21] Zhang W. Y., Zeng L. J. Experimental investigation and low-cycle fatigue life prediction of welded Q355B steel[J]. Journal of Constructional Steel Research, 2021, 178: 106497.
[22] GB/T 1228-2006. High strength bolts with large hexagon head for steel structure [S]. Beijing: China Planning Press, 2006.
[23] Qi Jingxuan. Study on seismic behavior of high-strength steel beam-to-column end-plate connections[D]. Shaanxi: Xi 'an University of Technology, 2017.
[24] AISC. Seismic Provisions for Structural Steel Buildings[S]. Chicago: American Institute of Steel Construction, 2016.
[25] Farooghi M. S. M. R., Ghobadi M. S. Seismic performance of retrofitted WFP connections joined to box column using ribs[J]. Journal of Constructional Steel Research, 2017, 137: 297-310.
[26] Wang K., Lu X. F., Yuan S. F., et al. Analysis on hysteretic behavior of composite frames with concrete-encased CFST columns[J]. Journal of Constructional Steel Research, 2017, 135: 176-186.
[27] Ma Hongwei, Lyu Dianmei, ZHAO Ying, et al. Seismic behavior of the symmetrical double-ribbed reinforced beam-column connections of steel frames[J]. Journal of Yangzhou University (Natural Science Edition), 2020, 23(01): 59-67.
[28] Ma Hongwei, ZHAO Ying, Wang Zijian, et al. Hysteretic behaviour analysis of new beam-column connections with expanded flange of steel frame[J]. Journal of Yangzhou University (Natural Science Edition), 2018, 21(1): 50-55.
[29] Song Q. Y., Heidarpour A., Zhao X. L., et al. Performance of flange-welded/web-bolted steel I-beam to hollow tubular column connections under seismic load[J]. Thin Wall Struct, 2017, 116: 250-264.

Advanced Steel Construction – Vol. 21 No. 2 (2025) 147–156
DOI:10.18057/IJASC.2025.21.2.6

STUDY ON SELF-VIBRATION CHARACTERISTICS AND SEISMIC RESPONSE OF LARGE-OPENING DRUM-HONEYCOMB-TYPE QUAD-STRUT SUSPEND- DOME STRUCTURE

Hong-Wei Tu [1], Hui Lv [1, 2, *], Shi-Lin Dong [2, 3], Zhong-Yi Zhu [4] and Lian Shao [1]

[1] *College of Civil Engineering and Architecture, Nanchang Hangkong University, Nanchang 330063, China*
[2] *Space Structures Research Center, Zhejiang University, Hangzhou 310058, China*
[3] *Zhejiang Provincial Key Laboratory of Space Structures, Zhejiang University,Hangzhou 310058, China*
[4] *Beijing Institute of Architectural Design, Beijing 100045, China*
** (Corresponding author: E-mail: lvhui@nchu.edu.com)*

ABSTRACT

The large-opening drum-honeycomb-type quad-strut suspend-dome structure is a new type of suspend-dome structure, which was improved from the traditional cable dome structure. It replaces the top chord of the cable dome with seamless steel pipes. The structure combines the characteristics of the suspend-dome and the cable dome. The bottom chord nodes connects four struts, two inclined cables and one ring cable. The Ansys finite element model is established to analyze the influence of initial prestress, rise-span ratio, thickness-span ratio, opening span and bottom chord arrangement schemes on the natural vibration characteristics of the structure, and three seismic waves are selected to analyze the seismic response of the structure. The results show that the 1-50 order natural frequency range of the structure is 1.038-19.796, the stiffness of the outer ring is stronger than that of the inner ring, the horizontal stiffness is stronger than the vertical stiffness, and the overall stiffness of the structure is good. The initial prestress, thickness-span ratio and opening span have great influence on the self-vibration frequency, while the rise-span ratio and the bottom chord arrangement schemes have the least influence. The seismic response analysis shows that the peak values of vertical nodes displacement are -44.75mm, -47.40mm and -45.27 mm, respectively, which are far less than the allowable deflection limit, the peak internal force coefficients of the members are 1.82%, 6.53% and 7.49%, respectively, and the variation range is within the allowable range, The large-opening drum-honeycomb-type quad-strut suspend-dome structure has good structural stiffness, and the strength of the inner ring members should be appropriately strengthened to resist the dynamic effects such as earthquake.

ARTICLE HISTORY

Received: 7 August 2024
Revised: 24 December 2024
Accepted: 1 January 2025

KEYWORDS

Building structure;
Large-opening drum-honeycomb-type quad-strut suspend-dome;
Finite element analysis;
Self-vibration characteristics;
Seismic response

1. Introduction

As an important branch in the field of construction, large-span space structures benefit from the extensive use of prestressing technology. Suspend-dome structure is an important member of long-span string structure system, which is mainly composed of rigid top-chord reticulated shell, flexible bottom-chord high-strength cable and intermediate brace connection, which combines the structural characteristics of a single-layer mesh shell and a cable dome, and possesses the advantages of low cost, beautiful modeling, high structural rigidity, and low construction difficulty[1]. At the end of the last century, the Japanese scholar Kawaguchi put forward the new space structure system of Suspend-dome[2], which was introduced into China at the beginning of this century, and has been widely used in various types of large-scale public venues in China. For example, the badminton gymnasium for 2008 Olympic Games[3], Guiyang Olympic sport center[4], Zhangjiajie Circus City main stadium with suspended substructure suspend-dome structure[5]. In recent years, with the continuous development and advancement of suspend-dome, more and more complex structural forms have been put forward and applied in practical projects, such as Tianjin University of Traditional Chinese Medicine stadium project[6], conjoined suspend dome structure of Zhaoqing New District stadium[7], and loop-free suspend-dome after removal cables [8].

The difference between the traditional cable dome structure and the suspend-dome structure is that it is a flexible structure, and when the structure is subjected to large loads, the top chord spine cable is prone to slacken and quit working, resulting in a decline in the stiffness of the structure, excessive displacement and other phenomena. And because of its use of flexible cable material, it is difficult to control the accuracy of tensioning construction, and the construction is more difficult. Scholars at home and abroad have been carrying out research on the perfection and improvement of this kind of structure.

In 2005, academician Dong Shilin's team[9]proposed Kiewitt cable dome and hybrid new dome based on the advantages and disadvantages of the existing cable dome forms, and comprehensively considered the structural topology and mechanical characteristics. The prestress level was theoretically calculated using the overall feasible prestress theory. This example can provide theoretical support for the improvement of the cable dome structure. In 2010 , Dong Shilin's team[10] proposed a spatial structural form combining the top chord single-layer mesh shell and the bottom flexible cable structure, which developed the stress characteristics of the cable dome structure and reduced the difficulty of laying panels at the later stage of construction, and applied the method to sunflower-type, rib-ring-type, and Kiewitt-type cable domes. In 2017, Zhang Ailin[11] improved the traditional ridge-rod ring-braced cable dome structure, replaced all the flexible cables of the top reticulated shell with rigid rods, and proposed a new type of ridge-rod ring-braced cable dome. The static and parameter analysis was carried out, which solved the shortcomings of the traditional cable dome structure, such as the relaxation of the top chord cable under compression and the large number of inclined cables, and enriched the selection of the cable dome structure.In 2019, Sun Guojun[12] proposed a rigid support dome on the basis of the cable dome, replacing all the cables in the bottom part of the original cable dome with rigid tie rods, which solved the problem of difficult construction positioning of the prototype structure. The self-vibration characteristics test was carried out to study the feasibility of the dome.

The above scholars' research on the cable dome and suspend-dome structure has made up for the lack of such space structures in China, and enriched the selection and program of space structures. Based on the above scholars' attempts and researches on this kind of space structure, this paper proposes a large-opening drum-honeycomb-type quad-strut suspend-dome structure, which was based on the improvement of the traditional cable dome with the same topological configuration[13], which possesses stronger structural stiffness and deformation resistance, and is able to solve the some of the intrinsic deficiencies of the cable dome structure, according to which, large-opening drum-honeycomb-type quad-strut suspend-dome structure is established, and an Ansys finite element model is developed to study the structure under load. Accordingly, the Ansys finite element model is established, and the self-vibration characteristics under the load state and the influence of its structural parameters on the self-vibration frequency of the structure are studied, as well as the seismic response, to explore the feasibility of the large-opening drum-honeycomb-type quad-strut suspend-dome structure, and to help improve the theoretical basis of the new structural system.

2. large-opening drum-honeycomb-type quad-strut suspend-dome structure

2.1. Finite element modeling

The plan and section of the large-opening drum-honeycomb-type quad-strut suspend-dome structure are shown in Fig.1 and Fig2. The overall structure

consists of top chord mesh shell and bottom chord, with the top chord mesh shell mainly divided into ridge rods (JG) and ring rods (HG), and the bottom chord mainly divided into struts (CG), ring cable (HS), and inclined cables (XS). As can be seen from Fig.1, the bottom chord nodes are located below the hexagonal honeycomb grid, and each bottom chord node connects a total of four struts and two inclined cables, and passes through one ring cable.

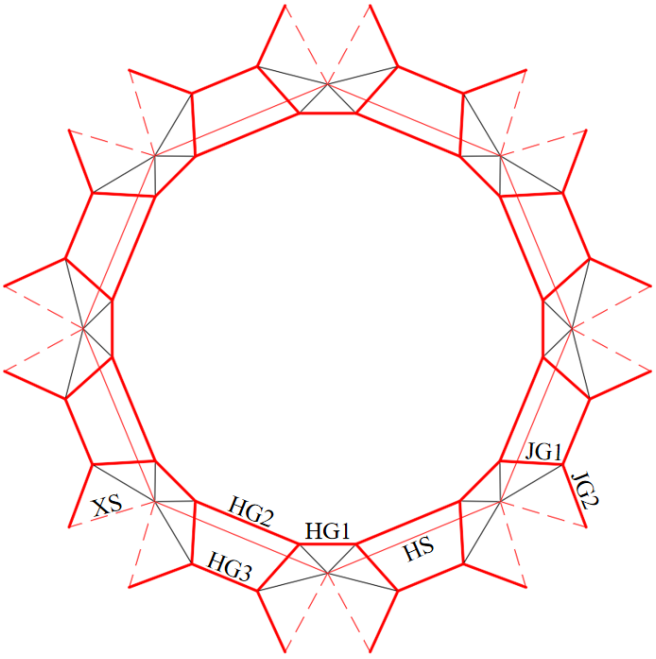

Fig. 1 Planar gragh

The arrangement of the bottom chord nodes is shown in Fig.2, where *L* is the span, *h* is the thickness of the mesh shell, *f* is the sagittal height of the mesh shell, 1a, 1b and 2a are the top chord nodes of the structure, and 1' is the bottom chord node.

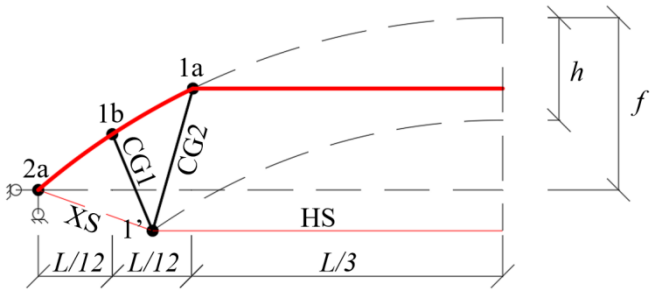

Fig. 2 Sectional graph

2.2. Finite element modeling

Ansys finite element software is applied to analyze the self-vibration characteristics and dynamic time history analysis of the large-opening drum-honeycomb-type quad-strut suspend-dome structure, and to investigate the mechanical response analysis of the model under the loading condition. The span of the large-opening drum-honeycomb-type quad-strut suspend-dome structure is set to be 120m, the ring equivalent fraction is 16, the rise-span ratio and the thick-span ratio are taken as 0.10, the sagittal height is 12m, and the opening diameter is 80m. The ridge rod, ring rods and struts are all made of Q235B seamless steel pipes, with yield strength of 234 Mpa and modulus of elasticity of 2.06×105 Mpa, and the inclined cable and ring cable are made of high-strength stranded wires, with tensile strength of 1,270 Mpa and modulus of elasticity of 1.90×105 Mpa.The cross-section dimensions of the selected members and the length-to-slender ratio are in line with the specification requirements.

The peripheral support of the structure adopts the fixed hinge support, and Link180 unit is applied to simulate the top chord and bottom chord respectively, and the Keyopt function of Ansys finite element software is used to set up the tensile and compressive members, only tensile members and only compressive members. In the subsequent analysis of self-vibration characteristics, it is necessary to apply load to the structure, in which the constant load is 0.5kN/m^2 and the live load is 0.6kN/m^2. Specify the analysis type as dynamic analysis, and turn on the large deformation effect and stress stiffening. The bottom chord cable system is an active tension system, while the top chord mesh shell is a passive tension system, so only the initial prestress of the bottom chord cable system needs to be determined, and then the prestress distribution of the top chord mesh shell can be obtained. The initial prestress distribution of the bottom chord cables can be calculated according to the calculation method used in the literature of [14]，[15]and[16], In this paper, the concept of overall feasible prestress is used to calculate the initial prestress value of various components. For the suspend-dome structure, it is necessary to find the general prestress state X, find a set of *a*, so that the prestress of the same set of components is equal, and the prestress modal combination can correctly obtain the initial prestress. Let *X* be the overall feasible prestress mode. according to the balance equations of each node, the initial prestress values of various components are obtained,

$$T_1 + T_2\alpha_2 + ... + T_s\alpha_s = X \tag{1}$$

In Eq. (1), *a* is 1 and *X* is the unit feasible prestress. For the structure with n component types, it can be written as :

$$X = \{x_1 x_2 x_3 \ ... \ x_i x_i x_i \ ... \ x_n x_n x_n\}^{\mathrm{T}} \tag{2}$$

Let x_i be the *i*-class component, then (2) can be organized as follows :

$$T_1\alpha_1 + T_2\alpha_2 + ... + T_s\alpha_s - X = 0 \tag{3}$$

Briefly :

$$\tilde{T}\,\tilde{\alpha} = 0 \tag{4}$$

Of which :

$$\tilde{T} = [T_1 T_2 \ ... \ T_i \ ... \ T_s - e_1 - e_2 \ ... - e_n] \tag{5}$$

In Eq. (5), T_i is the independent self-stress mode, the base vector e_i is the *i*-type member, the struts axial force is -1 (the cable axial force is +1), and the axial force of the remaining members is 0. The unknown number $\tilde{\alpha}$ is :

$$\tilde{\alpha} = \{\alpha_1 \alpha_2 \ ... \ \alpha_s x_1 x_2 \ ... \ x_n\}^{\mathrm{T}} \tag{6}$$

The singular value decomposition of $\tilde{T}$ can be obtained :

$$\tilde{T} = USV^{\mathrm{T}} \tag{7}$$

In Eq. (7), *U* and *V* are the left and right singular vector matrices of $\tilde{T}$, respectively, and *S* is the singular value matrix. Suppose the rank of *T* is r, then the r+1 column to s+n column vector in the right singular vector matrix *V* is the solution of $\tilde{\alpha}$, and the initial prestress corresponding to each group of components is the value of r+1 column to s+n column in $\tilde{\alpha}$. So far, the overall feasible prestress of the structure can be obtained. The initial prestress value of the large-opening honeycomb quad-strut suspend-dome structure is shown in Table 1.

Table 1
Component Names and Specifications

Name of members	Section size (m^2)	Prestress (kN)
JG1	0.0217	4394
JG2	0.0274	5547
CG1	0.0184	-1266
CG2	0.0159	-845
HG1	0.0487	9854
HG2	0.0372	7134
HG3	0.0235	4752
XS	0.0123	4351
HS	0.0282	10000

The numerical analysis model is generated, as shown in Fig.3.

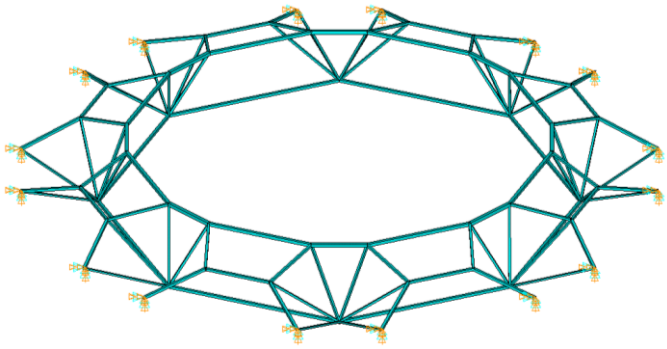

Fig. 3 Ansys Model

3. Structural self-vibration characterization

3.1. Self-vibration properties

Taking the structural parameters described in the previous section as an example, 1 times constant load and 0.5 times live load are applied to the structure, and the self-vibration frequency and vibration pattern diagrams of the large-opening drum-honeycomb-type quad-strut suspend-dome structure are observed through the self-vibration modal analysis of the structure in the first 50th order, which is shown in Fig.4. The self-vibration frequency of the structure in the 1st-50th order ranges from 1.04 to 19.79, and the self-vibration frequency is high, and the self-vibration frequency in the 1st-16th, 23rd-29th, and 44th-48th orders rises slowly, and the self-vibration frequency in the three stages rises in a stepwise manner, and the low-order self-vibration frequency rises slowly and is distributed relatively densely, while the self-vibration frequency of the high-order rises larger and is distributed more sparsely. From the topological configuration of the structure, the structure is centrosymmetric, so the self-vibration frequencies basically appear in pairs.

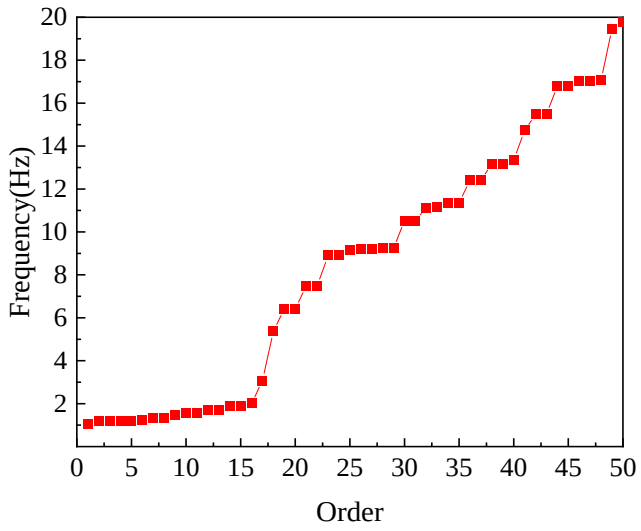

Fig. 4 Structural self-vibration frequency

Mass participation coefficient is also an important parameter in structural dynamics analysis, which is mainly used to measure the degree of mass participation in natural vibration in each direction of each mode. As shown in Fig 5, the mass participation coefficient of the structure in the ROTZ direction is the largest in the 0-6 order vibration. After the 6th order, the mass participation coefficients in the ROTX and ROTY directions are also greatly improved. After the 16th order, the mass participation coefficients in the Z, X and Y directions have been greatly improved. When the 50th order is reached, the cumulative mass participation coefficients in all directions reach 1. It can be seen that the ROTX, ROTY and ROTZ directions are the most involved in the natural vibration, followed by the Z direction.

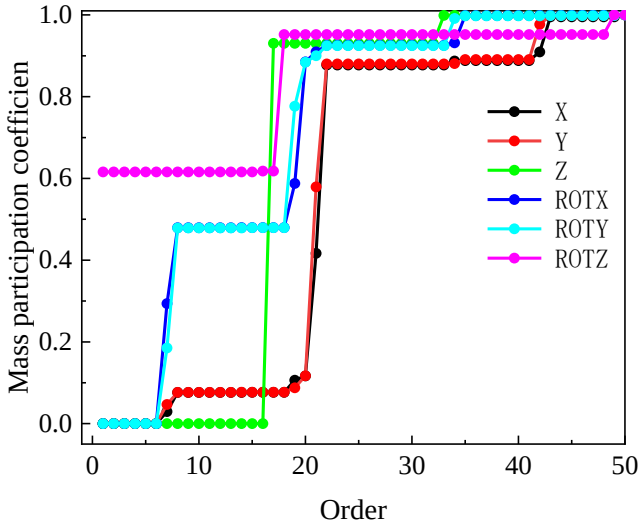

Fig. 5 Mass participation coefficien

In the structural vibration pattern in Fig.6, the 1st order vibration pattern is mainly for the horizontal torsion of the inner and outer ring rod, and the vertical displacement is small; the 2nd and 3rd order vibration pattern is for the structural symmetry of the 4 places of the ring rod vertical staggered vibration, and the structural torsion did not occur; the 4th and 5th order vibration pattern is for the structural symmetry of the vertical staggered vibration of the two places, and the structural torsion did not occur; the 6th order vibration pattern is for the inner circle of the ring rod of every grid staggered vibration is mainly up and down; The 7th and 8th order vibration patterns are symmetrical two-point vertical torsion. The 9th order vibration mode is dominated by the adjacent 1b node staggered vertical vibration; the 10th order vibration mode is the structure symmetrical four-point 1b node vertical vibration. It can be concluded that the deformation points of the low-order vibration mode are mainly distributed near the inner ring bar, and the deformation points are gradually transferred to the outer ring as the order rises. As far as the large-opening drum-honeycomb-type quad-strut suspend-dome structure is concerned, the stiffness of the inner ring is lower than that of the outer ring, the vertical stiffness is weaker than that of the horizontal stiffness, and the overall stiffness of the structure is better.

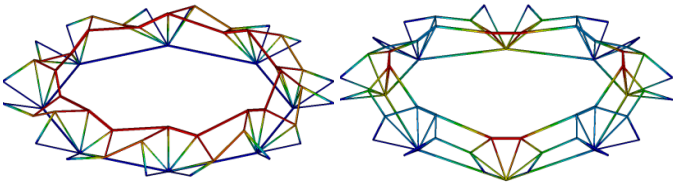

（a）1st（1.0376）　（b）2 and 3th（1.1728）

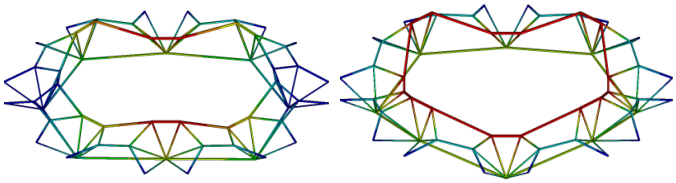

（b）4 and 5th（1.2073）　（d）6th（1.2304）

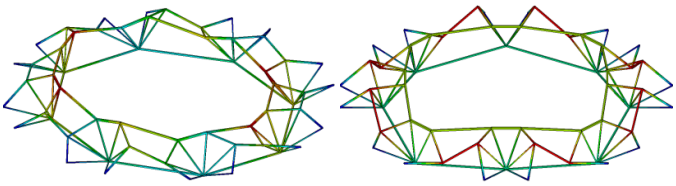

（e）7 and 8th（1.3546）　（f）9th（1.4804）

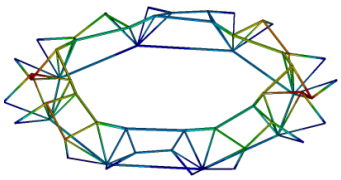

（g）10th（1.5451）

Fig. 6 Structural vibration pattern

3.2. parametric analysis

The large-opening drum-honeycomb-type quad-strut suspend-dome structure has a variety of structural parameters such as initial prestress, rise-span ratio, thickness-span ratio, opening diameter, and bottom chord arrangement. For this kind of large-span spatial steel structure, its structural parameters have a certain degree of influence on the structural performance. Therefore, in order to further investigate the structural performance of the large-opening drum-honeycomb-type quad-strut suspend-dome structure, it is necessary to conduct parametric analyses of the structure to investigate the degree of influence of each type of parameter on the structural self-vibration characteristics. The following parametric analyses were performed under the loading conditions in the previous section.

3.2.1. Initial prestress

The initial prestress of the large-opening drum-honeycomb-type quad-strut suspend-dome structure is set to be 1P, and the structural self-vibration frequency of the structure is investigated at prestress levels of 0.5-3.0P in steps of 0.5P. With other parameters kept constant, it can be concluded from Fig.7 that under the six initial prestress conditions, all six curves show the same upward trend, and the curves have no obvious difference in the frequency in the 1-17th order, and the frequency is kept at a lower level with a slower upward trend; in the 18th-19th order the curves have an obvious upward trend, and they start to show an obvious dispersion in the 18th order up to the 50th order, and then in the 20th- 50th order, the curves basically show the same rate of increase, and at the same order, the self-vibration frequency of 0.5-3.0P increases sequentially. Under the same conditions, the structural stiffness rises with the increase of prestress level.

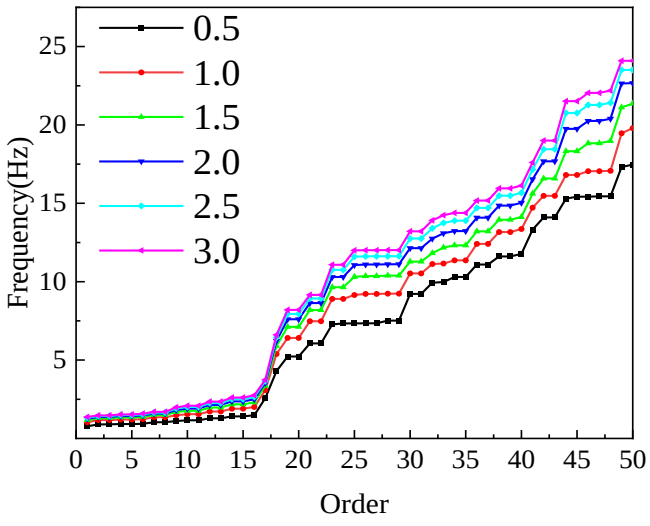

Fig. 7 Prestress level

3.2.2. Rise-span ratio

The rise-span ratio is the ratio of structural sagittal height to span, which is an important parameter of space structure. According to the structural characteristics of the large-opening drum-honeycomb-type quad-strut suspend-dome structure, the rise-span ratio can be categorized into 0.4-0.16, which can be derived from Fig.8, where the distribution of the curves is more intensive and the overall difference is smaller. In order 1-17, the curves have basically the same upward trend and the trend is slower; in the interval of order 18-21, the curves basically overlap and the upward trend is faster; in the interval of order 22-30 the curves are obviously dispersed, and the rise-span ratio is the lowest in order 0.16-0.14, the highest in order 0.06-0.08, and the rest are in the middle; in the interval of order 31-40 the curves enter into overlap, and then they are gradually dispersed after order 41 . It is concluded that the effect of structural rise-span ratio on structural self-vibration characteristics is insignificant.

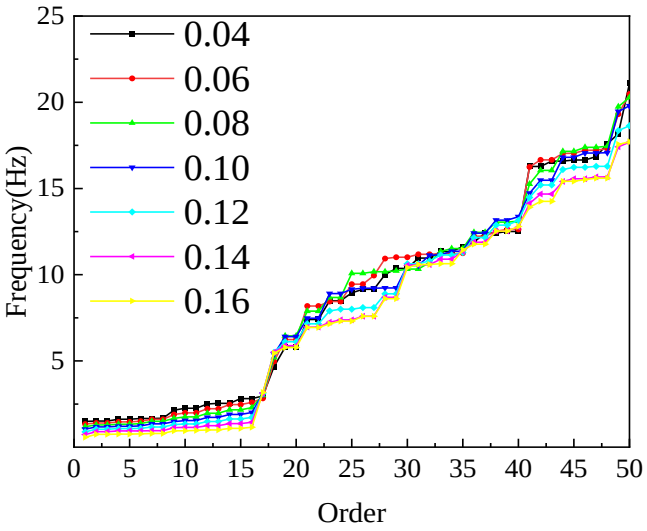

Fig. 8 Rise-span ratio

3.2.3. Thickness-to-span ratio

The thickness-to-span ratio is the ratio of the thickness of the structure to the span, and in the large-opening drum-honeycomb-type quad-strut suspend-dome structure, the thickness-to-span ratio will be between 0.06-0.16. From Fig.9, it can be concluded that there is no much difference between the curves in the 1-17 order interval; the curves are scattered obviously after that, and their frequencies gradually increase with the thickness-to-span ratio of 0.06-0.12, and only individual dispersion occurs with the thickness-to-span ratio of 0.14-0.16, with the frequency of the size of the structure being basically the same. From this, the influence of the structure's thickness-to-span ratio on the self-vibration characteristics is the most obvious.

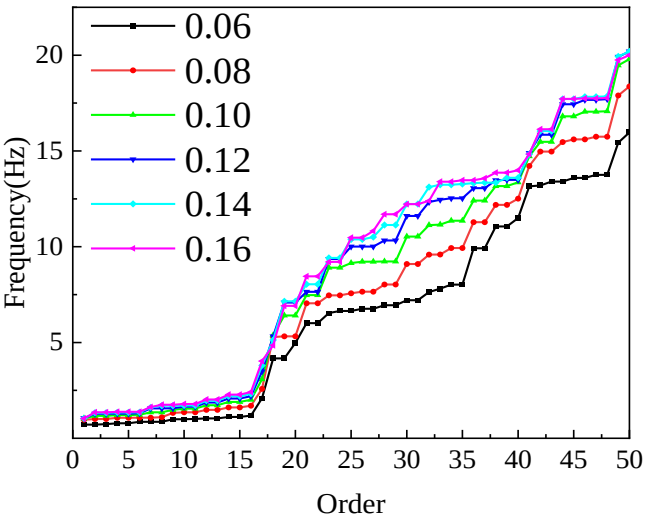

Fig. 9 Thickness-span ratio

3.2.4. Opening diameter

Since this type of suspend-dome structure has a large opening, the span of the opening is also an important morphology parameter, and within the allowable range of the opening size of this type of suspend-dome structure, the diameter of the opening of 60-100m is taken as a parameter to be analyzed. From Fig.10, it can be concluded that the curves show the trend of dispersion from the beginning, and in the interval of order 1-17, the curves rise slowly, and then rise faster, and the curves do not overlap significantly during the whole period, and from the overall pattern, the self-vibration frequency basically increases with the expansion of the structural diameter of the openings.

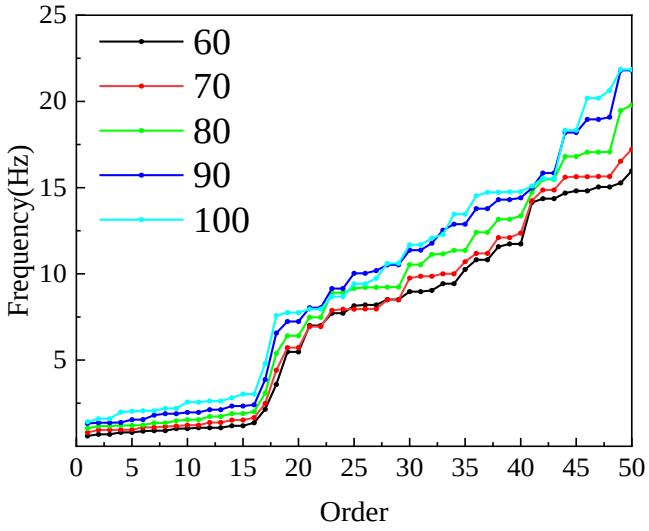

Fig. 10 Opening diameter

3.2.5. Bottom chord arrangement schemes

The large-opening honeycomb quad-strut suspend-dome structure has three bottom chord arrangement schemes, that is, the distance between the bottom chord node and the center of the structure. The distance gradually increases with the scheme 1-3, and the angle between the struts (CG) and the horizontal plane also decreases. From Fig.11, it can be concluded that the curves of the three bottom chord arrangement schemes do not show obvious dispersion and are basically in the same trend, with individual small dispersion only in the middle section and the rear end, but it can still be seen that there are minor differences in the bottom chord arrangement schemes. It is concluded that its bottom chord arrangement schemes has the least influence on the self-vibration characteristics of the structure.

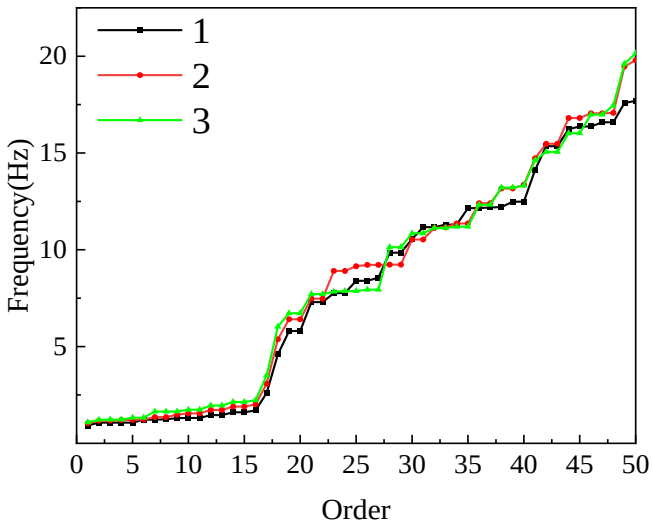

Fig. 11 Bottom chord arrangement schemes

Taken together, the magnitude of the influence of each parameter on the self-vibration frequency of the structure can be classified as thickness-to-span ratio > prestress level > opening diameter > rise-span ratio > bottom chord arrangement schemes.

4. Structural seismic response analysis

The large-opening drum-honeycomb-type quad-strut suspend-dome structure is a tension system consisting of an top single-layer mesh shell and bottom ring cables. As a new type of suspend-dome structure improved from the traditional cable dome structure, and therefore it is necessary to perform seismic response analysis. In this section, the structure with parameters of prestress level 1P, rise-span ratio 0.10, thickness-span ratio 0.10, opening diameter 80m and bottom chord arrangement scheme 2 is analyzed.

4.1. Seismic wave selection

In this section, the seismic time-course analysis is carried out for the large-opening drum-honeycomb-type quad-strut suspend-dome structure, and according to the GB50011-2010 "Code for Seismic Design of Buildings" 5.1.2[17], the structure should be selected with at least two actual recorded seismic waves and one artificially generated by the simulation when the seismic response analysis is carried out.

The seismic effects is related to the spatial location and the structure itself, the seismic conditions in this paper in accordance with the Areas with seismic fortification intensity of level 8 for calculation, the maximum ground acceleration of 70cm/s^2. and according to the provisions of JGJ7-2010 "Technical Specification for Space Frame Structures" 4.4.10[18], the value of the damping ratio is selected as 0.02, as well as the first and second order of the self-vibration frequency for the calculation of the Rayleigh damping coefficient. In this paper, the classical EI-Centro seismic wave, Tianjin Ninghe seismic wave and an artificial seismic wave are selected for seismic response simulation, and the original seismic wave is shown in Fig.12 to Fig.14, in which the peak acceleration of the EI-Centro seismic wave is 341.7 cm/s^2, the peak acceleration of the Tianjin Ninghe seismic wave is 145.8 cm/s^2, and the peak acceleration of the artificial seismic wave is 817 cm/s^2. The duration of all three seismic wave inputs is 20s.

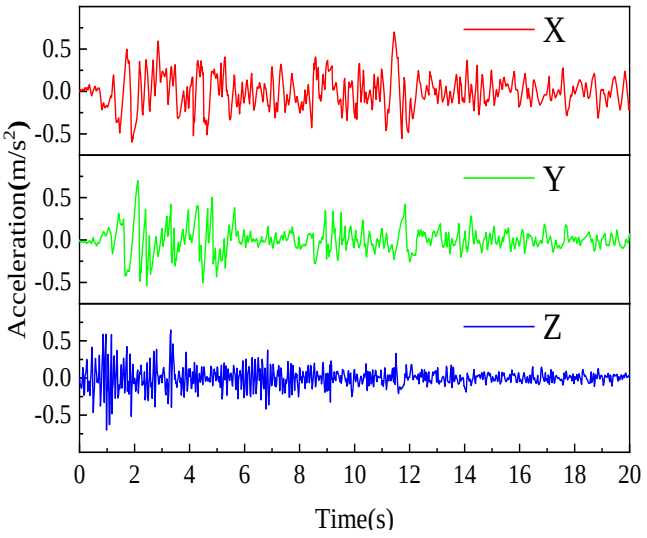

Fig. 12 EI-Centro seismic wave

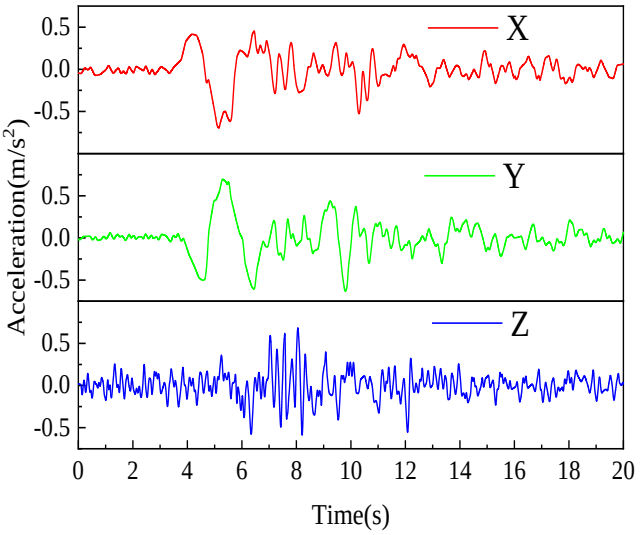

Fig. 13 Tianjin Ninghe seismic wave

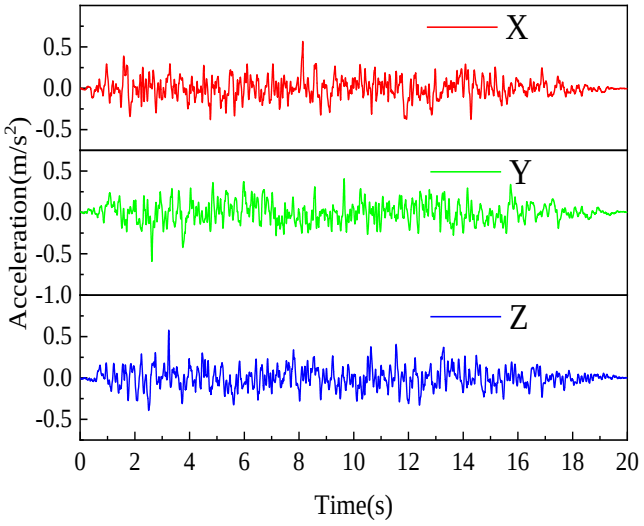

Fig. 14 Artificial seismic wave

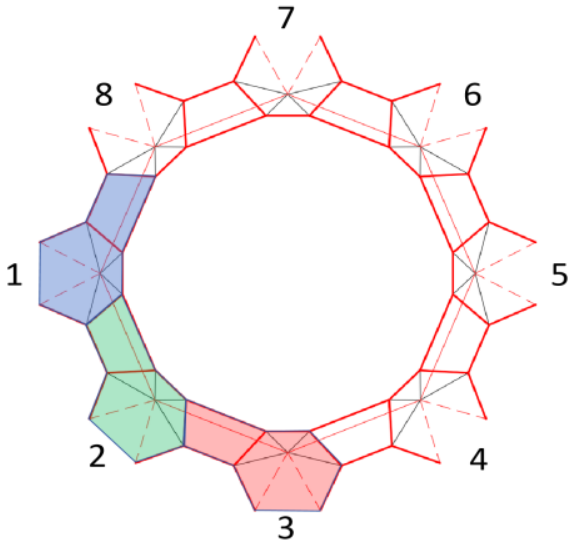

Fig. 15 Sub-structures

When conducting seismic time-course analysis on structures, The original seismic wave cannot be directly used for calculation, the amplitude should be adjusted according to equation (1). And the three seismic waves are three-way seismic waves, the peak acceleration before input should be adjusted according to the requirements of the specification, the X direction, the Y direction and the Z direction in accordance with the ratio of 1:0.85:0.65.

$$A'(t) = (A'_{max}/A_{max})A(t) \tag{8}$$

In Eq.(8). $A'(t)$ *is* the seismic time-course curve. A'_{max} is the peak acceleration of the curve. which is the peak acceleration of a magnitude 8 multiple-occurrence earthquake selected in the code. $A(t)$ is the original seismic time-course curve. A_{max} is the peak acceleration of the original time-curve of the earthquake.

The large-opening drum-honeycomb-type quad-strut suspend-dome structure is divided into 8 sub-structures, and its sub-structures are schematically shown in Fig.15. For space limitation reasons, specific sub-structures will be selected for analysis in the seismic response analysis in this chapter.

4.2. Structural displacement response

For space limitation reasons, in this section, the analysis is based on EI-Centro seismic wave response and nodes 1a, 1b and 1' of the first, second and third sub-structure are selected for displacement analysis. From Fig.16, it can be concluded that among the three nodes in each sub-structure, the displacement in the Z direction is the largest, followed by the X direction and the Y direction is the smallest, indicating that the seismic action has less effect on the structure in the X and Y directions, and due to the effect of the structure's self-weight, the initial displacement in the Z direction of the three nodes is larger, and the curve patterns in the three directions are basically similar to those of the EI-Centro seismic acceleration curves.

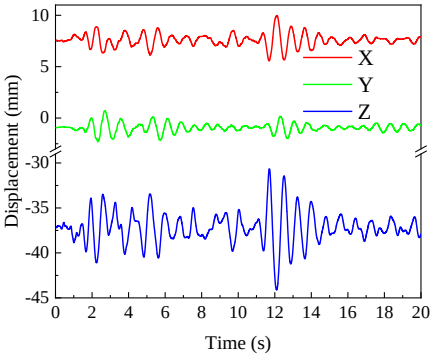

（a）The 1a of first sub-structure

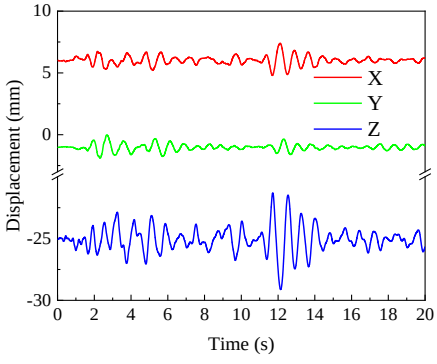

（b）The 1b of first sub-structure

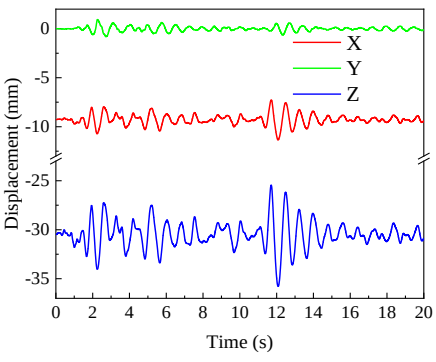

（c）The 1’ of first sub-structure

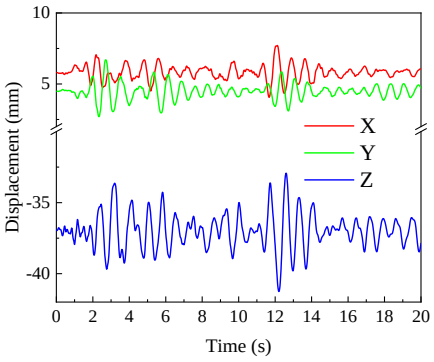

（d）The 1a of second sub-structure

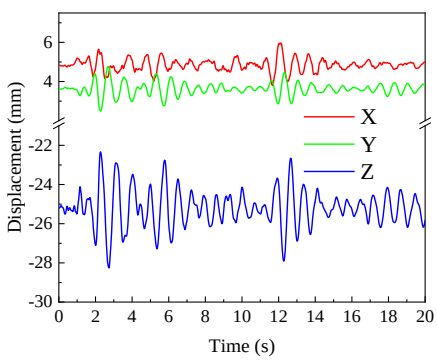

（e）The 1b of second sub-structure

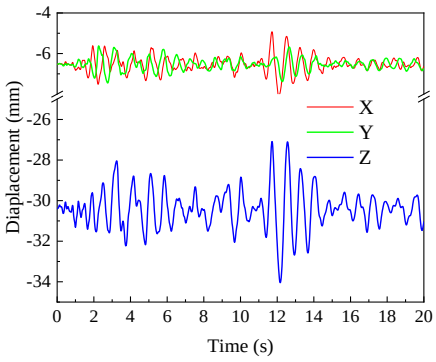

（f）The 1’ of second sub-structure

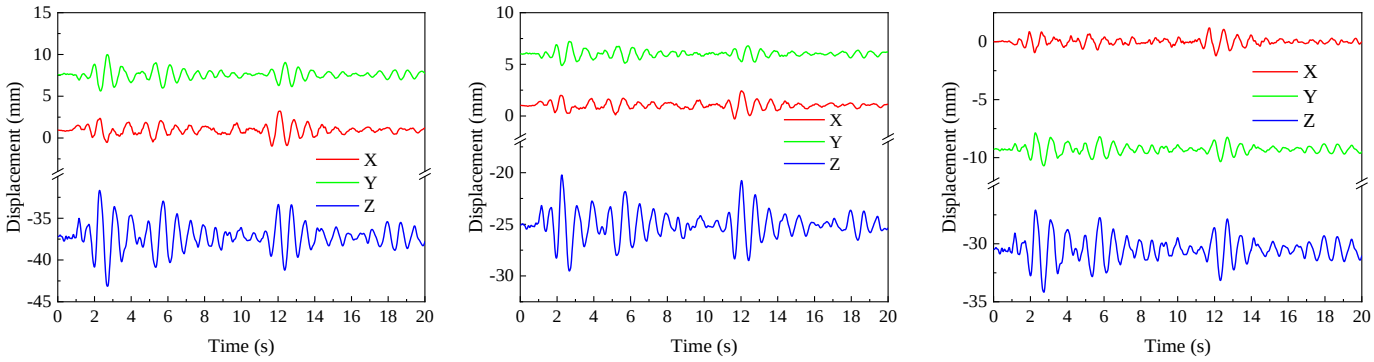

（g）The 1a of third sub-structure （h）The 1b of third sub-structure （i）The 1’ of third sub-structure

Fig. 16 Nodal displacement time-course curves under EI-Centro seismic waves

Table 2
Vertical displacement of nodes

Seismic waves	Nodes	Maximum displacement (mm)	Time (s)
EI-Centro seismic wave	1a	-44.75	12.06
	1b	-30.58	12.06
	1’	-35.79	12.08
Tianjin Ninghe seismic wave	1a	-47.40	0.44
	1b	-32.82	0.44
	1’	-38.09	0.44
Artificial seismic wave	1a	-45.27	20.00
	1b	-31.26	20.00
	1’	-36.52	20.00

The peak displacement of the nodes in the X and Z directions of the first substructure appears at about 12s, and the peak displacement of the nodes in the Y direction appears at about 2.5s. The initial displacement in the X direction has a certain offset, and the absolute value is between 5-10 mm. The initial displacement in the Y direction is small, basically around 0. The peak time of node displacement in the X and Y directions of the second substructure is similar to that of the first substructure, and the initial displacement is offset, the offset of the two is similar, while the peak displacement of the 1b node in the Z direction is advanced to about 2.5s. The peak time of node displacement in X and Y directions of the third substructure is similar to that of the first substructure. The initial displacement offset of the X direction node is small, which is basically around 0. The initial displacement offset of the Y direction node is large, and the peak displacement of the three nodes in the Z direction is advanced to about 2.5 s. It can be concluded that under the action of earthquake, the substructures in the symmetry axis direction represented by 1-3 substructures produce uneven deformation, and the displacement response time of different substructures in the Z direction is also different. Under the action of horizontal seismic waves, the displacement in the X and Y directions is small, showing that the bottom chord quad-strut form of the large-opening honeycomb quad-strut suspend-dome structure has better lateral stiffness.

In Tab.2, under the action of each seismic wave, the peak Z direction nodal displacements are -44.75mm, -47.40mm and -45.27mm, which are much smaller than the permissible deflection limit of *Lc* / 300 specified in the GB50017-2017 "Standard for Design of Steel Structures" [19], which is 133.3 mm, and *Lc* is the total overhanging span.

4.3. Structural deformation response

The structural deformation reflects the stiffness change of the structure under seismic action. Fig.17 to Fig.19 shows the structural deformation of the structure under the action of each seismic wave, in Ansys the deformation is set as a displacement vector sum, which is the vector sum of X, Y and Z directions. As the structure under seismic action in the Z direction displacement is larger, the remaining two directions displacement is smaller, in Fig.19 can be seen, the three deformation diagrams to vertical displacement is dominated, and are biased to one side, the pattern is basically the same, the maximum deformation were 46.24mm, 48.95mm and 46.68mm. It shows that the structure has basically the same ability to resist vertical deformation under the action of three seismic waves, and shows good structural stiffness.

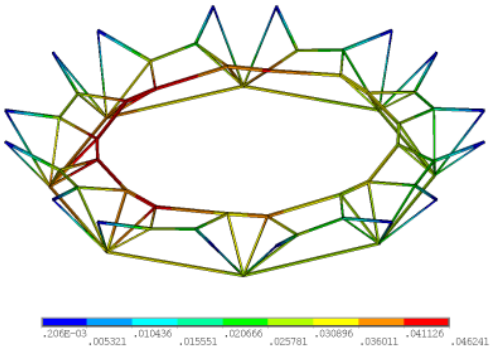

Fig. 17 EI-Centro seismic wave

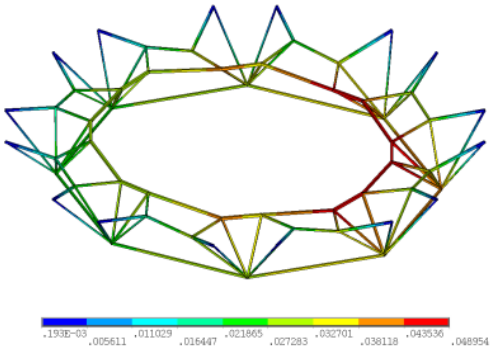

Fig. 18 Tianjin Ninghe seismic wave

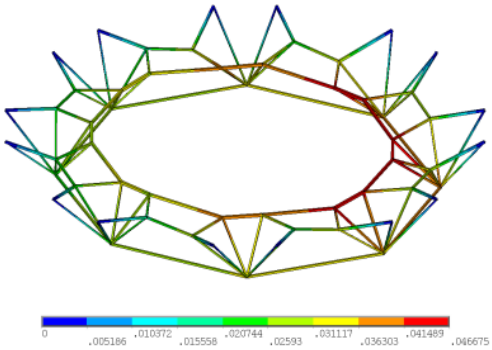

Fig. 19 Artificial seismic wave

4.4. Structural internal force response

In this section, the analysis is still based on the EI-Centro seismic wave response, and Fig.20 shows the various types of members in the first sub-structure, and Tab.3 shows the maximum internal force coefficients of the various types of rods and their rate of change under the three seismic waves. As shown in Fig.20, the time-course curves of the internal forces of the ridge rods and the ring rods are zigzag and dense, while those of the gusset rods, diagonal ropes, and ring cables are sparse, and the top chord mesh shell is a horizontal member, so it can be seen that the top chord mesh shell is more sensitive to seismic effects, while the struts, as a vertical member, have the second highest sensitivity to seismic effects, and the inclined cable and the ring cables, as a flexible material, are the least sensitive to seismic effects. Due to the effect of structural self-weight, the internal force of ridge rod and ring rod decreased compared to the initial prestress of the structure, while the struts, inclined cables and ring cables increased.

As shown in Tab.3, the peak coefficients of the internal forces of the members under the three seismic waves are 1.82%, 6.53%, and 7.49%, respectively, and their variations are within the allowable range. In the ridge rods, the peak internal force of JG1 is smaller than that of JG2; in the struts, the peak internal force of CG1 is smaller than that of CG2; in the ring rods, the peak internal forces of HG1 and HG2 are smaller than that of HG3; and the peak internal force of the ring cables is smaller than that of the inclined cables, so it can be seen that the closer the structure is to the inner circle of the members, the more obvious it is subjected to seismic effects. In the design of this type of structure, attention should be paid to the appropriate strengthening of the inner ring members to resist seismic effects.

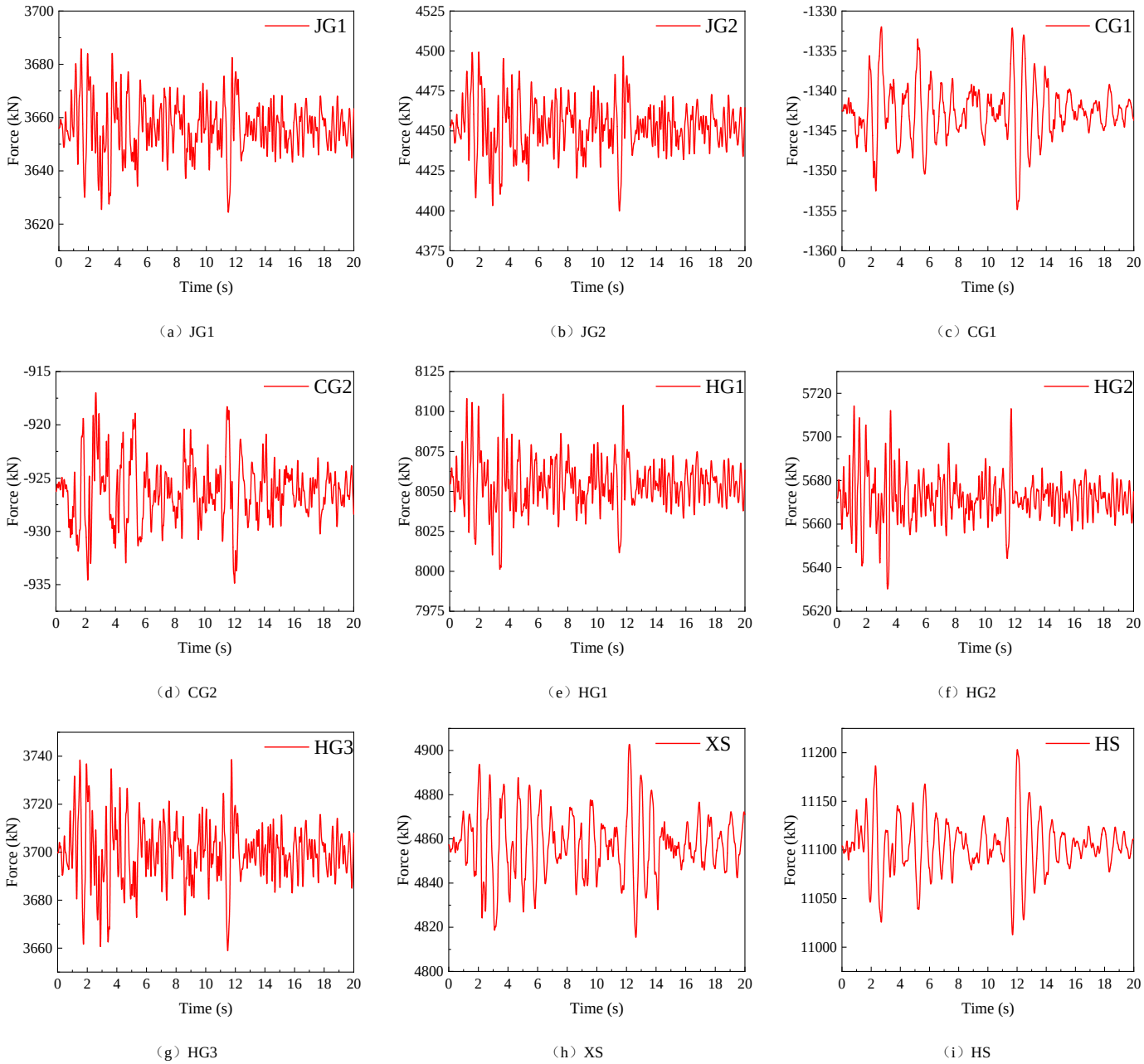

Fig. 20 Time-course curves of internal forces in members under EI-Centro seismic waves

Table 3
Internal force coefficients of members

Seismic waves	Members	Initial internal force coefficients	Maximum internal force coefficients	Rate of change
EI-Centro seismic wave	JG1	1.00	1.0085	0.85%
	JG2	1.00	1.0114	1.14%
	CG1	1.00	1.0100	1.00%
	CG2	1.00	1.0113	1.13%

	HG1	1.00	1.0072	0.72%
	HG2	1.00	1.0078	0.78%
	HG3	1.00	1.0112	1.12%
	XS	1.00	1.0182	1.82%
	HS	1.00	1.0090	0.90%
	JG1	1.00	1.0506	5.06%
	JG2	1.00	1.0647	6.47%
	CG1	1.00	1.0186	1.86%
	CG2	1.00	1.0653	6.53%
Tianjin Ninghe seismic wave	HG1	1.00	1.0324	3.24%
	HG2	1.00	1.0255	2.55%
	HG3	1.00	1.0595	5.95%
	XS	1.00	1.0249	2.49%
	HS	1.00	1.0126	1.26%
	JG1	1.00	1.0572	5.72%
	JG2	1.00	1.0732	7.32%
	CG1	1.00	1.0223	2.23%
	CG2	1.00	1.0749	7.49%
Artificial seismic wave	HG1	1.00	1.0360	3.60%
	HG2	1.00	1.0335	3.35%
	HG3	1.00	1.0671	6.71%
	XS	1.00	1.0298	2.98%
	HS	1.00	1.0098	0.98%

Note: The initial internal force coefficient for each member is 1.00, and the maximum internal force coefficient is equal to the ratio of the maximum internal force to the initial internal force

5. Conclusions

This paper applies the method of finite element analysis to investigate the self-vibration characteristics of the large-opening drum-honeycomb-type quad-strut suspend-dome structure proposed in this paper in the loading state with the effects of its structural parameters on the self-vibration frequency of the structure, as well as the seismic response, and the following conclusions are drawn through the comparative analyses:

(1) Under the condition of applying 1 times of constant load and 0.5 times of live load, the structure was subjected to the self-vibration modal analysis of the first 50 orders, and the self-vibration frequency of the structure in the range of 1.038-19.796 for the 1st-50th orders is higher, which indicates that its structural stiffness is better, and its self-vibration frequency occurs in pairs due to the centrosymmetric shape of the topological configuration of the structure. Its low-order frequency is more dense, and the rising trend is slower, and the overall self-vibration frequency shows a stepwise rise, while the middle and high-order frequency rises faster and is more sparsely distributed. In addition, the mass in the ROTX, ROTY and ROTZ directions is more involved in the whole process of natural vibration, followed by the Z direction.The first ten orders of the vibration pattern first appeared horizontal torsion, followed by vertical deformation, and vertical deformation points with the rise of the order gradually transferred to the outer ring. In terms of the large-opening drum-honeycomb-type quad-strut suspend-dome structure, the outer ring stiffness is stronger than the inner ring, and the horizontal stiffness is stronger than the vertical stiffness, and the overall stiffness of the structure is better.

(2) The influence of the large-opening drum-honeycomb-type quad-strut suspend-dome structure on the self-vibration frequency of the structure was investigated for different parameters such as initial prestress, rise-span ratio, thickness-span ratio, opening diameter, and bottom chord arrangement schemes. It is finally concluded that the initial prestress, thickness-to-span ratio, and opening diameter have a greater effect on the self-vibration frequency of the structure, while the rise-span ratio and bottom chord arrangement schemes have the least effect. The influence of each parameter on the self-vibration frequency of the structure can be categorized as thickness-to-span ratio > prestress level > opening diameter > rise-span ratio > bottom chord arrangement schemes.

(3) Finally, this paper selected EI-Centro seismic wave, Tianjin Ninghe seismic wave and an artificial seismic wave for seismic response simulation, and analyzed that the seismic action on the structure is the most obvious Z-direction displacement, the X and Y-direction displacement is smaller, and the other three initial displacements are shifted to different degrees. In addition, the maximum nodal displacements of the structure under seismic wave action are all much smaller than the allowable deflection limits of the code. The structure generally exhibits better lateral and vertical stiffness.

(4) From the deformation diagrams of the maximum displacement vector and the structure, the structure is mainly deformed in the vertical direction, and all of them are biased to one side, and the maximum deformation is small, which has better ability to resist the deformation of seismic action.

(5) From the time-course curves of internal force of each member of the structure, the mesh shell of the structure is more sensitive to seismic action, and the struts, inclined cables and ring cables are the least sensitive, and the peak internal force of each member has a smaller amount of change compared with the initial internal force. The closer the structure is to the inner ring, the larger the peak internal force coefficient is, and the more obvious the seismic effect is, so attention should be paid to strengthen the strength of the inner ring members to resist earthquakes and other effects.

(6) There are some deficiencies in the research of this paper. For example, it focuses on numerical simulation, but fails to carry out the model test of the suspend-dome structure to verify the accuracy and reliability of the numerical simulation. Therefore, it is necessary to further complete the experimental study of the structure when the conditions permit. As a large-span spatial structure, the cable-strut failure and progressive collapse of the structure need to be further explored.

References

[1] Zhao Wenyan, ZhaoChuang, Pan Wenzhi, et al. Research on the Temporary Support System for Super Large-Span Ribbed-Type Suspen-Dome [J]. Progress in Steel Building Structures, 2023, 25 (01): 98-104.

[2] Kawaguchi M, Abe M, Tatemichi I. Design, tests and realization of “suspend-dome” system[J]. Journal of the International Association for Shell and Spatial Structures, 1999, 40(3):179-192.

[3] Zhang Ailin, Ge Jiaqi, Liu Xuechun. Design and research of the large-span steel structure of the badminton gymnasium for 2008 Olympic Games [J]. Journal of Building Structures, 2007, (06)：1-9.

[4] Fu Shaohui, Zhang Ling. Architecture inlaid in the mountains-Guiyang Olympic Sports Center Planning and Main Stadium Design [J]. Architectural Journal, 2011, (09): 86-87.

[5] Shu ganping, Pan Rui, Wang Siqing, et al. Analysis and assessment of progressive collapse resistance of a chord dome roof with suspended substructure in the main hall of Zhangjiaiie Circus City [J].Building Structure, 2022, 52(16): 37-44.

[6] Yu Jinghai, Wang Zhengkai, Yan Xiangyu, et al. Structural design of suspend-dome structure roof of new gymnasium of Tianjin University of Traditional Chinese Medicine [J]. Building Structure, 2015, 45(16): 1-5+90.

[7] Qu Tong, Chen Jinyu, Tan Jian. Progressive collapse resistance analysis on conjoined suspend-dome structure of Zhaoqing New District Stadium [J]. Building Structure, 2016, 46(21)：75-79.

[8] Liu Renjie, Zou Yao, Xue Suduo, et al. Influence on static performance of loop-free suspend-dome after removal of cables [J]. Journal of Building Structures, 2020, 41(S1): 1-9.
[9] Yuan Xingfei, Dong Shilin. New forms and initial prestress calculation of cable domes [J]. Engineering Mechanics, 2005, (02)：22-26.
[10] Dong Shilin, Wang Zhenhua, Yuan Xingfei. Static behavior analysis of a space structure combined of cable dome and single-layer lattice shell [J]. Journal of Building Structures, 2010, 31(03): 1-8.
[11] Zhang Ailin,Bai Yu,Liu Xuechun,et al. Static behavior analysis of new-type ridge tube cable dome with annular struts[J]. Spatial Structures,2017,23(03)：11-20.
[12] Sun Guojun, Li Xiaohui, Xue Suduo, et al. Experiment on Self-Vibration Characteristics of Levy-Type Rigid Bracing Dome [J]. Journal of Tianjin University (Science and Technology), 2019, 52(07): 719-724.
[13] Lv Hui, Chu Yiyi, Dong Shilin, et al. Static performance and parameter analysis of large-opening drum- honeycomb-type cable dome with quad-strut layout [J].Spatial Structures, 2023, 29 (03).
[14] Hui Lv, Hao Zhang, Zhong-Yi Zhu, Shi-Lin Dong and Xin Xie. Structural morphology and dynamic characteristics analysis of drum-shaped honeycomb-type iii cable dome with quad-strut layout [J]. Advanced Steel Construction, 2024, 1 (20): 81-92.
[15] LV H, CHEN Z Q, DONG S L, et al. Analytical Study of Structural Conformation and Prestressing State of Drum-Shaped Honeycomb Quad-Strut Cable Dome Structure with Different Calculation Methods[J]. Buildings, 2024, 14(1): 179.
[16] LV H, LIU D W, DONG S L, et al. Conformation and Static Performance Analysis of Pentagonal Three-Four Strut Hybrid Open-Type Cable Dome[J]. Advanced Steel Construction, 2023, 19(4): 403-410.
[17] Ministry of Housing and Urban-Rural Development of the People's Republic of China. Code for Seismic Design of Buildings：GB50011-2010 [S].China Architecture & Building Press, 2010.
[18] Ministry of Housing and Urban-Rural Development of the People's Republic of China. Technical specification for space frame structures：JGJ 7-2010 [S]. China Architecture & Building Press, 2010.
[19] Ministry of Housing and Urban-Rural Development of the People's Republic of China. Standard for Design of Steel Structures：GB50017-2017 [S]. China Planning Press, 2017.

Advanced Steel Construction – Vol. 21 No. 2 (2025) 157–173
DOI:10.18057/IJASC.2025.21.2.7

TENSILE BEHAVIOR OF T-STUB TO HOLLOW SECTION COLUMN USING THREAD-FIXED ONE-SIDE BOLTS AT HIGH TEMPERATURES

Yang You [1, 2], Jing-Yu Wu [3, 4] and Bin Yang [5, *]

[1] *School of Transportation and Civil Engineering, Shandong Jiaotong University, China*
[2] *Shandong Key Laboratory of Technologies and Systems for Intelligent Construction Equipment, Shandong Jiaotong University, China*
[3] *Qingdao Geological Exploration Institute of China Metallurgical Geology Bureau, China*
[4] *School of Civil Engineering, Shandong University, Jinan, Shandong Province 256001, China*
[5] *Department of Civil and Environmental Engineering, The Hong Kong Polytechnic University, Hong Kong, China*
** (Corresponding author: E-mail: bin24.yang@connect.polyu.hk)*

ABSTRACT

The Thread-fixed One-side Bolt (TOB), which utilizes internal threads in the bolt hole instead of a nut, enables installation from one side, thereby overcoming the challenge of connecting closed-section components, such as steel tube columns, which are not suitable for traditional bolt connections. This study establishes and validates a Finite Element Model (FEM) to investigate the mechanical performance of TOB connections under high temperature conditions. The results show that the wall thickness of the column has a significant influence on the performance of the connection; an increase in wall thickness substantially enhances both stiffness and bearing capacity. For columns with thinner walls, applying preload can improve stiffness. Furthermore, increasing the material strength of the column wall improves bearing capacity but has little effect on stiffness. For columns with insufficient wall thickness, the mechanical performance of the connection can be significantly enhanced by installing Internal Constraint Components (ICC) within the tube. Based on the FEM analysis results, a calculation method for the bearing capacity of TOB connections, accounting for high-temperature deformation and material degradation, is proposed. This method accurately predicts the yield bearing capacity at different temperatures. This research provides theoretical support for the design and application of TOB connections in engineering.

ARTICLE HISTORY

Received: 7 July 2024
Revised: 25 December 2024
Accepted: 1 January 2025

KEYWORDS

One-side bolt;
High temperature;
Tensile behavior;
Closed section

1. Introduction

The blind bolt, or one-side bolt, is a type of fastening system designed to provide a bolting option for structures where access is only available from one side. This situation is common in construction and manufacturing industries where it is either impossible or impractical to access both sides of the structure being connected, such as closed steel sections. The development of blind bolts arose from the need for an effective fastening solution in situations where Traditional Bolts (TB) were not feasible. TB require access to both sides of the structure for installation: one side to insert the bolt and the other side to secure the nut. In many modern construction and manufacturing scenarios, such as in hollow steel structures or areas with restricted access, this two-sided access is not possible. Blind bolts were developed to address this limitation, offering a reliable and robust fastening solution that can be installed from one side only [1].

Before the advent of blind bolts, the installation of closed-section steel components such as steel tube columns could only be completed through welding. Welded connections in steel structures offer strong and continuous connections but have notable disadvantages. They require skilled labor and precision, making the process costly due to the need for specialized equipment and rigorous inspections, including X-ray or ultrasonic testing. Welds can be prone to brittle fractures, especially in high-strength steels and under adverse conditions like low temperatures or high-impact loads. The welding process can introduce residual stresses and deformations in steel members, potentially compromising structural integrity. Additionally, welded connections may have lower fatigue strength and are more susceptible to corrosion. On-site welding presents challenges due to environmental factors, affecting weld quality. Repairs or modifications in welded structures can be cumbersome, often necessitating extensive cutting and re-welding.

Due to the various disadvantages of welding connections, the emergence of blind bolts immediately attracted widespread attention. Many researchers began to study the mechanical properties of blind bolts. Currently, the most researched is the Hollo Bolt [2]. During installation, the bolt is inserted into a pre-drilled hole, and then the bolt is tightened, which activates the expansion mechanism on the blind side, completing the connection. Wang et al. [3] investigated the tensile performance of connections using Hollo Bolt through experiments and the numerical simulation. Their experiments used T-stub connections and they established design equations for the stiffness and load-bearing capacity of such T-stub connections using Hollo Bolt. Cabrera [4] studied the pre-tension force of Extended Hollo-Bolts. The results showed that the special anchoring mechanism of this type of bolt leads to a pre-tension force coefficient much larger than that of TB. If conventional bolt pre-tension coefficients are used to apply torque to these bolts, it may result in excessive pre-tension forces. Pan et al. [5] conducted experimental research on the low-cycle fatigue performance of Hollo Bolt-connected T-stub connections. Based on the experimental results, they analyzed the typical failure modes, strength degradation, and energy dissipation of the connections. Furthermore, they proposed an energy-based damage model and equations for calculating fatigue life. Pascual et al. [6][7] studied the fire response of Square Hollow Section (SHS) column connections using Hollo bolt, finding that size of the column section and bolt type have a minor impact on the fire behavior. However, the presence of concrete significantly slows the temperature increase rate. Song [8] found that applying fire protection measures to steel beams or reducing the load ratio of steel beams can effectively enhance the fire resistance of Hollo Bolt connection. However, placing binding bars in the connection or changing the material of columns has a limited impact on the fire performance of Hollo Bolt connections. However, the structure of the Hollo Bolt itself is complex, which leads to greater manufacturing difficulty and a cost that can be more than ten times higher than that of traditional bolts. Additionally, the bolt relies on the deformation of the outer sleeve to provide anchorage, and once installed, it is difficult to remove, which is unfavorable for later maintenance. As a result, the use of Hollo Bolt is somewhat limited.

In addition to the Hollo Bolt, there are other methods for achieving one-sided bolt installation. The Ajax ONESIDE bolt features a special foldable washer that can pass through the bolt hole when folded. Once inserted, a special tool allows the washer to unfold on the blind side, completing the anchorage. Lee et al. [9] found that the Ajax ONESIDE bolt connection in T-stub to hollow steel tube column connections meets the requirements for semi-rigid connections. Research by Hosseini [10] shows that Ajax ONESIDE bolt connections perform satisfactorily under monotonic and repeated shear forces, meeting the demand in EN 1993-1-8 [11] for bolted connections. Similarly, one-side anchoring can be achieved by incorporating a rotatable pin on the bolt shank, which, after passing through the bolt hole, rotates perpendicular to the hole for anchorage. Alternatively, both the nut and bolt hole can be made elliptical, with the nut slightly smaller. The nut passes through the bolt hole when aligned parallel, and the bolt is then rotated to change the orientation from parallel to perpendicular for blind-side anchoring. Wan [12] and Sun [13] found that the aspect ratio of the bolt head has minimal impact on the yield load capacity of the connection. An aspect ratio of 1.7 for the bolt head balances bolt slippage and stress concentratio7n around the bolt hole, achieving the most advantageous connection.

Although the aforementioned blind bolts enable one-side installation, their performance is not satisfactory enough. For example, the load-bearing capacity of Ajax ONESIDE bolts depends on the strength of the folded washer, and the

strength of the bolt shaft itself is difficult to fully utilize, making it hard to achieve the same performance as traditional high-strength bolts. Attaching a rotatable pin to the bolt shank weakens the cross-section of the bolt, affecting both its tensile and shear load-bearing capacities. Using bolts with elliptical nuts and bolt holes also affects the shear capacity along the long axis of the bolt hole. Li et al. [14] conducted experiments comparing the connection performance of different types of blind bolts and traditional bolts. The results showed that the strength and stiffness of joints connected with existing blind bolts were less than half of those using traditional bolts (TB). As a result, many researchers are continuously working on improving the blind bolts to achieve better mechanical performance [15]-[19]. By directly setting threads inside the bolt hole, nuts can be replaced to anchor bolts for one-side installation, known as Thread-fixed One-side Bolts (TOB). TOB is structurally simple and convenient for installation, allowing the use of standard bolts and tools. This type of connection has been widely used in bolt-ball joints and some mechanical structures. However, as the wall thickness and strength of typical steel tube columns are generally less than nuts, the effectiveness of TOB connections needs verification. You [19][20] and Wang [21] conducted experiments on TOB connections and found that bolt pull-out failure does not occur even with limited wall thickness before overall connection yielding. However, the limited number of experimental specimens presents challenges in establishing and fully validating precise load-bearing capacity equations. Additionally, it is difficult to observe the deformation process of connections and the stress-strain distribution within the threaded holes, particularly the yield line distribution on the surface of steel tube columns without nut constraints, through experimental methods. Furthermore, the influence of key parameters such as bolt pre-tension, material strength, and elevated temperatures warrants further investigation.

Based on existing experiments, this paper establishes and validates a Finite Element Model (FEM) to study the mechanical performance of TOB bolted connections at elevated temperatures. The main failure modes of the connections and the causes of failure are analyzed, and the degradation patterns of the load-bearing capacity and stiffness of the connection at high temperatures are discussed. Additionally, based on the FEM analysis results, a method for calculating the load-bearing capacity of TOB bolted connections at different temperatures is proposed and discussed.

2. Finite element model

2.1. Establishment of the model

To accurately simulate the mechanical performance of TOB bolted connections under varying temperatures, it is essential to account for factors such as material nonlinearity under the combined effects of thermal and force fields, nonlinear contact relationships between different parts, and geometric nonlinearity. Additionally, while analyzing the overall macroscopic performance, the performance of microscopic components, such as the threads inside the bolt hole and on the bolt shank, must also be considered. Therefore, establishing the model is highly complex and requires certain simplifications.

To reduce computational difficulty and improve efficiency, this paper focuses on analyzing the tensile area of TOB bolted connections in the model. Following the component method, a connection can be divided into several simple components. Using the component method, a connection can be divided into several simple components. Analyzing these components separately and then combining them can represent the overall behavior of the connection. According to P398 [22], the bolted beam-column end-plate connections can be divided into different parts such as tensile area, compression area, vertical shear area, and horizontal shear areas. From the perspective of load transfer mechanism, TOB and TB differ only under tensile forces. Therefore, in this paper, only the tensile area of the beam-column end-plate connection was selected for analysis to reduce computational complexity, as shown in Fig. 1.

Considering the symmetry of the tensile zone, only a 1/8 model was established for analysis. Corresponding boundary conditions were applied on the symmetry planes, as shown in Fig. 2. The load on the connection was applied in the form of displacement. In the model, all components used hexahedral linear reduced integration elements C3D8R. The model was meshed with cubic grids of 0.3mm edge length, with local refinement at critical areas such as the threads inside the bolt hole and on the bolt shank.

High-strength steel and ordinary structural steel exhibit different reduction speeds at high temperatures due to variations in composition and processing, as shown in Fig. 3. Ignoring these differences may lead to inaccurate simulation results. Therefore, in the FEM of this paper, different constitutive relationships were used for ordinary structural steel and bolts. Ordinary structural steel followed the stress-strain relationship model and high-temperature reduction factors recommended by EN 1993-1-2 [24], while the bolts were modeled based on experimental data from Pang et al [25]. The constitutive relationship models for ordinary structural steel and bolts in the FEM are shown in Fig. 4.

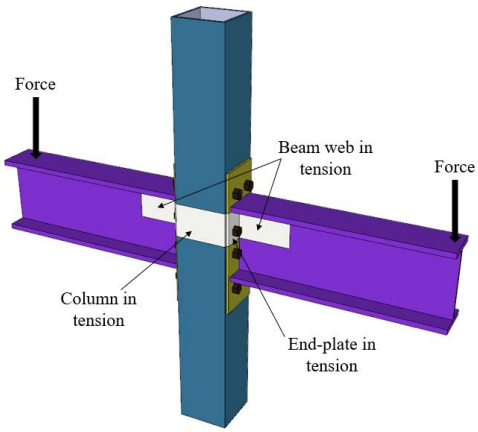

Fig. 1 The Tension zone of a bolted end-plate connection

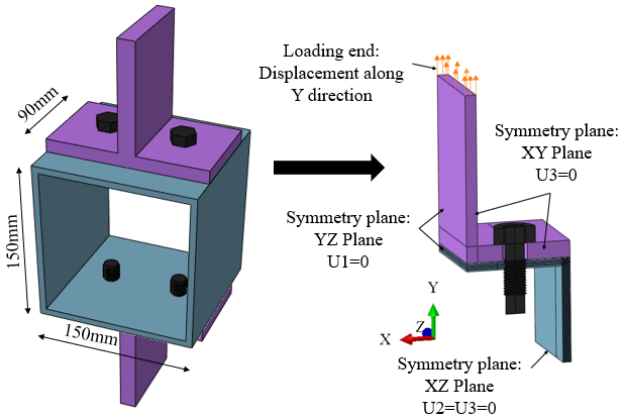

Fig. 2 The boundary conditions and loads of the FEM

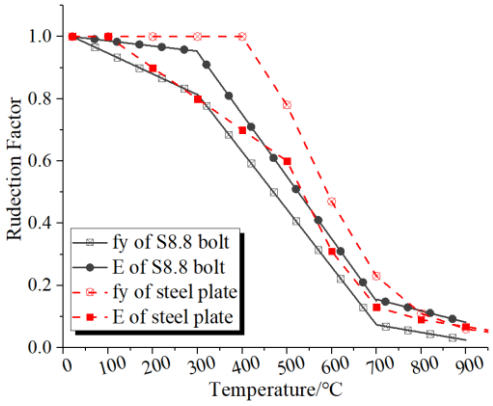

Fig. 3 Comparison of the reduction factor of mild steel and high strength bolt[24][25]

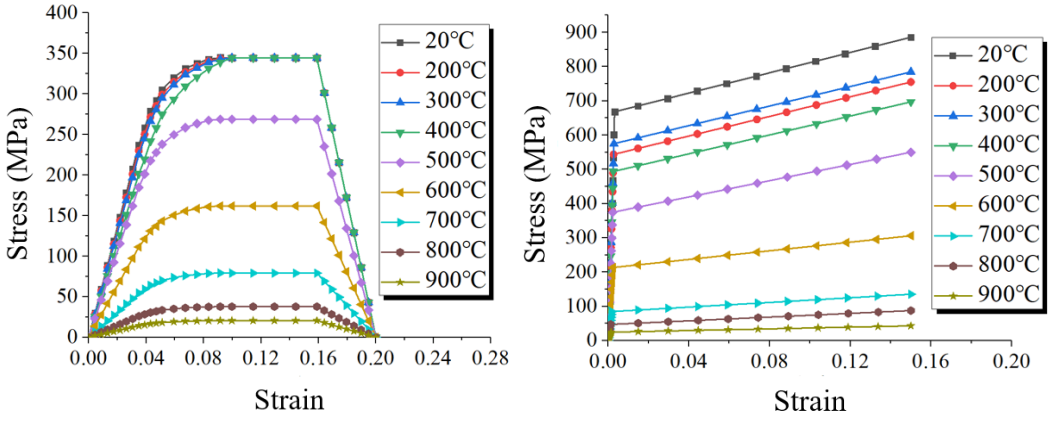

(a) mild steel (Q350) (b) bolt

Fig. 4 The consecutive law of mild steel and bolt applied in FEM.

In finite element modeling analysis, such as using Abaqus software, it is necessary to convert nominal stress-strain data to true stress-strain data. This is because true stress-strain more accurately reflects the material's real mechanical behavior during the plastic deformation process. Nominal stress-strain is defined based on the initial cross-sectional area and length of the specimen, assuming these parameters remain constant during deformation. However, in reality, the cross-sectional area changes significantly as deformation occurs, especially in the large plastic deformation stage. In contrast, true stress-strain considers the instantaneous cross-sectional area and cumulative deformation effects, providing a more precise description of the material's mechanical response. This true stress-strain relationship not only better meets the requirements of material models in finite element analysis but also avoids computational errors caused by the limitations of engineering stress-strain under large deformation conditions. Therefore, Equations (1), (2), and (3) were used in the FEM to convert nominal stress σ_{nom} and nominal strain ε_{nom} into true stress σ_{true} and true strain ε_{true}, respectively.

$$\varepsilon_{true} = \ln(1+\varepsilon_{nom}) \tag{1}$$

$$\sigma_{true} = \sigma_{nom}(1+\varepsilon_{nom}) \tag{2}$$

$$\varepsilon_{pl} = \varepsilon_{true} - \frac{\sigma_{true}}{\varepsilon} - \varepsilon_{thermal} \tag{3}$$

In terms of contact relationships, the model employs a general contact approach where the normal direction is set to hard contact, and the tangential contact is defined using the Coulomb friction model. Referring to the Chinese code GB50017-2017 [26] and other relevant studies [27]-[32], the FEM in this paper assumes a friction coefficient of 0.3 for tangential contact.

The model includes initial step and two analysis steps. The initial step is set to define the boundary conditions and the thermal field. The first analysis step is used to apply the preload of bolt, while the second analysis step involves the application of displacement load.

2.2. Validation of the model

To verify the accuracy of the model calculations, three sets of test specimens were designed and tested at both room and high temperatures. These tests provided a basis for validating the FEM model's accuracy. The test specimens included two T-stubs and a steel tube, connected by four bolts. The bolt holes on the surface of the steel tube were threaded to provide anchorage for the TOB. The bolt holes on the T-stub were plain holes, 2mm larger than the TOB. Other relevant information can be found in Fig. 5 and Table 1. The bolts used were standard grade 8.8 high-strength bolts, with thread dimensions conforming to Chinese standards GB/T 192-2003 [33] and GB/T 192–-2003 [34].

The test was conducted using a universal testing machine with a load capacity of 1000 kN and an accompanying electric furnace, as shown in Fig. 6. Prior to loading, the bolts were pre-tensioned according to the requirements in GB 50017-2017 [26]. The assembled specimens were then installed on the testing machine for preloading. The main steps of preloading involved loading the specimen from 0 kN to 10 kN, then unloading back to 0 kN while keeping the grips of the testing machine tight. This preloading process helps to reduce potential slippage and deformation during the actual test, ensuring accurate loading and measurement.

Table 1
Test specimens

	Column wall thickness t_c/mm	T-stub flange thickness t_c/mm	H-section steel flange thickness t_c/mm	Bolt diameter D/mm
S1	6	12		16
S2	12	12		16
S3	6	12	6	16

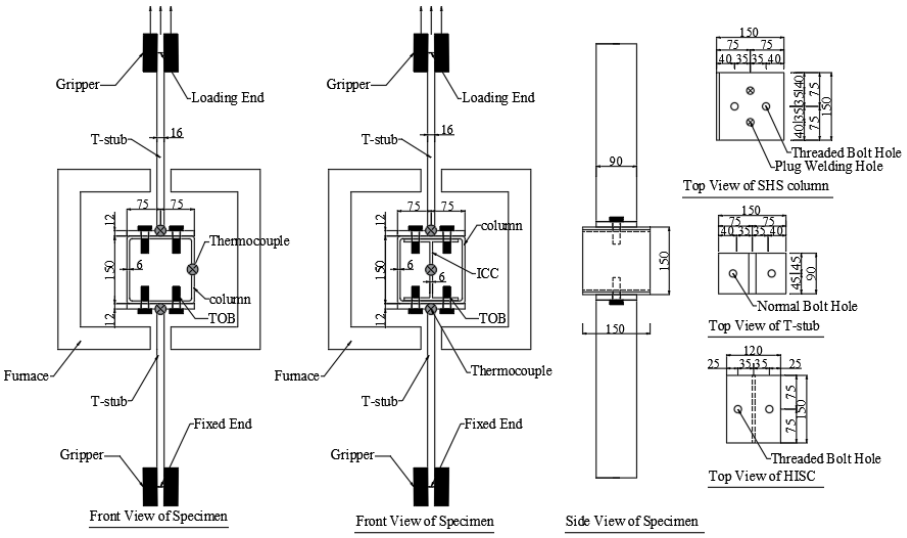

Fig. 5 Test specimen

After preloading, the specimens were loaded to failure at a rate of 2 mm/min. During loading, the deformation and load were automatically recorded by the control computer of the testing machine. Dial gauges were also installed to measure the deformation of the test specimens, verifying the data recorded by the testing machine. This ensured the accuracy and reliability of the measurement results.

The high-temperature test was conducted using steady-state method. The specimens were first heated to the specified temperature and maintained for 30 minutes, with one end clamped and the other free to prevent additional stress from temperature changes. Preloading was then performed. After completing the preloading, the specimens were loaded to failure at a rate of 2 mm/min. The preloading process and data measurement methods were the same as those used in the room temperature tests. Before the tests, corresponding steel samples were retained and processed into standard specimens to test their material properties. The actual measured material properties were used for modeling and verification.

The load-displacement curves of TOB bolted connections show apparent non-linear characteristics after the initial elastic stage and lack a distinct yield plateau, making it difficult to directly determine the yield bearing capacity (F_Y). By employing the tangent method, the yield bearing capacity F_Y of the connections at different temperatures can be determined [35]-[37]. Additionally, the ultimate bearing capacity (F_U) of the connections can be obtained from the highest point of the curves, as shown in Fig. 7

Fig. 8 compares the FEM and experimental results of the S1 group. The steel tube in the S1 group had a wall thickness of only 6mm. As the load increased, the walls of the steel tube deformed. The two side walls deformed inward, while the top and bottom surfaces deformed outward. Due to the deformation of the steel tube, disengagement occurred between the threaded hole and the TOB, resulting in a nonuniform stress and strain distribution inside the threaded hole. This nonuniformity ultimately resulted in the pullout of the TOB and the failure of the connection. The phenomena observed in the simulation were consistent with those observed in the test.

The S2 group specimens initially formed a plastic zone at the intersection of the web and flange of the T-stub. Subsequently, the deformation rapidly increased, leading to significant deformation of the bolt. However, only discontinuous and minor plastic strain accumulation occurred in the threads inside the bolt hole, indicating no damage to the threads within the bolt hole.

Fig. 6 Test setup

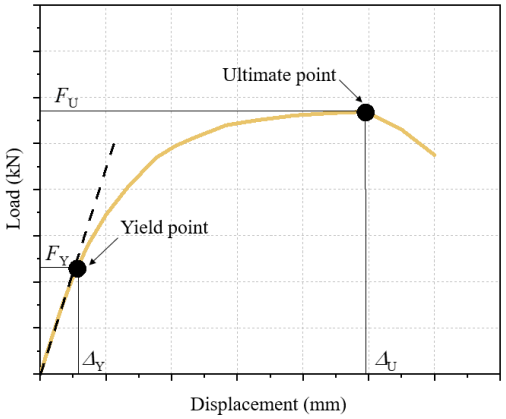

Fig. 7 Load-displacement curve

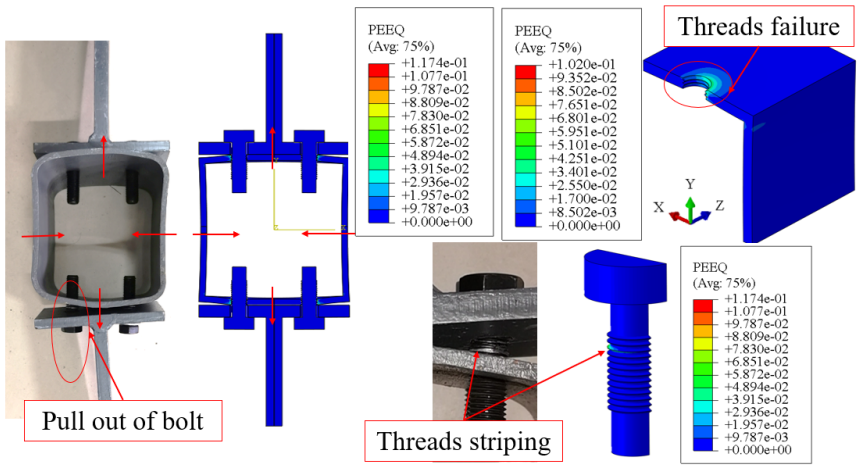

(a) Comparison of S1 group

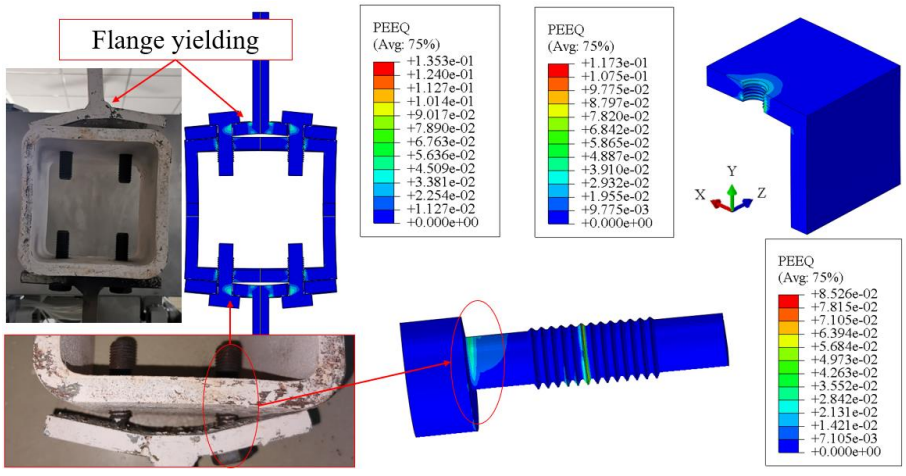

(b) Comparison of S2 group

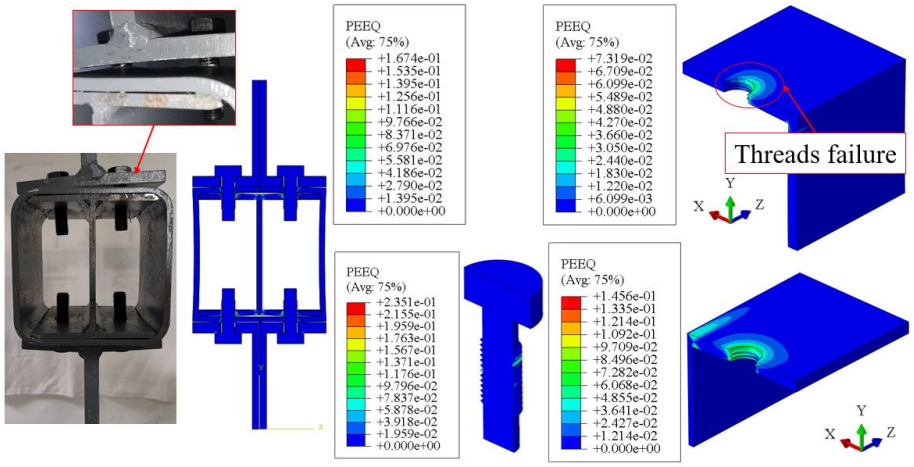

(c) Comparison of S3 group

Fig. 8 Comparison of simulation result and test result

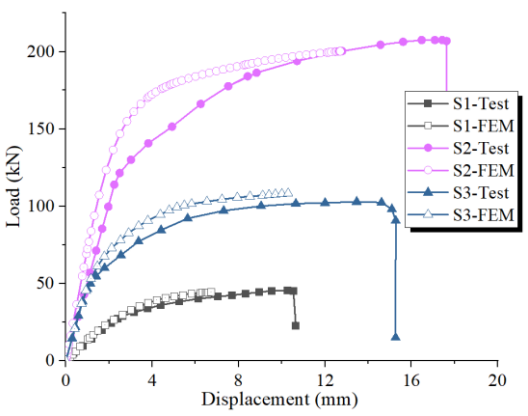

(a) Comparison of load-displacement curves at 20℃

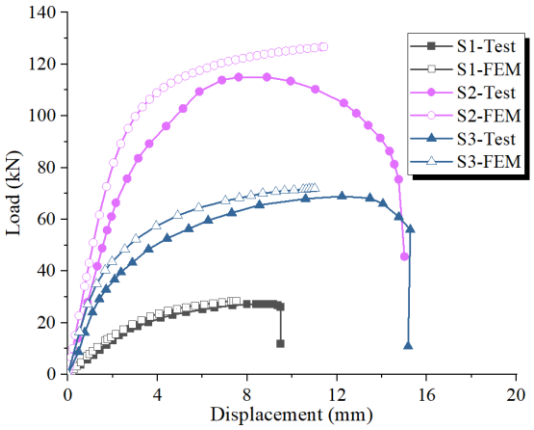

(b) Comparison of load-displacement curves at 500℃

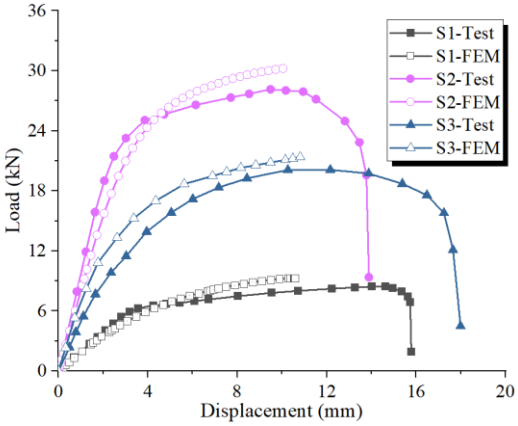

(c) Comparison of load-displacement curves at 700℃

Fig. 9 Comparison of simulation result and test result

For the S3 group specimens, the overall deformation of the connection was small, but significant plastic strain was observed in the threads of the bolt holes in both the steel tube column and the infilled H-section steel, consistent with the bolt pullout phenomenon observed in the test.The simulation results for each group of specimens were consistent with the phenomena observed in the tests.

Fig. 9 compares the load-displacement curves of different specimens. Compared to the S1 group, both the S2 and S3 groups show significant improvements in yield load capacity F_Y, ultimate load capacity F_U, deformation capacity, and stiffness at the same temperature. For instance, at room temperature, the yield load capacity F_Y and ultimate load capacity F_U of the S2 group are approximately 4.2 times and 4.1 times those of the S1 group, respectively. This improvement is primarily attributed to the change in the anchorage capacity of the threaded hole. The failure mode of the S1 group specimens is tube column wall yielding, which leads to the separation of the threaded hole and TOB when the column wall deforms. As a result, the connection fails quickly after yielding. In contrast, for the S2 and S3 groups, after yielding, the separation between the TOB and the threaded hole does not occur immediately, allowing for further increase in the load-bearing capacity after connection yielding.

It should be noted, however, that although both the S2 and S3 groups have a bolt anchorage depth of 12 mm, the load-displacement curves of the two groups exhibit significant differences. Under the same temperature, the initial stiffness, yield load capacity F_Y, and ultimate load capacity F_U of the S2 group are all higher than those of the S3 group. Specifically, at the same temperature, the yield load capacity F_Y and ultimate load capacity F_U of the S2 group are approximately 2.5 times and 2.1 times those of the S3 group, respectively, as shown in Table 2. This difference arises because the Internal Constraint Components and the steel tube column wall work separately, with only minimal interaction between them. This suggests that directly increasing the thickness of the steel tube wall is more efficient than installing Internal Constraint Components.

The comparison in Fig. 9 shows that the load-displacement curves obtained from finite element calculations closely match those from test results. Table 2 shows that the relative error between the model's output of the yielding load (F_Y) and ultimate load (F_U) and the experimentally obtained load capacity increases with the rise in temperature (θ), but remains within the range of -8.1% to 16.8%. Overall, the finite element model established in this paper can accurately reflect the failure characteristics of TOB connections at different temperatures. Additionally, the model's load-displacement curves and load capacities are consistent with test results, demonstrating good accuracy.

Table 2
Comparison of test result and simulation result

	Temperature θ (℃)	Test			FEM			Error (FEM - Test) / Test	
		Failure mode	Yielding load F_Y (kN)	Ultimate load F_U (kN)	Failure mode	Yielding load F_Y (kN)	Ultimate load F_U (kN)	Yielding load F_Y (kN)	Ultimate load F_U (kN)
S1	20	mode1	28.1	41.9	mode1	27.8	44.5	-1.1%	6.2%
	500	mode1	17.2	27.2	mode1	15.8	28.5	-8.1%	4.8%
	700	mode1	5.5	7.5	mode1	6.2	8.2	12.7%	9.3%
S2	20	mode2	118.8	173.4	mode2	113.4	180.3	-4.5%	4.0%
	500	mode2	68.5	113.2	mode2	68.8	112.7	0.4%	-0.4%
	700	mode2	17.5	25.9	mode2	19.2	29.1	9.7%	12.4%
S3	20	mode1	45.2	82.1	mode1	47.1	77.5	4.2%	-5.6%
	500	mode1	26.2	48.5	mode1	26.1	48.4	-0.4%	-0.2%
	700	mode1	7.2	13.1	mode1	7.5	15.3	4.2%	16.8%

3. Parameter analyzes and discussion

3.1. Influence of tube wall thickness

Based on the parameters of the connection, including the bolt diameter D, steel tube wall thickness t_c, and T-stub thickness t_T, four potential failure modes for TOB connections are identified: tube column wall yielding (mode 1), T-stub flange yielding accompanied by bolt failure (mode2), T-stub flange yielding (mode3), and bolt fracture failure (mode4). Notably, failure mode 1 results in a failure mechanism for TOB connections that differs significantly from that of TB connections. This is due to the absence of deformation restraint from the nut on the steel tube column wall and the lack of anchorage provided by the nut. In contrast, other failure modes do not involve damage to the steel tube column or the threaded hole, resulting in no significant difference in the failure mechanism between TOB and TB connections. Given the multiple potential failure modes of the TOB connection, this paper focuses its analysis primarily on failure mode 1 for convenience.

For TOB connections, the steel tube wall thickness (t_c) determines the anchoring depth that the threaded hole can provide. Additionally, the wall thickness (t_c) also influences the deformation capability of the steel tube, which in turn affects the contact relationship between the threaded hole and the TOB. Therefore, the steel tube wall thickness (t_c) is one of the most crucial parameters influencing the behavior of TOB connections. Using the verified FEM, the failure mechanisms of TOB connections with different steel tube wall thicknesses (t_c) and their reduction under high temperatures were analyzed. During the analysis, the bolt diameter (D) of the selected connections was consistently 16mm, and the steel tube section width (b_c) was 150mm. The analysis of the model is limited to temperatures below 800°C. This is because, after exceeding 500°C, the material properties of steel, including elastic modulus, yield strength, and ultimate strength, undergo a significant degradation. At temperatures of 800°C or higher, steel essentially loses its load-bearing capacity. According to the data provided in the European standard EN1993-1-2, at 800°C, the yield strength of ordinary steel is only 11% of its value at room temperature, and the elastic modulus is only 9% of its room temperature value. Therefore, before reaching 800°C, the connection will have already failed under the action of sustained loads, making further discussion of conditions at or above 800°C unnecessary.

At the same temperature θ, as the tube wall thickness (t_C) increases, the failure mode of the connection gradually changes from tube column wall yielding (mode 1) to T-stub flange yielding accompanied by bolt failure (mode 2). Fig. 10 and Fig. 11 show the stress and strain distribution in the threads inside the bolt hole for the connection with 6mm t_C (mode 1) and 12mm t_C (mode 2), respectively, at different temperatures θ when reaching the yield load (F_Y).

For connection with 6mm t_C, when reaching the yield bearing capacity F_Y, the stress distribution inside the threaded hole is nonuniform due to the deformation of the steel tube. The plastic equivalent strain PEEQ mainly occurs on the side with higher stress, as shown in Fig. 10 (a). With the increase in temperature, the deformation of the connection increases, leading to even more uniform stress and strain distribution inside the threaded hole, as depicted in Fig. 10 (b). This nonuniform stress distribution caused by column wall deformation leads to the failure of the connection.

For connection with 12mm t_C, the greater stiffness of the tube means that, upon reaching the yield bearing capacity F_Y, the deformation mainly occurs in the flange of the T-stub. The stress distribution in the threads inside the bolt hole is uniform, and the plastic strain predominantly occurs at the root of the threads in the lower part, while the upper threads remain elastic. This indicates that the threads inside the hole can provide sufficient anchorage for the bolt, as shown in Fig. 11.

Fig. 12 (a) indicates that the initial stiffness K of the connection rapidly increases with the increase in tube wall thickness t_C. However, when the fire temperature θ exceeds 500°C, a significant decrease in the initial stiffness K is observed. The influence of tube wall thickness t_C on the initial stiffness K becomes substantially less significant. At temperatures θ exceeding 700°C, the connections almost completely lose their load-bearing capacity, and the effect of variations in t_C on the initial stiffness K becomes negligible.

Similarly, when the fire temperature θ does not exceed 500°C, increasing in t_C can significantly improve the yield load F_Y and ultimate load F_U. However, as the temperature θ exceeds 500°C, the load-bearing capacity of the connection substantially decreases, and the influence of steel tube wall thickness t_C on the load-bearing capacity reduces. When the temperature θ exceeds 700°C, the influence of tube wall thickness t_C on the load-bearing capacity of the connection becomes minimal.

Fig. 12 (b) and (c) shows that the reduction factors of tensile load at the same temperature are not significantly different, and the failure mode does not change with variations in temperature. This indicates that the mechanical performance of TOB connection is stable under different temperatures.

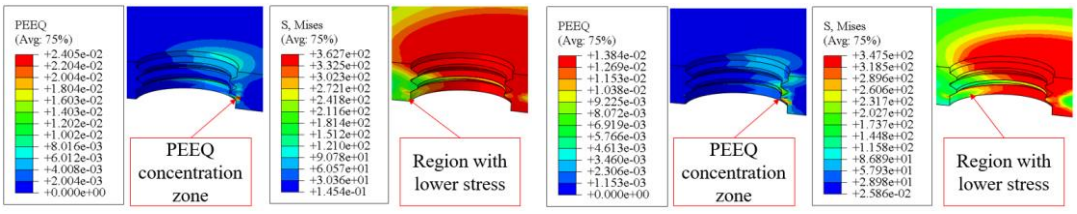

(a) θ=20°C (b) θ=500°C

Fig. 10 The state of the hole threads under yielding load F_Y (t_C=6mm)

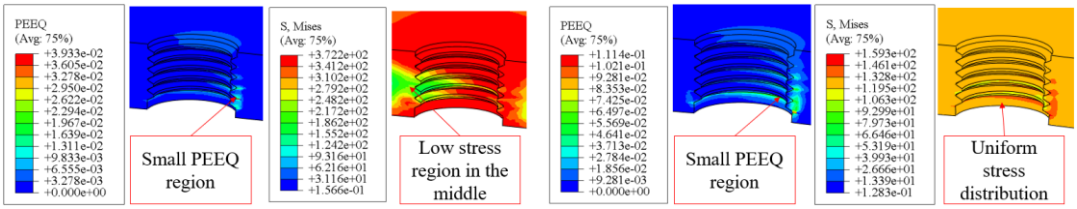

(a) θ=20℃ (b) θ=500℃

Fig. 11 The state of the hole threads under yielding load F_Y (t_C=12mm)

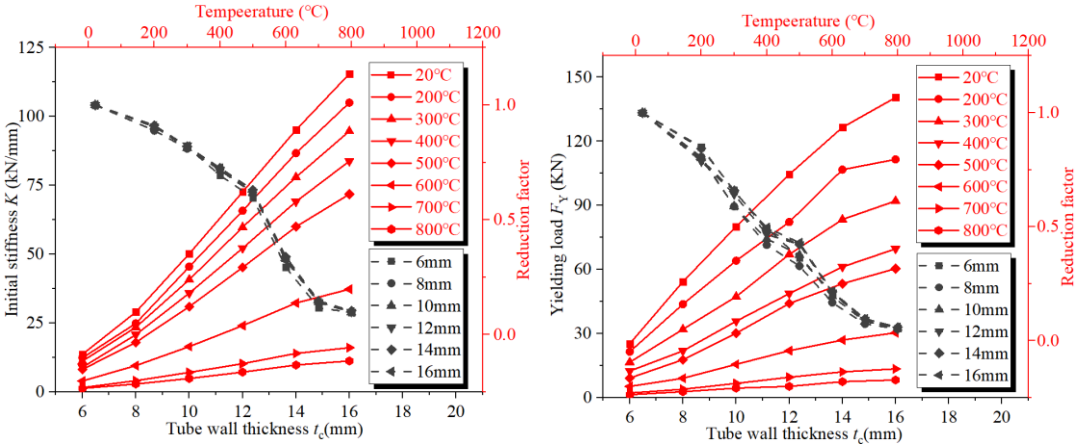

(a) Initial stiffness K (b) Yielding Load F_Y

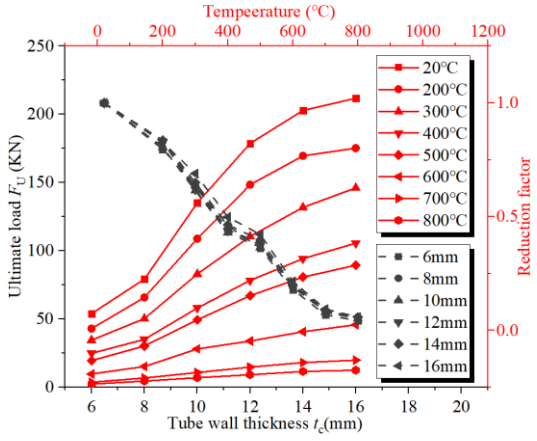

(c) Ultimate Load F_U

Fig. 12 Influence of column thickness t_C on the tensile behavior of connections

3.2. Influence of preload

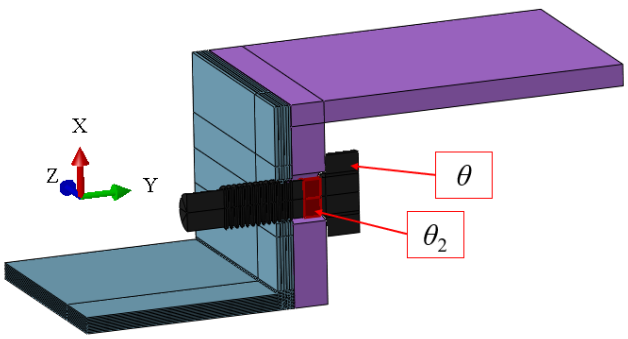

Fig. 13 Method to apply preload of bolt in FEM

Controlling the magnitude of the applied preload P is one of the key means to ensure the quality of bolted connections. An appropriately bolt preload P can make the bolt more effective in transferring loads and reliably connect the various components together. For TOB connections, in most cases, the strength of the threaded hole is inferior to that of a standard high-strength nut, and the tube wall thickness t_C is also typically less than the thickness of the nut. Therefore, it is necessary to research whether the bolt preload P can be applied to TOB in accordance with the requirements of Chinses code GB50017-2017 [26], and the influence of the preload P on the connection under different temperatures θ.

To consider the different degradation speeds of the elastic modulus E of ordinary structural steel and bolts under high fire temperatures on the bolt preload P, this paper applies the preload in the FEM by changing the temperature. Before applying the load to the model, imposing a different temperature θ_2 on a part of the bolt shaft than on other parts of the model. The temperature difference induces axial deformation in the bolt equivalent to the effect of the preload P. This simulates the impact of the bolt preload P on the load-bearing performance of the TOB connection, as shown in Fig. 13.

The distribution of stress and PEEQ inside the threaded hole after applying the bolt preload P, as obtained from the FEM, are shown in Fig. 14 and Fig. 15. After the application of preload P, the stress distribution within the threaded hole is nonuniform, decreasing from top to bottom. Under different temperatures θ, the plastic strain in the threaded hole caused by the pre-tension force does not exceed 0.02, indicating that the threads inside the hole remain in the elastic state.

Therefore, the specified preload P can be applied to TOB in accordance with the Chinese code GB50017-2017 [26] at different temperatures θ.

Two connection groups were analyzed as examples, with bolt diameter D being 16mm, T-stub flange thickness t_T being 12mm, and tube wall thicknesses

t_C being 6mm and 12mm respectively, the influence of bolt preload P on the TOB connection was analyzed. Fig. 16 compares the load-displacement curves of the two groups of connections before and after the application of bolt preload P. The changes in load-bearing performance, such as initial stiffness K, yield bearing capacity F_Y, and ultimate bearing capacity F_U, are listed in Table 3. The comparison reveals that after applying preload P, there is no significant change in the load-displacement curves, with only a slight increase in initial stiffness K that becomes less significant as temperature θ rises, nearly negligible above 400℃. The yield load F_Y and ultimate load F_U at different temperatures remain unchanged after the application of preload P. Furthermore, the bolt preload P does not change the failure mode of the connections.

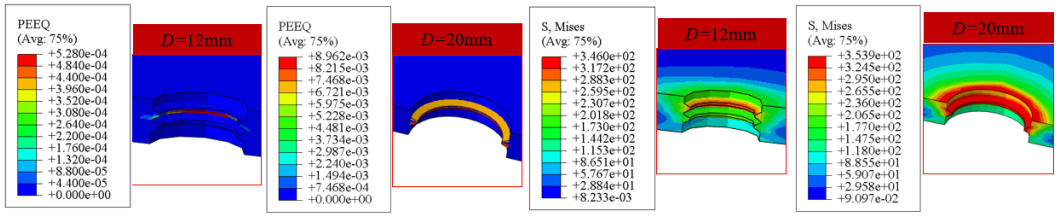

(a) θ=20℃

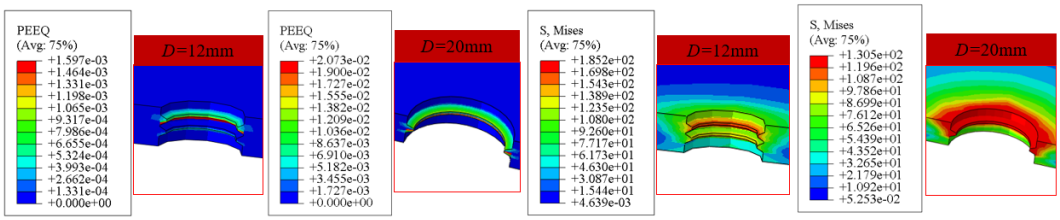

(b) θ=500℃

Fig. 14 Distribution of stress and strain inside bolt hole under preload P (t_C=6mm)

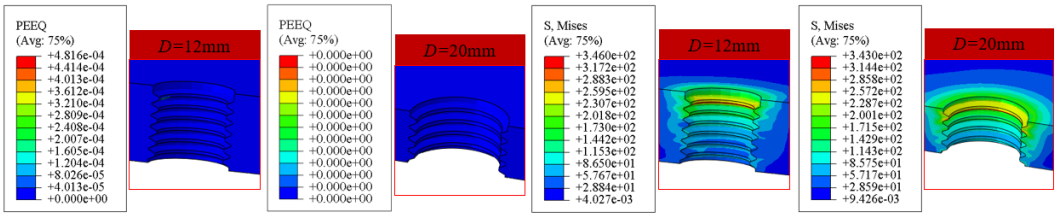

(a) θ=20℃

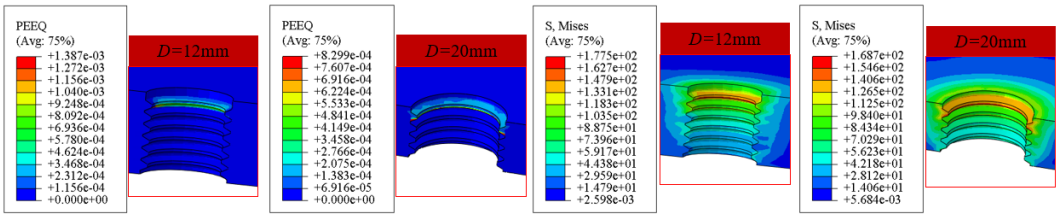

(b) θ=500℃

Fig. 15 Distribution of stress and strain inside bolt hole under preload P (t_C=12mm)

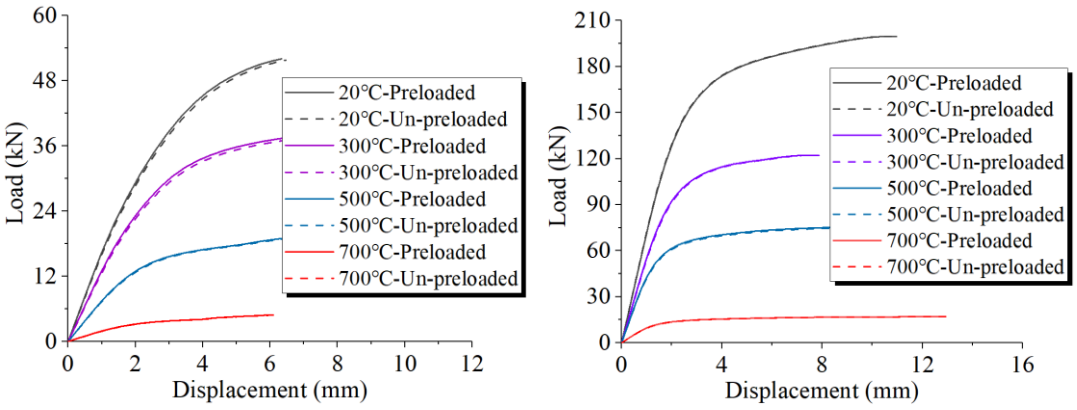

(a) t_C=6mm (b) t_C=12mm

Fig. 16 Comparison of preloaded and un-preloaded connections

Table 3
Comparison of preloaded and un-preloaded TOB connections

Temperature θ (℃)	Tube wall thickness t_c(mm)	Un-preloaded				Preloaded P			
		Initial stiffness K (kN/mm)	Yielding load F_Y(kN)	Ultimate Load F_U(kN)	Failure mode	Initial stiffness K (kN/mm)	Yielding load F_Y(kN)	Ultimate Load F_U(kN)	Failure mode
20	6	13.7	25.3	54.0	mode1	14.6	25.3	54.0	mode1
200		12.4	21.5	43.0	mode1	13.1	21.5	43.0	mode1
300		11.2	16.6	34.5	mode1	11.4	16.6	34.5	mode1
400		9.0	12.5	24.9	mode1	9.0	12.5	24.9	mode1
500		8.2	9.2	16.5	mode1	8.2	9.2	16.5	mode1
600		4.0	5.3	9.7	mode1	4.0	5.3	9.7	mode1
700		1.6	2.2	3.7	mode1	1.6	2.2	3.7	mode1
800		1.3	1.4	2.3	mode1	1.3	1.4	2.3	mode1
20	12	72.6	104.5	178.7	mode2	74.7	104.5	178.7	mode2
200		65.8	82.2	148.4	mode2	67.8	82.2	148.4	mode2
300		59.8	67.1	110.5	mode2	59.8	67.1	110.5	mode2
400		52.2	48.7	78.3	mode2	52.2	48.7	78.3	mode2
500		45.2	44.1	67.1	mode2	45.2	44.1	67.1	mode2
600		24.1	22.0	33.9	mode2	24.1	22.0	33.9	mode2
700		10.3	9.6	14.8	mode2	10.3	9.6	14.8	mode2
800		7.2	5.3	9.2	mode2	7.2	5.3	9.2	mode2

3.3. Influence of material properties

FEM simulations were conducted to analyze the influence of steel tube strength on the load-bearing performance under various temperatures θ. The analysis focused on connections composed of tube columns made from commonly used engineering materials: Q235, Q345, and Q460 steel grades. The analyzed connections all featured a bolt diameter (D) of 16mm, a tube section width (b_c) of 150mm, and a T-stub flange thickness (t_T) of 12mm. The materials of the T-stub and the steel tube were consistent, and the bolts were S8.8 high-strength bolts.

Fig. 17 compares the influence of tube material properties on the initial stiffness K. For connections with the same tube wall thickness (t_C), the initial stiffness K is essentially the same at a given temperature θ, and the reduction coefficient of initial stiffness K at different temperatures θ is also largely similar. This indicates that the initial stiffness K is primarily determined by dimensional parameters of the connection itself, such as the steel tube wall thickness (t_C). Changing the material of the steel tube does not influence the initial stiffness K of the connection.

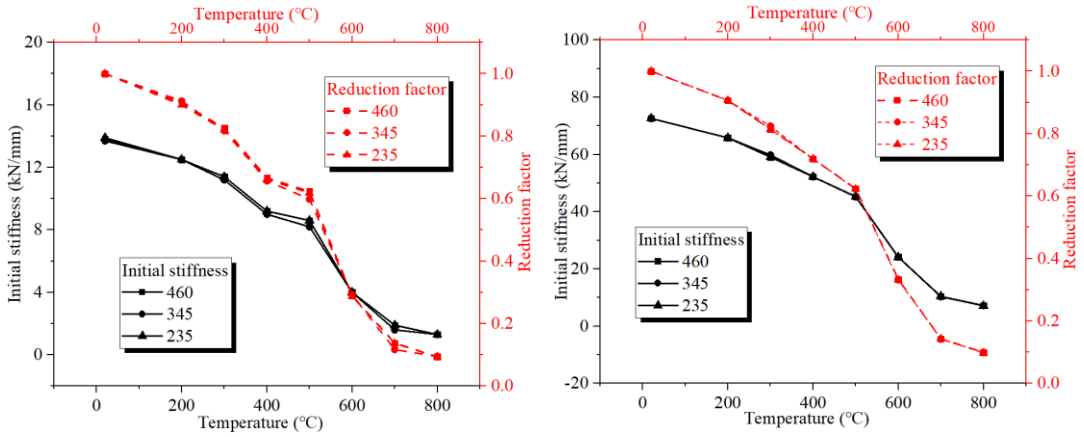

(a) t_C=6mm (d) t_C=12mm

Fig. 17 Influence of material property of steel tube on the initial stiffness K

Fig. 18 and Fig. 19 respectively compare the influence of material properties on the yield load (F_Y) and ultimate load (F_U). The comparison shows that the material properties have a significant influence on the load-bearing capacity of the connection. Taking the connection with a tube wall thickness (t_C) of 6mm as an example: when the steel tube material is Q235, Q345, and Q460, the yield load F_Y at ambient temperature is 13.2kN, 18.1kN, and 23.5kN, respectively, and the ultimate load F_U is 27.7kN, 38.5kN, and 49.9kN, respectively. Compared to the Q235 steel material connections, the Q345 steel material connections show an increase of 37% and 39% in F_Y and F_U, respectively, while the Q460 steel material connections exhibit increases of 78% and 80% in F_Y and F_U, respectively. For other connections with different tube wall thicknesses t_C, the pattern of material performance affecting their load-bearing capacity is essentially consistent, as shown in Fig. 18 and Fig. 19.

As the temperature θ increases, there is a rapid decrease in the load-bearing capacity of the connections. When the fire temperature θ rises to 500°C, both the yielding load (F_Y) and the ultimate load (F_U) of the connections decreased to approximately 50% of their capacity at ambient temperatures. Furthermore, as the temperature θ further increases to 700°C, the load-bearing capacity of the connections declines to about 10% of the ambient temperature capacity, indicating a near-total loss of load-bearing ability. In this case, although enhancing the strength grade of the steel can marginally increase the load-bearing capacity of the connections, this improvement is negligible.

Fig. 18 and Fig. 19 also compare the reduction factors of the load-bearing capacity of connections at varying temperatures θ. It is observed that changing the material strength does not affect the deterioration speed of the yielding load (F_Y) and ultimate load (F_U). Moreover, while changing the material strength of the connections significantly improves their load-bearing capacity, it does not result in a change in the failure mode of the connections.

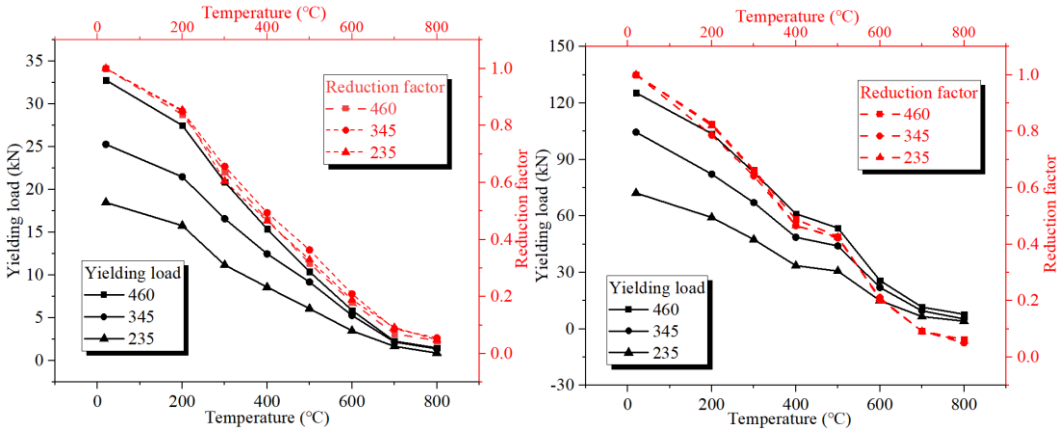

(a) t_C=6mm (d) t_C=12mm

Fig. 18 Influence of material property of steel tube on yielding load F_Y

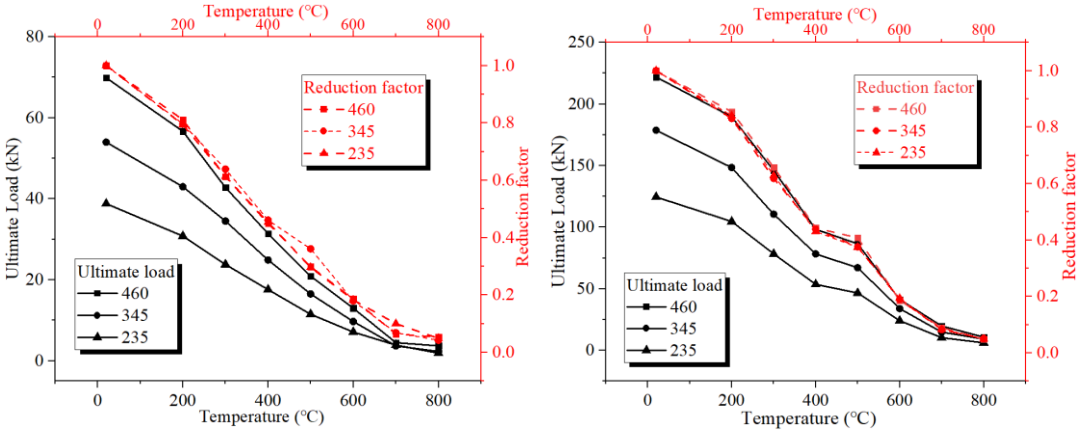

(a) t_C=6mm (d) t_C=12mm

Fig. 19 Influence of material property of steel tube on ultimate load F_U

Table 4
Comparison of connections with different tube materials

Tube wall thickness t_c(mm)	Temperature θ(°C)	Initial stiffness K (kN/mm)			Yielding load F_Y(kN)			Ultimate Load F_U(kN)			Failure mode		
		235	345	460	235	345	460	235	345	460	235	345	460
6	20	13.9	13.7	13.8	18.5	25.3	32.8	38.8	54.0	69.9	mode1	mode1	mode1
	200	12.5	12.5	12.5	15.8	21.5	27.5	30.8	43.0	56.7	mode1	mode1	mode1
	300	11.4	11.2	11.4	11.2	16.6	20.9	23.8	34.5	42.8	mode1	mode1	mode1
	400	9.2	9.0	9.2	8.6	12.5	15.4	17.6	24.9	31.4	mode1	mode1	mode1
	500	8.6	8.2	8.6	6.1	9.2	10.4	11.5	16.5	20.9	mode1	mode1	mode1
	600	4.0	4.0	4.0	3.5	5.3	5.9	7.1	9.7	13.0	mode1	mode1	mode1
	700	1.9	1.6	1.9	1.7	2.2	2.3	3.9	3.7	4.5	mode1	mode1	mode1
	800	1.3	1.3	1.3	0.9	1.4	1.5	1.9	2.3	3.7	mode1	mode1	mode1
12	20	72.6	72.6	72.6	72.2	104.5	125.4	124.5	178.7	221.9	mode2	mode2	mode2
	200	65.8	65.8	65.8	59.2	82.2	103.7	104.6	148.4	189.6	mode2	mode2	mode2
	300	59.1	59.8	59.1	47.5	67.1	83.2	78.3	110.5	146.0	mode2	mode2	mode2
	400	52.2	52.2	52.2	33.6	48.7	61.2	53.6	78.3	98.3	mode2	mode2	mode2
	500	45.2	45.2	45.3	30.7	44.1	53.6	46.6	67.1	86.5	mode2	mode2	mode2
	600	24.1	24.1	24.2	15.1	22.0	25.7	24.1	33.9	41.3	mode2	mode2	mode2
	700	10.4	10.3	10.4	6.6	9.6	11.6	10.3	14.8	19.8	mode2	mode2	mode2
	800	7.1	7.2	7.2	4.1	5.3	7.8	6.2	9.2	10.8	mode2	mode2	mode2

3.4. Influence of internal constraint component

Closed-section steel columns exhibit superior torsional and flexural properties, hence the wall thickness (t_C) is typically quite small. To prevent premature failure of the connections compared to other components, it may be necessary to reinforce the connection regions of steel tube columns. Additionally, the tube wall thickness (t_C) is a critical parameter that directly influences the failure mode and load-bearing capacity of TOB connections. Therefore, to ensure the effectiveness of TOB connections, reinforcing the connection areas is also essential. One approach to strengthening these areas involves installing an Internal Constraint Component (ICC) inside the steel tube, such as an H-shaped steel.

The installation of the ICC can be carried out as follows, as illustrated in Fig. 20:

1. Cut openings in the column at the connection area to serve as plug welding holes.
2. Insert the ICC into the specified position.
3. Temporarily weld the ICC in place through the plug welding holes.
4. Create threaded holes penetrating both the steel tube column and the ICC.

This method addresses the challenges of limited construction space in closed-section steel tube columns. It ensures reliable fixation of the ICC within the steel tube and guarantees the quality of threaded hole machining, preventing issues like misalignment of bolt holes or discontinuous threads.

However, it is inevitable that there will be a gap between the ICC and the column wall, resulting in discontinuity of the hole threads. Moreover, the stress distribution on the bolt shank is not uniform, leading to discontinuous deformation and load distribution between the ICC and the column wall. Consequently, it is essential to research how the ICC and the column wall work together and to evaluate the reinforcing effect of the ICC on the TOB connections.

FEM analysis has been conducted to assess the load-bearing performance of TOB connections utilizing H-shaped steel as the ICC. The studied connections had a tube wall thickness (t_C) of 6mm, a bolt diameter (D) of 16mm, a T-stub flange thickness (t_T) of 12mm, and an H-shaped steel flange thickness (t_H) ranging from 6mm to 16mm.

With the increase in the flange thickness of the H-shaped steel (t_H), the reinforcing effect of the ICC on the connection gradually increases. Consequently, the failure mode of the connection changes from tube column wall yielding (mode 1) to T-stub flange yielding accompanied by bolt failure (mode 2). For H-shaped steel flange thicknesses (t_H) below 12mm (equivalent to twice the tube wall thickness t_C), the connections typically exhibit failure mode 1. Conversely, when the flange thickness (t_H) of the H-shaped steel is 12mm or more, the connections exhibit failure mode 2. Fig. 21 and Fig. 22 show the stress distribution and the PEEQ within the threaded holes of the connection when the yielding load F_Y is reached. It is observed that the stress distribution inside the threaded holes of the connection is nonuniform, with overall stress in the threaded holes on the H-shaped steel flange being greater than that on the steel tubular column. This indicates that the H-shaped steel provides additional anchorage force for the TOB. Moreover, under the yielding load F_Y, only minor PEEQ occurs locally in the threaded holes of both the H-shaped steel and the steel tubular column, suggesting that the threaded holes still effectively provide reliable anchoring for the bolts.

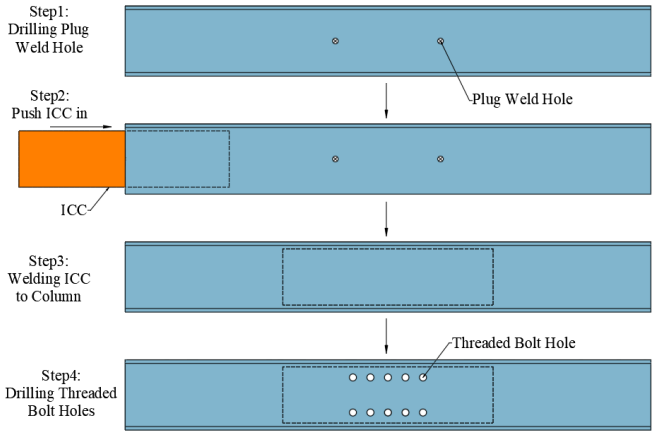

Fig. 20 Progress of installing the ICC inside the column

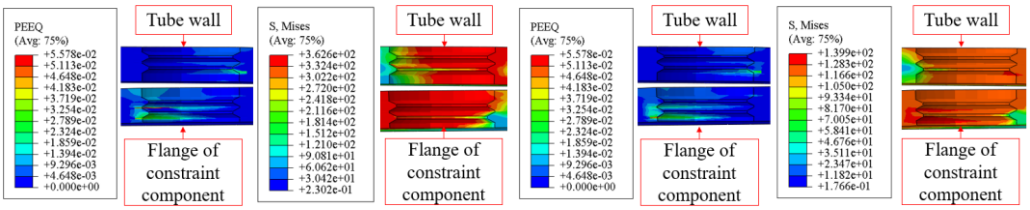

(a) θ=20℃ (b) θ=500℃

Fig. 21 State of the hole threads under yielding load F_Y (t_H=6mm)

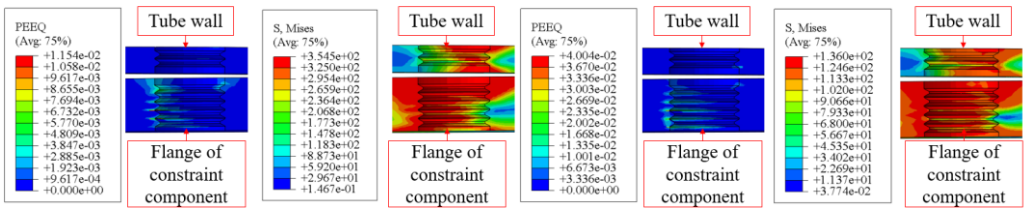

(a) θ=20℃ (b) θ=500℃

Fig. 22 State of the hole threads under yielding load F_Y (t_H=12mm)

Fig. 23 compares the relationship between the initial stiffness K, yielding load F_Y, and ultimate load F_U of the connection with the flange thickness t_H of the H-shaped steel. When t_H does not exceed 12mm, initial stiffness K, yielding load F_Y, and ultimate load F_U of the connection all increase rapidly with the increase of t_H. However, once t_H reaches 12mm, the influence becomes minimal. This is attributed to a change in the failure mode of the connection. Below 12mm t_H, the failure mode is tube column wall yielding (mode 1), where the load-bearing performance of the connection is determined by the resistance tube column wall. For larger t_H values, the failure mode changes to T-stub flange yielding accompanied by bolt failure (mode2). In this case, the resistance of the column wall to out-of-plane deformation exceeds the bending resistance of the T-stub flange. As a result, further increases in t_H less influential on the load-bearing capacity of the connection. Despite the significant differences in stiffness and load-bearing performance among connections with varying t_H, their degradation under high temperatures are similar. Fig. 23 shows that the degradation speed of initial stiffness K, yielding load F_Y, and ultimate load F_U at high temperatures are consistent across different connections.

Taking connections with t_H of 6mm and 12mm as examples, the impact of the material strength of the ICC on the connection was compared, as shown in Fig. 25. The strength of the ICC has no significant effect on the initial stiffness K of the connection. However, the material strength of the ICC significantly influences the yielding load F_Y and ultimate load F_U of the connection at different temperatures. For instance, at a temperature θ of 20°C, increasing the strength of the ICC from Q235 to Q460 led to an increase of 84% and 86% in the yielding load F_Y and ultimate load F_U, respectively for a connection with t_H of 6mm. For a connection with a t_H of 12mm, the increases were 41% in F_Y and

38% in F_U. Nonetheless, changing the strength of the ICC did not alter the failure mode of the connection, nor did it significantly change the degradation speed of the yielding load F_Y and ultimate load F_U at high temperatures.

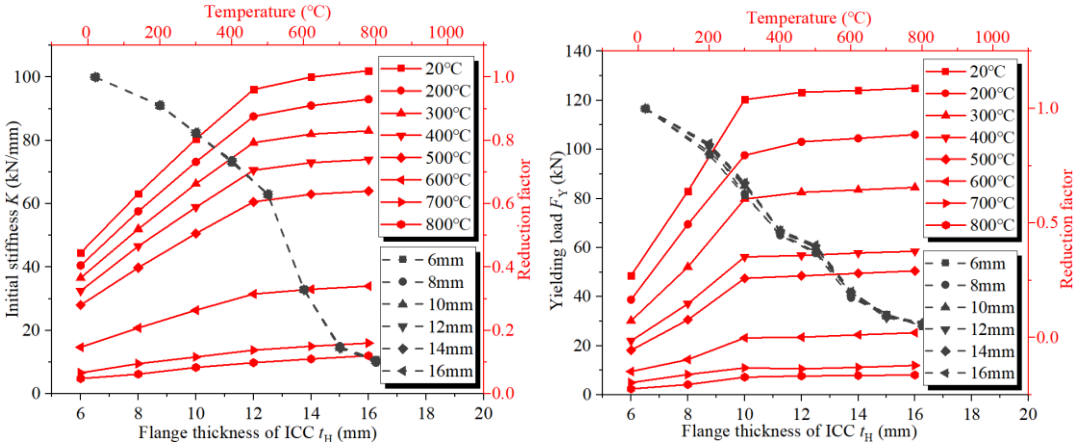

(a) Initial stiffness K (b) Yielding Load F_Y

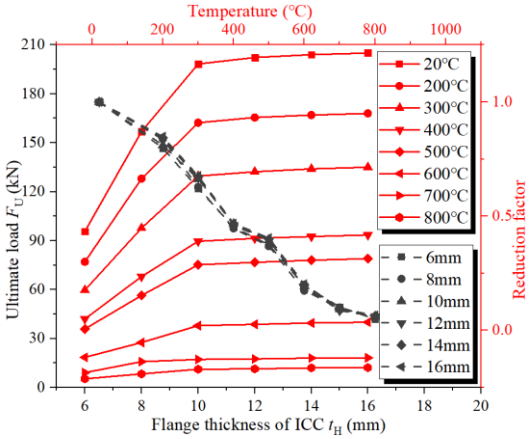

(c) Ultimate Load F_U

Fig. 23 Influence of flange thickness of ICC t_H on the tensile behavior of connections

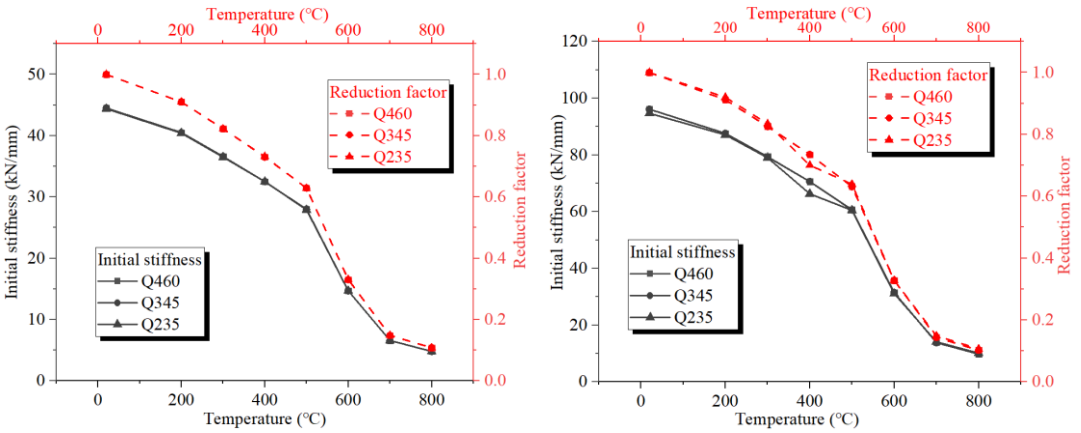

(a) t_C=6mm (d) t_C=12mm

Fig. 24 Influence of material property of ICC on initial stiffness K

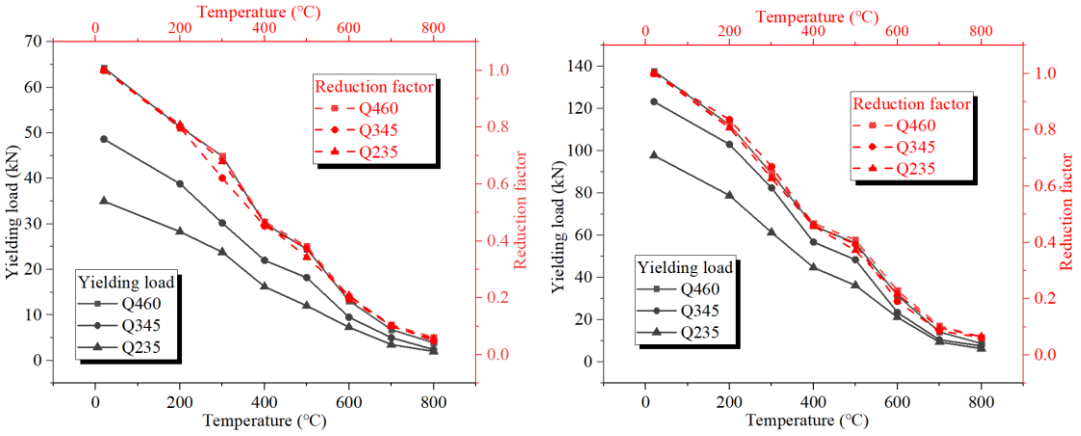

(a) t_C=6mm (d) t_C=12mm

Fig. 25 Influence of material property of ICC on yielding load F_Y

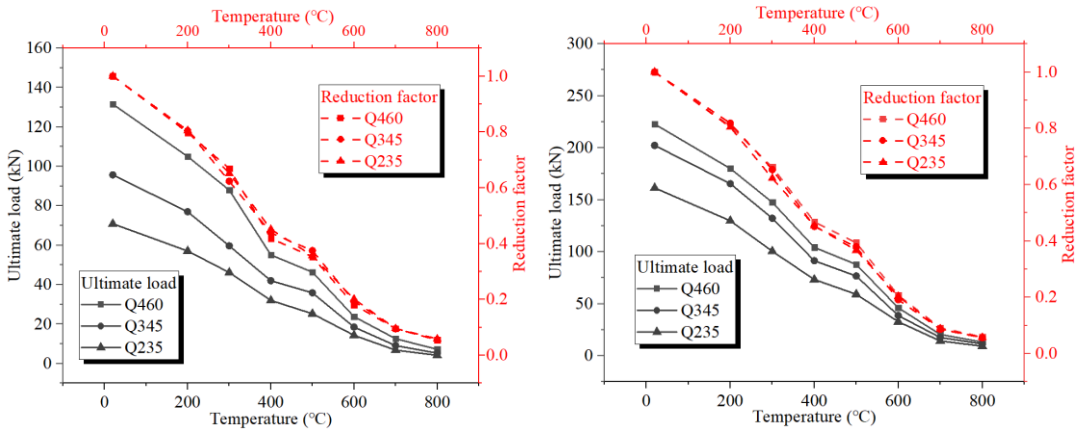

(a) t_C=6mm (d) t_C=12mm

Fig. 26 Influence of material property of ICC on ultimate load F_U

4. Calculation of the tensile resistance

4.1. Calculation method for failure mode 1

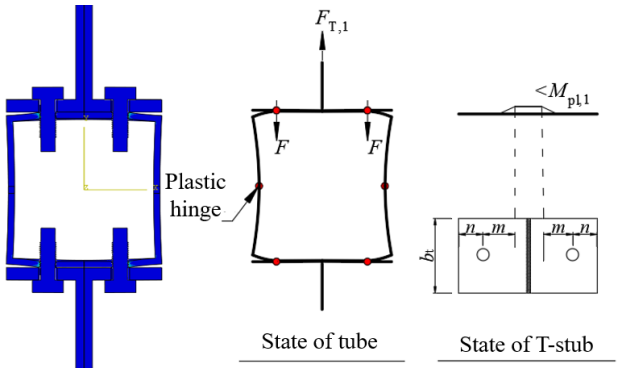

Fig. 27 Calculation model of mode 1

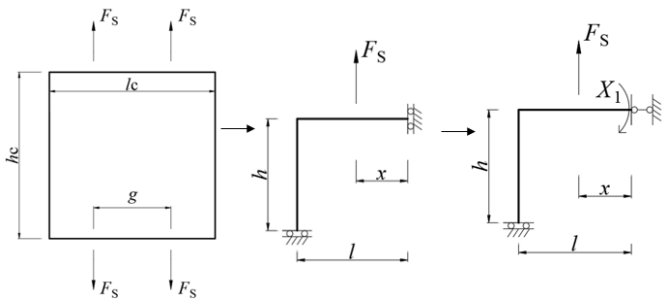

Fig. 28 Simplified calculation model

When the connection exhibits failure mode 1, characterized by tube column wall yielding, the primary features include minor deformation of the T-stub and significant out-of-plane deformation of the steel tube wall. The deformation of the steel tube sidewalls is predominantly horizontal, while the top and bottom surfaces mainly exhibit vertical deformation. Based on the deformation characteristics of the steel tube, a simplified computational model can be established as shown in Fig. 27. Due to the symmetry of the connection, a quarter-section of the steel tube structure with sliding supports at both ends can be use for analyzing, as shown in Fig. 28.

The simplified quarter model is subjected to a concentrated force, F_S, at the bolt axis position, with a height of h and a length of l, and the distance from the concentrated force F_S to the sliding support is x. Since this simplified model constitutes a statically indeterminate structure, it cannot be directly solved using conditions of static equilibrium and moment balance. Instead, the method of forces from structural mechanics can be applied, decomposing a sliding support into a hinged support and an equivalent bending moment X, as shown in Fig. 28. The deformations under the concentrated force F_S and under the bending moment X can then be determined using the principle of virtual work.

By ensuring deformation compatibility at the sliding supports before and after simplification, a new equilibrium equation (4) can be established. Solving this equation yields the magnitude of the bending moment X_1, which in turn allows for the construction bending moment diagram of the entire steel frame.

$$\delta X + \Delta_F = \Delta \tag{4}$$

Here δ is the angle of rotation at the sliding support when X=1, representing the structural flexibility coefficient under the action of bending moment X; Δ_F is the angle of rotation of the structure in the direction of bending moment X caused by the external force F_S; Δ is the actual displacement at the point of release of the redundant support in the original structure. Since the sliding support in the original structure do not allow rotation, Δ is zero at this point.

The bending moment diagrams under the bending moment X=1 and under the action of the concentrated force F_S are shown in Fig. 29. Then, according to the principle of virtual work, it can be determined:

$$\delta = \int_0^l \frac{1\times 1}{EI} ds + \int_0^l \frac{1\times 1}{EI} ds = \frac{2l}{EI} \tag{5}$$

$$\Delta_F = \int_0^l \frac{F_S \times (l-x)}{EI} ds + \int_{l-x}^l \frac{F_S \times s}{EI} ds = \frac{1}{EI} Fl(l-x) + \frac{1}{2EI} x(2l-x) \tag{6}$$

By combining Eqs (4), (5), and (6), it can be derived that:

$$X = \frac{F_S(l-x)}{2} + \frac{F_S x(2l-x)}{4l} \tag{7}$$

By superimposing the bending moment diagrams in Fig. 29, the bending moment diagram for the original steel frame can be obtained, as shown in Fig. 30. Furthermore, this allows for the determination of the magnitude of the bending moment M_H at the sliding support in the upper right corner of the steel frame:

$$M_H = \frac{F_S(l-x)}{2} + \frac{F_S x(2l-x)}{4l} \tag{8}$$

FEM results indicate that significant deformation occurred both at the bolt axis and at the midpoint of the side wall of the steel tube, suggesting that yielding has likely occurred at these locations. Therefore, by isolating the section at the sliding support, the stress distribution can be observed as shown in Fig. 31. In the area affected by M_H, there is no axial force influence, and the equilibrium conditions of the isolated section yield the following:

$$M_H = \frac{f_y l_{eff} t_c^2}{4} \tag{9}$$

Here, l_{eff} is the length of yield line. By combining Equations (8) and (9), it can be obtained that:

$$F_S = \frac{f_y l_{eff} t_C^2 l}{2l^2 - x^2} \tag{10}$$

The above derivation is based on the premise of minimal deformation of the connection. However, in reality, connections that exhibit failure mode 1 have relatively thin steel tube walls and exhibit significant out-of-plane deformation upon yielding. This deformation is especially pronounced at high temperatures, where the elastic modulus of the connection rapidly decreases, leading to even more pronounced deformation. Therefore, the impact of large deformations on the load-bearing capacity of the connection cannot be ignored. When failure mode 1 occurs, the deformation of the connection primarily consists of inward horizontal displacement of the side walls and outward vertical displacement of the top and bottom surfaces, denoted as Δ_V and Δ_H, respectively, as shown in Fig. 32. In the case of small deformations, the following equilibrium equation can be obtained:

$$M_H = M_V + F(l-x) \tag{11}$$

In the case of large deformations, the following equilibrium equation can be established:

$$M_{H,large} = M_{V,large} + F_{large}(l - x - \Delta_V) \tag{12}$$

Assuming that large deformations of the connection only alter the magnitude of the bending moment without changing the distribution pattern of the bending moment diagram, that is:

$$\frac{M_{H,large}}{M_{V,large}} = \frac{M_H}{M_V} \tag{13}$$

By combining Eqs (11), (12), and (13), it can be derived that:

$$F_{S,large} = \frac{1 - x - \Delta_V}{1 - x} F_S \tag{14}$$

Therefore, the bearing capacity reduction coefficient k_Δ considering the influence of large deformation can be obtained:

$$k_\Delta = \frac{1 - x - \Delta_V}{1 - x} \tag{15}$$

To determine the value of k_Δ, it is also necessary to determine the magnitude of Δ_V. In order to simplify the calculation, it is assumed that Δ_V is 3% of the width of the tube, that is:

$$\Delta_V = 0.03 b_C \tag{16}$$

Here, b_c is the width of the tube. Considering the strength reduction of steel at high temperatures, the calculation method of bearing capacity of the connection at high temperature $F_{S,\theta}$ considering large deformation can be obtained:

$$F_{S,\theta} = \Delta_V \frac{f_{y,\theta} l_{eff}^2 t_C^2 l}{2l^2 - x^2} \tag{17}$$

$$F_{T,1} = 2F_S \tag{18}$$

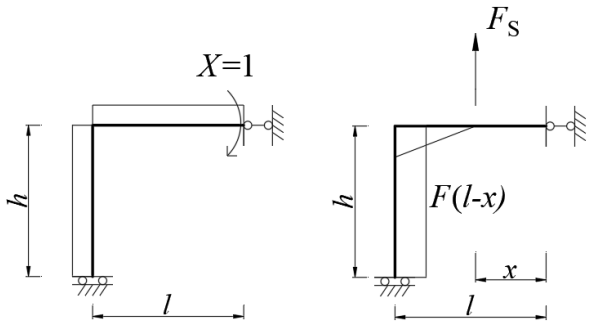

Fig. 29 The bending moment diagram under X=1 and F_S

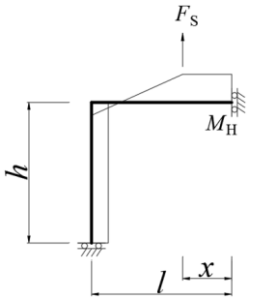

Fig. 30 The solved bending moment diagram of the steel frame

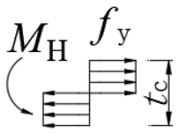

Fig. 31 The stress distribution of the section near the support

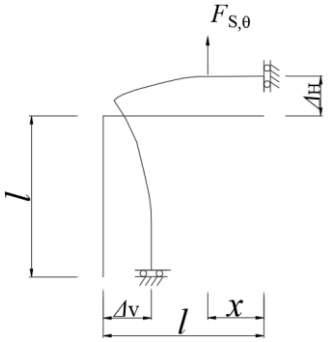

Fig. 32 The frame under large deformation

4.2. Calculation method for other failure modes

When the connection exhibits failure mode 2, T-stub flange yielding accompanied by bolt failure, the deformation of the steel tube is minor. The deformation is primarily concentrated on the T-stub, where a yield line forms at the junction between the web and flange of the T-stub. Simultaneously, the bolt reaches its maximum load-bearing capacity and fractures. The internal energy consumed by the yield line is:

$$M_{pl}=0.25l_{eff}t_t^2 f_y \tag{19}$$

By separately analyzing the flange of the T-stub, it can be considered as a beam, with its bending moment diagram shown in Fig. 33. Additionally, the beam is subjected to the combined effects of the external force $F_{T,2}$, the prying force Q, and the bolt tension F_b. From the conditions of static equilibrium, it can be derived that:

$$F_{T,2}+2Q=2F_b \tag{20}$$

Additionally, the balance condition of the bending moment at the junction between the T-stub flange and the web can be obtained as follows:

$$M_{pl}=mF_b-(m+n)Q \tag{21}$$

where m and n are the dimensional parameters of the T-stub, as shown in Fig. 33.

By combining Eqs (19), (20), and (21), and eliminating the prying force Q, the load-bearing capacity $F_{T,2}$ of failure mode 2 can be obtained:

$$F_{T,2}=\frac{2nF_b+2M_{pl}}{m+n} \tag{22}$$

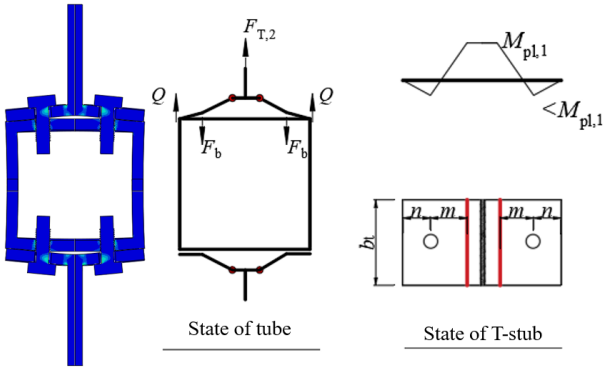

Fig. 33 Calculation model of the connection failed by mode 2

Through a similar method, the load-bearing capacity of connections exhibiting failure mode 3 can also be derived. When the connection experiences failure mode 3, characterized by T-stub flange yielding, the deformation of the steel tube is minimal, while the deformation of the T-stub flange is more pronounced. Yield lines occur at the intersection of the web and flange of the T-stub as well as at the bolt holes, leading to the simplified calculation model shown in Fig. 34. The T-stub is simplified as a beam for analysis, subjected to the combined effects of a prying force Q, external force $F_{T,3}$, and bolt tension F_b, where the bending moment diagram is characterized by reaching M_{pl} at both the positions corresponding to the bolt holes and at the intersection of the T-stub web and flange. Thus, through the conditions of static equilibrium and bending moment equilibrium, it can be obtained that:

$$F_{T,3}+2Q=2F_b \tag{23}$$

$$M_{pl}=mF_b-(m+n)Q \tag{24}$$

$$M_{pl}=Qn \tag{25}$$

By combining Eqs (23), (24), and (25), it can be derived that:

$$F_{T,3}=\frac{4M_{pl}}{m} \tag{26}$$

When the connection exhibits failure mode 4, bolt fracture failure, the deformation of both the steel tube and the T-stub is relatively minor, and the load-bearing capacity of the connection is solely determined by the load-bearing capacity of the bolt. The model for calculating this type of connection is shown in Fig. 35. The equation for calculating its load-bearing capacity is:

$$F_{T,4}=\sum F_b \tag{27}$$

$$F_b=\frac{\pi d^2}{4} f_{yb} \tag{28}$$

where d is the effective diameter of the bolt, and $f_{y,b}$ is the yield strength of the bolt.

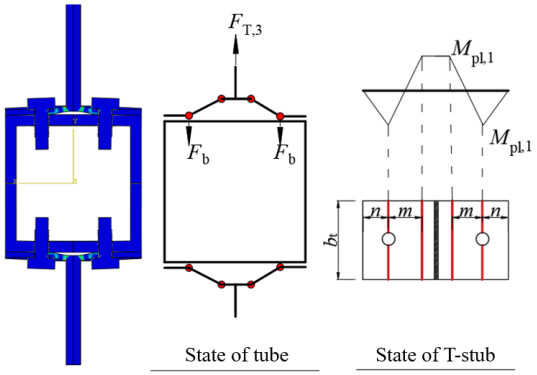

Fig. 34 Calculation model of the connection failed by mode 3

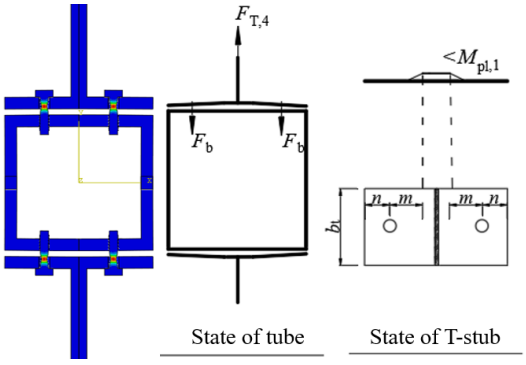

Fig. 35 Calculation model of the connection failed by mode 4

4.3. Calculation method for connections with ICC

For connections with ICC, the potential failure modes are the same as those without ICC. When the connection experiences failure modes 2, 3, or 4, the location of failure is independent of the ICC, thus the calculation method remains the same as for the connections without ICC. However, when failure mode 1 occurs, the cooperative action between the ICC and the steel tube must be considered. FEM analysis reveals that for connections with ICC experiencing failure mode 1, the out-of-plane deformation of the tube wall is significantly restricted upon reaching its yield load F_Y, and both the bolts and T-stub remain in the elastic state. Based on these characteristics, the following assumptions can be mad:

1. Ignore the effect of the plug welding between the ICC and the tube wall;
2. Ignore the axial deformation of the bolt in the ICC and the tube wall;
3. Ignore the out-of-plane deformation of the steel tube sidewall.

In calculations, both the steel tube wall and the ICC are treated as beam to establish the calculation model shown in Fig. 36.

The deformations produced at the bolt axis by the tube wall and the ICC are denoted as δ_{SHS} and δ_H, respectively. Given that the axial deformation of the bolt shank in the gap between the tube and the ICC is neglected, the following deformation compatibility relationship is established:

$$\delta_{SHS} = \delta_H \tag{29}$$

In addition, based on the equilibrium of forces:

$$F_S = F_{SHS} + F_H \tag{30}$$

Where F_S is the total anchorage of the threads within the hole, which is also equal to the axial force on the bolt shank; F_{SHS} is the load carried by the threaded holes of the tube; F_H is the load carried by the threaded holes of the H-shaped steel flange, acting as the ICC. Based on the unit load method, which relies on the principle of virtual work, expressions for δ_{SHS} and δ_H can be separately derived. The derived expression for δ_H is as follows:

$$\delta_H = \frac{F_H l x^2}{6EI_H}\left(3 - \frac{x}{l}\right) \tag{31}$$

$$I_H = \frac{b_H t_H^2}{12} \tag{32}$$

I_H, b_H, and t_H represent the moment of inertia for bending resistance, width, and flange thickness of the ICC, respectively. The expression for δ_{SHS} is as follows:

$$\delta_{SHS} = \frac{1}{EI_{SHS}}\left(\frac{2}{3}F_{SHS}(l-x)^3 + \frac{F_{SHS}(l-x)^4(2x-l)}{4l^2}\right) \tag{33}$$

$$I_{SHS} = \frac{b_c t_c^2}{12} \tag{34}$$

I_{SHS}, b_c, and t_c represent the moment of inertia for bending resistance, width, and thickness of the tube wall, respectively. Through Equations (29) and (30), the relationship between F_{SHS} and F_H can be established:

$$F_{SHS} = 2\frac{I_{SHS}}{I_H}\frac{l^2x^2(3l-x)}{8(l-x)^3l^2 + 3(l-x)^4(2x-l)}F_H \tag{35}$$

Hence, the influence coefficient k_H of ICC is:

$$k_H = \frac{F_S}{F_{SHS}} = \frac{F_{SHS} + F_H}{F_{SHS}} = \frac{(8(l-x)^3l^2 + 3(l-x)^4(2x-l))I_H + 2l^2x^2(3l-x)I_{SHS}}{2l^2x^2(3l-x)I_{SHS}} \tag{36}$$

Given that the effect of plug welding is not considered, the ICC and the tube only transfer load through bolts, thus the ICC does not change the bending moment distribution pattern of the tube wall but only changes its magnitude. Therefore, Eq (17) can still be applied to solve for the bending moment on the tube column, leading to the conclusion that:

$$F_S = k_H\frac{f_y l_{eff} t_c^2 l}{2l^2 - x^2} \tag{37}$$

$$F_{T,1} = 2F_S \tag{38}$$

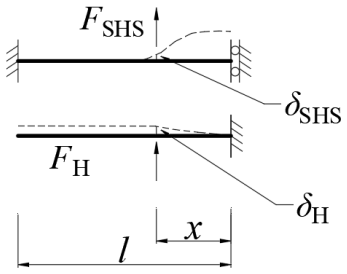

Fig. 36 Calculation model for the connection with ICC failed by mode 1

4.4. Accuracy analysis of calculation methods

The calculated load F_E of the connections at different temperatures θ using the derived equations, compared with the yielding load F_Y obtained from FEM calculations are shown in Fig. 37. It is observed that for TOB connection without ICC, the calculated load F_E at different temperatures θ derived from the equations closely matches the yielding load F_Y obtained from the FEM, with an average F_E to F_Y ratio of 1.012, a standard deviation of 0.084, and a coefficient of variation of 0.083. For connections with ICC, the disparity between calculated load F_E and the yielding load F_Y obtained from FEM is slightly larger, with an average F_E to F_Y ratio of 0.969, a standard deviation of 0.121, and a coefficient of variation of 0.125. However, the overall accuracy remains satisfactory.

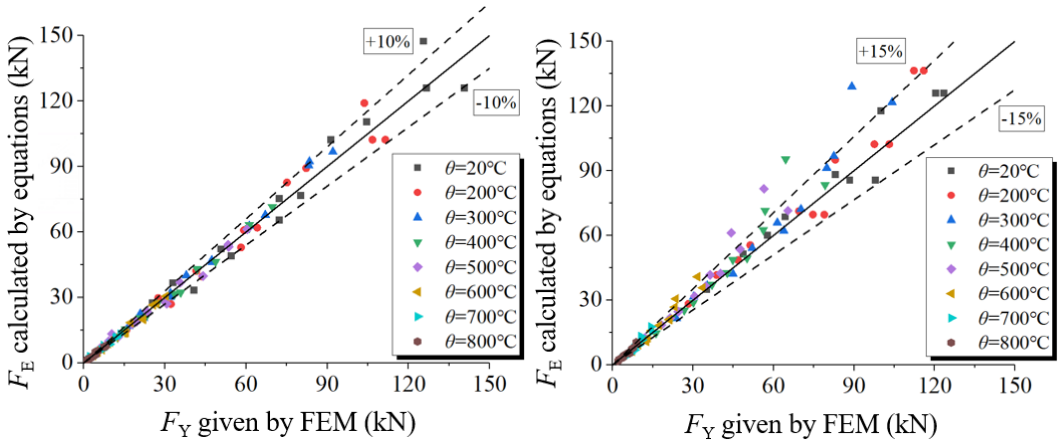

(a) connections without ICC (b) connections with ICC

Fig. 37 Comparison of the simulation result and calculation results

5. Conclusions

This study developed and validated a finite element model to analyze the mechanical performance of T-stub to steel tube connections bolted by TOB under high-temperature conditions. The key findings and contributions are as follows:

(1) Based on the parameters of the connection, there are four potential failure modes for TOB connections: tube column wall yielding (mode1), T-stub flange yielding accompanied by bolt failure (mode2), T-stub flange yielding (mode3), and bolt fracture failure (mode4).

(2) Bolt preload forces, as per the Chinese Code GB50017-2017, slightly enhance the initial stiffness of the connection but have minimal influence on the load-bearing capacity. The influence of preload diminishes as temperature increases.

(3) The failure mode and initial stiffness of the connection are influenced by dimensional parameters but are less affected by the tube strength. Steel

strength improvement significantly enhances the yielding and ultimate load, though its influence diminishes at higher temperatures.

(4) Installing Internal Constraint Components (ICC) effectively enhances connection performance, especially for tubes with smaller wall thicknesses. The material strength and flange thickness of ICCs significantly influence the stiffness and failure mode of the connection.

(5) A method for calculating the load-bearing capacity of TOB connections under high temperatures has been introduced and validated through comparisons with FEM results. The proposed method accurately predicts the yielding load capacity of TOB connections, both with and without ICC, across different temperature conditions.

Acknowledgments

This paper was supported by the Natural Science Foundation of Shandong Province (ZR2023QE324, ZR2024ME215).

Nomenclatures and variables

F_y	Yielding load
F_u	Ultimate load
F_T	calculated tension resistance
M_{pl}	bending strength of T-stub flange
$l_{eff,f}$	length of the yielding line
t_f	thickness of T-stub flange
b	width of the T-stub
m	distance between weld toe and bolt hole
e	end distance of T-stub flange
TOB	Thread-fixed One-side Bolt
TB	Traditional Bolt
FEM	Finite Element Model
PEEQ	plastic equivalent strain

References

[1] You Y, Li Y, Lin C, et al. Post-fire behavior of square hollow section column connections using thread-anchored blind bolts[C]//Structures. Elsevier, 2024, 59: 105706.

[2] Lindapter. Type HB – Hollo-bolt. Cavity fixings 2, Product brochure. UK: Lindapter International; 2012. p. 41–3.

[3] Wang Z Y, Wang Q Y. Yield and ultimate strengths determination of a blind bolted endplate connection to square hollow section column[J]. Engineering structures, 2016, 111: 345-369.

[4]. Cabrera M, Tizani W, Ninic J, et al. Experimental and numerical analysis of preload in Extended Hollo-Bolt blind bolts[J]. Journal of Constructional Steel Research, 2021, 186: 106885.

[5] Pan H, Chen J, Liu Y. Low-cycle fatigue behavior on the tensile region of Hollo-bolted angle connections[J]. Journal of Constructional Steel Research, 2023, 208: 107967.

[6] Pascual A M, Romero M L, Tizani W. Fire performance of blind-bolted connections to concrete filled tubular columns in tension[J]. Engineering Structures, 2015, 96: 111-125.

[7] Pascual A M, Romero M L, Tizani W. Thermal behaviour of blind-bolted connections to hollow and concrete-filled steel tubular columns[J]. Journal of Constructional Steel Research, 2015, 107: 137-149.

[8] Song T Y, Tao Z, Razzazzadeh A, et al. Fire performance of blind bolted composite beam to column joints[J]. Journal of Constructional Steel Research, 2017, 132: 29-42.

[9] Lee J, Goldsworthy H M, Gad E F. Blind bolted T-stub connections to unfilled hollow section columns in low rise structures[J]. Journal of Constructional Steel Research, 2010, 66(8-9): 981-992.

[10] Hosseini S M, Mamun M S, Mirza O, et al. Behaviour of blind bolt shear connectors subjected to static and fatigue loading[J]. Engineering Structures, 2020, 214: 110584.

[11] BS EN 1993-1-8. Design of Steel Structures - Part 1-8: General Rules - Design of Joints. European Committee for Standardization, Brussels (2005)

[12] Wan C, Bai Y, Ding C, et al. Mechanical performance of elliptical one-sided joints: Loading direction and bolt row effects[J]. Journal of Constructional Steel Research, 2022, 197: 107461.

[13] Sun L, Liu M, Liu Y, et al. Studies on T-shaped one-side bolted connection to hollow section column under bending[J]. Journal of Constructional Steel Research, 2020, 175: 106359.

[14] Li Y L, Zhao X L. Study on stainless steel blind bolted T-stub to concrete-filled stainless steel tube connections[J]. Engineering Structures, 2022, 257: 114107.

[15] Fan S, Wang J, Duan S, et al. Experimental study on forming mechanism and mechanical properties of novel self-tightening one-side bolt[J]. Engineering Structures, 2023, 283: 115915.

[16] You Y, Li Y, Lin C, et al. Postfire Performance of Thread-Anchored Blind-Bolted Connection[J]. Journal of Structural Engineering, 2023, 149(12): 04023173.

[17] You Y, Zhang S, Xing D, et al. Study on tensile behavior and design methods of thread-fixed one-side bolted joints to concrete-filled steel tubes[J]. Journal of Constructional Steel Research, 2024, 222: 108958.

[18] Li G Q, Jiang Y H, Zhong Y L, et al. Studies on resistance behavior of modified blind-bolts under pure tension and shear[J]. Journal of Constructional Steel Research, 2023, 210: 108114.

[19] You Y, Zhu H, Liu X, et al. Post fire tensile behavior of thread-fixed one-side bolt strengthened by backing plate[J]. Engineering Structures, 2022, 252: 113577.

[20] You Y, Liu M, Liu Y, et al. Experimental studies on thread-fixed one-side bolted T-stubs in tension at elevated temperatures[J]. Journal of Constructional Steel Research, 2020, 171: 106139.

[21] Wang P, You Y, Wang Q, et al. Post-fire tensile behavior of hole-anchored bolted T-stub connection[J]. Journal of Constructional Steel Research, 2021, 187: 106941.

[22] P398. Steel Construction Institute. Joints in Steel Construction: Moment-Resisting Joint to Eurocode 3 (2014)

[23] Wang W, Zhang Y, Xu L, et al. Mechanical properties of high-strength Q960 steel at elevated temperature[J]. Fire safety journal, 2020, 114: 103010.

[24] BS EN 1993-1-2. Design of Steel Structures - Part 1-2: General Rules - Structural Fire Design European Committee for Standardization, Brussels (2005)

[25] Pang X P, Hu Y, Tang S L, et al. Physical properties of high-strength bolt materials at elevated temperatures[J]. Results in Physics, 2019, 13: 102156.

[26] GB 50017–-2017. Code for Design of Steel Structure. China Architecture Publishing & Media Co. Ltd. Beijing (2017). (in Chinese)

[27] Wang F, Zhao O, Young B. Testing and numerical modelling of S960 ultra-high strength steel angle and channel section stub columns[J]. Engineering Structures, 2020, 204: 109902.

[28] Pijpers R J M, Slot H M. Friction coefficients for steel to steel contact surfaces in air and seawater[C]//Journal of Physics: Conference Series. IOP Publishing, 2020, 1669(1): 012002.

[29] Wang P, You Y, Xu Q, et al. Shear Behavior of Lapped Connections Bolted by thread-fixed one-side bolts at elevated temperatures[J]. Fire Safety Journal, 2021, 125: 103415.

[30] Yu H, Burgess I W, Davison J B, et al. Numerical simulation of bolted steel connections in fire using explicit dynamic analysis[J]. Journal of Constructional Steel Research, 2008, 64(5): 515-525.

[31] Wang P, You Y, Liu M, et al. Behavior of thread-fixed one-side bolted T-stubs with backing plates at ambient and elevated temperatures[J]. Journal of Constructional Steel Research, 2020, 170: 106093.

[32] You Y, Gu H, Wang Q, et al. Fire behavior of novel Thread-anchored One-side bolted connection with internal component[J]. Journal of Constructional Steel Research, 2022, 194: 107337.

[33] GB/T 192–-2003. National Standard of Peoples Republic of China, General Purpose Metric Screw Threads-basic Profile. China Construction Press (2003). (in Chinese)

[34] GB/T 196–-2003. National Standard of Peoples Republic of China, General Purpose Metric Screw Threads-basic Dimensions. China Construction Press (2003). (in Chinese)

[35] Liu Y, You Y, Bai Y, et al. Behavior of Square Hollow Section column connection using Thread-anchored One-side Bolt under tensile force at high temperature[J]. Journal of Building Engineering, 2022, 50: 104150.

[36] You Y, Le L, Xiao J, et al. A numerical investigation of the tensile behavior of the thread-fixed one-side bolted T-stubs at high temperature[J]. Steel and Composite Structures, 2022, 45(4): 605.

[37] Wang P, Sun L, Liu M, et al. Experimental studies on thread-fixed one-side bolted connection of beam to hollow square steel tube under static bending moment[J]. Engineering Structures, 2020, 214: 110655.

Advanced Steel Construction – Vol. 21 No. 2 (2025) 174–181
DOI:10.18057/IJASC.2025.21.2.8

EXPERIMENTAL STUDY ON SHEAR PERFORMANCE OF TWO-STORY COMPOSITE COLD-FORMED THIN-WALL STEEL EXTERIOR WALL

Yun-Peng Chu, Hui Xia * and Ya-Xin Xiao

School of Civil Engineering and Architecture, Southwest University of Science and Technology, Mianyang 621010, China
** (Corresponding author: E-mail: 2511830340@qq.com)*

ABSTRACT

This study investigates the shear performance of composite cold-formed thin-wall steel walls, particularly in two-story configurations. 9 test groups with varying axial compression and anchor bolt types were examined. Results show that, compared to single-story walls, the two-story walls exhibit lower energy dissipation and ductility, with floor joints being the weak link under cyclic loading. Out-of-plane instability and buckling failure often occur at the floor joint, which is critical to maintaining wall strength. The inter-layer tension bar has little effect on enhancing shear capacity. As axial pressure increases, out-of-plane instability worsens, and simply improving the vertical compressive strength of the floor joint with anchor bolts is insufficient to mitigate this issue. However, double-nut anchor bolts significantly improve the wall's load-bearing capacity. Therefore, the use of anchor bolts at floor joints is recommended to enhance the shear capacity of multi-story structures.

ARTICLE HISTORY

Received: 10 September 2024
Revised: 24 December 2024
Accepted: 1 January 2025

KEYWORDS

Cold-formed thin-wall steel two-story wall;
Cyclic loading;
Experimental study;
Shear performance;
Failure mode

1. Introduction

The composite cold-formed thin-wall steel two-story exterior wall composed of upper and lower single walls connected by a floor joint, formed by joining the boundary track with the top and bottom tracks through self-drilling screws. This construction method, where components are fabricated in the factory and assembled on-site, follows the technical specifications for low-rise cold-formed thin-walled steel framing buildings (JGJ/T 421–2018) [1]. The composite wall, connected by self-drilling screws, is subjected to external loads, enabling quick and straightforward industrialization of building construction.

Extensive experimental studies and theoretical analyses have been conducted to evaluate the shear performance of single-layer configurations of these walls. These results have been applied in engineering practice [2], and shaking table tests have shown good seismic performance under frequent (7-degree) and rare (9-degree) earthquakes. However, these walls tend to experience minor damages, such as screw dislodgment and cracking under large earthquakes [3]. In multi-story buildings, horizontal seismic impacts increase with the number of floors, raising concerns about whether the practices outlined in the specification [1] can effectively resist these heightened seismic effects.

The force transfer at the floor joint is discontinuous due to the construction method. When the top of the wall experiences horizontal seismic action, bending moments and shear forces develop at each floor level [4]. Existing wall seismic tests [5] indicate that the strain on the interlayer steel tension band increases significantly, whereas the strain on the inner layer steel tension band increases to a lesser extent. This discrepancy highlights that the connection quality between the upper and lower walls is a critical factor influencing overall structural resistance. Therefore, the negative impact of discontinuous interlayers on shear capacity must be considered. Experimental studies [6-8] have shown that reducing keel spacing improves the shear capacity of the wall by 9–31%, depending on the wall structure. This increase in bearing capacity is attributed to the increased number of self-drilling screws due to reduced spacing. Gad [9] emphasized that stud spacing influences the failure load of the panel cladding wall, while increasing the keel section size and thickness improves shear capacity but reduces ductility and energy dissipation. Alabi et al. [10] evaluated the direct strength method of thin-walled steel members under the combined action of long axis compression and bending. Hu et al. [11] proposed an analysis model and calculation formula for the shear capacity of PFCFS composite walls. Zhang [12] proposed a formula for calculating the shear capacity of cold-formed thin-walled steel composite walls based on threaded connection failure.

Research on shear performance has mainly focused on intermediate walls, with little consideration given to exterior walls. The exterior wall differs due to the solid alignment of panels on the outer side and a permanently established boundary track at the floor joint, resulting in asymmetry along the wall's thickness direction. This structural difference leads to distinct failure modes and shear performance when compared to intermediate walls. Therefore, it is crucial to conduct experimental research to clarify the shear capacity and failure modes of the TCS wall, and further derive the stiffness theory for the external wall.

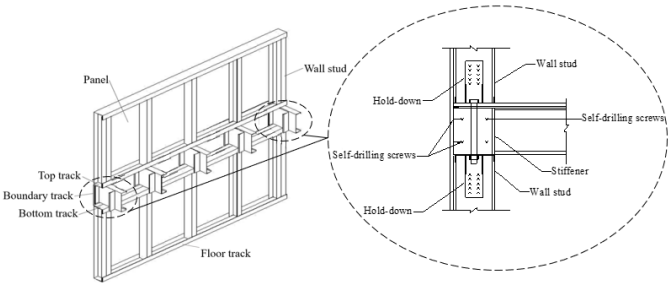

Fig. 1 Connection recommended by Regulation (JGJ/T 421–2018)

2. Experimental program

2.1. Material tests

The material utilized was Q235B galvanized steel with a nominal thickness of 1.0mm. The yield strength was improved due to multiple cold forming. Specimens followed the GB/T228.1–2010 [13] standard (Fig. 3). Three specimens underwent testing, yielding the following average results: a yield stress of 311.16 MPa, an elastic modulus of 160.19 GPa, and a yield strain of 0.19%. The fracture tensile strain reached 0.22, with the stress at fracture being 292.45 MPa. The ultimate strength recorded was 379.07 MPa, coupled with an elongation of 22.44%.

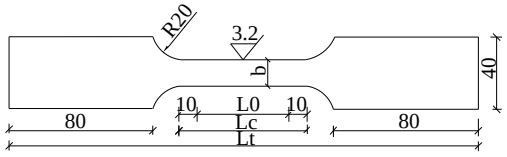

Fig. 2 Size of material properties specimen

2.2. Specimens design

9 specimens were designed based on different column web heights, types of anchor bolts and axial pressure ratios. The specimens were divided into 3 groups. The A group was the specimen with a web section height of 160 mm.

The B group was the specimen with a web section height of 89 mm. Through these two groups, the effects of different anchor bolt forms and different axial pressures on the shear performance of the wall were investigated. The C group was the specimen with a web section height of 89 mm basing on the specification [1]. It was used to obtain the influence of axial pressures on the shear performance of the wall.

All walls used double-sided cladding with full-scale sizes per specification [1]. Walls had 5 evenly spaced studs (3000 mm high) and 5 tracks (600 mm apart), with a 200 mm floor joint contributing to a total width of 2400 mm. Detailed component specifications are presented in Table 1. Wall studs were fixed to the boundary track with ST4.2 × 13 screws, spaced 100 mm apart (Fig. 3). The floor joint was 200 mm long. The wall stud at the boundary was an "I-shape" built-up section made of two C-sections (C89 or C160), while the central wall had a single C-section.

Table 1
Component specification

Components	Material	Specification
boundary track	thin-walled cold-formed steel	U200 mm × 40 mm × 1 mm
top and bottom tracks		U160 mm × 40 mm × 1 mm
floor track		C200 mm × 40 mm × 10 mm × 1 mm
wall stud		C160 mm × 40 mm × 10 mm × 1 mm
flat strap		40 mm × 1 mm

3 types of anchor bolts connected the wall sections: a-type, a 4.6-grade coarse bolt (40 mm diameter) with pressure-only nuts (Fig. 4(a)). The b-type anchor bolt (12 mm) was an anti-pull design with a nut and gasket at one end, relying on hold-down to transfer tensile pressure between floors and wall stud (Fig. 5(b)). The c-type anchor bolt (16 mm) had two pairs of nuts and gaskets at each end, forming a double nut design (Fig. 5(c)), allowing synchronized deformation of the top and bottom tracks. The differences in configuration was shown in Fig. 5. The specimen number and composition were shown in Table 2.

2.3. Test device

The testing apparatus primarily consisted of an MTS electro-hydraulic servo-controlled testing machine, a stationary frame, a reaction wall, a distribution beam, a ground track, and a reaction floor (Fig. 6). The distribution beam was constructed from 20a I-beam steel. During the experimentation, a 1000 kN jack was positioned atop the wall specimen. Between the distribution beam and the top track, a roller was placed, designed to move horizontally in tandem with the specimen, ensuring smooth load application. To mitigate specimen instability due to lateral eccentric loading, a support rod was horizontally positioned at the specimen's apex (Fig. 5). At the specimen's base, the U-shaped bottom track was bolted to the ground track using 20a channel steel, securing the assembly firmly in place. This setup was designed to maintain the integrity of the specimen under various loading conditions, allowing for accurate and reliable test results.

Table 2
Specimen number and composition

Serial number	Group	Specimens	Wall stud section (mm)	Vertical force (kN)	Number of anchor bolts	Panel type
1	A	WT-1	C160 × 40 × 10 × 1	30.2	2(b)	9mm Oriented strand board
2		WT-2	C160 × 40 × 10 × 1	40.3	2(b) and 3(a)	
3		WT-3	C160 × 40 × 10 × 1	30.2	2(b) and 3(a)	
4	B	WT-4	C89 × 44.5 × 12 × 1	40.3	2(b) and 3(a)	
5		WT-5	C89 × 44.5 × 12 × 1	30.2	2(b) and 1(a)	
6		WT-10	C89 × 44.5 × 12 × 1	40.3	2(b) and 3(c)	
7		WT-13	C89 × 44.5 × 12 × 1	30.2	2(b) and 3(c)	
8	C	WT-6	C89 × 44.5 × 12 × 1	40.3	2(b)	
9		WT-7	C89 × 40 × 10 × 1	30.2	2(b)	

Table 3
Test variables

Test variables	Specimens	Wall stud section (mm)	Vertical force (kN)	Number of anchor bolts
Wall stud section	WT-1	C160×40×10×1	30.2	2（b）
	WT-7	C89×40×10×1		
	WT-2	C160×40×10×1	40.3	2(b)+3(a)
	WT-4	C89×44.5×12×1		
Vertical force	WT-2	C160×40×10×1	40.3	2(b)+3(a)
	WT-3		30.2	
	WT-10	C89×44.5×12×1	40.3	2(b)+3(a)
	WT-13		30.2	
Number of anchor bolts	WT-1	C160×40×10×1	30.2	2（b）
	WT-3			2(b)+3(a)
	WT-4	C89×44.5×12×1	40.3	2(b)+3(a)
	WT-10			2(b)+3(c)
	WT-5	C89×44.5×12×1	30.2	2(b)+1(a)
	WT-12			2(b)+3(c)

2.4. Loading system

Prototype of the test was a 4-story cold-formed thin-walled steel house with a total height of 12 m. The length, width and each layer height were 12.8m, 10.8m and 3m respectively. The structural plane layout was shown in Fig. 7. The floor dead load, live load and the weight of the wall were 1.42 kN/m^2, 2.0 kN/m^2 and 1.0 kN/m^2 respectively. The weight of the doors and windows at the opening of the wall had been considered. The roof live load was 0.5 kN/m^2. Considering the conditions for 3-story and 4-story buildings, and referencing the calculation results in Section 4.4 of the monograph [14],

axial compressions of 30.2 kN and 40.3 kN were applied to the top of the wall during the experiment. The horizontal force was applied by a 1000 kN horizontal actuator.

The axial force on the specimen was applied in a single attempt, after which the initial displacement meter readings were documented. The loading system was detailed in Table 4. A low cyclic load was administered in the horizontal direction via displacement control, with increments of 5 mm per level. Each displacement stage was repeated thrice until the specimen succumbed to destruction.

2.5. Point arrangement

Strain data was captured using the DH3815N system, with ten strain gauges adhesively affixed to each specimen. The positioning of the strain gauges was illustrated in Fig. 8. Strain gauges numbered 1 through 5 were designated for assessing strain on the bolts, whereas gauges 6, 8, and 10 were tasked with gauging strain on the wall studs. Gauges 7 and 9 were specifically utilized for measuring strain on the diagonal tie bars. Fifteen YHD100 displacement meters were used: D1 for bottom track horizontal displacement, D2-D8 and D11 for wall elevations, D9-D10 for out-of-plane displacement, D12-D13 for vertical displacement at the base, and D14-D15 for the bottom track vertical displacement. The displacement and load values at the loading point were recorded using the displacement and force sensors attached to the actuator.

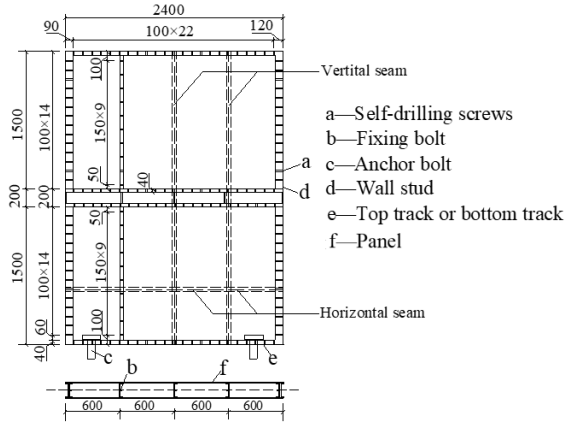

Fig. 3 The composite cold-formed thin-wall steel two-story exterior wall

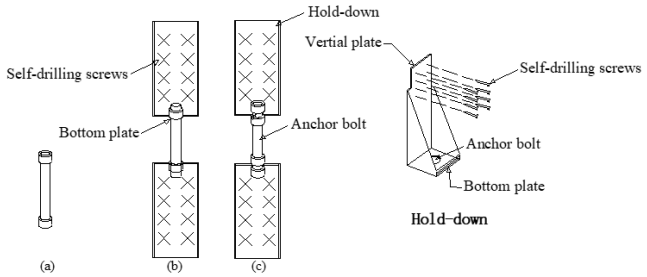

Fig. 4 Connection diagram

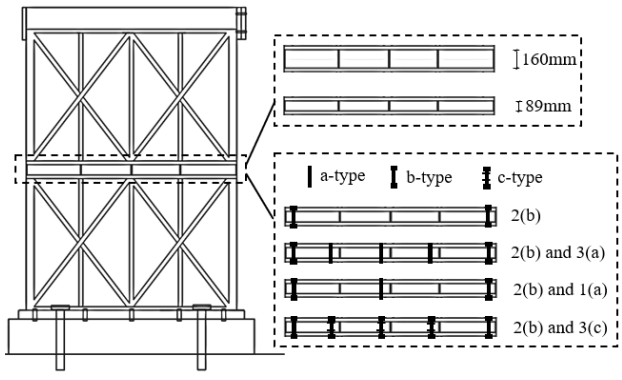

Fig. 5 Differences in configuration

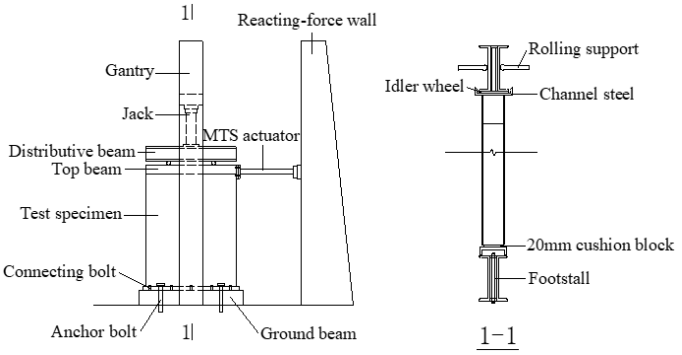

Fig. 6 Test equipment and site layout

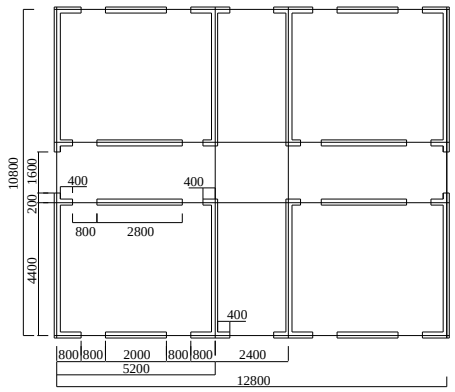

Fig. 7 Plan layout of the prototype

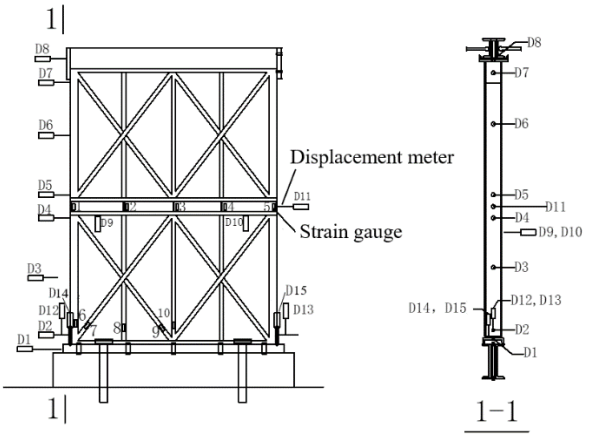

Fig. 8 Displacement meter and strain gauge arrangement

Table 4
Loading system

Load level	Displacement amplitude (mm)	Cycle index	Load level	Displacement amplitude (mm)	Cycle index
1	±5.0	3	2	±10	3
3	±15	3	4	±20	3
5	±25	3	6	±30	3
7	±35	3	8	±50	3
9	±55	3	10	±60	3
11	±65	3	12	±70	3

3. Test phenomena and failure characteristics

From the beginning of the test to the final destruction, it was divided into the following stages. Firstly, after the axial compression force was applied, the wall had a small out-of-plane displacement. Secondly, due to the discontinuity of the floor joint, the vertical load was transmitted to the floor track, the supporting stiffeners, and the boundary tracks, resulting in the local buckling

of the specimen. Finally, the self-drilling screws between the components were pulled out.

3.1. Group A

WT-1, designed per specification [1], showed small out-of-plane displacement at the floor joint after applying 30.2 kN vertical load (Fig. 9(a)). The out-of-plane displacement of WT-2 and WT-3 with three a-type anchor bolts was very small. The compressive capacity was obviously improved. When loaded to the limit state, due to the lack of constraints between the anchor bolt and the top and bottom tracks, the pressure is easily redistributed to the floor track after the anchor bolts fails, causing obvious buckling deformation (Fig. 9(b)). After the self-drilling screw at the corner of the wall was pulled out, the wall was separated from the keel (Fig.9(c)). After removing the outer OSB (oriented strand board), in addition to the obvious plastic deformation of the boundary track and the floor track, the keel of the upper and lower wall sections was intact (Fig. 9(d)). There was no local buckling of the bottom track. However, there is a vertical gap between the webs of the spliced section connected by self-drilling screws. In practical engineering applications, the self-drilling screws connected the two limbs should be encrypted.

3.2. Group B

WT-4 and WT-5 exhibited similar behavior. After applying axial compression, WT-5's floor track buckled slightly with one a-type anchor bolt. The WT-4 floor track with 3 a-type anchor bolts had no buckling. At a horizontal displacement of ± 35 mm, WT-5's floor track displayed localized buckling (Fig. 10(a)). Concurrently, the self-drilling screws connecting the corner panel to the keel failed (Fig. 10(b)). Local buckling occurred in the U-shaped track at the bottom of the wall stud (Fig. 10(c)).

After the three a-type bolts of WT-10 and WT-13 were replaced by c-type bolts, the compressive capacity was significantly improved. Upon applying axial compression to the top of the wall, the floor track exhibited no signs of buckling. When the horizontal loaded reaches ± 55 mm, the boundary tracks bulged outward obviously. The self-drilling screws connecting the wallboard and the keel at the floor joint squeezed the hole wall repeatedly. Then the screw hole on the panel became larger, and the slipping occurred between the drilling screw and the keel. The screw was pulled out when the loading displacement was greater. At the bottom, the self-drilling screws connecting the wall stud and the hold-down were damaged by shearing.

3.3. Group C

According to the practice of floor joint recommended by the specification [1], WT-6 and WT-7 showed similar failure modes. Upon the application of a horizontal displacement of ± 45 mm, pronounced local buckling was observed at the terminus of the floor track (Fig. 11(a)). During the continuous loading process, the boundary tracks bulged outwards. The out-of-plane deformation of the floor joint was obvious (Fig. 11(b)). The keel at the bottom of the wall stud was separated from the wallboard due to the pull-out of the self-drilling screws (Fig. 11(c)). Therefore, the number of self-drilling screws in this area should be increased. Local buckling of the bottom tack occurred under pressure. Compared with other specimens with the same vertical force, the failure characteristics appeared earlier and more obvious.

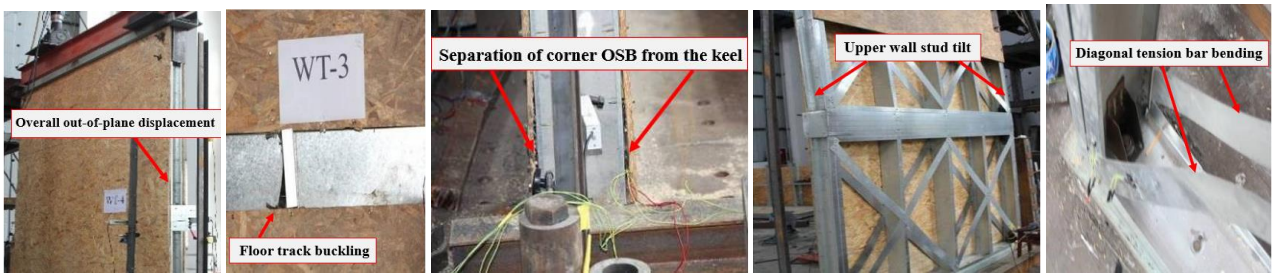

(a) (b) (c) (d) (e)

Fig. 9 Failure phenomena of A group. (a) Overall out-of-plane displacement. (b) Floor track buckling. (c) Separation of corner OSB from the keel. (d) Upper wall stud tilt. (e) Diagonal tension bar bending

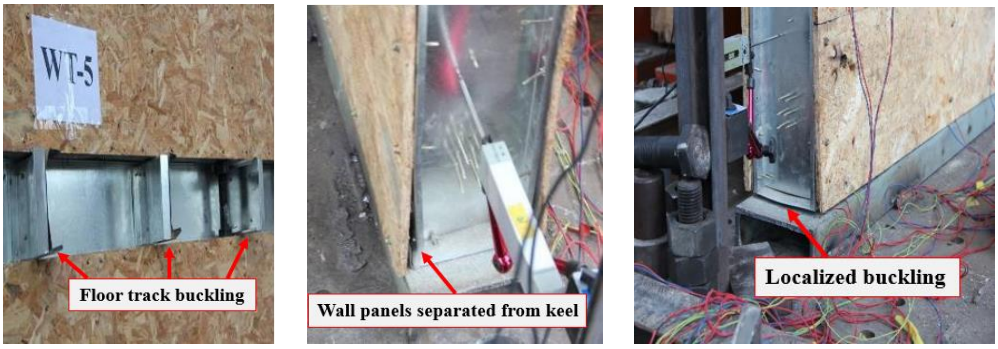

(a) (b) (c)

Fig. 10 Failure phenomena of B group. (a) Floor track buckling. (b) Wall panels separated from keel. (c) Localized buckling of the bottom track

(a) (b) (c)

Fig. 11 Failure phenomena of C group. (a) Boundary track buckling. (b) Wall panels separated from keel. (c) Self-drilling screws failure

4. Experiment results and analyses

4.1. Hysteresis curve

Load P was collected by the force sensor in the MTS actuator. Displacement Δ was the horizontal displacement of the top of the wall (at the upper guide rail). The load-displacement (P-Δ) curves of each specimen were shown in Fig. 12. Axial compression significantly impacted the energy dissipation capabilities of the specimens. Compared to specimens with an axial compression of 30.2 kN, those with an axial compression of 40.3 kN (WT-2, WT-4, WT-6, and WT-10) exhibited noticeably lower bearing capacity and reduced hysteresis curve characteristics. During the loading process of WT-4, the area of hysteresis curve increases little and no-load slip occurs. The reason was that the a-type anchor bolt end was lack of constraints under the cyclic load, which makes it prone to tilt failure. Top and bottom tracks were prone to local buckling failure after the failure of the anchor bolt. When WT-3 was loaded to -70mm cycle, WT-5 was loaded to ±40mm, and WT-13 was loaded to -45mm, the bearing capacity suddenly decreased. The main reason was the sudden out-of-plane displacement at the floor joint. Although the specimens can continue to bear load, their out-of-plane displacement increases significantly with loading. WT-6 and WT-7 were designed in adherence to the specification, with WT-6 exhibiting superior energy dissipation capacity than WT-7, thereby demonstrating the profound influence of axial compression on such specimens. Upon progressing to the failure state, the energy dissipation capacity of WT-6 and WT-7 remained relatively stable per cycle. The main reason was that the rigid motion of the upper and lower wall sections occurred almost along the floor joint and only the shear deformation of boundary track and the cyclic inclination of anchor bolts occurred at the floor joint. All the specimens had no apparent load drop section except for WT-3 and WT-5. For the side wall (wall single side with the boundary track), due to the asymmetric arrangement of structural members, the specimen had out-of-plane instability upon reaching the failure stage. As a result, most of the specimens had no obvious bearing capacity decline section. The local buckling of the floor track under compression led to a gradual reduction in the specimen's load-bearing ability. It can continue to bear the load, but the self-drilling screws on the external panel of the connection were loose. Consequently, the structural design should be enhanced to increase the compressive capacity of the floor joint. Merely bolstering the support stiffeners was insufficient to satisfy the load-bearing requisites.

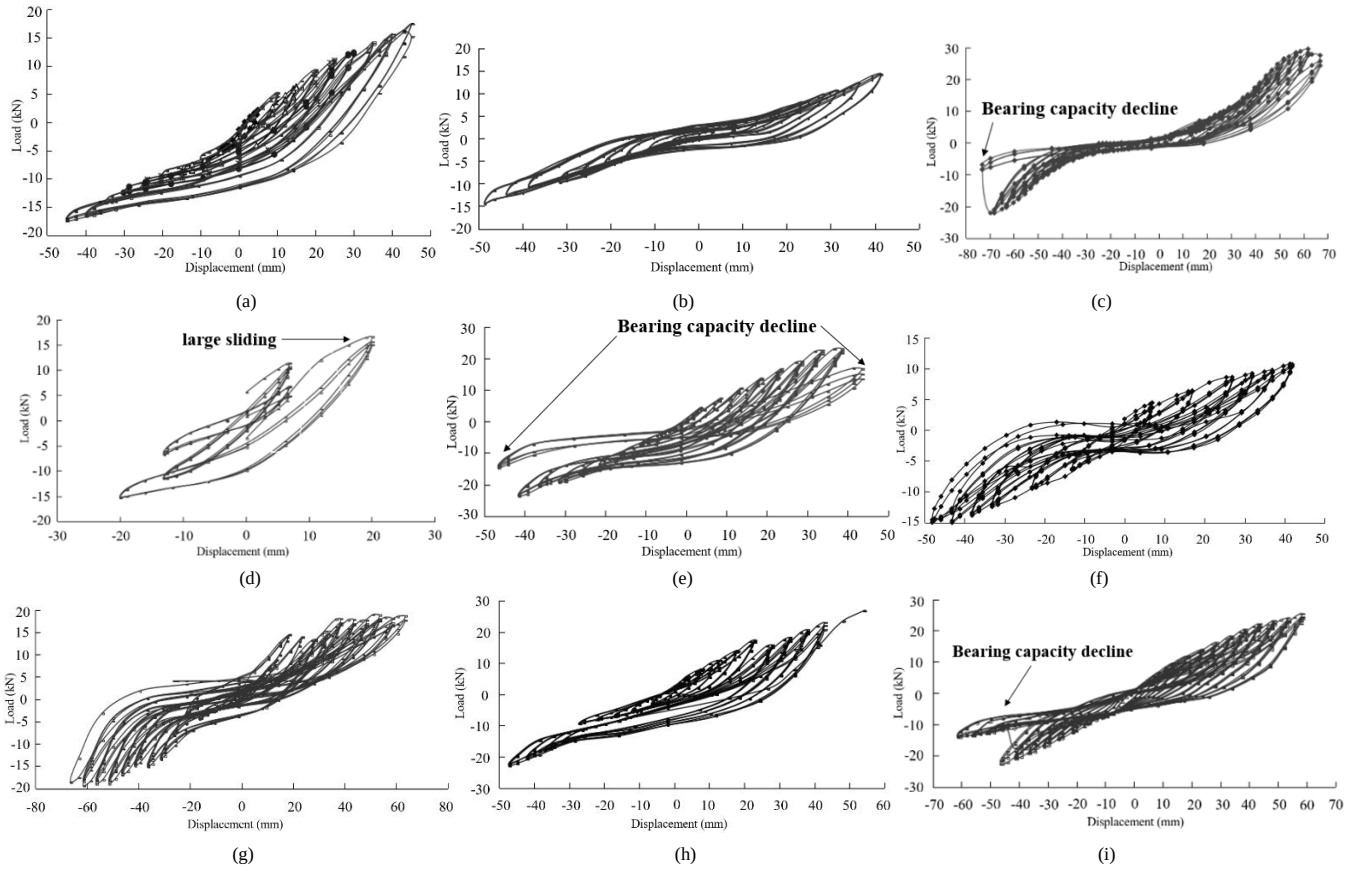

Fig. 12 Load-displacement curves. (a) WT-1. (b) WT-2. (c) WT-3. (d) WT-4. (e) WT-5. (f) WT-6(g) WT-7 (h) WT-10 (i) WT-13

4.2. Determination of yield point and failure load of specimen

The floor track exhibited significant deformation during loading, with the self-drilling screws at the edge of the floor joint becoming noticeably loose. According to European norms [15], 0.4 P_{max} was taken as the shear strength elastic limit of the wall, and that was the yield load. After loading to the ultimate load P_{max}, Sudden out-of-plane instability often occurred, resulting in the wall not continuing to load. Therefore, the failure load P_u took the same value as P_{max}. The P_y、Δ_y、P_{max}、Δ_{max}、P_u and Δ_u calculated by each specimen are summarized in table 5.

The bearing capacity of A group specimens was strongly influenced by both axial pressure and the type of anchor bolt used. With the same type of anchor bolts, the axial compression of WT-2 was higher than that of WT-3, resulting in a 51.8% reduction in ultimate bearing capacity. In contrast, WT-1, with three additional a-type anchor bolts, achieved at least a 26.8% increase in ultimate bearing capacity compared to WT-3. However, a comparison of WT-1 and WT-2 indicates that simply increasing the number of a-type anchor bolts did not significantly improve the bearing capacity. In Group B, following an increase in axial compression, WT-6 exhibited a 56.5% reduction in bearing capacity compared to WT-7. Additionally, the axial pressure had a considerable impact on specimens with extra anchor bolts, with WT-10 showing a minimum increase of 25.04% over WT-13. The C group further explored the effect of increased axial compression on bearing capacity. With increased axial pressure, the bearing capacity of WT-6 dropped by 56.5% compared to WT-7. On the basis of the C group of specimens, the B group was compared, which considered the increase of bearing capacity after adding different numbers of a-type anchor bolt. WT-5's bearing capacity was 1.22 times greater than that of WT-7, and WT-4's bearing capacity was 1.22 times higher than WT-6's. For the same count of different types of anchor bolts, WT-10's ultimate bearing capacity was 1.29 times that of WT-4, demonstrating a significant reinforcement effect. The inclusion of c-type anchor bolts markedly improved the shear capacity of the wall. However, the structural asymmetry caused by the boundary track and skin wall panels may lead to sudden out-of-plane instability, thus diminishing the wall's load-bearing capacity. Consequently, it is crucial to reinforce the out-of-plane support for the wall.

4.3. Energy dissipation and ductility performance

Cumulative energy dissipation is the sum of all hysteresis curve areas. The ductility coefficient is the ratio of the failure displacement to the yield displacement of the component ($\mu=\Delta_u/\Delta_y$). The cumulative energy dissipation and ductility coefficient were list in Table 5: When comparing identical structural specimens under varying axial compressions, it was found that WT-2's cumulative energy dissipation was 65.9% lower than that of WT-3, WT-6's was 67.7% lower than WT-7's, and WT-10's was 39.9% lower than WT-13's. As axial pressure increased, the cumulative energy dissipation capacity showed a clear decline. After adding 3 c-type anchor bolts, the influence of axial pressure was decreasing. The reason is that the double nuts reinforce the confinement of the top and bottom tracks. Consequently, the anchor bolts can more effectively synchronize the deformation between the upper and lower wall sections, thereby enhancing the resistance to failure. WT-10 exhibited an energy dissipation capacity that was 3.33 times higher than WT-4's, largely because WT-4 lacked the rod end restraint under cyclic loading. Following anchor bolt failure, the internal forces were redistributed to the boundary and floor track, exacerbating the specimen's out-of-plane instability. The ductility of the specimens was different after forward and reverse loading. Mainly because the forward loading was unstable and the reverse cannot continue to load. The anti-buckling ability of the floor track in the plane of the wall was improved after adding the c-type anchor bolt. Although minor deformations may lead to reduced energy dissipation capacity and ductility, there was a notable increase in the wall's bearing capacity.

Table 5
Summary of main test values

Specimens	Direction	Yield limit		Ultimate limit		Destructive load		μ	Ability to accumulate energy
		P_y(kN)	Δ_y(mm)	P_{max}(kN)	Δ_{max}(mm)	P_u(kN)	Δ_u(mm)		
WT-1	Positive	6.98	40.15	17.44	45.02	17.44	45.02	1.12	20952
	Negative	-6.98	-38.08	-17.44	-45.02	-17.44	-45.02	1.18	
WT-2	Positive	5.75*	17.31*	14.37	41.40	14.37	41.40	2.39*	10502
	Negative	-5.75	-20.40	-14.37	-48.63	-14.37	-48.63	2.38	
WT-3	Positive	11.91	34.71	29.77*	66.93	25.30	66.27	1.91	30768
	Negative	-8.85	-44.02	-22.12	-68.12*	-18.81	-70.50*	1.60	
WT-4	Positive	6.64	15.96	16.59	20.01*	16.59	20.01*	1.25	6263*
	Negative	-7.08	-25.75	-17.71	-26.21	-17.71	-26.21	1.02*	
WT-5	Positive	9.25	31.45	23.12	38.48	19.65	41.20	1.31	23929
	Negative	-9.51	-38.88	-23.77	-41.54	-20.20	-43.52	1.12	
WT-6	Positive	4.26	30.03	10.65	41.91	10.65*	41.91	1.40	8752
	Negative	-5.82	-36.70	-14.55*	-48.10	-14.55	-48.10	1.31	
WT-7	Positive	7.53	34.47	18.83	53.47	18.83	53.47	1.55	27080
	Negative	-7.76	-56.94*	-19.41	-61.57	-19.41	-61.57	1.08	
WT-10	Positive	9.17	33.16	22.93	42.81	22.93	42.81	1.29	20758
	Negative	-9.17	-26.20	-22.93	-47.23	-22.93	-47.23	1.80	
WT-13	Positive	10.16*	45.43	25.41	58.46	25.41*	58.46	1.29	34566*
	Negative	-9.10	-39.34	-22.75	-46.55	-19.33	-48.31	1.23	

Note: The parameter with * represents the maximum absolute value or the minimum absolute value of the parameter.

4.4. Rigidity degradation

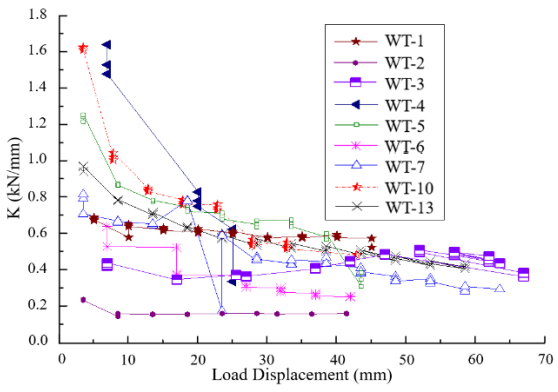

Fig. 13 Stiffness degenerated curve

The stiffness of the specimen under cyclic loading will decrease with the increase of the number of cycles and the load, which is called stiffness degradation. Rigidity can be expressed by ring stiffness *K*, referring to the method in regulation [16]. The stiffness degradation curve was shown in Fig. 13: The stiffness declined rapidly when the displacement reached between 10 mm and 30 mm. This rapid degradation was attributed to the detachment of self-drilling screws at this stage, coupled with local buckling of the floor track under compression. The accumulation of various damages caused the stiffness of the specimen to decrease. After the displacement was loaded to 60 mm, the specimen had out-of-plane displacement, resulting in the stiffness degradation to a minimum and unable to continue to bear. The degradation of WT-10 occurred more gradually compared to the other specimens, owing to the constraint imposed by the c-type anchor bolts on the top and bottom beams. Under cyclic loading, these bolts enabled better cooperation between the upper and lower wall sections, slowing stiffness degradation until the self-drilling screw disengaged. WT-4 had the maximum initial stiffness due to the increase of three a-type anchor bolts. But the degradation rate was faster. The reason was that the anchor bolt is fail, during the large displacement loading stage under cyclic load.

4.5. Strain-displacement curve

The strain-displacement curve was shown in Fig. 14. According to the material test, the yield strain was 1900×10^{-6}. The keel strain on all specimens had not reached the yield strain. When WT-10 was loaded to the failure state, the maximum strains of the middle vertical keel and the diagonal tension bar were 1826×10^{-6} and 121×10^{-6}, respectively, which proved that the material utilization rate was low and its effect was not obvious.

Under the same load, the keel strain of the A group of specimens was lower than that of the other groups. The maximum strain on the keel was 152×10^{-6} when loaded. The stress did not reach 10 % of the yield strength value. However, the self-drilling screw pull-out or out-of-plane instability of the whole wall had occurred, indicating that the material utilization rate was low after the cross section increases. In practice, reducing the keel section size may be considered.

The effectiveness of anchor bolts at the floor joint was pronounced. In WT-4, the anchor bolt's maximum micro-strain reached 1148×10^{-6} at the limit state. The maximum micro-strain of the WT-10 anchor bolt hit 1623×10^{-6}

upon failure. Therefore, incorporating c-type anchor bolts in engineering practice is recommended to improve the compressive strength of the floor joint.

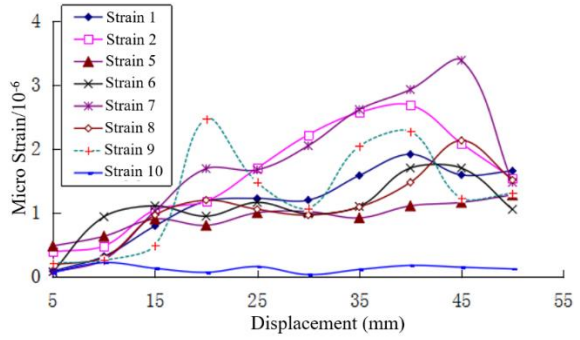

(a)

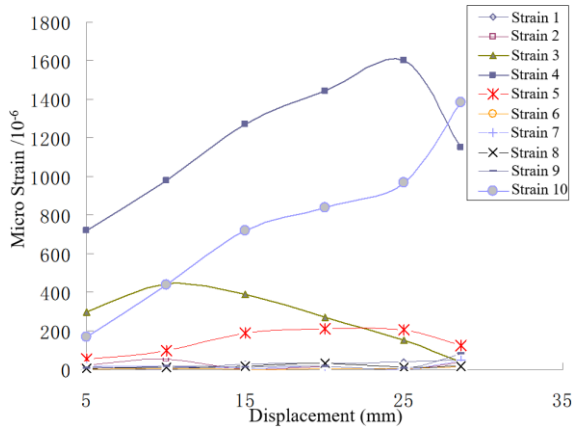

(b)

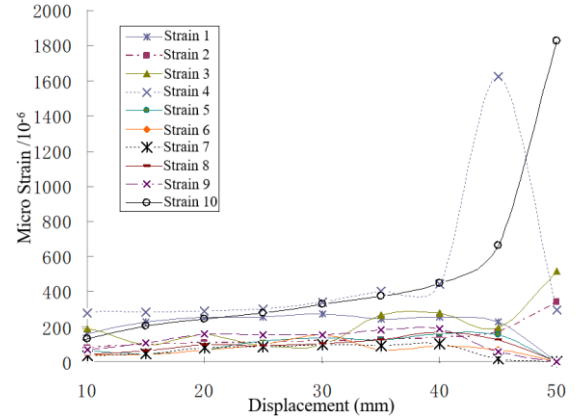

(c)

Fig. 14 Load-strain curve. (a) WT-1. (b) WT-4. (c) WT-10

5. Theoretical calculations of anti-lateral stiffness of the wall

The experimental data shows significant displacement at the floor joint, which requires attention. Given the current ambiguity in theoretical models, further refinement of stiffness calculations is necessary. This effort holds profound implications for structural assessment and offers valuable insights for the engineering design of the walls. At the initial stage of loading, the shear stiffness of anchor bolt is large. The lateral displacement at the floor joint is very small. The total lateral displacement of the wall is mainly caused by the lateral displacement of the upper and lower walls. But loaded to the late anchor bolt tilted. Following the tilting of the self-drilling screws on the shear member, the lateral stiffness becomes exclusively dependent on the boundary track and the external panels. Consequently, the lateral stiffness of the the wall's floor joint ought to encompass the lateral stiffness of the anchor bolt and the shear stiffness of the external panel. The shear stiffness calculation of the floor joint should include both the boundary track and the panel outside it.

5.1. Shear deformation calculation of wall panel

Fig. 15 is the shear deformation diagram of the boundary track and the external panel at the floor joint. It can be obtained Eq. (1) from $\tau = G\gamma$.

$$\frac{P}{Lt} = G\frac{\Delta_p}{H} \tag{1}$$

It can be seen from Eq. (1) that both the boundary track and the external panel of the floor joint can bear the shear force. It can be obtained Eq. (2).

$$\Delta_p = \frac{PH}{Lt_1G_B} + \frac{PH}{Lt_2G_S} \tag{2}$$

In which: Δ_p is the shear deformation of the wall panel. P is the horizontal shear force on the top of the wall. H is the height of the wall. L is the width of the wall. t_1 is the thickness of the external panel of the wall. t_2 is the thickness of the boundary track. G_B is the shear elastic modulus of the wall external panel. G_S is the shear elastic modulus of the boundary track. The shear deformation of the wall is shown in Fig. 15.

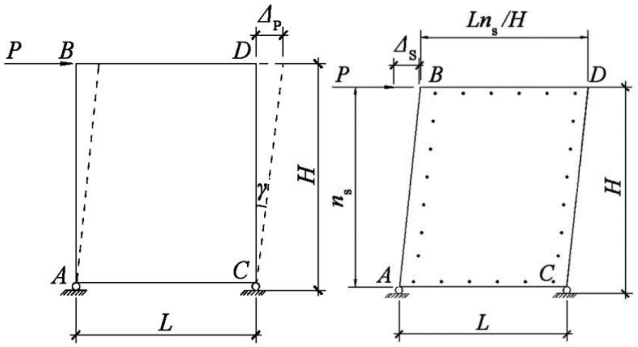

(a) (b)

Fig. 15 Shear deformation. (a) Shear deformation of wall panel. (b) Shear deformation caused by screws slip of wall panel

5.2. Shear deformation caused by sliding of self-drilling screws on wall panel

According to Reference [17], in the steel skeleton wall, the shear deformation caused by the slip of the self-drilling screw on the wall panel is calculated by the slip of the screw. Because the limit of panel size, a wall is often composed of many wall panels. There are joints between the two wall panels. The spacing between the surrounding and internal self-drilling screws of each wall panel is usually different. For the convenience of formula derivation, it is assumed: the actual wall is equivalent to only one wall panel. Screws are distributed around the panel, with uniform spacing in length and width directions, and the number is based on the average pitch. The shear force of each screw is equal and the screw slip is the same (Fig. 16). According to the above assumptions, the ratio of H to L is approximately equal to the ratio of the number of screws on the corresponding side. The shear force of a single screw is:

$$q_s = \frac{P}{n_s} * \frac{H}{L} \tag{3}$$

In which: P is the horizontal shear force on the top of the wall. n_s is the number of self-drilling screws along the height of the wall.

Under the action of P, the slip of a single self-drilling screw is S_s. According to the principle that the external force work is equal to the internal force work, it can be obtained Eq. (4).

$$P\Delta_S = 2q_sS_sn_s + 2q_sS_s \cdot \frac{Ln_s}{H} = 2PS_s\left(\frac{H}{L}+1\right) \tag{4}$$

That is:

$$\Delta_S = 2S_s\left(\frac{H}{L}+1\right) \tag{5}$$

fs is the shear force of the self-drilling screw to reach the maximum shear bearing capacity of the connection, and S0 is the slip at this time. Ss is the amount of screw slip when the maximum shear capacity is not reached. It can be obtained Eq. (6).

$$\frac{S_0}{S_s} = \frac{f_s}{q_s} \tag{6}$$

That is:

$$S_s = \frac{q_s S_0}{f_s} = \frac{PHS_0}{f_s n_s L} \tag{7}$$

Substituting the Eq. (3) and (6) into the Eq. (5), it can be obtained Eq. (8).

$$\Delta_S = \frac{2PHS_0}{f_s n_s L}\left(\frac{H}{L}+1\right) \tag{8}$$

5.3. Calculation of Horizontal Shear Deformation at Floor Joint

The calculation of horizontal shear deformation at floor joint includes the boundary track and the panel. The shear stiffness can be expressed as Eq. (9).

$$K = \frac{P}{\Delta} = \frac{Lt_1G_B}{H} + \frac{Lt_2G_S}{H} + \frac{f_s n_s L}{2HS_{01}\left(\frac{H}{L}+1\right)} + \frac{f_B n_s L}{2HS_{02}\left(\frac{H}{L}+1\right)} \tag{9}$$

That is:

$$\Delta = \frac{P}{K} \tag{10}$$

In which: H=2400 mm, L=200 mm, t_1=9 mm, G_B=1348.72 N/mm^2, t_2=1 mm, G_S=79230.77 N/mm^2, $f_b=\beta f_c dt_2$=1×205×4.2×1=861 N/mm^2, n_s=17, $f_s=f_B=\beta f_c dt$, f_c=25.83 N/mm^2.

Under the action of frequent earthquakes: S_{01}=0.35 mm, S_{02}=1.5 mm, substituted into the formula (10), it can be obtained $\Delta=1.28\times10^{-4}$P mm.

Under the action of rare earthquakes: S_{01}=1.25 mm, S_{02}=3.5 mm, substituted into the formula (10), it can be obtained $\Delta=1.30\times10^{-4}$P mm.

Through the calculation formula for the shear stiffness at the floor joint, the maximum lateral displacement can be further obtained. In the experiment, the bearing capacity of the wall is more than 10kN. Under the action of frequent and rare earthquakes, the maximum horizontal lateral displacement at the floor joint can be further obtained, which can reach 1.28mm and 1.3mm, respectively. Considering that the wall panel is relatively brittle, when loading to the elastic-plastic deformation stage under rare earthquakes, the OSB at the floor joint will be split due to shear action. To mitigate lateral displacement at the floor joint and prevent the failure of the outer panel following the tilting of anchor bolts, it is advisable to integrate reinforcing components at the floor joint.

6. Conclusion

The shear performance of the composite cold-formed thin-wall steel two-story exterior walls with different axial pressures and different types of anchor bolts is experimentally studied. The following conclusions are obtained:

(1) The self-drilling screws at the corner of the floor joint, the bottom of the wall, between the keels and between the keel and the wallboard are prone to loosening. Anti-pulling screws should be used to replace ordinary screws., and the number of self-drilling screws in these parts should be increased.

(2) Axial compression has a great influence on the bearing capacity and energy dissipation capacity of the wall. As the axial compression intensifies, the floor track becomes susceptible to local buckling and out-of-plane displacement at the floor joint, leading to a swift onset of instability and subsequent failure of the wall.

(3) The floor joint is the weak part of the wall. Utilizing the a-type anchor bolt enhances its compression resistance. However, due to the lack of rod end constraint, the cyclic load is easy to cause the failure of the anchor bolt. And then the pressure is redistributed to the floor track to cause rapid failure of the wall.

(4) Stress analysis reveals that the use of a double nut anchor bolt results in a 1.22-fold increase in load-bearing capacity. The bearing capacity is increased by 1.29 times and the energy dissipation capacity is increased by 3.33 times after using three double nut anchor bolts. The shear performance of the wall is obviously improved. It is recommended to use double nut anchor bolts at floor joints of multi-story buildings to enhance both load-bearing capacity and energy dissipation.

References

[1] JGJ227-2011 Technical specification for low-rise cold-formed thin-walled steel framing buildings, S. Beijing: China Architecture & Building Press, 2011.

[2] J.H. YE, Z.Y. Zhou. Discussion on light steel construction and development, J. Journal of Harbin institute of technology. 48 (6) (2016) 1-9.

[3] X.M. Zhai, X.X. Zha, K. Wang, et al. Shake table tests of a full-scale two-story plate-type modular composite building with semi-rigid corner connections, J. Engineering Structures. 289 (2023) 116-325.

[4] Y. Shi, X.W. Ran, G. Xiong, et al. Numerical modeling on shear performance of braced cold-formed steel composite walls, J. Journal of Constructional Steel Research. 198 (2022) 107-579.

[5] W.H. Liu, L. Deng, W.J. Zhong, et al. Parametric study on the pull-out performance of screw connections in cold-formed thin-walled steel structures, J. Engineering Structures. 274 (2023) 115-007.

[6] Liusi Dai, Xianzhong Zhao, Kim J.R. Rasmussen, Cyclic performance of steel storage rack beam-to-upright bolted connections, J. Journal of Constructional Steel Research. 148 (2018) 28-48

[7] Lewandowski MJ, Gajewski M, Gizejowski M, Numerical analysis of influence of intermediate stiffeners setting on the stability behaviour of thin-walled steel tank shell, J. Thin-Walled Structures. 90 (2015) 119-127

[8] Xu L, Martínez J, Strength and stiffness determination of shear wall panels in cold-formed steel framing, J. Thin-Walled Structures. 44 (10) (2006) 1084-1095.

[9] Gad EF, Duffield CF, Hutchinson GL, Lateral Performance of Cold-formed Steel-framed Domestic Structures, J. Engineering Structures. 21(1) (1999) 83-95.

[10] Song Hu, Li Zhou, Yong Huang, Experimental investigation on the seismic performance of phosphogypsum-filled cold-formed thin-walled steel composite walls, J. Thin-Walled Structures. 186 (2023) 110664.

[11] Xiuhua Zhang, Enyuan Zhang, Yizhuo Zhang, Study on shear performance of cold-formed thin-walled steel walls sheathed by paper straw board, J. Engineering Structures. 245 (2021)112873.

[12] M.A. Alabi-Bello, Y.C. Wang, M. Su, An assessment of different direct strength methods for cold-formed thin-walled steel beam-columns under compression and major axis bending, J. Structures. 34 (2021) 4788-4802.

[13] GB/T 228.1-2010(GB/T 228.1-2010 Metallic materials-Tensile testing, S. Beijing: Standards Press of China, 2010.

[14] Y.P. Chu, Y. Yao, Y.J. Deng, et al. Multi-storey ultra-thin-walled cold-formed steel structure housing system, M. Science Press. 2021.

[15] R. WANG, Y. YAO, Y.P. CHU. Wind-induced Response Numerical Simulation of Multilayer Cold-formed and Thin-walled Steel Structure under Different Wind Angle, J. Building Science. 11 (2015) 103-108.

[16] ECCS-TW1.3. Recommended testing procedure for assessing the behavior of structural steel elements under cyclic loads, R. ECCS Pub, 1986.

[17] Bai JL, Ou JP. Seismic failure mode improvement of RC frame structure based on multiple lateral load patterns of pushover analyses, J. Science China Technological Sciences. 54(11) (2011) 2825-2833.